A. D. MCCXXIV

UNIVERSITA' DEGLI STUDI DI NAPOLI FEDERICO II

Dottorato di Ricerca in Ingegneria Informatica ed Automatica

Comunità Europea
Fondo Sociale Europeo

ANALYSIS AND APPLICATION OF BIFURCATIONS IN SYSTEMS WITH IMPACTS AND CHATTERING

RICARDO ALZATE CASTAÑO

Tesi di Dottorato di Ricerca

XXI Ciclo

Novembre 2008

Il Tutore

Prof. Mario di Bernardo

Il Coordinatore del Dottorato

Prof. Luigi P. Cordella

Dipartimento di Informatica e Sistemistica

via Claudio, 21- I-80125 Napoli - ☎ *[#39]* (0)81 768 3190 - *[#39]* (0)81 768 3186

ANALYSIS AND APPLICATION OF BIFURCATIONS IN SYSTEMS WITH IMPACTS AND CHATTERING

By
Ricardo Alzate Castaño

SUBMITTED IN PARTIAL FULFILLMENT OF THE
REQUIREMENTS FOR THE DEGREE OF
DOCTOR OF PHILOSOPHY
AT THE
UNIVERSITY OF NAPLES - FEDERICO II
NAPLES, ITALY
NOVEMBER 2008

A mi familia,
que nunca me abandonó...

Abstract

In this Thesis we present the implementation and characterization of a practical impact oscillator: the cam-follower system. Complex dynamics experienced by the system after variation of the rotational speed of the cam ω taken as parameter, are analyzed through experimental, numerical and analytical tools. The most representative feature captured experimentally and reproduced after accurate simulation of the model, is the coexistence between a single-impacting periodic orbit and a multi-impacting trajectory with chattering, all of this occurring over a representative range of parameter values. Exhaustive numerical and analytical investigation including: Monte Carlo simulations, numerical continuation, calculation of basins of attraction and local analysis of perturbations, allowed to demonstrate that the interruption of complete chattering motion creates a sudden transition to chaos in the multi-impacting orbit characterized by a scaled and translated sequence of grazing bifurcations. An expression for the map local to the interruption of complete chattering is derived after performing expansion in series of the solutions; i.e. by analysis of variational equations, with further numerical validation. Additional work includes the extension of the local results for an accurate derivation of the equivalent Poincaré map describing the periodic chattering orbit.

Key words: Chattering, Cam-follower, Coexistence, Experiment, Local map.

Acknowledgements

The author would like to acknowledge:

The Professors of the National University of Colombia: Gerard Olivar Tost, Fabiola Angulo García and Germán Castellanos Domínguez, because through them this opportunity started one day of August 2005 in the green mountains of Manizales - Colombia.

Prof. Mario di Bernardo (supervisor), Prof. Francesco Garofalo (head of SINCRO group), Prof. Luigi P. Cordella (academic coordinator of the Ph.D. program in Computer Science and Automation) and all the staff members of the Department of Computer Science and Systems (DIS). Also to Sig. Fiorenzo Canestrelli, Sig. Aldo Corbo and staff members of the Ph.D. administration office; as well as to Dott.sa Marta Maciocia from the International House Program. All of them in behalf of the University of Naples - FEDERICO II, allowed the possibility of performing my doctoral studies in Italy.

Dr. Petri T. Piiroinen from the National University of Ireland - Galway, for his clever advices at the right moment. Also to Prof. Tom Sherry, Ms. Noelle Gannon and staff members of the Department of Mathematical Physics at NUIG. To Pauline, Ms. Piiroinen. Thank to them, Ireland became an important and unforgettable experience.

Prof. Chris Budd and the Ph.D. student Stephen Pring, both from the University of Bath - U.K. for the interesting discussions concerning the dynamics of impact oscillators. In particular, to Stephen for his patience to explain me how to perform series expansions.

Dr. Phanikrishna Thota, for sharing his knowledge on continuation; Dr. Joanna Mason for the kindly help on interpretation of BA; the Ph.D. student Athanasios Polynikis and in general to all the Docs, PostDocs and staff of the Engineering Mathematics Department at Bristol University - U.K. for the good time i spent there (including many nonlinear coffees).

Dr. Stefania Santini, the Ph.D. students Umberto Montanaro and Gustavo Osorio, and the M.Sc. students Giuseppe Giordano and Giovanni Rea, all of them from the University of Naples - FEDERICO II, for their important support and contributions in experimental activities.

Sig.ra Annamaria Bova, for thousands of favours.

Ing. Salvatore Carotenuto, Ing. Vincenzo Autiero, Ing. Claudio Briante, Ing. Achille Caldara, Ing. Maria Romano, Ing. Pietro De Lellis, Dr. Francesco Sorrentino, Dr. Sabato Manfredi and other members of SINCRO (nonlinear systems, networks and control) group.

Again to Prof. Olivar and the group ABC dynamics, for their hospitality during my research visit to the DIEE&C at UNAL - Manizales.

Prof. Enric Fossas from the Technical University of Cataluña UPC and staff members and visitors of the CRM (Centre de Recerca Matemática) at the Universidad Autónoma de Barcelona - Spain, during the thematic activity on complex non-smooth dynamical systems.

Jerzy Piotr Nowakowski, Jurema López Castro and Nicola Tammaro, for being my friends.

Elizabeth Carvajal and Javier. Also Raúl Santiago Muñoz. For the good moments in Barcelona.

Valentina Echeverri Ocampo, Adriana Díaz Arias and Mauricio Orozco Alzate, for the good moments in the Netherlands. Again to Adriana and Joe, for their hospitality during the DDE2008 conference at Delft.

Jaime Marín and Carolina, for the familiar Christmas environment of 2007.

Ms. Katherine Davies and Jeremy, in Bristol.

Carlos Lino Rengifo, Juan Diego Pulgarín, Rafael Meneses and Francy Elena, Cesar Augusto Ortíz, Eliana Riquett, Juan Felipe Franco and Santiago Salamanca, for bring their encouragement from Colombia.

Dr. Vanessa Moreno from UPC - Barcelona and Dr. Ana Lucia Pérez from U. de Antioquia - Colombia.

Ing. Alfonso Giuliano and Ing. Fabio Ferrara for contribute to the research with their Bachelor degree projects.

Also, i want to thank God.

Napoli, Italia **Ricardo Alzate Castaño**
Novembre 28, 2008

This research has been funded by the University of Naples - FEDERICO II through a three year scholarship **Borsa di Studio 2006-2008**. In 2007, an assignment for a brief research period in the U.K. was sponsored by the **Programa di scambi internazionali con Università ed istituti di ricerca stranieri per la mobilità di breve durata di docenti, ricercatori e studiosi**. In 2008, an additional contribution was assigned to develop a research period in Ireland: **Bando di selezione per titoli e colloquio per l'assegnazione di un contributo integrativo a favore di dottorandi di ricerca che si recano all'estero**. Other activities were supported by the European project **SICONOS** and the Italian project **MACSI-PRIN**.

Table of Contents

List of Figures

List of Tables

Chapter 1

Introduction and motivation

Studying the interaction of components in multivariate and complex structures, has been considered traditionally as an interesting challenge for researchers in many disciplines, specially when addressing large scale problems. Examples include the analysis and modelling of populations, economies, climates and most modern problems dealing with networking and information management. The level of applicability, development and extension of the mathematical models is in general conditioned by the quantity of interacting elements that can be handled, suggesting in most of the cases employment of reduced equivalent representations, using the lowest allowable set of features describing accurately the particular situation, or in technical terms, using the minimum number of *degrees of freedom* [18].

Dynamical systems can then, be considered as a set of stimuli-response schemes on a given environment, that in the most simple case will reflect the behaviour of a fundamental entity as a result of external influences. Specifically, this last approach has been employed in mechanics for the analysis of *single-degree of freedom* (SDOF) models, when studying dynamics associated to particles, excited generally by smooth-periodic forces. For instance, the pioneering work of Budd and Dux [20] reduces the problem associated with dynamics of flows in a boiler, into a SDOF model with sinusoidal excitation. There, interactions of fluids with walls of a heat-exchanger were considered as instantaneous collisions, well modelled in terms of restitution laws. Hence, preliminary work and results on impacting oscillators by Holmes [81], Whiston [99, 98], Thompson [88] and Peterka [68, 69, 70], could then be successfully applied.

1.1 Impact oscillators as PWS systems

Piecewise-smooth (PWS) *systems* represent dynamical models where solution trajectories in the state-space are constrained to delimited areas, each described by particular sets of differential equations. Therefore, depending on the type of discontinuity experienced by the system flow between such areas, a rough classification of PWS systems can be obtained, contributing towards a new general theory of nonsmooth dynamical systems, as described in [33] and later in Chapter 2. Of particular interest for this Thesis are *hybrid* PWS systems where in a SDOF model, a rigid boundary maps the velocity component instantaneously. Consider as an illustration, the toy model employed by Budd and Dux in [20, 22], where dynamics of a normalized single degree of freedom harmonic oscillator composed of an undamped-driven mass bouncing against a wall, can be described in terms of the hybrid structure (see Figure 1.1):

$$\begin{aligned} \ddot{x} + x &= g(t), \quad x < \sigma \\ \dot{x} &\to -r\dot{x}, \quad x = \sigma, \end{aligned} \tag{1.1}$$

with $g(t) = cos(\omega t)$ representing an external periodic driving-force and $0 < r < 1$ being the coefficient of restitution for inelastic collisions, applied over the state each time the mass reaches the boundary $x = \sigma$.

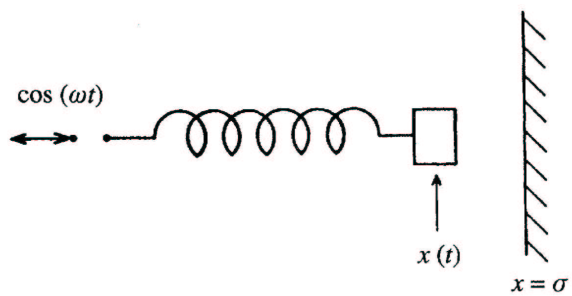

Figure 1.1 — A simple impact oscillator, reproduced from [22].

These type of nonsmooth models are denominated *impact oscillators* and have been the subject of much research effort in dynamical systems and control for many years. Starting with the preliminary work of Whiston, Peterka and Nordmark [99, 68, 69, 56], it has been shown that this class of dynamical systems can exhibit a rich bifurcation scenario involving the occurrence of both classical bifurcations (saddle-node, period-doubling, etc) and so-called *discontinuity-induced bifurcations* (DIBs) [33].

DIBs are unique to piecewise-smooth dynamical systems and are associated with the nontrivial interaction between system trajectories and discontinuity boundaries (or manifolds) in phase-space where the states (or vector field) become non smooth. In impacting systems, the most notable type of DIB is the *grazing* bifurcation of a limit cycle, observed when, under parameter variations, a limit cycle becomes tangential to the system discontinuity manifold. Grazing bifurcations have been shown to be associated to a wide range of dynamical transitions including nonsmooth folds and sudden transitions from periodic to chaotic behaviour (see [33] and references therein for further details).

1.2 Novel dynamical scenario

Apart from grazing, another important feature of impacting systems is the possibility for an infinite sequence of impacts to accumulate in finite time. This phenomenon, also termed as *chattering* or Zeno behaviour in the literature [22, 58, 57, 80], has been shown to be the key to uncover the intricate structure of the system dynamics, as for example to predict the topology of its basins of attraction or regions where *sticking* occurs. Figure 1.2, illustrates a trajectory experiencing periodic complete-chattering motion.

Sticking in impact oscillators corresponds to the mass remaining in contact with the impacting obstacle over a finite time interval and has been recently related to the occurrence of so-called sliding solutions in piecewise-smooth flows [34]. In [57], it has been proposed that a new type of DIB occurs in impacting systems when, under parameter variations, a complete chattering sequence (leading to sticking) is interrupted. Basically, when one or more parameters are varied, a periodic orbit characterized by an infinite number of impacts accumulating in finite time suddenly looses its stability as the chattering sequence becomes incomplete with the trajectory escaping the sticking region after a finite (large) number of impacts.

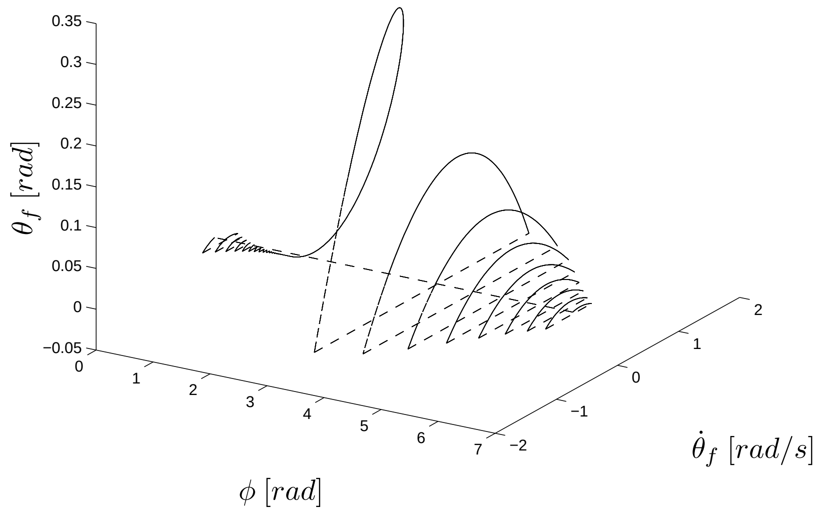

Figure 1.2 — Periodic multi-impacting orbit with chattering, depicting the trajectory of a particle colliding infinitely with a rigid body before being released.

The phenomenon described above has been observed by some authors in the existing literature and given the name of “rising bifurcation” or “chattering interruption”. Figure 1.3 depicts annihilation of sticking in an orbit with complete chattering.

A reference to this phenomenon can be found in [92], while numerical evidence of its occurrence in a two-degree-of-freedom impacting oscillator is reported in [95], [96], [97]. Therefore a pressing open problem is to fully investigate this novel bifurcation phenomenon which is unique to impacting systems. It is worth mentioning here that despite its theoretical and numerical observation, this phenomenon has seldom been shown to occur experimentally.

1.3 Application-driven research

As the analysis of bifurcations in piecewise-smooth systems is further expanded, it is becoming increasingly important to carry out an extensive experimental investigation and validation of the theoretical results obtained. Complex behaviour in impacting systems has been observed experimentally in a number of papers in the literature. Examples include the early work on impact oscillators in [12], [14], [46], [63], [91], [84]. More recent papers include the work by Wiercigroch et al reported in [101] and the results of Piiroinen et al on impacting pendula [73]. For further details see also the books [17], [100] and references therein.

Particularly cumbersome dynamics can be observed in the case of impact oscillators with moving boundaries. For example, in [24], it is suggested that a novel bifurcation phenomenon termed as corner-impact can occur in discontinuously-forced impact oscillators.

In applications, the occurrence of complex behaviour in impacting systems has been recently detected in an important class of devices: *cam-follower systems* [6, 65, 66]. These are widely used in a large range

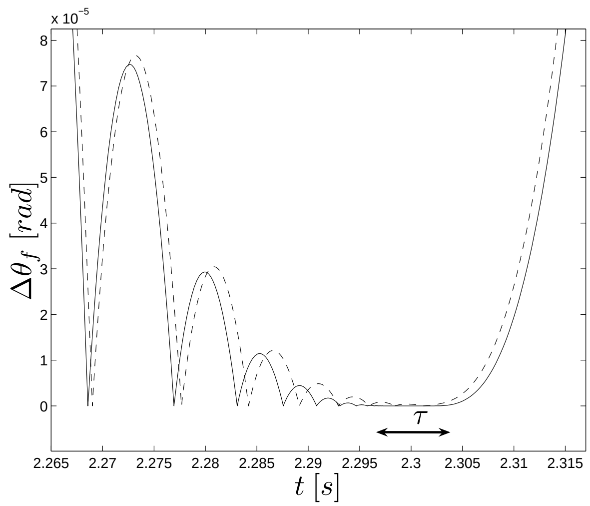

Figure 1.3 — Evolution in time of solution trajectory with chattering, in the case complete (solid) for $\omega = 152.65$ *rpm* and interrupted (dashed) for $\omega = 152.69$ *rpm*, with τ denoting the interval of sticking. This graph is a $2D$ version of Figure 1.2 with $\phi \equiv t$.

of mechanical devices, most notably in internal combustion engines [44] [61]. In these systems, an appropriately shaped rotating cam imparts to the follower a desired motion that is used to operate a device of interest (see [61] for further details). In [65, 66] it was observed that cam-follower devices can exhibit complex behaviour which was conjectured to be due to chattering and its interruption. Figure 1.4 depicts a cam-follower system interacting with the valve train of an internal combustion engine (ICE).

Cam-follower systems can be modelled and consequently treated, as SDOF impact oscillators with a moving boundary [6, 65, 66].

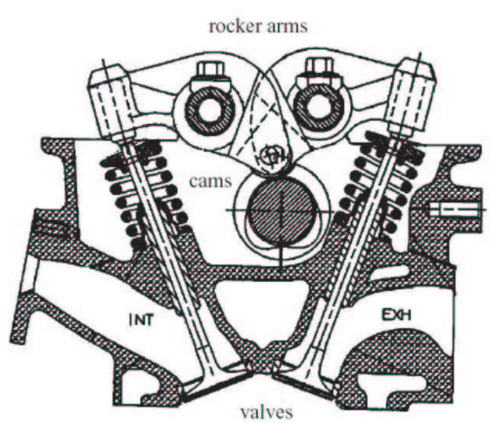

Figure 1.4 — An overhead camshaft automotive valve-train, reproduced from [61].

1.4 Motivation and outline

The aim of this Thesis is the analytical study and experimental validation of the complex behaviour of impacting dynamical systems with particular attention to those phenomena caused by the interruption of complete chattering motion in a practical impact oscillator: the cam-follower system.

The content of the Thesis is organized as follows:

Chapter 2. Smooth and nonsmooth dynamical systems: an overview. Definitions of theoretical concepts on which subsequent Chapters are based. In particular, an overview of dynamical systems is given from continuous systems of differential equations and their smooth bifurcations, until interaction of flows and maps in discontinuity-induced events. Impact oscillators are formally defined, as well as related concepts as chattering and sticking.

Chapter 3. Numerical analysis of PWS dynamical systems. Main tools and procedures for numerical analysis of dynamical systems are described, with special emphasis on simulation and path-following techniques. Time-stepping and event-driven simulation approaches are addressed, with a novel extended version for particular application on impacting models. Also, an additional topic on continuation for nonsmooth systems is introduced as an open problem with promising preliminary results.

Chapter 4. Cam-follower systems and the valve-float phenomenon in combustion engines. The application context of the general theory of piecewise-smooth dynamical systems introduced in Chapter 2, is formulated in terms of an experimental rig composed of an oscillating rocker-arm driven by a rotating profile, emulating the interaction between the cam-shaft and valves of an internal combustion engine (ICE). Description of design tips, implementation, modelling, parameter fitting and the experimental procedure for characterization of dynamics, are performed.

Chapter 5. Numerical bifurcation analysis. Numerical results obtained by simulating the equivalent model of motion derived in Chapter 4 are included, showing remarkable agreement with the experimental dynamics of the physical system. Particularly, a smooth period-doubling route to chaos is detected to coexist with a non-smooth sudden transition to chaos caused by interruption of periodic complete-chattering motion. Numerical evidence for both, the smooth and nonsmooth scenarios, is shown, as well as for its coexistence, by performing calculation of the corresponding basins of attraction (BA). A pseudo-analytical approximation for the map in a vicinity of the non-smooth event is also developed.

Chapter 6. Bifurcations involving Chattering in impacting systems. The numerical map derived in Chapter 5, is complemented with theoretical analysis based on variational equations. An equivalent unidimensional map is generated in the low-velocity impact region, for three study cases of the SDOF impact oscillator. Namely: a triple integrator model, a general periodically forced harmonic oscillator and the cam-follower impacting model. For this last, validation of the results generated with the analytical approximation of the map is performed by comparison with numerical simulations of the system flow.

Chapter 7. Conclusions. Main contributions of the research and future tasks as open problems, are listed.

1.5 Glossary of terms

The following acronyms are employed throughout the contents:

ABE - algebraic branching equation,

BA - basin of attraction,

BC - bottom-center crank position,

CEP - critical extreme position,

CPM - critical path motion,

DIB - discontinuity induced bifurcation,

DM - discontinuity mapping,

DOF - degree of freedom,

ICE - internal combustion engine,

IFT - implicit function theorem,

IVP - initial value problem,

LCP - linear complementary problem,

ODE - ordinary differential equation,

PWS - piecewise smooth,

RDFD - rise-dwell-fall-dwell motion program,

RF - rise-fall motion program,

RFD - rise-fall-dwell motion program,

rpm - revolutions per minute,

SDOF - single degree of freedom,

TC - top-center crank position.

Chapter 2

Smooth and nonsmooth dynamical systems: an overview

2.1 Introduction

Systems of differential equations are the most representative way to express mathematically physical phenomena. As a consequence, there are many available numerical and analytical tools aimed at solving explicitly in time (i.e. for dynamic evolutions) those systems of differential equations by means of the so-called initial and boundary value problems [41] [52]. This is particularly true for trajectories with a high order of differentiability. Therefore, it is possible to apply a broad set of techniques devoted to analyze and predict related behaviour in linear and nonlinear systems of equations [85] [102]. On the other hand, if discontinuities and other sources of non-smoothness are introduced, the explicit resolution of trajectories as well as further analysis will require a specific treatment that reduces the validity of traditional methodologies with an additional increase of complexity [33].

Hence, given the limitations in operational ranges introduced by practical environments, discontinuities appear to be a natural feature of realistic representation of systems, and consequently should not be neglected during analysis. Therefore, in addition to the vast existing literature on smooth dynamical systems [41] [52] [102] [85], a general theory of nonsmooth or piecewise-smooth dynamical systems has been recently developed [33], in order to explain the many phenomena associated with discontinuities, affecting the dynamics of continuous (flows), discrete (maps) and hybrid representations of systems.

In this Chapter, general ideas behind this new theory will be addressed, presenting a consistent framework to develop the analysis of nonsmooth bifurcation scenarios in impacting oscillators, the main scope of the Thesis.

2.2 Smooth dynamical systems

The qualitative theory of differential equations begins with a general definition of a dynamical system. This is written in terms of an $n-$dimensional state space (or phase space) $X \subset \Re^n$ with the usual topology, and an evolution operator ϕ that takes elements x_0 of the state space and evolves them through a "time" t, into a state x_t:

$$\phi^t : X \to X, \quad x_t = \phi^t (x_0) .$$

The time t takes values in an index set T, which can be both discrete (the integers $\mathbb{Z}$) or continuous (the real numbers $\Re$).

Definition 2.1 (Dynamical system)**.** *A state space X, index set T and evolution operator ϕ^t are said to define a **dynamical system** if*

$$\begin{array}{rcl} \phi^0(x) = x & \forall & x \in X, \\ \phi^{t+s}(x) = \phi^s\left(\phi^t(x)\right) & \forall & x \in X, t \in T, s \in T. \end{array} \tag{2.1}$$

*The set of all points ϕ^t for all $t \in T$ is called the **trajectory** or **orbit** through the point x. Equivalently, the **phase portrait** of the dynamical system is the partitioning of the state space into orbits.*

Definition 2.2 (Smoothness)**.** *A dynamical system satisfying* (2.1)*, is said to be **smooth of index r**, or C^r, if the first "r" derivatives of ϕ with respect to x exist and are continuous at every point $x \in X$.*

It is important to define also the repeatability or recurrent character of dynamics, allowing to gain understanding on the structure of the phase space from specific sets that remain invariant:

Definition 2.3 (Invariant set)**.** *An **invariant set** of a dynamical system* (2.1)*, is a subset $\Lambda \subset X$ such that $x_0 \in \Lambda$ implies $\phi^t(x_0) \in \Lambda$ for all $t \in T$. Additionally, an invariant set that is closed and bounded is called an **attractor** if:*

1. *for any sufficiently small neighborhood $U \subset X$ of Λ, there exists a neighborhood V of Λ such that $\phi^t(x) \in U$ for all $x \in V$ and all $t > 0$, and*
2. *for all $x \in U$, $\phi^t(x) \to \Lambda$ as $t \to \infty$.*

The set of all attractors of a given system typically describes the long-term observable dynamics. A dynamical system may have then many competing attractors, with their relative importance being indicated by the size of the set of initial conditions they attract:

Definition 2.4 (Domain of attraction)**.** *The **domain of attraction** or basin of attraction, of an attractor Λ, is the maximal set U for which $x \in U$ implies $\phi^t(x) \to \Lambda$ as $t \to \infty$.*

Another useful notion to define, are points in the phase space eventually approached infinitely often in the future, or approached infinitely often in the past:

Definition 2.5 (Limit point)**.** *A point p is an $\omega-$**limit point** of a trajectory $\phi^t(x_0)$, if there exists a sequence of times $t_1 < t_2 < \ldots$ with $t_i \to \infty$ as $i \to \infty$, such that $\phi^{t_i}(x_0) \to p$ as $t_i \to \infty$. If instead there exists a sequence of times with $t_1 > t_2 > \ldots$ and $t_i \to -\infty$ and $\phi^{t_i}(x_0) \to p$, then we say that p is an $\alpha-$**limit point** of x_0. The $\omega-$**limit set** of x_0, is the set of all possible $\omega-$limit points. The set of all such $\omega-$limit points for all $x_0 \in X$, is called the $\omega-$limit set of the system. This set is closed and invariant. A similar discourse applies for $\alpha-$limit points.*

2.2.1 Differential equations and flows

Given a system of ordinary differential equations (ODEs):

$$\dot{x} = f(x), \quad x \in \mathbb{D} \subset \Re^n, \tag{2.2}$$

where $\mathbb{D}$ is a domain, according to what stated previously, $\{X, T, \phi^t\}$ will define a dynamical system after setting $X = \mathbb{D}$, $T = \Re$ and letting $\phi^t(x) \equiv \Phi(x,t)$ be the solution operator, of **flow** that takes initial conditions "x" up to their solution at time t; i.e.

$$\frac{\partial}{\partial t}\Phi(x,t) = f(\Phi(x,t)), \quad \Phi(x,0) = x. \tag{2.3}$$

As an illustration, consider the periodically forced system:

$$\ddot{u} + 2\zeta\dot{u} + ku = a\cos(\omega t), \tag{2.4}$$

where by setting $X = \Re^2 \times S^1 \subset \Re^3$, with $x_3 = mod(t, 2\pi/\omega)$, we obtain:

$$\begin{aligned} \dot{x}_1 &= x_2, \\ \dot{x}_2 &= -kx_1 - 2\zeta x_2 + a\cos(x_3), \\ \dot{x}_3 &= 1. \end{aligned} \tag{2.5}$$

A phase portrait of (2.5) is depicted in Figure 2.1.

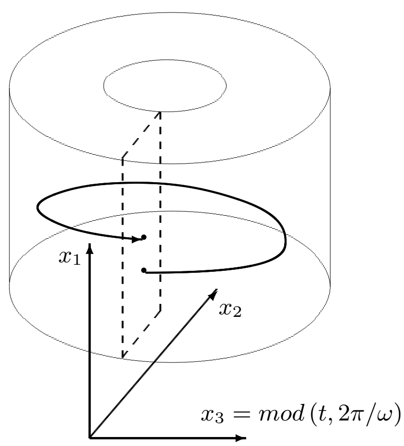

Figure 2.1 — Schematic description of the cylindrical phase space associated with the periodically forced system (2.5).

The case is the often considered of parameter dependence of system dynamics, we should write:

$$\dot{x} = f(x, \mu), \tag{2.6}$$

where $\mu \in \Re^p$ is a set of parameters. If we claim that f is smooth, we mean that the dependence on μ is as smooth as it is on x. Unless it is crucial, the notation employed will avoid the explicit parameter dependence of f.

Systems of ODEs can exhibit the following kinds of invariant sets, as depicted in Figure 2.2:

Equilibria. The simplest form of an invariant set of an ODE, is an equilibrium solution x^* which satisfies $f(x^*) = 0$. These are also called stationary points of the flow, since $\Phi(x^*, t) = \Phi(x^*, 0)$ for all t.

Limit cycles. The next most common complex kind of invariant set, would be a periodic orbit, which is determined by an initial condition x_p and a period T. Here T is defined as the smallest time $T > 0$ for which $\Phi(x_p, T) = x_p$. Periodic orbits form closed curves in the phase space. A periodic orbit that is isolated – i.e. does not have any other periodic orbit in its neighborhood – is termed a limit cycle.

Invariant tori. These are the nonlinear equivalent of two-frequency motion. Flow on a torus, may be genuinely quasi-periodic in that it contains no periodic orbits, or it may be phase locked into containing a stable and an unstable periodic orbit, which wind a given number of times around the torus.

Homoclinic and heteroclinic orbits. Another important class of invariant sets are connecting orbits, which tend to other invariant sets as time asymptotes to $+\infty$ and $-\infty$. Consider for example, orbits that connect equilibria. A homoclinic orbit is a trajectory $x(t)$ that connects an equilibrium x^* to itself; $x(t) \to x^*$ as $t \to \pm\infty$. A heteroclinic orbit connects two different equilibria x_1^* and x_2^*; $x(t) \to x_1^*$ as $t \to -\infty$ and $x(t) \to x_2^*$ as $t \to +\infty$. Homoclinic and heteroclinic orbits play an important role in separating the basins of attraction of other invariant sets.

Chaos. More complex invariant sets are chaotic, a term that might be defined in a number of different ways. Then following [33], we define:

Definition 2.6 (Chaotic invariant set)**.** *A closed and bounded invariant set Λ, is called **chaotic** if it satisfies the two additional conditions:*

1. *It has sensitive dependence on initial conditions; i.e. There exists an $\varepsilon > 0$ such that, for any $x \in \Lambda$, and any neighborhood $U \subset \Lambda$ of x, there exists $y \in U$ and $t > 0$ such that $\left|\phi^t(x) - \phi^t(y)\right| > \varepsilon$.*
2. *There exists a dense trajectory that eventually visits arbitrarily close to every point of the attractor; i.e. There exists an $x \in \Omega$ such that for each point $y \in \Omega$ and each $\varepsilon > 0$ there exists a time t, positive or negative, such that $\left|\phi^t(x) - y\right| < \varepsilon$.*

The first property says that initial conditions in the invariant set diverge from each other locally. The second property says that there is at least one trajectory in the invariant set such that not only eventually comes back arbitrarily close to itself, but to every point of the invariant set. This property ensures that we are talking about an attractor composed of a single piece, not two separate ones. This property is also known as topological transitivity.

2.2.2 Iterated maps

Given a discrete system or map, defined by the rule:

$$x \mapsto f(x), \quad x \in \mathbb{D} \subset \Re^n, \tag{2.7}$$

then $T = \mathbb{Z}$; that is, time is integer-valued, and the operator ϕ is just f. Evolving through time $m > 0$ involves taking the m-th iterate of the map;

$$\phi^m(x_0) = x_m = f(x_{m-1}) = f(f(x_{m-2})) = ... := f^{(m)}(x_0),$$

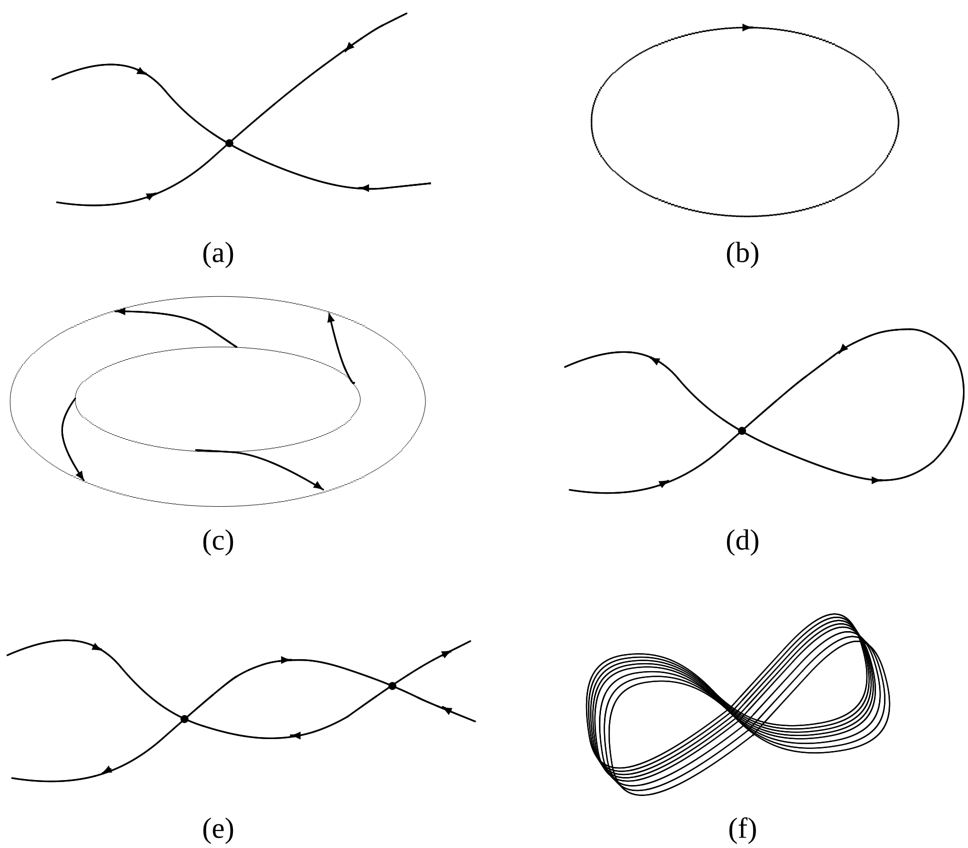

Figure 2.2 — Phase portrait representation of invariant sets of smooth flows: (a) equilibrium, (b) limit cycle, (c) invariant torus, (d) homoclinic orbit, (e) heteroclinic orbit and (f) chaotic attractor.

where a superscript (m) means $m-$fold composition

$$f^{(m)}\left(x_0\right)=\overbrace{f\circ f\circ ...\circ f\left(x_0\right)}^{m-times}.$$

Once again, it is possible to write $f\left(x,\mu\right)$ for systems that depend on parameters $\mu\in\Re^p$.

A useful way of studying one-dimensional maps is via cobweb analysis, that plot x_{n+1} against x_n by reflecting in the main diagonal. As an example , consider the logistic equation:

$$x\mapsto\mu x\left(1-x\right),\quad x\in\left[0,1\right],\quad 0<\mu\leq 4, \tag{2.8}$$

with associated cobweb diagrams depicted in Figure 2.3.

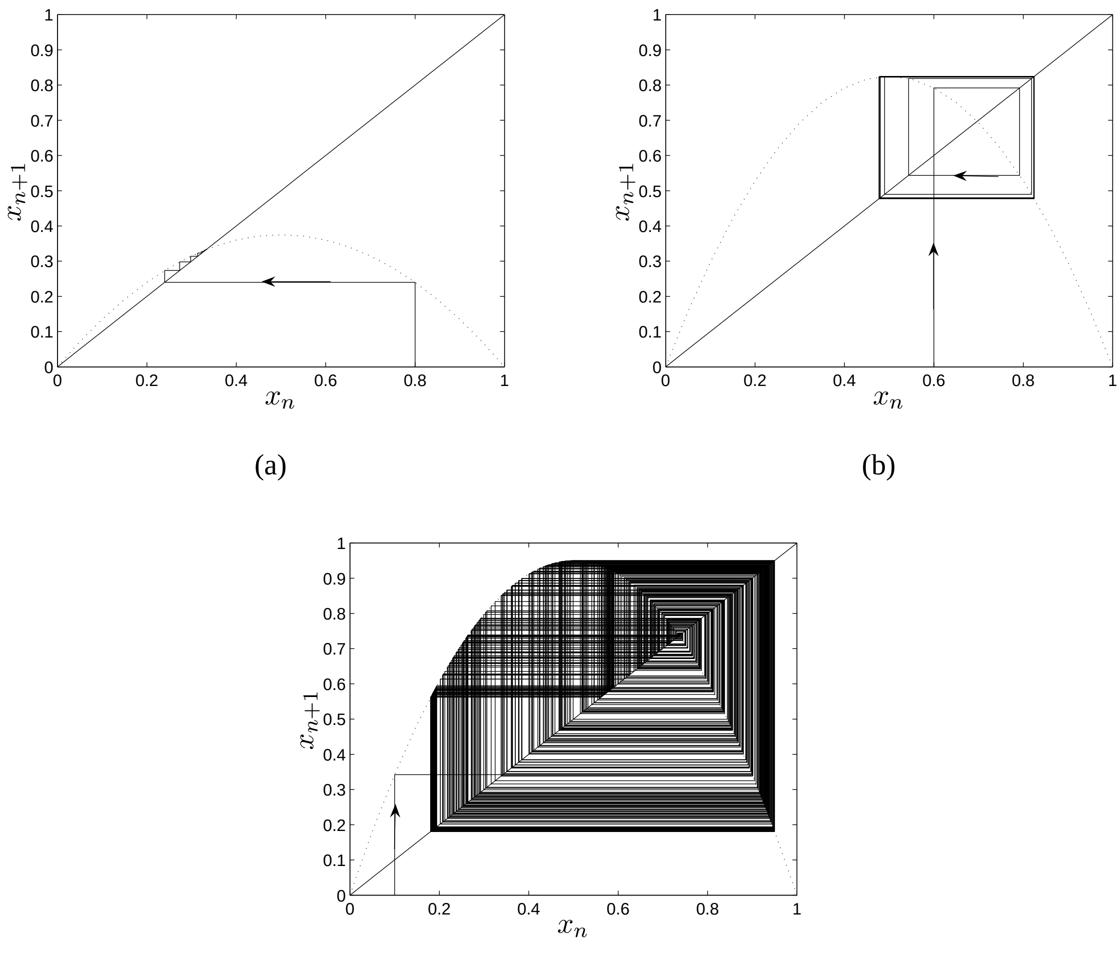

Figure 2.3 — Cobweb diagrams for the logistic map (2.8) showing: (a) convergence to a stable fixed point for $\mu=1.5$, $x_0=0.8$; (b) convergence into a periodic attractor for $\mu=3.3$, $x_0=0.6$; and (c) chaotic behaviour for $\mu=3.8$, $x_0=0.1$.

Definition 2.7 (Invertibility)**.** *A mapping* (2.7) *is said to be* ***invertible*** *for $x\in\mathbb{D}\subset\Re^n$ if given any $x_1\in\mathbb{D}$, there is a unique $x_0\in\mathbb{D}$ such that $x_1=f\left(x_0\right)$. In such a case, we define the inverse mapping $f^{(-1)}$ by*

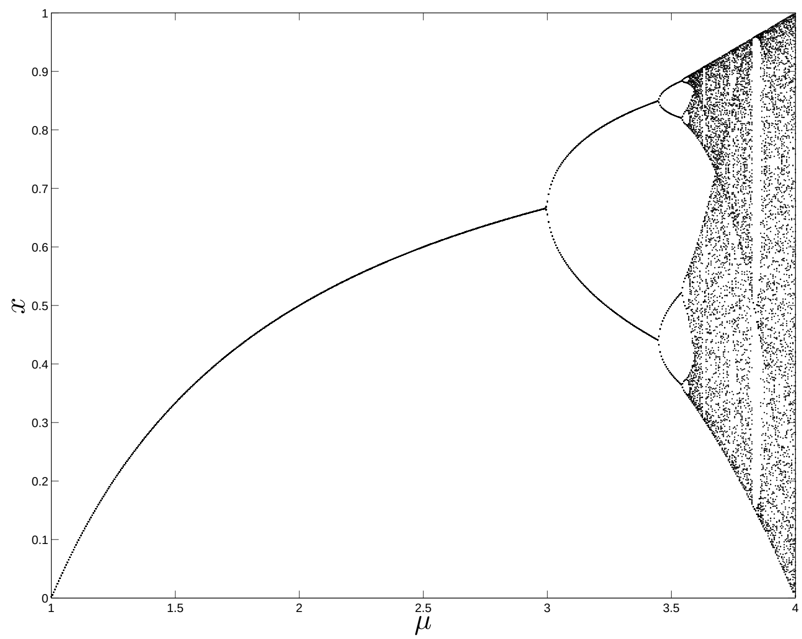

Figure 2.4 — Bifurcation diagram for the logistic equation (2.8), showing the period-doubling cascade to chaos as the parameter μ is increased.

$x_0 = f^{(-1)}(x_1)$ *for all points* x_1 *in* $f(\mathbb{D})$.

Smoothness of the dynamical system in the case of maps is given by the smoothness of the function f. Smooth – that is, at least C^1 – invertible maps, with smooth inverses, are referred to as diffeomorphisms.

Some important types of invariant sets for maps are listed below and illustrated in Figure 2.5:

> **Fixed points.** The simplest kind of invariant set of a map is a fixed point, which is a point x^* such that $f(x^*) = x^*$. Fixed points of maps have a close connection to periodic orbits of flows, through the induced map.
>
> **Periodic points.** Next in order of complexity come periodic points, which satisfy $f^{(m)}(x^*) = x^*$ for some $m > 0$. We refer to such a point as a period-m point of the map and its orbit as a period-m orbit. Clearly, each point $f^{(i)}(x^*)$, $i \leq m-1$ of a period-m orbit, is also a period-m point. These again are the close analogs of periodic orbits of flows, implying more intersections with a hyperplane of the state space to be defined later in the Chapter: the Poincaré section.
>
> **Invariant circles.** Analogous to invariant tori of flows are invariant closed curves of a map, which again may be defined by taking a Poincaré section of a torus. Such closed curves are topologically circles, and we can reduce the dynamics on an invariant curve, to that of a map of the unit circle to itself, a so-called circle map. Typically, as parameters vary, such curves lose their smoothness and eventually fail to exist as continuous invariant sets.

Chaos. Definition 2.6 of chaotic invariant sets also applies to maps. In contrast to flows where the phase space must be at least three-dimensional, non-invertible maps of dimension one can exhibit chaos. In the invertible case, at least two dimensions are required for this to occur.

As an illustration let's take again the logistic equation (2.8), where for $\mu > 1$, there are two fixed points at $x = 0$ and $x = (\mu - 1)/\mu$; for $1 < \mu < 3$, the non-trivial one is the unique attractor of the system; for $\mu > 3$, there are also two period-two points given by:

$$x = \frac{1 + \mu \pm \sqrt{\mu^2 - 2\mu - 3}}{2\mu}.$$

As μ is further increased, a chaotic attractor is born via a so called period-doubling cascade. See Figure 2.4 for an illustration. Note that in the chaotic range of μ-values, the attractor actually alternates between parameter intervals of chaos and intervals of periodic orbits appearing in the bifurcation diagram.

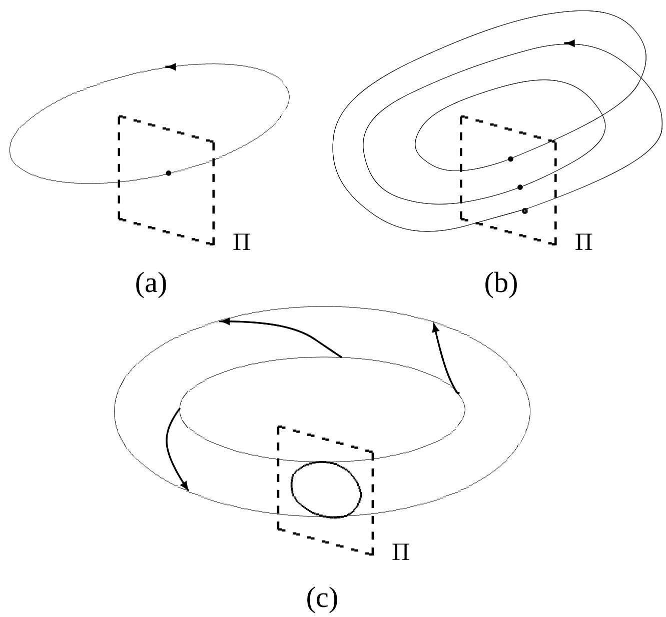

Figure 2.5 — Relationship between maps and flows obtained by taking a Poincaré surface Π (see section 2.2.5 below), through the phase space of the flow and considering the induced map from $\Pi \to \Pi$. Specifically, the graph illustrates the correspondence between: (a) fixed points and period-T limit cycles, (b) period-m points – for $m = 3$ – and higher-period limit cycles, (c) invariant circles and invariant tori.

2.2.3 Asymptotic stability

When considering dynamical systems with physical application, we are usually only interested in stable behaviour. Important notions of stability in dynamical systems, include that of either Lyapunov or asymptotic stability of an invariant set. In general, the former means stability in the weak sense that trajectories starting nearby to the invariant set remain nearby for all time, whereas the latter is more or less synonymous with the conception of an attractor in Definition 2.3. In any case, the stability is referred with respect of perturbations of initial conditions at fixed parameter values.

To formally define Lyapunov stability, consider a generic nonlinear system of the form (2.2) and assume that it has an equilibrium point that, without loss of generality, is at the origin; i.e. $f(0) = 0$.

Definition 2.8 (Lyapunov stability)**.** *The equilibrium state at the origin is said to be* ***Lyapunov stable*** *if for any $\varepsilon > 0$, there exists a $\delta > 0$ such that:*

$$\|x_0\| < \delta \Rightarrow \|\Phi(x_0, t)\| < \varepsilon, \quad \forall \quad t > 0.$$

Otherwise, the equilibrium will be assumed as ***unstable****.*

Definition 2.9 (Asymptotic stability)**.** *The equilibrium state at the origin is said to be* ***asymptotically stable*** *in the sense of Lyapunov, if:*

1. *it is stable;*
2. $\lim_{t\to\infty} \Phi(x_0, t) = 0$.

Thus, stability refers to the ultimate state of the dynamics not being altered under small changes to the initial conditions.

2.2.4 Structural stability

Another notion of stability, implies perturbation to the system itself rather than to initial conditions. This introduces the concept of structural stability: structurally stable systems are ones for which all "nearby" systems have qualitatively "equivalent" dynamics. In a more formal way:

> **Nearby**, refers to any possible perturbation of the system $f(x)$, including variation in parameters.
>
> **Equivalence** between two systems, relates the same dimension in their corresponding phase spaces, containing the same number and type of invariant sets, in the same general position with respect to each other. Mathematically, we want to say that two phase portraits are the same if there is a smooth transformation that stretches, squashes, rotates, but not folds one phase portrait into the other. Such transformations are called **homeomorphisms**, which are continuous functions defined over the entire phase space whose inverses are also continuous.

Definition 2.10 (Topological equivalence)**.** *Two dynamical systems $\{X, T, \phi^t\}$ and $\{X, T, \psi^t\}$ are* ***topologically equivalent*** *if there is a homeomorphism h that maps the orbits of the first system onto orbits of the second one, preserving the direction of time.*

For discrete time systems, two **topological equivalent maps** f and g, that satisfy:

$$f(x) = h^{-1}(g(h(x))) \Rightarrow h(f(x)) = g(h(x)),$$

for some homeomorphism h, are said to be **topologically conjugate**, and we can write more simply:

$$f = h^{-1} \circ g \circ h. \tag{2.9}$$

For ODEs, the homeomorphism should apply at the level of the flow:

Definition 2.11 (Topological conjugate in flows)**.** *Two flows $\Phi(x,t)$ and $\Psi(h(x),t)$, that correspond respectively to ODEs $\dot{x} = f(x)$ and $\dot{y} = g(x)$, are said to be **topologically conjugate** if there exists a homeomorphism h such that:*

$$\Phi(x,t) = h^{-1}(\Psi(h(x),t)). \tag{2.10}$$

Actually, for topological equivalence of flows, the conjugacy does not need to apply at each time t. Rather, we require the weaker condition that there is an invertible, continuous mapping of time $t \mapsto s(t)$.

Having defined what we mean by topological equivalence, we can now define structural stability:

Definition 2.12 (Structural stability)**.** *A flow – or discrete map – is **structurally stable** if there is an $\varepsilon > 0$ such that all C^1 perturbations of maximum size ε to the vector field (map) f lead to topological equivalent phase portraits.*

One key application of topological equivalence is to show that *normally* dynamical systems in the neighborhood of an invariant set, are topologically equivalent to the linearization of the system about that set.

Consider first an equilibrium x^* of $\dot{x} = f(x)$. Now, for small $y = x - x^*$, we can expand f as a Taylor series about x^* to write:

$$\dot{y} = f_x(x^*)\, y + \mathcal{O}\left(y^2\right),$$

where $f_x(x^*)$ given by $(f_x)_{i,j} = {}^{\partial f_i}\!/_{\partial x_j}$ is the Jacobian derivative of the vector field evaluated at x^*. Then, by dropping the $\mathcal{O}\left(y^2\right)$-term, the general solution to the linear system is:

$$y(t) = exp\left(f_x(x^*)\, t\right) y(0).$$

Usually, this can be expressed in terms of the eigenvalues and eigenvectors of $f_x(x^*)$. So, if the spectrum (set of eigenvalues) of $f_x(x^*)$ is in the left half-plane, then the solution of the linear system tends to zero as $t \to \infty$ and the equilibrium of the linear system is stable.

Definition 2.13 (Hyperbolic equilibrium)**.** *We shall refer to the **eigenvalues** of an equilibrium x^* of an ODE $\dot{x} = f(x)$, to mean the eigenvalues of the associated Jacobian matrix $f_x(x^*)$. An equilibrium is said to be **hyperbolic** if none of its eigenvalues lie on the imaginary axis.*

Similarly, consider a fixed point x^* of a map $x \mapsto f(x)$ (period-m points can be treated as well, since they are fixed points of $f^{(m)}$). Linearizing about this fixed point, we get $y \mapsto f_x(x^*)\, y$, with solution $y_n = |f_x(x^*)|^n\, y_0$.

Hence, $y_i \to 0$ as $i \to \infty$, satisfying the second of the conditions for asymptotic stability of the linearized system, if all eigenvalues μ_i of $f_x(x^*)$ lie inside the unit circle:

Definition 2.14 (Hyperbolic equilibrium maps)**.** *We shall refer to the **multipliers** λ_i of a fixed point x^* of a map $x \mapsto f(x)$ to mean the eigenvalues of the associated linearization $f_x(x^*)$. A fixed point is said to be **hyperbolic** if none of the multipliers lie on the unit circle.*

2.2.5 Poincaré maps

One of the main building blocks of the dynamics of a set of ODEs are its periodic solutions, and these provide a natural way to transform between flows and maps. Consider a limit cycle solution $x(t) = p(t)$ to (2.2) of period $T > 0$; that is, $p(t + T) = p(t)$. To study the dynamics near to such a cycle, we construct a Poincaré section, which is an $(n - 1)$- dimensional surface Π that contains a point $x_p = p(t^*)$ on the limit cycle and which is transverse to the flow at x_p. Let us introduce a notation that:

$$\Pi = \{x \in \Re^n : \pi(x) = 0\}, \tag{2.11}$$

for some smooth scalar function π. Then the transversality condition is that the normal vector $\pi_x(x_p)$ to Φ at x_p has a non-zero component in the direction of $\Phi_t(x_p, 0) = f(x_p)$. That is we require:

$$\pi_x(x_p) f(x_p) \neq 0, \tag{2.12}$$

where a subscript means differentiation with respect to that variable, so that $\pi_x(x_p)$ is the normal vector to Π at $x = x_p$.

Now, we can use the flow Φ to define a map P from Π to Π, called the Poincaré map, which is defined for x sufficiently close to x_p via:

$$P(x) = \Phi(x, \tau(x)),$$

where $\tau(x)$ is defined implicitly as the time closest to T for which:

$$\pi(\Phi(x, \tau(x))) = 0. \tag{2.13}$$

We can study the stability and possible bifurcations of the periodic solution, by studying the linearization P_x of the Poincaré map at x_p. Then, computing the total derivative with respect to x, we have:

$$P_x(x_p) = \Phi_x(x_p, T) + \Phi_t(x_p, T)\,\tau_x(x - p),$$

and from implicit differentiation of (2.13):

$$\tau_x(x_p) = -\frac{\pi_x(x_p)\,\Phi_x(x_p, T)}{\pi_x(x_p)\,\Phi_t(x_p, T)}.$$

Hence, a rank-one update of the time-T map $\Phi_x(x_p, T)$ around $p(t)$ can be defined as:

$$P_x(x_p) = \left(I - \frac{\Phi_t(x_p, T)\,\pi_x(x_p)}{\pi_x(x_p)\,\Phi_t(x_p, T)}\right)\Phi_x(x_p, T) = \left(I - \frac{f(x_p)\,\pi_x(x_p)}{\pi_x(x_p)\,f(x_p)}\right)\Phi_x(x_p, T). \tag{2.14}$$

The $n \times n$ matrix $\Phi_x(x_p, T)$ is referred to as the **Monodromy** matrix, and corresponds to the fundamental solution matrix up to time T of the linear variational equations:

$$\dot{y} = f_x(p(t))\,y, \tag{2.15}$$

around the periodic orbit $p(t)$. The direction of the flow $\Phi_t(x_p, t) = f(x_p)$ can easily be shown to solve (2.15) and, hence, $f(x_p)$ is an eigenvector of $\Phi_x(x_p, T)$ corresponding to the multiplier 1. Letting (2.14) act on $f(x_p)$, we see that this corresponds to an eigenvalue 1 of the linearized Poincaré map P_x. However, since this eigenvector does not lie in the linear approximation to Π, we will never see its effect when computing the Poincaré map taking only points $x \in \Pi$.

Other than this trivial eigenvalue, the eigenvalues of the Monodromy matrix are precisely the multipliers λ_i of the Poincaré map. We say therefore that a hyperbolic periodic orbit $p(t)$ is one whose Poincaré map has multipliers λ_i, $i = 1, 2, ..., (n-1)$ that are all off the unit circle.

Poincaré maps do not necessarily require a periodic orbit in order to be defined. A Poincaré section Π can be taken anywhere in the phase space, provided the flow is everywhere transverse to it (as in Figure 2.5). For transversality, we require that a condition equivalent to (2.12) applies through Π. So if we define Π as before, to be the zero set of a smooth function (2.11), then we are only interested in defining a Poincaré map for points x for which:

$$\pi(x) = 0; \quad \pi_x(x) f(x) \neq 0.$$

The map is defined by the first intersection with Π in the same sense. That is, $P(x) = \Phi(x, \tau(x))$, where $\tau(x)$ is the first time $t > 0$ such that $\pi(\Phi(x,t)) = 0$, and $\pi_x f(\Phi(x,0)) \pi_x f(\Phi(x,t)) > 0$; see Figure 2.6. Note that the map P may not be defined for the whole Poincaré section, since not all points need to return.

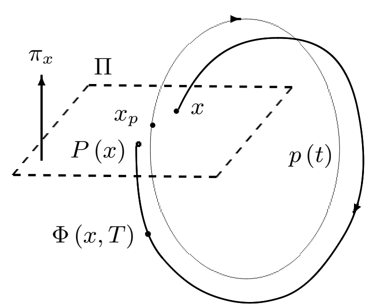

Figure 2.6 — Construction of a Poincaré map close to a periodic orbit $p(t)$.

One of the benefits of studying Poincaré maps rather than flows, is that they drop by one the dimension of the sets we need to consider. Thus, limit cycles of flows correspond to isolated fixed points of Poincaré maps; invariant tori correspond to closed curves of the map; and chaotic invariant sets decrease their fractal dimension by one.

2.2.6 Smooth Bifurcations

Broadly speaking, there are two notions of **bifurcation**, one analytical and the other topological. From the first point of view, bifurcations are branching points of parameterized sets of solutions $x(\mu)$ to nonlinear operators $G(x, \mu) = 0$. In simple words, a bifurcation is a point at which the Implicit Function Theorem IFT fails (see Chapter 3 for an alternative definition of the IFT, taken from [79]):

Theorem 2.1 (Implicit function theorem)**.** *Suppose that for some $\mu = \mu_0$ there exists a solution $x = x_0$ to a smooth nonlinear equation $G(x, \mu) = 0$, where $G : \Re^n \times \Re \to \Re^n$; then provided $G_x(x_0, \mu_0)$ is nonsingular, a smooth path of solutions $x(\mu)$ can be continued locally, with $x(x_0) = x_0$.*

Of particular importance, are changes to the number and nature of the attractors of the system. Then, we define bifurcation simply in terms of loss of structural stability upon varying a parameter for systems either in the form of a smooth vector field or map

$$x = f(x,\mu); \quad x \mapsto f(x,\mu), \tag{2.16}$$

for $x \in \Re^n$, $\mu \in \Re^p$.

Definition 2.15 (Bifurcation)**.** *A **bifurcation** occurs at a parameter value μ_0, if the dynamical system $\{X, T, \phi^t\}$ is not structurally stable. An **unfolding** of a bifurcation is a simplified system that for small $\mu \mapsto \mu_0$, contains all possible structurally stable phase portraits that arise under small perturbations of the system at the bifurcation point. The **codimension** of a bifurcation, is the dimension of parameter space required to unfold the bifurcation. A **bifurcation diagram**, is a plot of some measure of the invariant set of a dynamical system, against a single bifurcation parameter μ, which indicates stability.*

Hence, there are two main types of bifurcations:

Definition 2.16 (Local and global bifurcations)**.** *A **local bifurcation** arises due to the loss of hyperbolicity of an invariant set upon varying a parameter. All other bifurcations can be considered as **global**.*

Codimension-one smooth local bifurcations are depicted in Figure 2.7, with corresponding normal forms related to (2.16), given by:

- **fold**: $\dot{x} = \mu - x^2$;
- **transcritical**: $\dot{x} = \mu x - x^2$;
- **pitchfork**: $\dot{x} = \mu x - x^3$;
- **Hopf** (flows): $\begin{bmatrix} \dot{x}_1 \\ \dot{x}_2 \end{bmatrix} = \begin{bmatrix} \mu_1 & -\mu_2 \\ \mu_2 & \mu_1 \end{bmatrix} \begin{bmatrix} x_1 \\ x_2 \end{bmatrix} - \begin{bmatrix} x_1 \\ x_2 \end{bmatrix} \left(x_1^2 + x_2^2\right)$;
- **period doubling** (maps): $x \mapsto (1+\mu)\,x - x^3$.

For a deeper insight on local bifurcations see [41, 52, 102, 85, 33] and references therein.

Equivalently, examples of global bifurcations can be:

- **homoclinic** bifurcation, where the stable and unstable manifolds of the same invariant set form an intersection or tangency at a fixed parameter value (see Figure 2.8); and
- **boundary crisis** bifurcation, where stable and unstable manifolds of different invariant sets form an intersection in a heteroclinic connection that can cause the sudden appearance or disappearance of a chaotic attractor.

An interesting feature of smooth-dynamical systems is that they can exhibit cascades of local bifurcations under parameter variation. A well-known example is the period-doubling cascade, where a supercritical period-doubling at a parameter value μ_1 creates a stable period-2 orbit, followed by a further period doubling of the period-2 orbit at $\mu = \mu_2$, creating a stable period-4 orbit, and so on, as shown in Figure 2.4. Remarkably, we observe an universal scaling law, established by Feigenbaum:

$$\lim_{k\to\infty} \frac{\mu_k - \mu_{k-1}}{\mu_{k+1} - \mu_k} \approx 4.669. \tag{2.17}$$

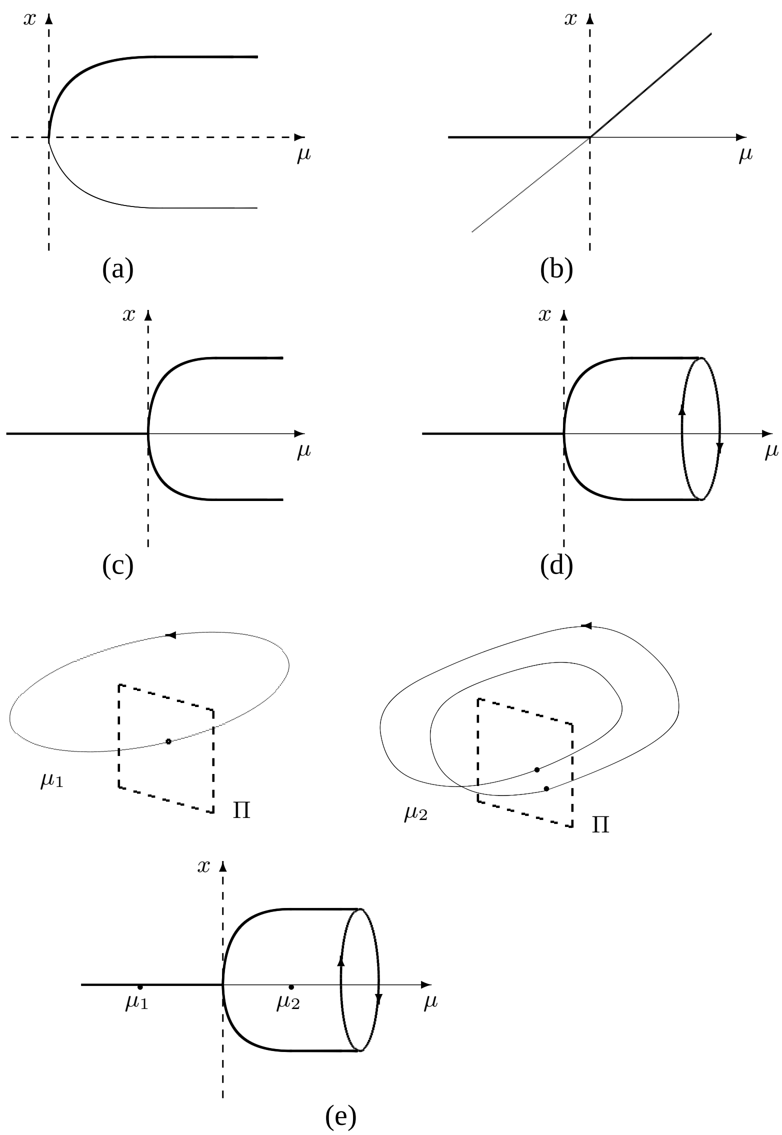

Figure 2.7 — Main codimension-one local bifurcations in smooth dynamical systems: (a) fold, (b) transcritical, (c) pitchfork, (d) Hopf, and (e) period-doubling on maps. In all graphs, a *tick* line means for stability of the branch, while a *thinner* represents instability.

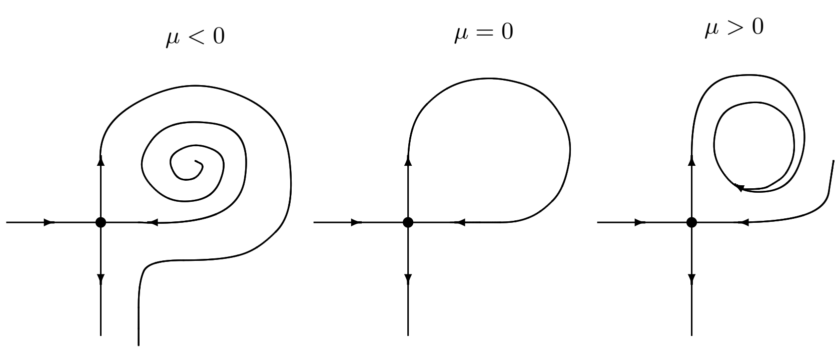

Figure 2.8 — Illustration for a homoclinic global bifurcation where, from a saddle node equilibrium, a single stable limit cycle is created.

That is, the period-doubling sequence converges to a finite μ-value and in the limit, the rate of convergence is the same for all systems.

Another interesting rule is given by Sharkovskii, predicting the existence of chaotic windows in smooth bifurcation cascades of unidimensional maps (See for instance [85]).

Non-smooth dynamical systems have shown to experience other types of cascades of stable periodic orbits close to a bifurcation point. These cascades do not generally follow standard rules to chaos, but experiences new features as non periodic windows or period-adding type of orderings [59], for which there are intervals of periodic motions of period n obeying the simple ordering $n < (n+1) < (n+2) < \ldots$ Additionally, in successive Chapters we will demonstrate evidence for more complex sequences of chaotic behaviour experienced in impacting oscillators as novel phenomenon introduced by discontinuities.

2.3 Piecewise-smooth dynamical systems

Moving now towards a systematic study of non-smooth dynamics, three particular classes of piecewise-smooth dynamical systems will be addressed: flows, maps and a combination of both in the so-called hybrid dynamical systems. Rather than rigorous mathematical proofs conditioned by the existence and uniqueness of solutions, a rather loose classification and description on non-smooth dynamics will be given, proven to be useful in explaining the dynamics observed in several application examples [33].

2.3.1 Piecewise-smooth ODEs

Definition 2.17 (Piecewise-smooth flow)**.** *A* ***piecewise-smooth flow*** *is given by a finite set of ODEs*

$$\dot{x} = F_i(x,\mu), \quad \forall \quad x \in S_i, \tag{2.18}$$

where $\bigcup_i S_i = \mathbb{D} \subset \Re^n$ *and each* S_i *has a non-empty interior. The intersection* $\Sigma_{ij} := \bar{S}_i \cap \bar{S}_j$ *is either an* $\Re^{(n-1)}$*-dimensional manifold, included in the boundaries* ∂S_j *and* ∂S_i*, or is the empty set. Each vector field* F_i *is smooth in both, the state* x *and the parameter* μ*, and defines a smooth flow* $\Phi_i(x,t)$ *within any open set* $U \supset S_i$*. In particular, each flow* Φ_i *is well defined on both sides of the boundary* ∂S_j*.*

A non-empty border between two regions Σ_{ij}, will be called a **discontinuity set**, **discontinuity boundary** or, sometimes, **switching manifold**. We suppose that each piece of Σ_{ij} is of codimension-one, i.e. is an $(n-1)$-dimensional smooth manifold embedded within the n-dimensional phase space. Moreover, we shall demand that each such Σ_{ij} is itself piecewise-smooth. That is, it is composed of finitely many pieces that are as smooth as the flow. See Figure 2.9.

Definition 2.18 (Degree of smoothness)**.** *The* ***degree of smoothness*** *at a point* x_0 *in a switching set* Σ_{ij} *of a piecewise-smooth ODE, is the highest order "*r*" such the Taylor series expansions of* $\Phi_i(x_0,t)$ *and* $\Phi_j(x_0,t)$ *with respect to "*t*" and evaluated at* $t=0$*, agree up to terms of order* $(r-1)$*. That is, the first non-zero partial derivative with respect to "*t*" of the difference* $\left.[\Phi_i(x_0,t) - \Phi_j(x_0,t)]\right|_{t=0}$ *is of order "*r*".*

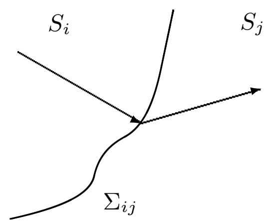

Figure 2.9 — Illustration for trajectories of a piecewise-smooth flow.

Now, consider an ODE local to a single discontinuity set Σ_{12} that can be written

$$\dot{x} = \begin{cases} F_1(x, \mu); & x \in S_1 \\ F_2(x, \mu); & x \in S_2, \end{cases}$$

where F_1 generates a flow Φ_1 and F_2 a flow Φ_2. We have

$$\begin{aligned} \left.\tfrac{\partial \Phi_i(x,t)}{\partial t}\right|_{t=0} &= F_i(x), \\ \left.\tfrac{\partial^2 \Phi_i(x,t)}{\partial t^2}\right|_{t=0} &= \tfrac{\partial F_i}{\partial t} = \tfrac{\partial F_i}{\partial \Phi_i}\tfrac{\partial \Phi_i}{\partial t} = F_{i,x} F_i(x), \end{aligned}$$

where a second subscript "x" means partial differentiation with respect to x. Similarly

$$\left.\frac{\partial^3 \Phi_i(x,t)}{\partial t^3}\right|_{t=0} = F_{i,xx} F_i^2(x) + F_{i,x}^2 F_i(x),$$

etc. So, if F_1 and F_2 differ in an m-th partial derivative with respect to the state x, we find that the flows Φ_1 and Φ_2 differ in their $(m+1)$-st partial derivative with respect to t.

Therefore, if $F_1(x) \neq F_2(x)$ at a point $x \in \Sigma_{12}$, then we have degree of smoothness one there. Systems with degree one are said to be of **Filippov type**.

Definition 2.19 (Sliding region)**.** *The **sliding region** of the discontinuity set of a system with degree of smoothness one, of the form*

$$\dot{x} = \begin{cases} F_1(x); & H(x) > 0 \\ F_2(x); & H(x) < 0, \end{cases} \tag{2.19}$$

where $F_1(x) = F_2(x)$ if $H(x) = 0$, is given by that portion of the boundary of the scalar function $H(x)$ for which

$$(H_x F_1) . (H_x F_2) < 0.$$

That is, $H_x F_1$ – the component of F_1 normal to H – has the opposite sign to $H_x F_2$. Thus, the boundary is simultaneously attracting (or repelling) from both sides.

See Figure 2.10 for an illustration of sliding motion of flows, depicting attracting and repelling sliding regions.

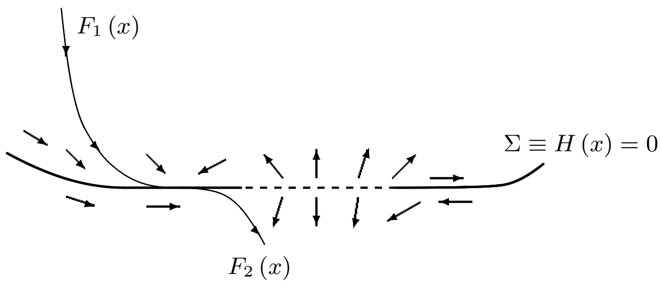

Figure 2.10 — A typical discontinuity boundary of a two-dimensional Filippov system, showing the behaviour of the vector fields at both sides. Solid and dashed intervals of the discontinuity boundary Σ, represents respectively: attracting and repelling sliding motion.

Two approaches exist in the literature for formulating the equations for flows that slide when written in the general form (2.19). These are the *Utkin's equivalent control method* and *Filippov's convex method*. For a deeper insight on such methods and further development and application examples on Filippov systems, readers are advised to consult [33].

2.3.2 Piecewise-smooth maps

Definition 2.20 (Piecewise-smooth map)**.** *A **piecewise-smooth map**, is described by a finite set of smooth maps*

$$x \mapsto F_i(x,\mu) \quad \forall \quad x \in S_i, \tag{2.20}$$

where $\bigcup_i S_i = \mathbb{D} \subset \Re^n$, and each S_i has a non-empty interior. The intersection Σ_{ij} between the closure (set plus its boundary) of the sets S_i and S_j – that is $\Sigma_{ij} := \bar{S}_i \cap \bar{S}_j$ – is either an $\Re^{(n-1)}$-dimensional manifold included in the boundaries ∂S_j and ∂S_i, or is the empty set. Each function F_i is smooth in both the state x and the parameter μ, for any subset U of S_i.

A set Σ_{ij} for a piecewise-smooth map is usually termed a border or discontinuity boundary that separates regions of phase space where different smooth maps apply. Examples of piecewise-smooth one-dimensional maps are given in Figure 2.11.

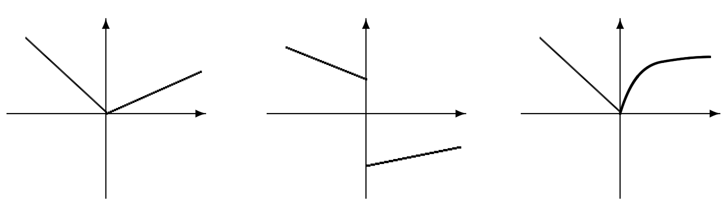

(a) (b) (c)

Figure 2.11 — Examples of piecewise-smooth one-dimensional maps: (a) piecewise-linear continuous map, (b) piecewise-linear discontinuous map, and (c) square-root piecewise-smooth map. In each case $S_1 = \{x < 0\}$, $S_2 = \{x > 0\}$ and $\Sigma_{12} = \{x = 0\}$.

Definition 2.21 (Order of singularity on maps)**.** *The* ***order of singularity*** *of a point* $\hat{x} \in \Sigma_{ij}$ *of a continuous piecewise-smooth map, is the order of the first non-zero term in the formal power-series expansion of* $F_1(x) - F_2(x)$ *about* $x = \hat{x}$*.*

Maps that are locally piecewise-linear and continuous – such as in Figure 2.11.(a) – are said to have an order of singularity one. Clearly, differentiation of these one-dimensional maps with respect to x leads to maps with singularities of one order lower. Then a point of discontinuity for a map with a jump – as in Figure 2.11.(b) – has a zero-order singularity at a point $x \in \Sigma_{ij}$ if $0 < \|F_1(x) - F_2(x)\| < \infty$.

2.3.3 Hybrid dynamical systems

Hybrid dynamical systems are combinations of maps and flows, giving rise to discontinuous, piecewise-smooth flows. They can arise both as models of impacting systems or in the context of the interaction between digital and analog systems. The notion of a *hybrid dynamical system* is a broad concept that encompasses a number of different formalisms in the literature. For example, *hybrid automata* are defined as dynamical systems with a discrete and a continuous part. The discrete dynamics can be represented as a graph whose vertices are the discrete states (or modes) and whose edges are transitions. The continuous states take values in $\Re^n$ and evolve along trajectories, typically governed by ODEs or differential algebraic equations.

Definition 2.22 (Piecewise-smooth hybrid system)**.** *A* ***piecewise-smooth hybrid system****, comprises a set of ODEs*

$$\dot{x} = F_i(x, \mu), \quad \forall \quad x \in S_i, \tag{2.21}$$

plus a set of reset maps

$$x \mapsto R_{ij}(x, \mu), \quad \forall \quad x \in \Sigma_{ij} := \bar{S}_i \cap \bar{S}_j. \tag{2.22}$$

Here $\bigcup_i S_i = \mathbb{D} \subset \Re^n$ *and each* S_i *has a non-empty interior. Each* Σ_{ij} *is either an* $\Re^{(n-1)}$*-dimensional manifold included in the boundary* ∂S_j *and* ∂S_i*, or is the empty set. Each* F_i *and* R_{ij} *are assumed to be smooth and well defined in open neighborhoods around* S_i *and* Σ_{ij}*, respectively.*

The application case considered in this Thesis, motivate to give particular emphasis to the special type of hybrid systems constituted by impact oscillators:

Definition 2.23 (Impacting hybrid system)**.** *An* ***impacting hybrid system****, is a piecewise-smooth hybrid system for which* $R_{ij} : \Sigma_{ij} \mapsto \Sigma_{ij}$*, and the flow is constrained locally to lie on one side of the boundary; that is, on* $\bar{S}_i = S_i \cup \Sigma_{ij}$*.*

We shall often refer to the reset map R_{ij} in this context as being the *impact law* or *impact rule*. The discontinuity boundaries Σ_{ij} will be referred to as *impact surfaces* and the event of a trajectory intersecting Σ_{ij} as an *impacting event* or just an *impact*.

We shall also consider a restrictive class of impacting hybrid systems that contain just one impact surface Σ. Suppose that such a surface Σ can be defined by the zero set of a smooth function $H(x)$,

$$\Sigma = \{x : H(x) = 0\}, \tag{2.23}$$

and let $S^+ = \{x : H(x) > 0\}$, such that the dynamics can be constrained to S^+ as in Figure 2.12.

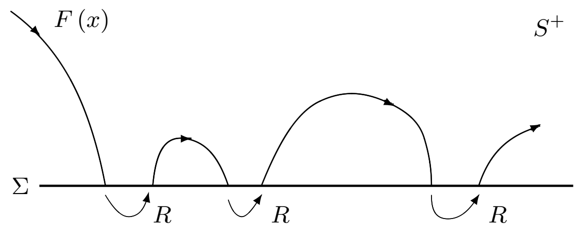

Figure 2.12 — The surface Σ, and a multiple impacting trajectory for an impacting hybrid system with a single discontinuity boundary.

Impacting systems, can be thought of as describing the dynamics local to any impact surface in a general, multiple region system. Locally, the dynamics may be written in the form:

$$\begin{aligned} \dot{x} &= F(x); \quad H(x) > 0, \\ x &\mapsto R(x); \quad H(x) = 0, \end{aligned} \tag{2.24}$$

for a smooth vector field F (which is well defined in a full neighborhood of Σ including for $H(x) < 0$) and a reset map R. Suppose an impact occurs at time t_0. Let x^- and x^+ represent the intersection of the flow with Σ, both, immediately before and immediately after the impact, so that $x^- = \lim\limits_{t \to t_0^-}$, $x^+ = \lim\limits_{t \to t_0^+}$. Hence, we can write the impact surface as:

$$x^+ = R\left(x^-\right). \tag{2.25}$$

In order to be definite, we shall also assume a restrictive class of impact law that depends on the normal velocity $v(x)$ at which the trajectory approaches the impact manifold, given by:

$$v(x) = dH/dt = H_x F. \tag{2.26}$$

Specifically, we suppose that:

$$R(x) = x + W(x) H_x F = x + W(x) v(x), \tag{2.27}$$

for a some smooth function $W(x) \in \Re^n$. To motivate why (2.27) is a reasonably form to take, note that we would like an impact law that takes a grazing trajectory (i.e. one for which $v(x) = 0$) to itself and that is a smooth function of $v(x)$ otherwise. More complex expressions are needed for dynamics with friction.

Given an impact rule of the form (2.27), the surface Σ can therefore be divided into three separate regions: Σ^-, Σ^+ and Σ^0, according to whether the normal velocity is, respectively, negative, positive or zero:

$$\begin{aligned} \Sigma^- &= \{x \in \Sigma : v(x) < 0\}; \\ \Sigma^+ &= \{x \in \Sigma : v(x) > 0\}; \\ \Sigma^0 &= \{x \in \Sigma : v(x) = 0\}. \end{aligned} \tag{2.28}$$

In general, if we write the impact law in the form (2.25), then we have $x^- \in \Sigma^-$ and $x^+ \in \Sigma^+$. In this case a flow in S^+ intersects Σ^-, is mapped to Σ^+ and then continues in S^+. The set Σ^0 is called the grazing set, and impacts close to it lead to subtle interesting dynamics that will be analyzed in Chapter 6.

Other formalisms for non-smooth systems including: complementarity systems, differential inclusions and control strategies, can be found in [33].

2.4 Impacting motion

Let us now consider the basic flow of the simple impacting system (2.24)-(2.27). Starting from an initial condition $x(0) = x_0$ in S^+, the ODE (2.24) generates a smooth flow $\Phi(x_0, t)$ up until the flow strikes Σ, say at time t_0. Suppose that this impact is transversal, so that the normal velocity $v(x(t_0)) < 0$. Hence $x^- = x(x_0) \in \Sigma^-$. This point is then mapped instantaneously under the action of the reset map to the point $x^+ = R(x^-)$. If $v(x^+) > 0$, so that $x^+ \in \Sigma^+$, then the flow moves away from Σ back into the set S^+ and is described by the flow $\Phi(x^+, t)$. In principle, this scenario can repeat arbitrarily often, as illustrated by Figure 2.12.

However, this is not the only possible dynamics of the system. Consider a grazing point for which $v(x^-) = 0$, where the impact map becomes the identity. In order to understand what happens, it is useful to define the *normal acceleration* of the flow with respect to the boundary:

$$a(x) = \frac{d^2H}{dt^2} = (H_xF)_x F = H_{xx}FF + H_xF_xF. \tag{2.29}$$

Now, in the case where $a(x^-) > 0$ at a grazing point, the curvature of the flow will cause the trajectory to immediately leave Σ. However, if $a(x) < 0$, then the flow will become stuck to the boundary, rather akin to the sliding flow of a Filippov system. Thus the *sticking subset* of the grazing set Σ^0 is determined by the conditions

$$\Sigma^0_- \equiv \left\{ \ x : H(x) = 0, \quad v(x) = 0, \quad a(x) < 0 \ \right\}.$$

The *sticking motion* evolves under the action of the vector field F, constrained to lie on the surface Σ. If we define the impact law according to (2.27), then it is possible to express the sticking vector field as

$$\dot{x} = F_s(x) = F(x) - \rho(x) W(x), \tag{2.30}$$

where

$$\rho(x) = \frac{a(x)}{(H_xF)_x W}. \tag{2.31}$$

To see that this corresponds to a sticking flow, note that in order to stick we require $H(x(t)) = v(x(t)) \equiv 0$. Differentiating the conditions $H(x) = 0$ and $v(x) = 0$ with respect to time, we have $H_x\dot{x} = 0$ and $v_x\dot{x} = 0$. The first of these conditions is satisfied identically when $H_xW = 0$, and the second condition if

$$0 = (H_xF)_x F - \rho (H_xF)_x W = a(x) - \rho (H_xF)_x W, \tag{2.32}$$

which defines ρ according to (2.31). Note that (2.30)-(2.31) defines a smooth flow $\Phi_s(x, t)$, which is also defined within a neighborhood of Σ, but for which the set $\Sigma = \{x : H(x) = 0\}$ is invariant. For the hybrid system, the sticking flow ceases to apply when the trajectory leaves Σ^0_-. At such a point $a(x) = 0$, but $\frac{da(x)}{dt} := a_x(x)\dot{x} > 0$ and hence the system moves into S^+ where the original flow Φ applies. The condition that the vector field remains in the sticking region is $\rho(x) > 0$.

Typically, unlike the sliding motion in Filippov systems, impacting systems do not enter a sticking region directly, but via a *chattering sequence*, also known in control theory as a *Zeno phenomenon*. Such a sequence begins if an impact occurs within Σ^-, close to the set Σ^0 with $v(x^+) \ll 1$ and $a(x^+) < 0$. There follows an infinite sequence of impacts, of successively reduced velocity, which converges in finite time, onto a point in the sticking set. After the accumulation of such a sequence, the motion will evolve in the sticking set in the manner described above and depicted in Figure 1.2.

2.4.1 Zeno phenomenon

For an illustration of the *Zeno phenomenon*, let consider the dynamics of a ball released under the action of gravity bouncing against a rigid wall, in correspondence with Figure 2.13.

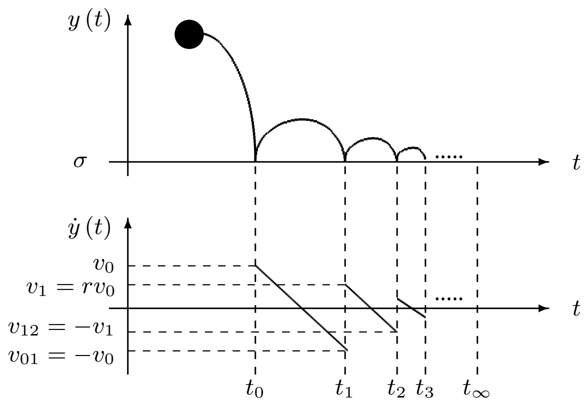

Figure 2.13 — Illustration of Zeno behaviour in the motion of a ball falling under the action of gravity.

Dynamics of motion are described by the set of equations

$$\begin{array}{ll} \ddot{y} = -g; & y > \sigma, \\ \dot{y}^{+} = -r\dot{y}^{-}; & y = \sigma, \end{array} \tag{2.33}$$

for $0 < r < 1$ being the coefficient of restitution for inelastic collisions and g representing the constant acceleration of the gravitational field.

The free-flight motion between collisions can be solved from (2.33) as

$$\begin{array}{l} \dot{y}(t - t_0) = -g(t - t_0) + \dot{y}(0); \\ y(t - t_0) = -\frac{g}{2}(t - t_0)^2 + \dot{y}(0)(t - t_0) + y(0), \end{array} \tag{2.34}$$

with $y(0) \equiv y(t - t_0)|_{t=t_0} = y_0$ and $\dot{y}(0) \equiv \dot{y}(t - t_0)|_{t=t_0} = v_0$.

Without loss of generality let's consider $t_0 = 0$, $y_0 = \sigma$ and $v_0 > 0$.

The time for the next impact, say t_1, should satisfy

$$\begin{array}{l} y(t_1 - t_0) = y(t_1) = \sigma = -\frac{g}{2}(t_1 - t_0)^2 + v_0(t_1 - t_0) + \sigma \\ \Rightarrow 0 = -\frac{g}{2}(t_1 - t_0)^2 + v_0(t_1 - t_0) = -\frac{g}{2}t_1^2 + v_0 t_1 \\ \Rightarrow t_1 = \left\{ \begin{array}{l} 0; \\ \frac{2v_0}{g}. \end{array} \right. \end{array} \tag{2.35}$$

The trivial solution $t_1 = 0 = t_0$ will be not considered under forward flowing in time. Then $t_1 = \frac{2v_0}{g}$, and the velocity immediately before the collision can be calculated from (2.34) as

$$\begin{array}{l} \dot{y}(t_1 - t_0) = \dot{y}(t_1) \equiv v_{01} = -g(t_1 - t_0) + v_0 \\ \Rightarrow v_{01} = -gt_1 + v_0 = -g\frac{2v_0}{g} + v_0 = -v_0. \end{array} \tag{2.36}$$

Using the boundary condition in (2.33), the velocity immediately after the collision becomes

$$\begin{aligned}&\dot{y}\left(t_1-t_0\right)^{+}=v_1=-r\dot{y}\left(t_1-t_0\right)^{-}=-rv_{01}\\&\Rightarrow v_1=rv_0.\end{aligned} \tag{2.37}$$

Repeating the procedure, we can get the time for the next collision t_2 in terms of the quantities at $t=t_0$, by

$$\begin{aligned}&y\left(t_2-t_1\right)=\sigma=-\tfrac{g}{2}\left(t_2-t_1\right)^2+v_1\left(t_2-t_1\right)+\sigma\\&\Rightarrow 0=-\tfrac{g}{2}\left(t_2-t_1\right)^2+v_1\left(t_2-t_1\right)\\&\Rightarrow \tfrac{g}{2}\left(t_2-t_1\right)=v_1\Rightarrow t_2=\tfrac{2v_1}{g}+t_1=\tfrac{2}{g}rv_0+\tfrac{2v_0}{g}=\tfrac{2v_0}{g}\left(r+1\right).\end{aligned} \tag{2.38}$$

Hence, the velocity before the second collision becomes

$$\begin{aligned}&\dot{y}\left(t_2-t_1\right)=v_{12}=-g\left(t_2-t_1\right)+v_1\\&\Rightarrow v_{12}=-g\left[\tfrac{2v_0}{g}\left(r+1\right)-\tfrac{2v_0}{g}\right]+rv_0=-2v_0r+rv_0=-rv_0,\end{aligned} \tag{2.39}$$

and immediately after

$$\begin{aligned}&\dot{y}\left(t_2-t_1\right)^{+}=v_2=-r\dot{y}\left(t_2-t_1\right)^{-}=-rv_{12}\\&\Rightarrow v_2=r^2v_0.\end{aligned} \tag{2.40}$$

From calculations for the third collision, we can easily get

$$t_3=\tfrac{2v_0}{g}\left(1+r+r^2\right);\quad v_{23}=-r^2v_0;\quad v_3=r^3v_0, \tag{2.41}$$

that can be generalized for the $(n+1)^{th}$ impact as

$$t_{n+1}=\tfrac{2v_0}{g}\left(1+r+r^2+...+r^n\right);\quad v_{[n,n+1]}=-r^nv_0;\quad v_{n+1}=r^{n+1}v_0. \tag{2.42}$$

Given that the acceleration is constant and negative, the particle is expected to experience complete chattering motion before get stuck. Then, an infinite number of collisions will occur. From (2.42) we have

$$\lim_{n\to\infty}t_{n+1}\equiv t_\infty=\frac{2v_0}{g}\sum_{i=0}^{\infty}r^i\equiv\frac{2v_0}{g}\left[\frac{1}{1-r}\right], \tag{2.43}$$

where the existence of the limit is assured given the conditions assumed for the coefficient of restitution; i.e. $|r|<1$.

Equation (2.43) confirms that under complete chattering regime, an infinite number of collisions accumulate in finite time. The possibility of handling with an infinite number of events is a challenge from the implementation viewpoint and will be treated later for simulation in Chapter 3.

Also in Chapter 6 a generalization of the results just derived, will be employed to explain the transition to chaos experienced by a practical periodically-forced impact oscillator.

2.5 Stability and bifurcations of non-smooth systems

The extension of well-established concepts for smooth systems – as those in section 2.2 – to the case of non-smooth systems, is still an open research area. Here, a pragmatic approach is established for studying the asymptotic and structural stability of the classes of piecewise-smooth flows, maps and hybrid systems given respectively by Definitions 2.17, 2.20 and 2.22. The aim is then to come up with an utilitarian definition of a discontinuity induced bifurcation (DIB) that allows to explain the dynamical transitions experienced in piecewise-smooth systems.

2.5.1 Asymptotic stability

It is a particularly cumbersome task, to provide necessary and sufficient conditions that guarantee the asymptotic stability of an invariant set of a piecewise-smooth system, if that set straddles the boundary between two regions S_i and S_j. Even the problem of assessing the asymptotic stability of an equilibrium that rests on a discontinuity boundary, is an open problem in general. As an example, let's consider the piecewise-linear system:

$$\dot{x} = \begin{cases} A^{-}x; & C^T x \leq 0 \\ A^{+}x; & C^T x \geq 0, \end{cases} \tag{2.44}$$

where $A^{\pm} \in \Re^{n\times n}$ and $C \in \Re^{n}$. We assume that the overall vector field is continuous across the hyperplane $\{x : C^T x = 0\}$, but the degree of smoothness is uniformly one. For the planar case, i.e. $n = 2$, a complete theory is possible and it can be shown that the equilibrium point $x = 0$ of (2.44) is asymptotically stable under certain strict conditions, provided the system obeys the property of *observability* often used in control theory:

Definition 2.24 (Observability)**.** *Two matrices $A \in \Re^{n\times n}$ and $C^T \in \Re^{p\times n}$, are said to be **observable**, if the observability matrix, $\mathbb{O}$, defined as:*

$$\mathbb{O} = \begin{pmatrix} C^T \\ C^T A \\ \dots \\ C^T A^{n-1} \end{pmatrix}$$

has full rank. Equivalently, for single-output systems, where $V \in \Re^{1\times n}$, observability implies $|\mathbb{O}| \neq 0$.

Theorem 2.2 (Asymptotic stability in piecewise-linear systems)**.** *Consider the system* (2.44) *with $n = 2$. Assume that the pair $\left(C^T, A^-\right)$ is observable. Then:*

1. *The origin is asymptotically stable if and only if*
   a) *neither A^- nor A^+ has a real non-negative eigenvalue, and*
   b) *if both A^- and A^+ have non-real eigenvalues, then $\frac{\sigma^-}{\omega^-} + \frac{\sigma^+}{\omega^+} < 0$, where $\sigma^{\pm} \pm i\omega^{\pm}$ $(\omega > 0)$ are the eigenvalues of $A^{\pm}$.*
2. *The system* (2.44) *has a non-constant periodic solution if and only if both A^- and A^+, have non-real eigenvalues and $\frac{\sigma^-}{\omega^-} + \frac{\sigma^+}{\omega^+} = 0$, where $\sigma^{\pm} \pm i\omega^{\pm}$ $(\omega > 0)$ are the eigenvalues of $A^{\pm}$. Moreover, if there is one periodic solution, then all other solutions are also periodic, and any such periodic solution has period equal to $\frac{\pi}{\omega^-} + \frac{\pi}{\omega^+}$.*

In higher dimensions, the problem becomes considerably more difficult. A seemingly paradoxical situation can occur where by the individual systems $\dot{x} = A^{-}x$ and $\dot{x} = A^{+}x$, the origin is asymptotically stable, but is unstable for the combined system (2.44). In essence, the paradox is caused by the geometric relationship between the eigenvectors of the matrices A^{-} and A^{+}. Clearly, if the eigenvectors of the two matrices were perfectly aligned, the stability of the matrices A^{-} and A^{+} would be sufficient to establish stability of the piecewise-linear system.

In the control theory literature, more general tools have been proposed for the stability analysis of piecewise-smooth dynamical systems. One of such techniques consists in providing a common *Lyapunov* function – or function $V(x)$ that is positive definite and decreasing along trajectories – for each of the vector fields defining the system dynamics in each of the phase space regions. However, finding such functions in practice is at best difficult.

A rather different approach, will be instead focusing on structural stability and bifurcation rather than on asymptotic stability of individual states or invariant sets. Since proving stability from first principles can be hard, one should instead attempt to classify all the mechanisms that can lead to instability as a parameter is varied. Along with the classification should come techniques, both analytical and numerical, for identifying which case occurs in a particular example system and for understanding the nearby dynamics.

2.5.2 Structural stability and bifurcation

Consider a general invariant set of a piecewise-smooth dynamical system as defined in Definitions 2.17, 2.20 and 2.22. Bifurcations that involve invariant sets contained within a single region S_i for all parameter values of interest, can be studied using smooth bifurcation theory. Also, it may be that the invariant set of a flow crosses several discontinuity boundaries, but nevertheless the Poincaré map associated with that invariant set is smooth. Thus, all the bifurcations discussed in section 2.2 can also occur in piecewise-smooth systems. However, other bifurcations are unique to PWS dynamics, and involve non-generic interactions of an invariant set with a discontinuity boundary.

For piecewise-smooth systems such as (2.18), (2.20) and (2.21)-(2.22), which define a dynamical system, one can adopt the same notion of bifurcation as in Definition 2.15, applied to the entire system. However, we may wish to highlight other events that might not be a bifurcation of the entire system in this classical sense. In control systems for example, it may be important to identify whether a certain switch is activated. In mechanical systems, we may need to know whether an attractor contains trajectories that impact or go beyond a certain threshold.

The transition that causes such an event, will typically represent an invariant set forming a new crossing of a discontinuity boundary, as a parameter is varied. For example, at a parameter value $\mu = \mu_0$, a limit cycle of a piecewise-linear flow, may become tangent to a discontinuity boundary Σ_{ij} at a grazing point. Alternatively, an equilibrium of a flow, or fixed point of a map, may approach a discontinuity boundary as $\mu \rightarrow \mu_0$. Now, if the degree of smoothness is sufficiently high, this will not affect the stability of these invariant sets and there will be no bifurcation in the sense of Definition 2.15.

In the Russian literature, the term **C-bifurcation** has been adopted for such transitions that involve an invariant set doing something structurally unstable with respect to a discontinuity boundary. When the invariant set is the fixed point of a map, these have also been termed **border-collision-bifurcations**. A broader concept, such of a **discontinuity-induced-bifurcation** (DIB), has been recently introduced in [33], and will be employed here to identify qualitative changes to the topology of invariant sets with respect to the discontinuity boundaries.

Then, proceeding in an analog manner as in the case of smooth systems, in order to define a bifurcation, let's first state proper definitions of topological equivalence and structural stability in piecewise-smooth systems:

Definition 2.25 (Piecewise-topological equivalence)**.** *Let $\{T, \Re^n, \phi^t\}$ and $\{T, \Re^n, \bar{\phi}^t\}$, be two hybrid piecewise-smooth dynamical systems of the form* (2.21)-(2.22)*, defined by countably many different smooth flows $\phi_i(x,t)$ and $\bar{\phi}_i(x,t)$, in finitely many phase space regions S_i and $\bar{S}_i$, respectively, $i = 1, ...N$, with smooth resets R_{ij} and $\bar{R}_{ij}$ applying, respectively, at each non-empty discontinuity boundaries Σ_{ij} and $\bar{\Sigma}_{ij}$. Two such piecewise-smooth systems are called **piecewise-topological equivalent** if:*

1. *They are topological equivalent; that is, there is a homeomorphism h that maps the orbits of the first system onto orbits of the second one, preserving the direction of time, so that $\phi^t(x) = h^{-1}\left(\bar{\phi}^s(h(x))\right)$ where the map $t \mapsto s(t)$ is continuous and invertible.*

2. *The homeomorphism h, can be chosen so as to preserve each of the discontinuity boundaries. That is, for each i and j, $h(\Sigma_{ij}) = \bar{\Sigma}_{ij}$.*

Despite the definition has been made for the case of hybrid dynamical systems, corresponding definitions for piecewise-smooth maps and flows can be stated in a similar way.

Definition 2.26 (Piecewise-structural stability)**.** *A piecewise-smooth system is **piecewise-structurally stable**, if there is an $\varepsilon > 0$ such that all C^1 perturbations of maximum size ε of the vector field (map) f, that leave the number and degree of smoothness properties of each of the boundaries Σ_{ij} unchanged, lead to piecewise-topological equivalent phase portraits.*

Definition 2.27 (Discontinuity-induced bifurcation)**.** *A **discontinuity-induced bifurcation** (DIB) occurs at a parameter value at which a piecewise-smooth system is not piecewise-structurally stable. That is, there exists an arbitrarily small perturbation that leads to a system that is not piecewise-topological equivalent.*

2.5.3 Types of discontinuity-induced bifurcations

According to [33], the most commonly occurring types of codimension-one DIBs, are listed below and depicted in Figure 2.14:

- **Border collisions of maps**. These are conceptually the simplest kind of DIB and occur when, at a critical parameter value, a fixed point of a piecewise-smooth map lies precisely on a discontinuity boundary Σ. For maps with singularity of order one, there is now a mature theory for describing the bifurcation that may result upon varying a parameter through such an event. Remarkably, the unfolding may be quite complex. Even in one dimension, a period-*one* attractor can jump to a period-*n* attractor for any arbitrary n, or to robust chaos without any periodic window. In general n-dimensional maps, bifurcation information on only the simplest kinds of periodic points is known.

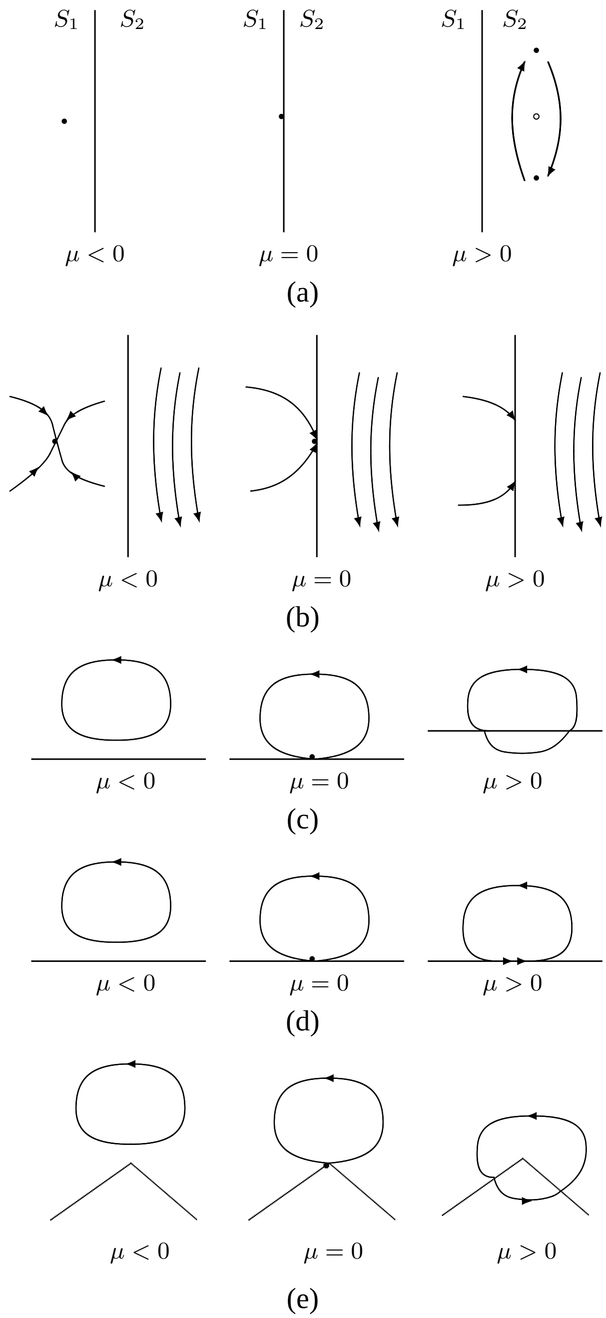

Figure 2.14 — Examples of DIBs: (a) border-collision in a map, (b) boundary equilibrium bifurcation, (c) grazing bifurcation of a limit cycle, (d) sliding bifurcation in a Filippov system and (e) a boundary intersection crossing.

- **Boundary equilibrium bifurcations**. The simplest kind of DIB for flows, occurs when an equilibrium point lies precisely on a discontinuity boundary Σ. In Filippov systems and hybrid systems with sticking regions, there is also the possibility of *pseudo-equilibria*, which are equilibria of the sliding or sticking flow but are not equilibria of any of the vector fields of the original system. There are thus possibilities where the equilibrium lies precisely on the boundary between a sliding or sticking region and a pseudo-equilibrium turns into a regular equilibrium. There is also the possibility that a limit cycle may be spawned under parameter perturbation of the boundary equilibrium, in a Hopf-like transition.

- **Grazing bifurcation of limit cycles**. One of the most commonly found DIBs in applications, is caused by a limit cycle of a flow becoming tangent to (i.e. grazing) with a discontinuity boundary. One might naively think that this can be completely understood as a border collision. However, this is not necessarily the case. Instead one has to analyze carefully what happens to the flow in the neighborhood of the grazing point. In fact, one can derive an associated map, the so-called *discontinuity map*. But the link between the singularity of the map and the degree of smoothness of the flow, is a subtle one that also depends on whether the flow is uniformly discontinuous at the grazing point.

- **Sliding and Sticking bifurcations**. There are several ways that an invariant set, such as a limit cycle, can do something structurally unstable with respect to the boundary of a sliding region in a Filippov system. The Poincaré maps developed for those kind of systems, have the property of typically being non-invertible in at least one region of phase space, owing to the loss of information backward in time inherent in sliding motion. Dynamics implying relay-control and dry-friction falls into such description. Also impacting systems, where sticking regions can be approached by infinite chattering sequences of impacts. In particular, the aim of this Thesis is such of bring evidence of a bifurcation phenomenon experienced on a practical impact oscillator: the cam follower system, after interruption of complete chattering sequences in the so-called **Chattering bifurcation**. See Chapter 6, for further details.

- **Boundary intersection crossing/corner collision**. Another possibility for a codimension-one event in a flow, is where an invariant set (e.g. a limit cycle) passes through the $(n-2)$-dimensional set formed by the intersection of two different discontinuity manifolds Σ_1 and Σ_2. An interesting case is such where the jumps in the vector field across Σ_1 and Σ_2 are such that their intersection can be considered as a *corner* in a single discontinuity surface. See [33] for applications of it in explanation for the dynamics of electronic power converters. Also in [66], Osorio et al have shown how a corner-collision bifurcation is the mechanism to loss stability in a cam-follower system, modelled as a discontinuously periodically-forced impact oscillator.

- **Some possible global bifurcations**. One example, involves a connection between the stable and the unstable manifolds of pseudo-equilibria, which are equilibria of a sliding flow but not of the individual flows either side of a discontinuity boundary.

2.6 Discontinuity mappings

The analysis of discontinuity-induced bifurcations in maps, is relatively straightforward; one merely has to consider the fate of iterates that land either side of the discontinuity. DIBs in piecewise-smooth flows or hybrid systems are far harder to analyze, because one must establish the fate of topologically distinct trajectories close to the structurally unstable event that determines the bifurcation. The concept of a *discontinuity* *map* (DM), first introduced by Nordmark [59] [60], is a key analytical tool that enables to study DIBs involving limit cycles and other invariant sets more complex than mere equilibria. This is a synthesized Poincaré map that is defined locally near the point at which a trajectory interacts with a discontinuity boundary. When composed with a global Poincaré map (for example around the limit cycle), ignoring the presence of the discontinuity boundary, one can then derive a (typically non-smooth) map whose orbits completely describe the dynamics in question.

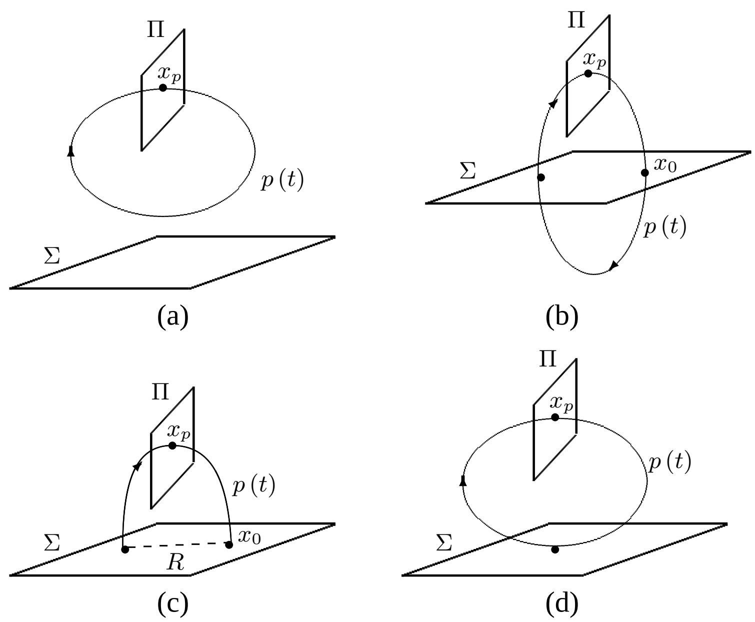

Figure 2.15 — (a) Simple periodic orbit $p(t)$ in a piecewise-smooth ODE that does not intersect any discontinuity surface. (b) Simple periodic orbit that intersects a single surface twice. (c) Equivalent to (b) but for an impacting hybrid system. (d) A grazing periodic orbit.

To illustrate why discontinuity maps are both necessary and useful, consider the piecewise-smooth flow illustrated in Figure 2.15-(a)(b), for which there is a Poincaré surface Π lying in one of the regions S_i, which is intersected transversally at the point x_p by a periodic orbit $p(t)$ of period T. For points $\hat{x} \in \Pi$, close to x_p, we may define a Poincaré map $P : \Pi \to \Pi$. It is natural to ask what form P takes when $\|x - x_p\|$ is small. The answer to this question takes three forms, and depends crucially upon the nature of the orbit $p(t)$. If $p(t)$ lies wholly inside S_i, as in Figure 2.15-(a) then nearby orbits will also lie inside S_i. In this case the time-T map starting from x will be the smooth flow map $P(x) = \Phi(x,t)$, which has a well-defined Taylor series:

$$P(x) = \Phi_{i,x}(x_p, T) + \mathcal{O}\left(\|x - x_p\|^2\right), \tag{2.45}$$

where $\Phi_{i,x}(x_p, T)$ is the Jacobian derivative with respect to x of the flow Φ_i around the periodic orbit, evaluated at $x = x_p$.

More interesting things happen if the periodic orbit $p(t)$ intersects discontinuity surfaces Σ_{ij}. Consider next the case illustrated in Figure 2.15-(b) where $p(t)$ has two transverse intersections with a discontinuity set Σ. In this case, it is tempting to write that the linearization of the Poincaré map, takes the form $P(x) = J_1 J_2 J_3.(x - x_p)$, where J_1, J_2 and J_3 are linearizations of the flows Φ_1, Φ_2 and Φ_3, respectively, for the appropriate times for the trajectory starting at x_p to, respectively, reach Σ for the first time, to pass between the first and second intersections of Σ, and to pass from Σ back to Π. However, this is not the case because, each time Σ is crossed transversally, one must apply a correction to the Poincaré map. This correction is necessary because the time taken from trajectories at points x close to x_p, to reach the discontinuity boundary Σ, will in general vary, and so a small error will be made in assuming that the linearization required is that of Φ_1 for a constant time. The correction to this error, is the discontinuity map in this case. The effect of the DM on the matrix J_1, is to multiply it by a so-called *saltation matrix*. A similar correction must be applied to the matrix J_2. Not introducing these corrections, will in general result in wrong conclusions being made about the Floquet multipliers of the periodic orbit $p(t)$. Note in this case, provided the form of the jump in the vector fields upon crossing Σ, is described by a smooth function, then the discontinuity mapping and the associated global Poincaré map around $p(t)$, will both be smooth. Similar considerations apply to impacting hybrid systems where a periodic orbit $p(t)$, has a single impact with a discontinuity surface as in Figure 2.15-(c).

Now consider for a moment the special case where the velocity normal to Σ is zero, so that the periodic orbit grazes the discontinuity surface, as in Figure 2.15-(d). Note that the trajectories starting from some initial condition $x \in \Pi$ near x_p, do not intersect Σ at all, whereas others intersect Σ with a low normal velocity. The discontinuity mapping in this case, is the identity for orbits that do not cross Σ, but is defined as the local correction that must be applied to initial conditions that do cross Σ, so that a Poincaré map can be applied as if Σ were not there. The effect of applying the DM to the map (2.45) in this case, is to introduce additional terms proportional to fractional powers of $\|x - x_p\|$, such as $\|x - x_p\|^{1/2}$ or $\|x - x_p\|^{3/2}$.

In the case that trajectories intersect discontinuity boundaries transversally, then typically one still has to compute a discontinuity mapping in order to derive a globally correct Poincaré map. This is because even through the trajectory itself may be continuous, there is a correction that must be to the first and higher derivatives of the flow. This correction arises because the discontinuity boundary acts like a new Poincaré section that is distinct from the fixed time-t section that is implicity defined for the flow.

In [33], detailed calculations for the DM of a single-degree-of-freedom impact oscillator are given. Also, these results are employed to explain the suddenly transition to chaos experienced after a periodic solution hits tangentially (grazes) the discontinuity boundary. Results are confirmed numerically and experimentally.

In Chapter 6 we will address the problem of creating an equivalent map for the overall trajectory again, when performing local analysis of a periodic orbit with complete chattering, in a practical cam-follower model. That implies additional difficulties in the analysis, given the theoretical possibility of handling an infinite series of events.

Chapter 3

Numerical analysis of PWS dynamical systems

3.1 Introduction

The analysis of dynamical systems described by sets of ordinary differential equations (ODEs), can be successfully performed by studying trajectories computed numerically in accordance with accurate models. This is particularly useful when it is not possible to derive analytical solutions in closed-form; a situation often experienced when handling realistic models as those including non-linearities and discontinuities.

In the particular case of piecewise-smooth dynamical systems (PWS), the integration algorithm employed to solve the initial value problems (IVP), should incorporate an additional routine aimed at the detection of intersections with the discontinuity surfaces. This results in an hybrid programming structure termed as event-driven, mixing a continuous operator (integrator) with a handler of discrete events. See Figure 3.1 for an illustration.

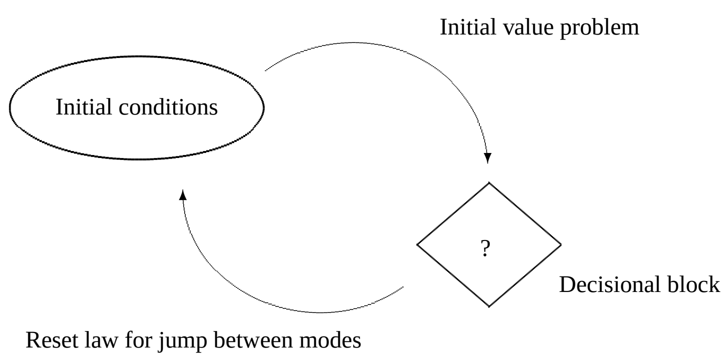

Figure 3.1 — Event-driven approach for scheduling between different operational modes.

Traditionally, such event-driven schemes have been employed to solve the dynamics of systems with discontinuous vector fields. See for example the algorithm proposed in [100]. A more flexible philosophy of programming, was recently proposed by defining decisional blocks in terms of Lie derivatives of the discontinuity boundaries along the vector field [33]. The term “flexible” is referred to the possibility of applying the code easily to any generalized PWS system by just providing the vector fields and the discontinuity surfaces. Routines have been developed for the case of Filippov systems [72] and more recently for impacting systems with chattering [58].

Besides the time-simulation of the dynamics, it is necessary to develop complementary routines in order to perform a complete characterization of the system dynamical scenarios. A clear example is the study on the parameter dependence of equilibria (bifurcation behaviour) by mean of the so-called “brute-force” techniques, where a rough exploration in the parameter space is made by assaying sets of initial conditions. A more effective strategy is that of introducing “path-following” techniques often called “continuation algorithms”. There are several available continuation packages as Auto [36], Loca [76] and Matcont [32], all of them allowing to locate and trace codimension-one and codimension-two smooth bifurcations for multivariate and arbitrarily higher order systems, with a reasonable computational effort.

Therefore, given the associated complexity and the incomplete characterization of novel (non-smooth) bifurcation scenarios, just few attempts have been performed in order to extend traditional methodologies of numerical analysis into PWS systems. Examples include the open-source SICONOS platform [2] and the improved package for Auto: $\widehat{TC}$ [89, 90], employed successfully for tracing trajectories with a handleable number of events. Hence, new developments and adaptation of conventional numerical techniques for the case of branch tracing in PWS dynamical systems, constitutes an interesting and open topic of research with many possibilities to explore.

In what follows, numerical strategies for the characterization of the dynamics of PWS systems are described and illustrated through examples derived from applications.

3.2 Simulation

As stated before, numerical solutions for systems with discontinuous and constrained trajectories can be approximated by a combination of continuous and discrete operators in particular algorithm configurations. Some representative examples are described below.

3.2.1 Time-stepping

As suggested by the name, this kind of algorithms perform calculations in a discrete-time based scheme, with a certain fixed step-size schedule. In terms of hybrid systems, this has been commonly formulated as a linear complementarity problem (LCP); i.e. a linear programming problem in which the solution space is partitioned in the many available modes. Therefore, existence and unicity conditions of solutions should be verified during each particular application.

Here, instantaneous jumps in the system states are smoothed by stiff (or fast in time) equivalent equations. Such situation allows to solve the equations by integration ignoring the exact location of the discontinuous events. After proper discretization, solutions to the LCP can be formulated as recursive “one-step” calculations. Hence, the step-size will constitute a critical design feature affecting the accuracy and even the existence of a given solution.

As an example of LCP in PWS dynamical systems, let’s consider the approach developed by Çamlibel et al in [25] where a piecewise-linear model for friction in mechanical systems and commutation in electrical circuits, has been approximated with relay switches. Specifically, the system considered is given by:

$$\begin{aligned} \dot{x}(t) &= Ax(t) + B\bar{u}(t) \\ \bar{y}(t) &= Cx(t) + D\bar{u}(t) \\ \bar{u}_i(t) &= \operatorname{sgn}\left(-\bar{y}_i(t)\right), \end{aligned} \tag{3.1}$$

with $\bar{u} \in \Re^m$, $x \in \Re^n$, $y \in \Re^m$ and A, B, C and D matrices of appropriate dimensions. Each pair $(-\bar{y}_i, \bar{u}_i)$ satisfies an ideal relay characteristic $\bar{u}_i = \operatorname{sgn}(-\bar{y}_i)$, where $\operatorname{sgn}(.)$ denotes the signum relation, often referred as $(-\bar{y}_i, \bar{u}_i) \in F_{relay}$. Then, after applying a backward Euler time-stepping discretization, system (3.1) becomes:

$$\begin{aligned} \tfrac{x_{j+1}-x_j}{h} &= Ax_{j+1} + B\bar{u}_{j+1} \\ \bar{y}_{j+1} &= Cx_{j+1} + D\bar{u}_{j+1} \\ (-\bar{y}_{j+1,i}, \bar{u}_{j+1,i}) &\in F_{relay}, \end{aligned} \tag{3.2}$$

where h is the chosen step-size and $\bar{u}_j$, x_j, $\bar{y}_j$ denote approximations at time instants $t_j = jh$, $j = 0, 1, 2, ...$

Consequently, equation (3.2) constitutes the algebraic one-step problem

$$\begin{aligned} \bar{y}_{j+1} = C\left(I - Ah\right)^{-1} x_j + \left[C\left(\tfrac{1}{h}I - A\right)^{-1} B + D\right] \bar{u}_{j+1} \\ (-\bar{y}_{j+1,i}, \bar{u}_{j+1,i}) \in F_{relay}, \end{aligned} \tag{3.3}$$

with state-update

$$x_{j+1} = (I - Ah)^{-1} x_j + \left(\frac{1}{h}I - A\right)^{-1} B\bar{u}_{j+1}. \tag{3.4}$$

Given an initial state $x(0) = x_0$, the scheme starts by setting $x_j = x_0$ and $j = 0$. Solving the one-step problem for j in (3.3) results in $\bar{u}_{j+1}$ and $\bar{y}_{j+1}$. Next, we can determine x_{j+1} from (3.4) as x_j and $\bar{u}_{j+1}$ are known. The counter j can be increased resulting in a new one-step problem. This cycle is repeated until a desired end-time T is reached. For a given step-size h, this procedure results in a sequence of approximations provided the one-step problems are solvable. Hence, a family of approximations, all functions of the step-size h, can be defined.

A linear complementarity problem is stated and solved in [25], demonstrating the convergence of solutions even when an infinite number of events (Zeno phenomenon or chattering, defined in Chapter 2) is expected to occur.

A disadvantage of this kind of approach, is the increased computational effort added by solving stiff equivalent problems (i.e. with small time steps) and the necessity of establish convergence conditions for each particular case of study.

Interested readers can check [48], [11] and [1] for further insights on time-stepping.

3.2.2 Event-driven

An alternative simulation approach is obtained by considering instantaneous resets at the discontinuity boundaries (events). This implies the accurate location of the time-instants at which such discontinuity boundaries are reached, representing a fundamental difference with time-stepping strategies where events are just ignored.

Recently in [72] and [58], a flexible way to detect events on a discontinuity surface[1] has been proposed by locating the zero level of a scalar function $H(x)$ in the domain of the state vector x. This general event-checking can be performed directly by the built-in subroutine of the ODE solver in Matlab, allowing to schedule transitions for successive modes by analyzing quantities derived from vector fields. Additional events; e.g. Poincaré surfaces, can be defined by users for general purposes in an equivalent way.

The decisional block, where simulation modes and state jumps are selected, depends on the particular PWS system under analysis. As an illustration, let's consider the treatment of Filippov systems developed in [72] taking a dynamical system of the form

$$\dot{x} = \begin{cases} F_i(x), & x \in S_i, \\ F_j(x), & x \in S_j, \end{cases} \tag{3.5}$$

for $x \in \Re^n$ and F_i, F_j being vector fields sufficiently smooth.

The state space consists of only two regions S_i and S_j:

$$\begin{aligned} S_i &= \{x \in \Re^n | H_{ij} > 0\}; \\ S_j &= \{x \in \Re^n | H_{ij} < 0\}, \end{aligned} \tag{3.6}$$

separated by a discontinuity surface Σ_{ij} defined in terms of a smooth scalar function $H_{ij}(x)$ as:

$$\Sigma_{ij} = \{x \in \Re^n | H_{ij}(x) = 0\}. \tag{3.7}$$

An important subset of Σ_{ij} is the one for which the vector fields are both pointing towards or away from the discontinuity boundary. Such a set constitutes the *sliding surface* and will be denoted as $\hat{\Sigma}_{ij}$, representing an open segment between the points $\hat{\Sigma}_{ij}^{+}$ and $\hat{\Sigma}_{ij}^{-}$. In the same way, these end points delimit two tangent surfaces defined by:

$$\begin{aligned} \Sigma_{ij}^{-} &= \{x \in \Re^n | \mathcal{L}_{F_i}(H_{ij}) = 0\}; \\ \Sigma_{ij}^{+} &= \left\{x \in \Re^n | \mathcal{L}_{F_j}(H_{ij}) = 0\right\}, \end{aligned} \tag{3.8}$$

with $\mathcal{L}_F$ denoting the Lie derivative of $H(x)$ in the direction of F, or equivalently:

$$\left\langle \frac{dH}{dx}, F \right\rangle, \tag{3.9}$$

for $\langle ., . \rangle$ as the scalar product operator.

Hence, as shown in Figure 3.2 there are 6 possible regions (or operational modes) available for selection, depending on the detection of the following events:

$$e(x,t) = \begin{cases} H_{ij}(x) = 0; \\ \mathcal{L}_{F_i}(H_{ij}) = 0; \\ \mathcal{L}_{F_j}(H_{ij}) = 0, \end{cases} \tag{3.10}$$

[1]Here all the treatment will be done by considering a single discontinuity boundary. Nevertheless, it can be extended to higher orders with an increased complexity in the corresponding routines derived.

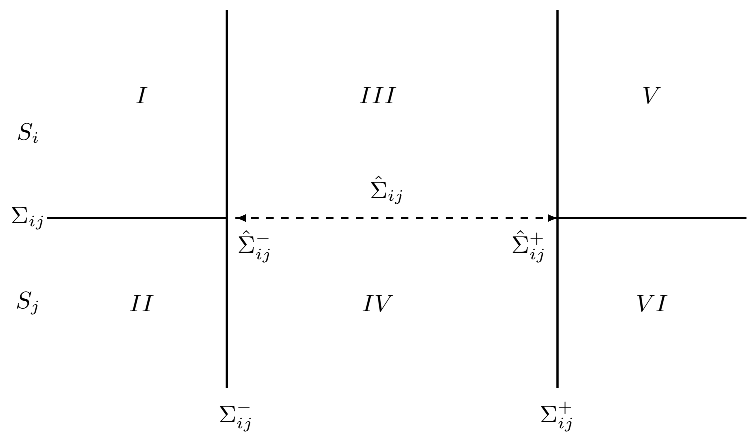

Figure 3.2 — Boundaries for operational regions in the event-driven approach for simulation of Filippov systems.

and the direction of the corresponding crossings.

These establish the set of conditions to be evaluated numerically as the event-driven strategy. Additional numerical considerations and results are clearly illustrated in [72].

3.2.3 Extended event-driven

A similar approach to the one described above for the case of Filippov systems, has been developed and implemented in [58] for impacting systems with chattering. We will refer to it in some detail, because most of the numerical results contained in this Thesis have been generated on the basis of this particular simulation strategy.

Essentially, by considering again a single discontinuity boundary represented by the zero set of a scalar function of the system states $H(x)$, the main question to solve by the decisional block is whether the particle will experience one of the operational modes: *impacting* with rejection, *sticking* (equivalent to the sliding condition) or *chattering*. Therefore, in an attempt to reproduce in a realistic manner the dynamics of the motion, an accurate set of events should be defined for detection of all the possible transitions.

Notice that from the beginning, the problem of including an infinite evaluation of events in finite time; i.e. chattering, has been considered and this imposes limitations in the performance of the event-driven approach.

Following Piiroinen and Nordmark in [58], consider the dynamical system described by:

$$\dot{x} = F(x), \quad x \in S \subset \Re^n, \tag{3.11}$$

where S is a subset of $\Re^n$ and F a vector field on S. By defining an impact surface (discontinuity surface) as the zero level of a scalar function $H : S \to \Re$, the motion can be constrained to the subset of S for which $H(x) \geq 0$.

Thus, it is possible to define – as in (3.9) – quantities relating H in terms of Lie derivatives in the direction of F:

$$\begin{gathered}\mathcal{L}_F(H)(x)=\left\langle \tfrac{dH}{dx},F\right\rangle ;\\ \mathcal{L}_F^k(H)(x)\equiv\mathcal{L}_F\left(\mathcal{L}_F^{k-1}(H)(x)\right);\\ \mathcal{L}_F^0(H)(x)=H;\\ v(x)=\mathcal{L}_F^1(H)(x);\\ a(x)=\mathcal{L}_F^2(H)(x).\end{gathered} \tag{3.12}$$

Through this fundamental operator, dynamical modes can be established by means of the following subsets of the state space S:

$$\begin{array}{ccc} S_k^+=\left\{x\in S|\mathcal{L}_F^k(H)(x)>0\right\}, & S_k^0=\left\{x\in S|\mathcal{L}_F^k(H)(x)=0\right\}, & S_k^-=\left\{x\in S|\mathcal{L}_F^k(H)(x)<0\right\},\\ \Sigma_k^+=\left(\bigcap\limits_{m=0}^{k-1}S_m^0\right)\cap S_k^+, & \Sigma_k^0=\left(\bigcap\limits_{m=0}^{k-1}S_m^0\right)\cap S_k^0, & \Sigma_k^-=\left(\bigcap\limits_{m=0}^{k-1}S_m^0\right)\cap S_k^-,\end{array} \tag{3.13}$$

for non-negative integers k.

Therefore, if an impact occurs $x\in\Sigma_1^-$ and we should apply an impact law given by:

$$R(x)=x+W(x)\,v(x), \tag{3.14}$$

for some analytic function $W:S\to\Re^n$, that in the case of a periodically forced SDOF (single-degree of freedom) impact oscillator corresponds to:

$$W=\begin{bmatrix}0\\ -(1+r)\\ 0\end{bmatrix}, \tag{3.15}$$

for $0<r<1$ being the coefficient of restitution for inelastic collisions. Hence, for $x\in\Re^3$ and $v(x)\equiv x_2$ the impact law reduces to the model of restitution of Newton:

$$R(x)\equiv R\left(\begin{bmatrix}x_1\\ x_2\\ x_3\end{bmatrix}\right)=x+\begin{bmatrix}0\\ -(1+r)\\ 0\end{bmatrix}v(x)=\begin{bmatrix}x_1\\ x_2-v(x)-rv(x)\\ x_3\end{bmatrix}\equiv\begin{bmatrix}x_1\\ -rx_2\\ x_3\end{bmatrix}. \tag{3.16}$$

Now, as already discussed in Chapter 2, under acceleration attracting the particle towards the surface an infinite number of collisions of decreasing velocity will be experienced. Moreover, as demonstrated later in Chapter 6 (see also [22] [57] [58]) by assuming a low-velocity impacting regime, it is possible to develop an equivalent mapping for the complete chattering event allowing to estimate numerically the locations of the accumulation time t_∞ and the state vector $x|_{t=t_\infty}$ just before entering the sticking condition. In [58] these quantities have been approximated to the first order by:

$$\begin{gathered}t_\infty=q(x)=\tfrac{1}{1-r(x)}\left(\tfrac{2}{a(x)}r(x)\right)v(x)+v(x)^2\,\mathcal{O}(1),\\ x|_{t=t_\infty}=Q(x)=x+\tfrac{1}{1-r(x)}\left(\tfrac{2F(x)}{a(x)}r(x)+W(x)\right)v(x)+v(x)^2\,\mathcal{O}(1),\end{gathered} \tag{3.17}$$

with $r(x)\equiv-(1+\mathcal{L}_W\mathcal{L}_F(H)(x))$, equivalent to the scalar value "r" in (3.16). See [58] for details.

In this way the chattering can be scheduled as an event, and then included in the set of modes and conditions constituting the decisional block of the hybrid algorithm. Following [58] the continuous trajectories are given by a sequence of functions $X_k : I_k \to \Re^n$, $k = 0, 1, ...$, where $I_k = [t_k, \bar{t}_k]$ is a sequence of time intervals. Also, there is a sequence of discrete states $S_k \in f, s$ (f for free flight and s for sticking) and vector fields $F_k : \Re^n \to \Re^n$ where:

$$F_k = \begin{cases} F, & S_k = f; \\ \bar{F}, & S_k = s. \end{cases} \tag{3.18}$$

By denoting the initial and final points of each trajectory as $x_k = X_k(t_k)$ and $\bar{x}_k = X_k(\bar{t}_k)$ respectively, it is possible to define also a function of event mappings $E_k : \Re^n \to \Re^n$, $e_k : \Re^n \to \Re$, such that:

$$\begin{aligned} &x_{k+1} = E_k(\bar{x}_k), \\ &t_{k+1} = \bar{t}_k + e_k(\bar{x}_k). \end{aligned} \tag{3.19}$$

Thus X_k is a trajectory of F_k in the time interval I_k, and for $t_k < t < \bar{t}_k$ we have $X_k(t) \in \Sigma_0^+$ if $S_k = f$, or $X_k(t) \in \Sigma_2^-$ if $S_k = s$. All of this taking place at an event surface defined as the zero level set of a scalar function $H_k : \Re^n \to \Re$. There are three possible events:

1. If there is a complete chattering event, then $E_k = Q(x)$, $e_k = q(x)$, $H_k = H$, and we require $\bar{x}_k \in \Sigma_1^-$, $S_k = f$, $x_{k+1} \in \Sigma_2^-$, $S_{k+1} = s$;
2. If there is a regular impact, then $E_k = R(x)$, $e_k = 0$, $H_k = H$, and we require $\bar{x}_k \in \Sigma_1^-$, $S_k = f$, $x_{k+1} \in \Sigma_1^+$, $S_{k+1} = f$;
3. And, if there is a release from sticking, then E_k is an identity mapping, $e_k = 0$, $H_k = a(x)$, and we require $\bar{x}_k \in \Sigma_3^+$, $S_k = s$, $S_{k+1} = f$.

In order to give a better numerical approximation in a vicinity of a tangent collision (grazing), it is convenient to extend the definition for the vector fields in (3.18), by:

$$F_k = \begin{cases} F, & S_k \in \{f^+, f^-\} \\ \bar{F}, & S_k = s \end{cases}, \tag{3.20}$$

with:

$$S_k = \begin{cases} f^+, & x \in S_1^+ \\ f^-, & x \in S_1^- \\ s, & x \in \Sigma_2^-. \end{cases} \tag{3.21}$$

Under this new assumption five events can occur, namely: "i" - an impact with negative velocity, "ii" - a complete chattering event, "iii" - release from sticking, "iv" - negative velocity becomes positive and "v" - positive velocity becomes negative. An illustration of the flow-diagram with the corresponding transitions is depicted in Figure 3.3.

Another important consideration related with the singularity of the impact map for collisions with zero-velocity, implies unbounded values of Jacobians when tracing trajectories with complete chattering (see [23] and references therein). In order to overcome this inconvenience, an augmented state vector has been also proposed in [58] for compensation of divergence in calculations.

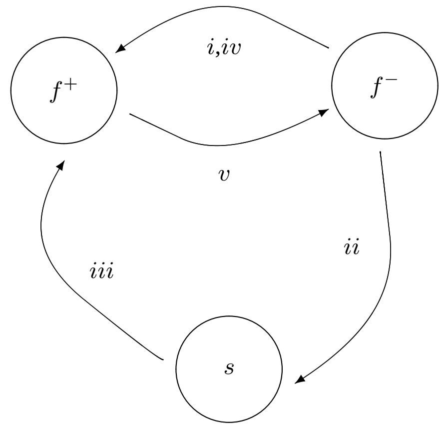

Figure 3.3 — Flow-chart for state transition in the extended vector field approach of an hybrid event-driven simulator.

Essentially, a new state vector $\hat{x} \in \Re^{n+2}$ is considered during low-velocity impacts:

$$\hat{x} = \begin{bmatrix} x \\ h \\ u \end{bmatrix}, \tag{3.22}$$

with u representing the outgoing velocity (after impacts) and h the quotient relating $H\left(x\right)/u$.

Hence, the extended impact mapping, the extended impact surface function and the extended vector field, can be defined respectively as:

$$\begin{aligned} &\hat{x} \leftarrow \hat{R}\left(\hat{x}\right) = \begin{bmatrix} R\left(x\right) \\ 0 \\ v\left(R\left(x\right)\right) \end{bmatrix}, \\ &\hat{H}\left(\hat{x}\right) = h, \\ &\dot{\hat{x}} = \hat{F}\left(\hat{x}\right) = \begin{pmatrix} F\left(x\right) \\ v\left(x\right)/u \\ 0 \end{pmatrix}. \end{aligned} \tag{3.23}$$

Such an extended simulator is then capable to approximate a trajectory under complete chattering motion with an improved precision, allowing to detect transitions into non-sticking mode of particular relevance for the application case considered in this Thesis. In Figure 1.3, simulated trajectories depict motions with complete chattering in solid and with null sticking-time (τ in Figure) dashed.

Additional references, procedures and explicit examples can be found in [58].

3.3 Characterization of the dynamics

As stated before, a simple way to get an insight on the behavioural features of a given system, is by studying the qualitative changes of stationary solutions under parameter variations. This can be particularly useful in a practical sense, given that modifications on environmental conditions can alter drastically characteristics of performance. Analogously, available theory of bifurcations and the possibility to obtain parametric models under deterministic external influences, allow to explain and predict with a mathematical basis, stability conditions. In the following, some numerical approaches aimed at construction of bifurcation diagrams are illustrated.

3.3.1 Brute-force bifurcation diagrams

A natural and intuitive manner to extract information on the parameter dependence of a dynamical model, consists in performing time simulations for different parameter values over the range of interest. It is then important to have a certain clarity about the allowed range of variations (parameter space) as well as an appropriate modelling describing accurately the case under analysis. Consequently, by plotting stationary values of system quantities as function of parameter(s), a general picture of the dynamical behaviour can be straightforwardly constructed.

As an example, consider Figure 5.1 showing the motion history of a constrained harmonic oscillator. In particular, dynamics are described by the evolution of an angular position θ_f (solid) driven by a periodic force $\hat{\theta}_c$ (dashed). The parameter corresponds with the forcing frequency ω, varied within the interval $\omega \in [130, 160]\, rpm$. The qualitative and quantitative changes for the stationary value of θ_f at a certain given phase ϕ_0 (representing the maximum of $\hat{\theta}_c$), are showed as a function of the parameter by dots in the main panel of the Figure. Each point represents the last 100 stroboscopic samples after simulation of 300 forcing cycles, in an attempt for annihilate transient components. Initial conditions for each simulation are the same; i.e. equal angle for the particle and the forcing at ϕ_0. The parameter has been swept bidirectionally in order to overcome hysteretic behaviour.

From the graph it is then evident that there are different solutions of motion, for different parameter values. Also there are coexistence and abrupt transitions between modes. This gives a general idea about the dynamical features of motion observed by variations of ω, as claimed.

An alternative way for characterization of dynamics in constrained harmonic oscillators is given by plotting information on the states at each collision during a forcing period. This is commonly referred as a numerical "impact-mapping", and can be employed to show – as depicted in Figure 5.9 – the transition between periodic regimes. It is then possible to develop impact-based bifurcation diagrams. See [63] for an interesting discussion on advantages and disadvantages of impact and stroboscopic maps in impacting oscillators.

3.3.2 Monte Carlo approach: an improved brute-forcing technique

It is well known that the dynamics of nonlinear systems (including PWS) are characterized by multiple solutions in state-space. This is actually reflected in the geometry of associated basins of attraction, justifying dynamical effects on a global scale. Then, as a way to cover a wider spectrum of solutions during brute-forcing procedures, a representative set of initial conditions should be strategically selected for simulation under each parameter value.

Such scheduling of initial conditions, often uses statistical considerations for enrichment of data samples by the so- called Monte Carlo method of programming [55], where by definition, repeated calculations of a given algorithm employing random information, allows to bring a better estimation for a deterministic solution. Mathematically, consider the dynamical system:

$$\dot{x} = f\left(x, t, \mu\right); \quad x \in \Re^n; \quad \mu, t \in \Re \tag{3.24}$$

for a certain parameter μ and x as the state vector in time t, with solution trajectories defined in terms of the flow function $\Phi : \Re^n \times \Re \rightarrow \Re^n$ satisfying:

$$\tfrac{\partial}{\partial t}\Phi\left(x, t\right) = f\left(\Phi\left(x, t\right), \mu\right); \quad \Phi\left(x, 0\right) = x. \tag{3.25}$$

A solution trajectory starting from x_0 at t_0, can be expressed at an arbitrary time instant t in terms of the flow function Φ, as $x(t) \equiv \Phi\left(x_0, t - t_0\right)$. Moreover, given the parameter dependence assumed for (3.24), stability conditions in solution trajectories are expected to be affected by variations on μ.

Hence, a set of initial conditions X_0 can be defined as:

$$X_0 = \left\{x_0 \in \Re^n | x_0^i \equiv \rho\left(\sigma, \eta\right), i = 1, 2.., n\right\}, \tag{3.26}$$

for ρ representing a probability density function with standard deviation σ and mean value η.

As an illustration, consider Figure 5.12 where a Monte Carlo brute-force simulation has been performed for the exemplification case of section 3.3.1. Here, $\rho\left(\sigma, \eta\right)$ was chosen to be uniformly-distributed with $\eta = 1/2$ and $\sigma^2 = 1/12$. Therefore, by defining a boundary of interest in the state-space, a grid of points belonging to it will be uniformly selected. Notice the appearance of several solution branches, invisible when simulating for a single initial condition (compare with the same parameter range on Figure 5.1).

3.3.3 Continuation

An evident disadvantage of brute-forcing techniques is related with the excessive computational effort derived from the many simulations needed to characterize efficiently a given range of parameters. Also, brute-force methods based on time simulations can only account for stable solutions. These situations can be avoided by introducing path following or "continuation" techniques, that employing a theoretical-based framework, allows to improve calculation of solution branches, even when they are unstable. This will concern the main subject of the remaining sections of the Chapter.

3.4 Path following techniques

So far, we have briefly described how to perform numerical evaluation of the qualitative changes in dynamical properties of systems by varying parameters. It is also possible to integrate mathematical tools in such a process, in order to reduce the amount of calculations involved. In this context, the Implicit Function Theorem (IFT), brings the theoretical foundation to develop a numerical method employed to trace or "continue" solution branches [49, 79, 37, 52]. In the following, the basic principles of continuation and some application examples are given.

3.4.1 Implicit function theorem and fundamentals on continuation

Roughly speaking, in a multivariate mathematical formulation it is always possible to express a given variable as a function of the others, whenever the set of conditions given by the IFT holds. This result can be further employed to describe the parameter dependence of equilibria in dynamical systems.

Hence following [79], let's consider the vector field composed of the n differential equations:

$$\dot{x} = f(x, \mu), \tag{3.27}$$

with $x \in \Re^n$ and $\mu \in \Re$, as in (3.24). The equilibria of such dynamical system is then defined by all the elements of the $(n+1)$-dimensional space (x, μ) for which $f(x, \mu) = 0$. The function f is often defined only on a subset of the $(n+1)$-dimensional space.

In general, the equation $0 = f(x, \mu)$ defines implicity one or more curves in its domain. The question is whether an equation $0 = f(x, \mu)$ implicity defines a function $x = F(\mu)$, in such a way that $0 = f(F(\mu), \mu)$ is still verified. The general statement is as follows:

Theorem. Implicit Function Theorem: *Given $f : \Re^n \to \Re^n$, assume that*

1) $f(x^*, \mu^*) = 0$.

2) f is continuously differentiable on its domain, and

3) $\left.\frac{\partial f}{\partial x}\right|_{(x^*, \mu^*)}$ is nonsingular.

Then, there is an interval $\mu_1 < \mu^* < \mu_2$ about μ^*, in which a vector function $x = F(\mu)$ is defined by: $0 = f(x, \mu)$, with the following properties holding for all μ with $\mu_1 < \mu < \mu_2$:

a) $f(F(\mu), \mu) = 0$,

b) $F(\mu)$ is unique with $x^* = F(\mu^*)$,

c) $F(\mu)$ is continuously differentiable, and

d) $\frac{\partial f}{\partial x}\frac{dx}{d\mu} + \frac{\partial f}{\partial \mu} = 0$.

By considering μ as the parameter of interest, the result just stated allows to trace a branch of equilibria for the dynamical system (3.27), within the parameter interval $\mu_1 < \mu < \mu_2$.

For an illustration, let's consider once more the last condition on the IFT; i.e:

$$\begin{array}{l} \frac{\partial f}{\partial x}\frac{dx}{d\mu} + \frac{\partial f}{\partial \mu} \equiv \frac{d}{d\mu} f(x(\mu), \mu) \\ \Rightarrow f(x(\mu), \mu) = 0 \\ \Rightarrow \frac{d}{d\mu} f(x(\mu), \mu) = 0 \\ \Rightarrow \frac{\partial f}{\partial x}\frac{dx}{d\mu} + \frac{\partial f}{\partial \mu} = 0 \Rightarrow \frac{dx}{d\mu} = -\frac{\partial f}{\partial \mu}\Big/\frac{\partial f}{\partial x}, \end{array} \tag{3.28}$$

Therefore, integration of (3.28) with respect to μ allows to solve for the equilibria of f. This constitutes the fundamental continuation algorithm, having a strong constraint in the nullity of the denominator term $\frac{\partial f}{\partial x}$, representing the Jacobian of the vector field f in terms of the state vector x. It is well known that such a Jacobian will have singularities at bifurcation points, and then the basic continuation procedure must be complemented by additional routines overcoming singularities and allowing detection and commutation between solution branches.

3.4.2 Predictors

A simple change of parameter, should be enough to avoid the singularity in (3.28). This redefinition of parameter is known as *Parameterization*, and essentially refers to a new measure taken along the branch of solutions chosen strategically to facilitate calculations [79]. As an example consider the *Arclength*, that for small segments of a curve can be defined as (see Figure 3.4 for an illustration):

$$\begin{aligned}&\Delta s^2 = \Delta x_1^2 + \Delta x_2^2 + ... + \Delta x_n^2 + \Delta\mu^2\\ &\Rightarrow 1 = \tfrac{\Delta x_1^2}{\Delta s^2} + \tfrac{\Delta x_2^2}{\Delta s^2} + ... + \tfrac{\Delta x_n^2}{\Delta s^2} + \tfrac{\Delta\mu^2}{\Delta s^2}\\ &\Rightarrow \lim_{\Delta s\to 0} \triangleq 1 = \left(\tfrac{d}{ds}x_1\right)^2 + \left(\tfrac{d}{ds}x_2\right)^2 + ... + \left(\tfrac{d}{ds}x_n\right)^2 + \left(\tfrac{d}{ds}\mu\right)^2.\end{aligned} \tag{3.29}$$

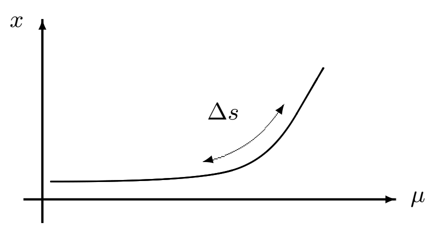

Figure 3.4 — Arclength in terms of the variable s, as the new parameter to express dependence of system quantities; i.e. $x \equiv x(s)$, $\mu \equiv \mu(s)$.

Taking the finite-differences approximation for the derivative of the extended state vector $X = (x, \mu)$ in terms of the new parameter s, we have:

$$\begin{aligned}&\tfrac{dX}{ds} \approx \tfrac{X_{(k+1)} - X_{(k)}}{s_{(k+1)} - s_{(k)}};\\ &\Rightarrow X_{(k+1)} \approx X_{(k)} + \left[s_{(k+1)} - s_{(k)}\right]\tfrac{dX}{ds} = X_{(k)} + \Delta s \left[\begin{array}{ccccc} \tfrac{d}{ds}x_1 & \tfrac{d}{ds}x_2 & ... & \tfrac{d}{ds}x_n & \tfrac{d}{ds}\mu \end{array}\right]\\ &\equiv X_{(k)} + \Delta s \vec{v}_s,\end{aligned} \tag{3.30}$$

where Δs is the variation step of the parameter and $\vec{v}_s$ represent a vector tangent to $f(X) = 0$ at $X_{(k)}$. Therefore, as depicted in Figure 3.5, (3.30) represents a tangent predictor for the next point of X.

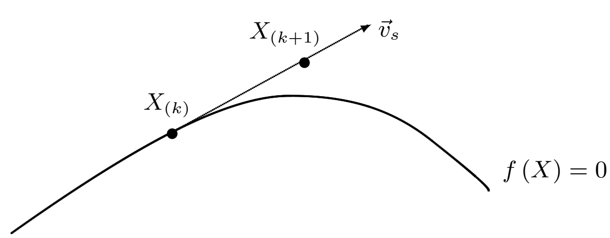

Figure 3.5 — Tangent predictor, showing a projection for the new coordinate of the extended state vector $X = (x, \mu)$.

In order to accomplish the continuation procedure, it is then necessary to constraint the prediction (3.30) to fit or to be as close as possible, to the branch of solutions; i.e. such that $f\left(X_{(k+1)}\right) = 0$. This can be performed by recalling the condition given at (3.29) as:

$$\begin{aligned}&1=\tfrac{d}{ds}x_1^2+\tfrac{d}{ds}x_2^2+...+\tfrac{d}{ds}x_n^2+\tfrac{d}{ds}\mu^2\\&\equiv\left[\begin{array}{ccccc}\tfrac{d}{ds}x_1 & \tfrac{d}{ds}x_2 & ... & \tfrac{d}{ds}x_n & \tfrac{d}{ds}\mu\end{array}\right]\left[\begin{array}{c}\tfrac{d}{ds}x_1\\ \tfrac{d}{ds}x_2\\ ...\\ \tfrac{d}{ds}x_n\\ \tfrac{d}{ds}\mu\end{array}\right]=\left\langle \vec{v}_s,\vec{v}_s^T\right\rangle,\end{aligned} \tag{3.31}$$

and consequently $\vec{v}_s$ is required to be a normalized tangent vector [52].

By considering now the derivative of $f(X)$ with respect to s:

$$\begin{aligned}&f(X)=0\\&\Rightarrow \tfrac{d}{ds}f(X)=\tfrac{\partial f}{\partial x}\tfrac{dx}{ds}+\tfrac{\partial f}{\partial \mu}\tfrac{d\mu}{ds}=0\\&\Rightarrow\left[\begin{array}{cc}\tfrac{\partial f}{\partial x} & \tfrac{\partial f}{\partial \mu}\end{array}\right]\vec{v}_s^T=0,\end{aligned} \tag{3.32}$$

it is possible to combine it with (3.31) to create the system of $(n+1)$ equations and $(n+1)$ unknowns:

$$\left[\begin{array}{c}J_s\\ \vec{v}_s\end{array}\right]_{(k)}\vec{v}_s^T=\left[\begin{array}{c}0\\1\end{array}\right], \tag{3.33}$$

for J_s representing the Jacobian of the extended state vector X. Then, under assumption of nonsingularity on the left hand side of (3.33), $\vec{v}_s$ at instant $(k+1)$ can be solved with information of the previous calculation and consequently from the tangent projection of X in (3.30).

Alternatively, predictors can be constructed by projecting the secant (instead of the tangent) or by simple extrapolation of points.

3.4.3 Correctors

The term predictor is usually associated with an algorithm of two stages, where prediction errors are improved by corrections. Basically, the idea consists in the creation of a system of $(n+1)$ equations by adding an extra constraint to $f(X)=0$ given by $g^k(X)=0$. Actually, the procedure is similar to what previously developed for calculation of the tangent vector $\vec{v}_s$.

More specifically, $g^k(X)$ will constrain the corrected values $X_{(k+1)}$ to fall into a specific hyperplane containing the predicted value $\tilde{X}_{(k+1)}$ (See Figure 3.6 for an illustration). The predictions are then based on the convergence of a Newton-Raphson algorithm, used to locate the zeros of the extended function $G(X)\equiv\left[\begin{array}{c}f(X)\\ g^k(X)\end{array}\right]$. Such an algorithm, take the first order expansion in series of the function around an initial guess X_0:

$$G(X_1)\approx G(X_0)+\left.\frac{dG}{dX}\right|_{X=X_0}(X_1-X_0), \tag{3.34}$$

and then, in order for X_1 to be a zero of $G(X)$, it is necessary to schedule:

$$\begin{aligned}&0=G(X_0)+\left.\tfrac{dG}{dX}\right|_{X=X_0}(X_1-X_0),\\&\Rightarrow\frac{-G(X_0)}{\left.\tfrac{dG}{dX}\right|_{X=X_0}}=\delta X=(X_1-X_0),\\&\Rightarrow X_1=X_0+\delta X,\end{aligned} \tag{3.35}$$

If $G(X_1) \neq 0$, the process will be repeated until it reaches a given tolerance. For an initial guess close to a zero of the function, the algorithm is expected to converge in few iterations.

Following Kuznetsov [52], a possible choice of the hyperplane $g^k(X)$ can be:

1. Natural continuation [Figure 3.6-(a)], for $g^k(X) = X_{(k+1)} - \tilde{X}_{(k+1)}$; where the solution is constrained to fall in a plane perpendicular to a selected direction, that in practice is usually chosen as the one with the higher variation rate.

2. Pseudo-arclength continuation [Figure 3.6-(b)], for $g^k(X) = \left\langle X_{(k+1)} - \tilde{X}_{(k+1)}, \vec{v}_s \right\rangle$; where solutions are constrained to fall in the direction orthogonal to the unitary tangent vector $\vec{v}_s$. The method is evidently not recommended for tracing dynamics with quick variations.

3. Moore-Penrose continuation [Figure 3.6-(c)], for $g^k(X) = \left\langle X^i_{(k+1)} - \tilde{X}_{(k+1)}, \vec{v}^i_s \right\rangle$; this is an optimized version of the previous, where a number of "i" intermediate calculations of the unitary tangent vector $\vec{v}_s$, are incorporated to the partial results; in other words, "i" intermediate predictions are accomplished during corrections.

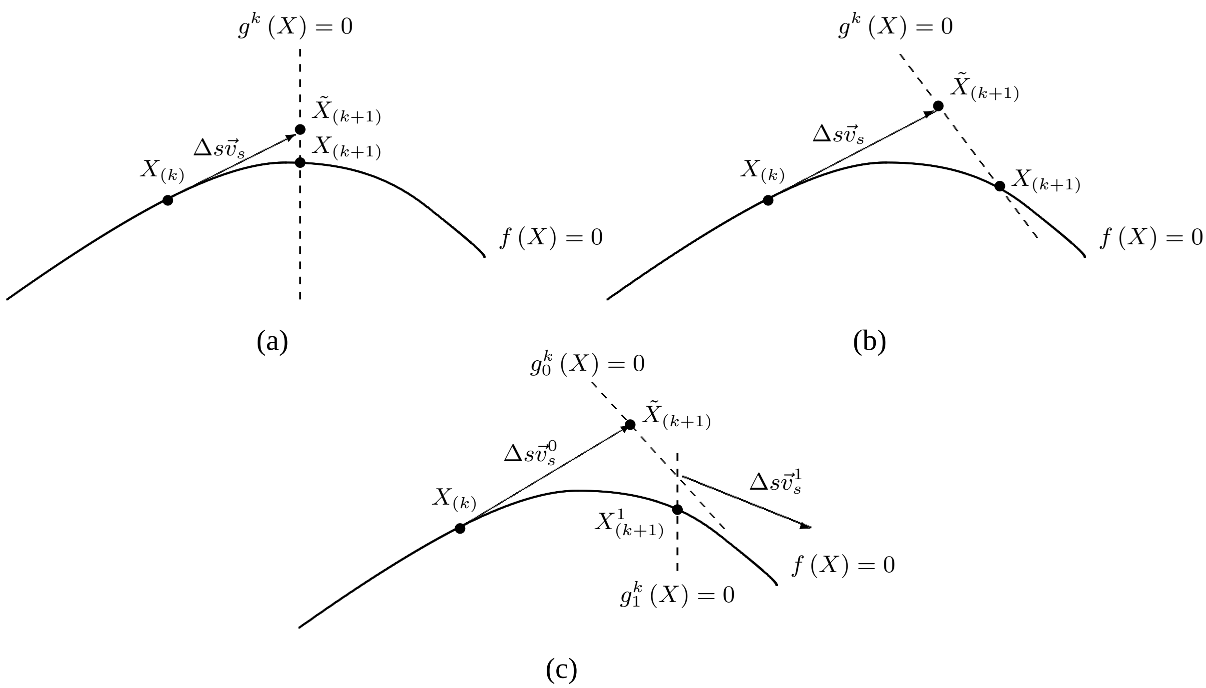

Figure 3.6 — Illustration of hyperplane selection during the correction stage of continuation algorithms: (a) Natural continuation, (b) Pseudo-arclength continuation and (c) Moore-Penrose continuation.

3.4.4 Step control

The rate of convergence of a predictor-corrector scheme is evidently affected by the prefixed value assigned to the parameter variation-rate Δ_s. Also, a convenient assignment to this value will determine a better precision on predictions, therefore reducing the required amount of correction steps.

Hence, it is possible to think in many sophisticated ways to schedule Δ_s, ranging from fixed heuristic values until dynamic adaptive assignments. Let's consider as an illustration, the recipe suggested in [52]:

- Decrease the step size and repeat the corrections, if no convergence occurs after a prescribed number of iterations;
- Increase the step size, if the convergence requires only a few iterations; and
- Keep the current step, if the convergence happens after a "moderate" number of iterations, shown to be efficient in practice.

3.4.5 Test functions and branch-selection

All the results on continuation developed so far, are applicable over a single branch of solutions. Then, in order to link the dynamical behaviour of many equilibria, it is necessary to detect whether a bifurcation takes place along the branch.

This is accomplished by detection of the zero-crossing of a monitor or "test" scalar function, say Ψ, evaluated in parallel to the calculation of branch points. Then, if:

$$\Psi\left(X_{(k)}\right)\Psi\left(X_{(k+1)}\right) < 0, \tag{3.36}$$

a bifurcation has been verified to take place between $X_{(k)}$ and $X_{(k+1)}$.

Usual choice for $\Psi\left(X\right)$ can be:

- $\max\left\{\Re\left(\lambda I - J\right)\right\}$, for J as the system Jacobian, looking forward for an eigenvalue with zero real part,
- $\left|\frac{d}{dx}f\left(x,\mu\right)\right|$, given the singularity of the Jacobian at a bifurcation point.

Once located, the bifurcation point should verify the algebraic branching equation (ABE) [49] [52]:

$$a\gamma_1^2 + 2b\gamma_1\gamma_0 + c\gamma_0^2 = 0, \tag{3.37}$$

with γ_0 and γ_1 being the basis of a plane tangent to the intersection of two branches in a single bifurcation point, and $\{a, b, c\}$ the coefficients of the quadratic multivariate expansion of $f\left(x,\mu\right)$ in a vicinity of the bifurcation (see [52] for further details).

Therefore, by considering one of this basis to follow the direction of the unitary vector $\vec{v}_s$ tangent to the branch calculated until the detection of the bifurcation, (3.37) can be solved for the remaining. In such a way, the predictor (3.30) can be selected (commuted) to trace the new bifurcation branch.

3.5 Path following in PWS dynamical systems

Path following techniques – as described through the Chapter – allow the possibility of tracking branches of equilibria in dynamical systems. The same idea should be extensible for tracing of periodic solutions (unable to exhibit single equilibrium points) and for detection of non-smooth bifurcations of branches. More specifically, path-following techniques should be employed to continue piecewise-smooth dynamical systems.

In the following, some application examples for tracing of periodic solutions in PWS dynamical systems are given as an attempt to overcome difficulties appearing naturally when trying to address continuation of nonsmooth dynamics.

3.5.1 Shooting method continuation in impact-oscillators

Dynamical systems exhibiting periodic solutions of the form:

$$\begin{aligned} \Phi\left(X^{*},T\right) &= X^{*}, \\ \Phi\left(\Phi\left(X^{*},t\right),T\right) &= \Phi\left(X^{*},t\right) \quad \forall \quad t\in[0,T), \end{aligned} \tag{3.38}$$

with $\Phi\left(X,t\right)$ representing the system flow as defined in (3.25), $X=(x,\mu)$ and T the period of the solution, can be manipulated numerically by considering a simple translation:

$$\bar{f}\left(X^{*}\right)=\Phi\left(X^{*},T\right)-X^{*}=0, \tag{3.39}$$

allowing to apply all the treatment of section 3.4.

In particular following [71], let's consider the predictor given by the linear extrapolation:

$$\begin{aligned} \mu_{(k+1)} &= \mu_{(k)}+\Delta\mu, \\ x_{(k+1)} &= x_{(k)}+\left(\frac{\mu_{(k+1)}-\mu_{(k-1)}}{\mu_{(k)}-\mu_{(k-1)}}\right)\left(x_{(k)}-x_{(k-1)}\right), \end{aligned} \tag{3.40}$$

assuming the period of the solution as parameterization; i.e. $\mu\equiv T$, and then $X=(x,T)$.

Therefore, by choosing $\bar{g}^{k}\left(X\right)$ as a convenient Poincaré section, the corrections will be constrained to fall in the hyperplane that allows to accomplish the boundary condition; i.e. $\Phi\left(X^{*},0\right)=\Phi\left(X^{*},T\right)$. As an example, take the case of a periodically forced harmonic oscillator, where x_3 represents the phase of the motion. If $\bar{g}^{k}\left(X\right)=x_3-\phi_0$, solutions will be constrained to converge into a fixed phase value $x_3=\phi_0$. See Figure 3.7 for an illustration.

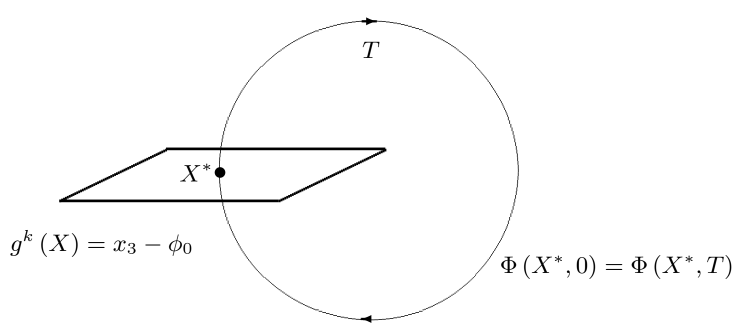

Figure 3.7 — Poincaré section containing the boundaries of a solution trajectory, after completion of an orbit with period T.

From a numerical point of view, location of the X points implies the convergence for the Newton-Raphson iterations on the extended system $\bar{G}(X) = \begin{bmatrix} \bar{f}(X) \\ \bar{g}^k(X) \end{bmatrix}$:

$$\begin{array}{l} \begin{bmatrix} X \\ T \end{bmatrix}_{(k+1)} = \begin{bmatrix} X \\ T \end{bmatrix}_{(k)} - D \begin{bmatrix} \Phi\left(X_{(k)}, T_{(k)}\right) - X_{(k)} \\ g^k\left(X_{(k)}\right) \end{bmatrix}, \\ D = \frac{d}{dX}\bar{G}(X)\big|_{X=X_{(k)}} = \begin{bmatrix} \frac{d}{dx}\Phi(X,t) - I & \frac{d}{dt}\Phi(X,t) \\ \frac{d}{dx}g^k(X) & 0 \end{bmatrix}_{X=X_{(k)}}. \end{array} \tag{3.41}$$

In doing so, after having an initial guess about X^* and T for a periodic orbit of type (3.38), variations on T will lead to convergence of (3.40)-(3.41) into the next point of the branch $X^*_{(k+1)}$.

Despite these results are being applicable to smooth systems, they have also a strong relevance for dynamics of constrained (PWS) harmonic oscillators, given the periodic nature of the solutions involved. Figure 3.8 shows results for continuation of a periodic branch on an impact oscillator model. Here, the discontinuous shape of the motion is remarkable from subfigure (a). Analogously, the evolution of eigenvalues – in subfigure (b) – confirms the crossings of the unit-circle during the period doubling and saddle node bifurcations depicted in subfigure (c).

More interesting is the numerical analysis of non-smooth bifurcations, where criteria for detection depends on the specific type of applications. For example, again in the case of a constrained harmonic oscillator, interruption of chattering will lead to a discontinuity induced bifurcation (See Chapter 6 for a deeper discussion on it). Then, the bifurcation will take place if the sticking time τ is null, and therefore $\Psi(X) = \tau(X)$. Figure 3.9 depicts this situation in detail, showing a branch tracing for the main solution in (a) and detection of the first bifurcation point in (c) with detailed criterion in (b). Notice that in this case the monitor function Ψ doesn't cross the zero, and consequently the general condition (3.36) cannot be verified. This can be taken as a proof of the exceptions representing nonsmooth phenomena.

3.5.2 Multiple-shooting in a PWS continuation package

We now discuss how to verify a boundary value problem over the entire cycle of the trajectory. This in general, is not a convenient procedure given the risk of divergence in the Newton approach for points calculated far from solutions. As an alternative, it is possible to split the periodic orbit in many subintervals, assuring the correction to work locally in any of them.

In other terms, consider once more the periodic solution (3.38) with period T. Let's divide the boundary value problem for its existence in m subintervals of T; i.e. $T \equiv [0, T_0) \cup [T_0, T_1) \cup ... \cup [T_{m-2}, T_{m-1})$, satisfying the boundary condition $\Phi(X, 0) = \Phi(X, T_{m-1}) = X^*_0$. See Figure 3.10 for an illustration.

Then, it is possible to perform calculations on the extended system $\bar{G}(X) = \begin{bmatrix} \bar{f}_i(X) \\ \bar{g}^k(X) \end{bmatrix}$ for $i = 0, 1, ..., (m-1)$, by

$$\begin{array}{l} \Phi(X, T_0) - X^*_1 = 0; \\ \Phi(X, T_1) - X^*_2 = 0; \\ ... \\ \Phi(X, T_{m-1}) - X^*_0 = 0; \\ g^k_0(X) = 0, \end{array} \tag{3.42}$$

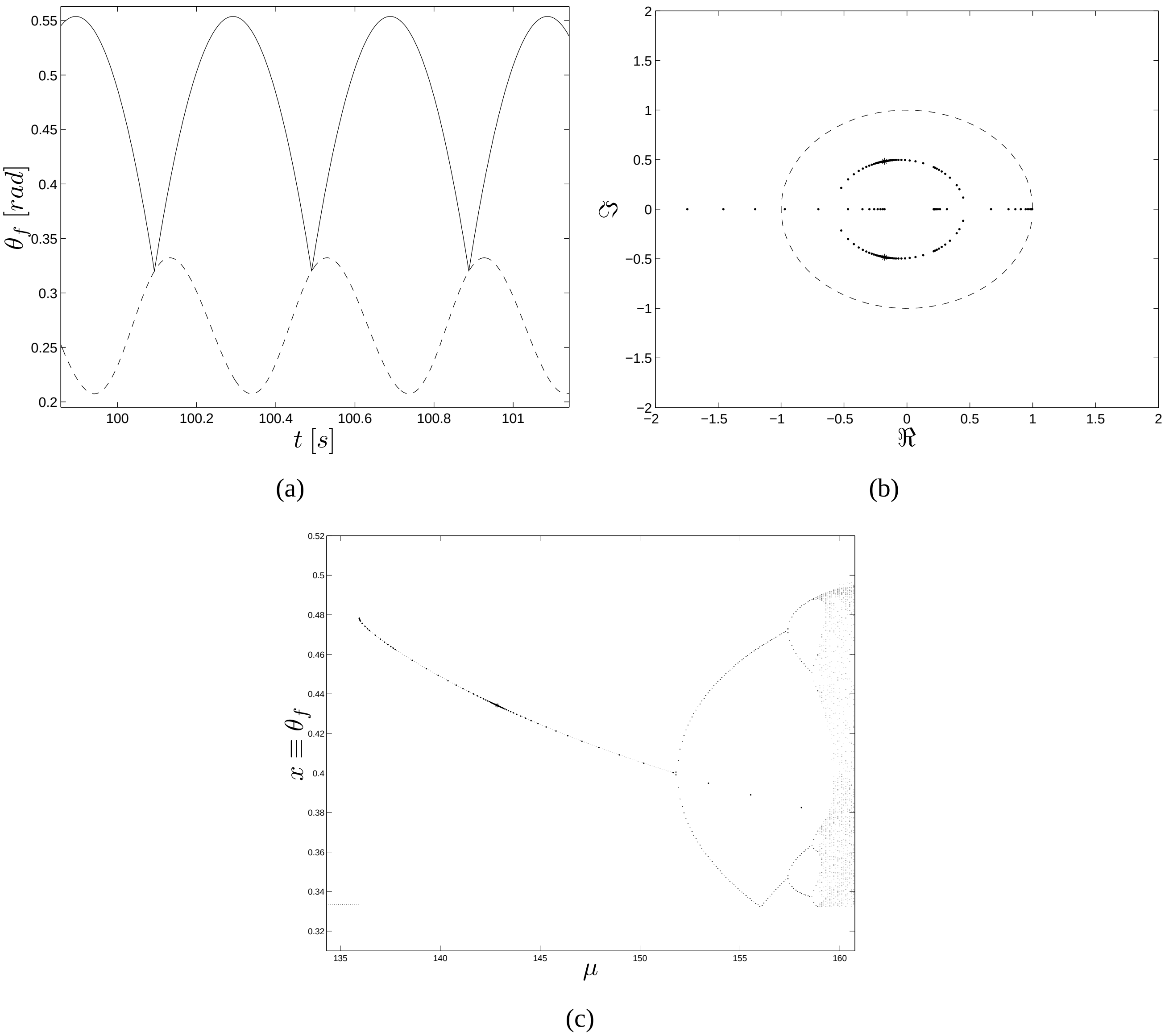

Figure 3.8 — Numerical continuation of PWS dynamics. (a) Discontinuous periodic trajectory. (b) Evolution of eigenvalues across the unit-circle. (c) Solution branch and superposition of continuation estimates.

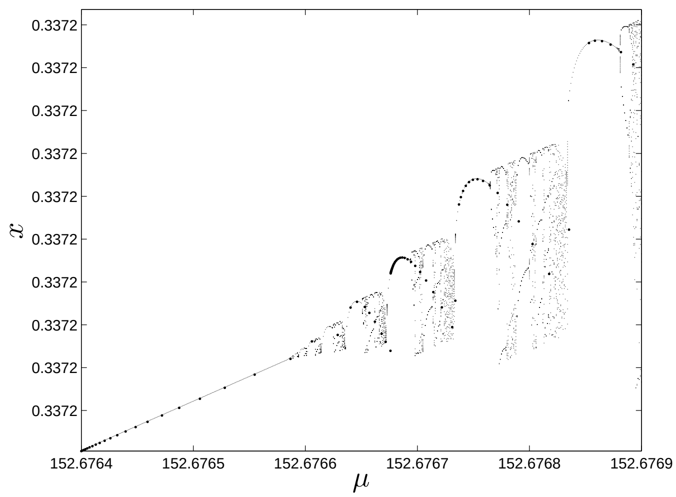

(a)

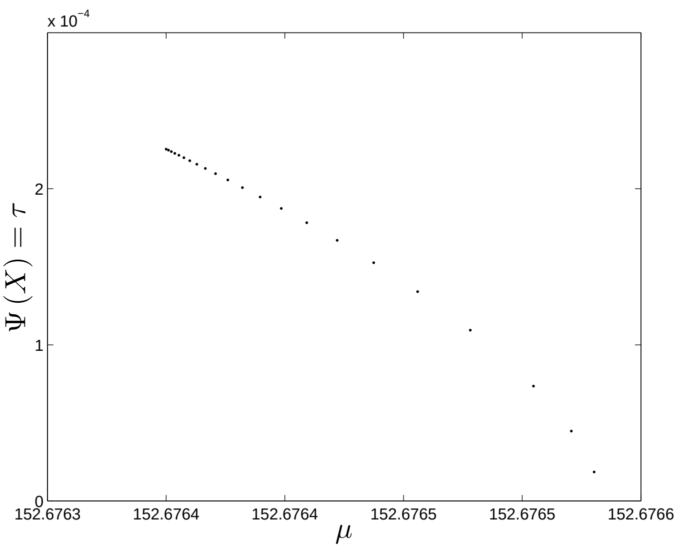

(b)

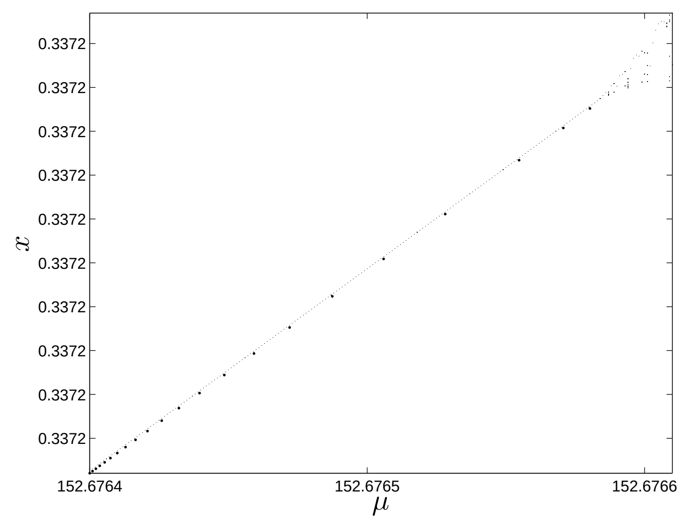

(c)

Figure 3.9 — Numerical continuation of a solution branch involving a nonsmooth bifurcation. (a) Branch tracing showing replication of main solution by path following. (b) Detection of bifurcation by monitoring the zero of the sticking time τ. (c) Verification of bifurcation detection by comparing values on horizontal axis.

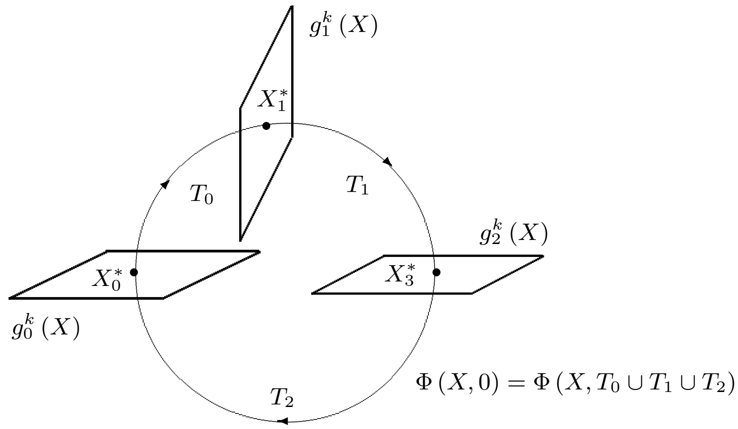

Figure 3.10 — Poincaré sections containing the boundaries of a solution trajectory, after completion of subintervals in an orbit with period T.

in a similar way to what performed in (3.41). Moreover, it is possible to approximate accurately the functions describing the flow for every subinterval by optimized routines known as "collocation" methods.

In particular, $\widehat{TC}$, a special toolbox developed for the AUTO continuation package, employs orthogonal collocation to perform path following of PWS dynamical systems.

In essence, by employing the same ideas expounded in section 3.2, the routines just need information about the vector fields of the system and the discontinuity boundaries for the associated reset mappings, in order to construct the periodic trajectory and apply on it the multiple shooting technique of (3.42).

As an illustration, Figure 3.11 depicts the discontinuous flow of a periodic solution of an impact oscillator. Notice that here two main discontinuities are present: 1) the reset of phase at the completion of any forcing period and 2) the jump in the velocity by means of the impact mapping. Analogously, Figure 3.12 contains the continuation of the periodic branch. From it is remarkable the overcoming of singularity in the turning point (saddle-node). Compare with results of the single shooting in Figure 3.8.

For further details on $\widehat{TC}$, see [89, 90].

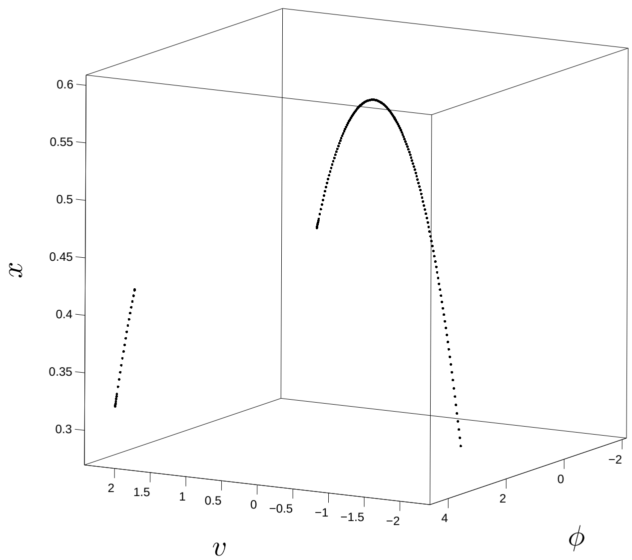

Figure 3.11 — System flow, in a three dimensional space showing the discontinuity nature of system dynamics.

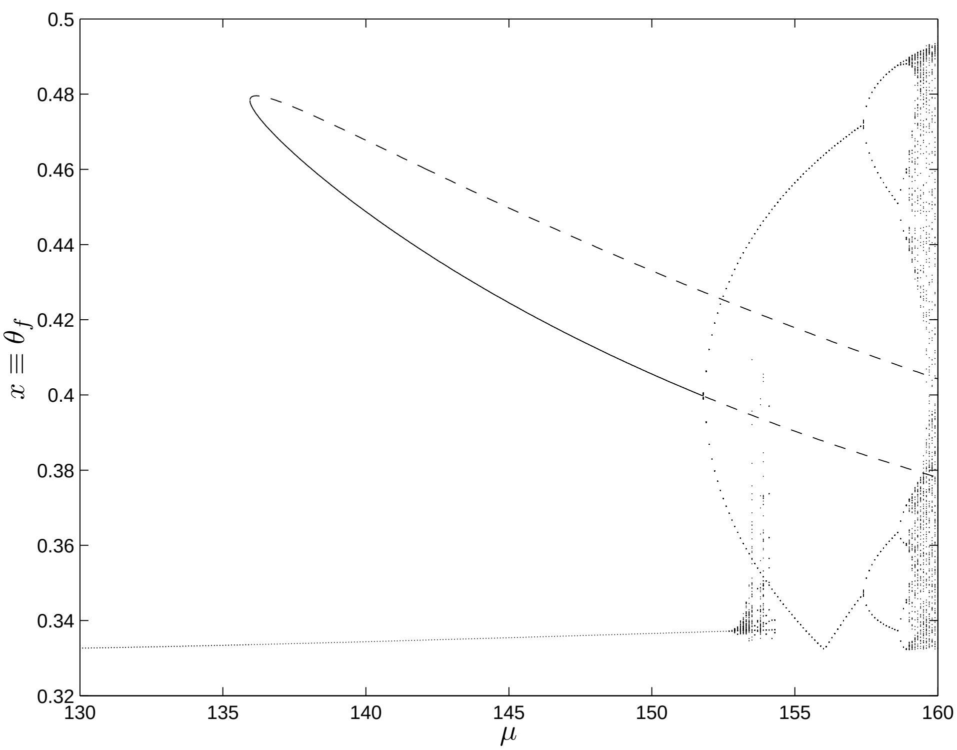

Figure 3.12 — Continuation of the periodic branch by employing the orthogonal collocation based package $\widehat{TC}$. Notice that the unstable (dashed) branch shown in the Figure, cannot be followed unless continuation techniques are used.

Chapter 4

Cam-follower systems and the valve-float phenomenon in combustion engines

4.1 Introduction

A number of dynamical systems contain discontinuities due to the presence of structural components with displacement constraints. Examples include bouncing or hopping systems, vibro-mechanical impacts in machine vibrations, loosely connected members, and gearing systems with fatigue-induced over-tolerances. All represent situations where impacting oscillator models can provide a valuable insight to understand the observed dynamical behaviour [33]. Although such systems typically operate in linear regimes over certain parameter ranges, the discontinuities in the force-deflection relationship have been shown to produce characteristic non-linear behaviour, such as amplitude jumps, subharmonics and chaos [91]. An impact could be either desirable, when it represents the base of operation, as for example in pneumatic hammers, impact printers and heat exchangers, or undesired when is destructive and should be eliminated, as for instance in gear-boxes [100].

In this context, cam-follower systems can be chosen as a very general and relevant benchmark problem, since they are widely used in various machines and mechanical engineering devices [61]. For instance, all types of automated production machines including screw machines, spring winders and assembly machines, rely heavily on this kind of systems for their operation.

The most common application is to the valve train of internal combustion engines (ICE) [44], where the effectiveness of the ICE is based on the proper working of a cam-follower system. For this specific application, the presence of discontinuities can be really critical and must be avoided or controlled since the purpose of the valve train is to open and close both the intake and exhaust valves of the ICE. A typical pushrod valve train contains the following components: cam, follower, pushing rod, rocker arm and valve springs. As the camshaft rotates, the cam imparts a translation motion to the follower and pushrod (see Figure 1.4). The pushrod then pivots the rocker-arm which opens the valve. The valve springs provide the restoring force to close the valve after the maximum lift is obtained.

During operation, it is important to keep all the mechanical parts in close contact with each other so that the motion of the mechanism perfectly reflects the motion of the cam. Unfortunately, in practice, as the engine speed increases, the valve train motion can be different from the ideal kinematic behaviour due to inertia of components, and the surge of valve springs. These phenomena lead to valve floating and bouncing, which can seriously deteriorate the engine performance. For instance, valve floating occurs when the inertial force of the valve train components exceeds the force of the valve springs, thus allowing components to separate and causing the valve to exceed the maximum lift of kinematic motion and close with an abnormally high velocity. Valve bouncing instead occurs when the valve closes against the seat with a sufficiently high velocity, such that it physically bounces off the seat and remains open as the piston begins the compression cycle, thus allowing the air-fuel mixture going out of the combustion chamber. Reduction in valve bouncing and/or valve floating is established as primary goal of valve designs including cam-follower mechanisms.

All the applications based on a cam-follower, require a deeper insight in the system dynamics; i.e. taking explicitly into account the occurrence of gaps between connecting components. Obviously, embedding possible collisions in the representative model, generates discontinuities and nonlinearities in the system equations, reducing the applicability and the effectiveness of traditional model analysis tools.

To this aim, the general theory of piecewise-smooth dynamical systems described so far in Chapter 2, can be successfully applied to explain the main dynamical scenarios experienced by cam-follower devices, modelled as lumped-parameter single-degree-of-freedom impacting oscillators. Also, as the analysis of bifurcations in piecewise-smooth systems is further expanded, it is becoming increasingly important to carry out an extensive experimental investigation and validation of the theoretical results obtained. Complex behaviour in impacting systems has been observed experimentally in a number of papers in the literature. Examples include the early work on impact oscillators in [12], [14], [46], [63], [91], [84]. More recent papers include the work by Wiercigroch et al reported in [101] and the results of Piiroinen et al on impacting pendula [73]. (For further references see also the books [17], [100] and references therein). Particularly cumbersome dynamics can be observed in the case of impact oscillators with moving boundaries. For example, in [24], it is suggested that a novel bifurcation phenomenon termed as corner-impact can occur in discontinuously forced impact oscillators.

This Chapter will be concerned with the description and implementation of an experimental rig composed of an oscillating rocker-arm driven by a rotating profile, emulating the interaction between the cam-shaft and valves on an ICE. Modelling and validation between numerical simulations and experimental data will be performed. More extensive analysis will be presented in Chapters 5 and 6.

Related results have been published in [6] and [10].

4.2 Cam-follower systems

Following [61], a *cam* can be defined as a specially shaped piece of metal or other material arranged to move the follower in a controlled fashion. The follower motion may be either rotational or translational. As an example, Figure 4.1-(a) shows a rotating cam driving an oscillating (rotating or swinging) follower. Notice that a spring is used to maintain the contact between cam and follower. This is referred to as a *force-closed* cam joint, meaning that an external force is needed to keep them together.

Figure 4.1-(b), shows an alternative arrangement to connect the follower to the cam, that does not need a spring. A track to groove in the cam traps the roller follower and now can both push and pull. Actually it just pushes in both directions. This is called a *form-closed* joint, as the cam is formed around the follower, capturing it by geometry. This type of cam, when used for valve actuation in engines, is also known as

desmodromic, from the French word *desmodromique* meaning to *force to follow contour* [61]. Both, *form* and *force closed* cams, are used extensively in machinery.

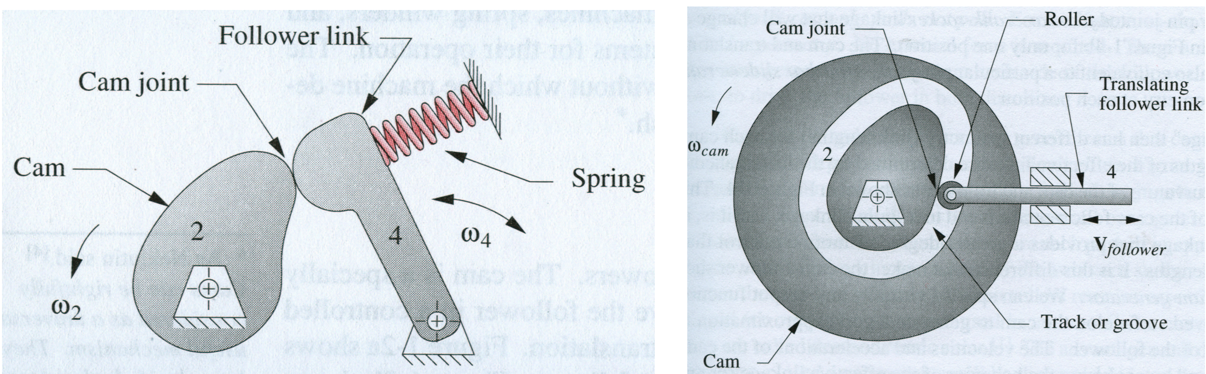

Figure 4.1 — Illustration of types of cam-follower joint: (a) force-closed and (b) form-closed configurations, reproduced from [61].

4.2.1 Typical arrangements and geometries

Cam-follower systems can be classified in several ways: by type of follower motion, by type of joint closure, by type of follower, by type of motion constraints or by type of motion program:

Type of follower motion

Figure 4.1-(a) shows a system with an oscillating (rotating or swinging) follower. All three terms are used interchangeably. An alternative configuration can be a translating (sliding) follower. The choice between these two types of cam-follower is usually determined by the type of output motion desired. If true rectilinear translation is required, then the translating follower is needed. If a pure rotation output is needed, then the oscillator is the obvious choice.

Type of joint closure

Force and form closure were introduced earlier. Another variety of form-closed cam-follower arrangement is the conjugate cams, with two cams fixed on a common shaft that are mathematical conjugates of one another. Desmodromic cams can be also conjugate. See Figure 4.2, for an illustration of a conjugate cam pair.

Type of follower

Follower in this context, refers only to that part of the follower link which contacts the cam. Three common arrangements are: flat-faced (Figure 4.1-(a)), mushroom (curved, Figure 4.3) and roller. The roller follower has the advantage of lower (rolling) friction than the sliding contact of the other two, but can be more expensive. Flat-faced followers can package smaller than roller followers for some cam designs; they are often favored for that reason, as well as cost for some automotive valve trains. Many modern automotive engine valve trains now use roller followers for their lower friction. Roller followers are commonly used in production machinery where their ease of replacement and availability from bearing manufacturers'stock in any

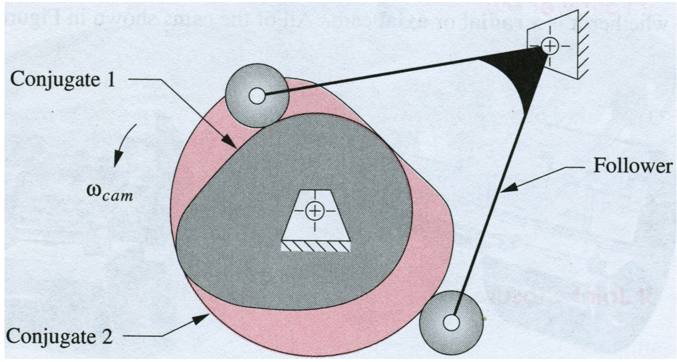

Figure 4.2 — A conjugate desmodromic cam pair, reproduced from [61].

quantities are advantages. Flat-faced or mushroom followers are usually custom designed and manufactured for each application.

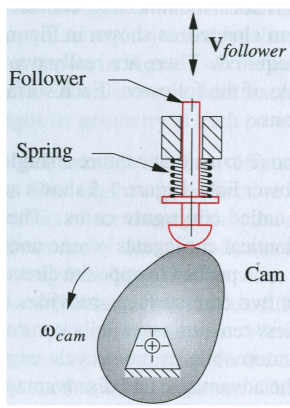

Figure 4.3 — Mushroom type of follower shape, reproduced from [61].

Type of cam

The direction of the follower's motion relative to the axis of rotation of the cam determines whether it is a *radial* or *axial cam*. Cams in Figures 1.4-4.3, are all radial cams because the follower motion is generally in a radial direction. Figure 4.4, shows an axial cam whose follower moves parallel to the axis of cam rotation. This arrangement is also called a *face cam* if open (force-closed) and a *cylindrical* or *barrel cam*, if grooved or ribbed (form-closed). Another possible configuration is the three-dimensional cam or *camoid* in a combination of a radial and axial cams. This is a two-degree-of-freedom system. The two inputs are the rotation of the cam about its axis and translation of the cam along its axis. The follower motion is a function of both inputs. The follower tracks along a different portion of the cam depending on the axial input.

Type of motion constraints

There are two general categories of motion constraint: critical extreme position (CEP – also called endpoint specification) and critical path motion (CPM). CEP refers to the case in which the design specifications define only the start and finish positions of the follower (i.e. the extreme positions) but do not specify any constraints on the path motion between those extreme positions. This case is easier for design because of

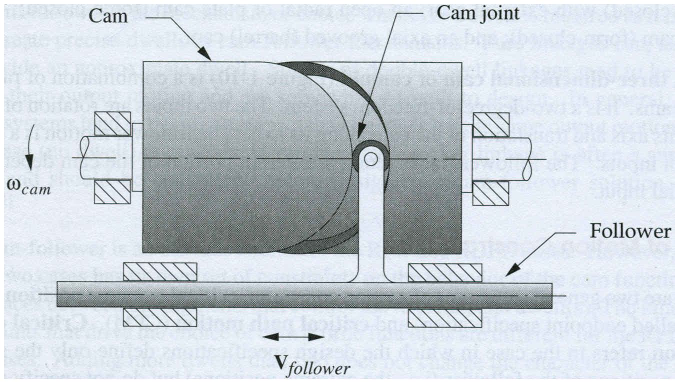

Figure 4.4 — Axial, cylindrical or barrel cam with form-closed translating follower, reproduced from [61].

the freedom to choose the cam functions that control the motion between the extremes. CPM is a more constrained problem, because the path motion and/or one or more of its derivatives are defined over all or part of the interval of motion. This requires the generation of a particular function to match the given constraints.

Type of motion program

The motion program rise-fall (RF), rise-fall-dwell (RFD) and rise-dwell-fall-dwell (RDFD), all refer mainly to the CEP case of motion constraint. They define how many dwells are present in the full cycle of motion, either none (RF), one (RFD), or more than one (RDFD). Dwells, defined as no output motion for a specified period of input motion, are an important feature of cam-follower systems. See Figure 4.5 for an example of a timing diagram including path restrictions and dwells on a cam program specification.

Segment Number	Function Used	Start Angle	End Angle	Delta Angle
1	Constant velocity rise	0	60	60
2	Dwell	60	90	30
3	Constant acceleration fall	90	150	60
4	Dwell	150	180	30
5	Cubic displacement rise	180	240	60
6	Dwell	240	270	30
7	Simple harmonic fall	270	330	60
8	Dwell	330	360	30

(a)

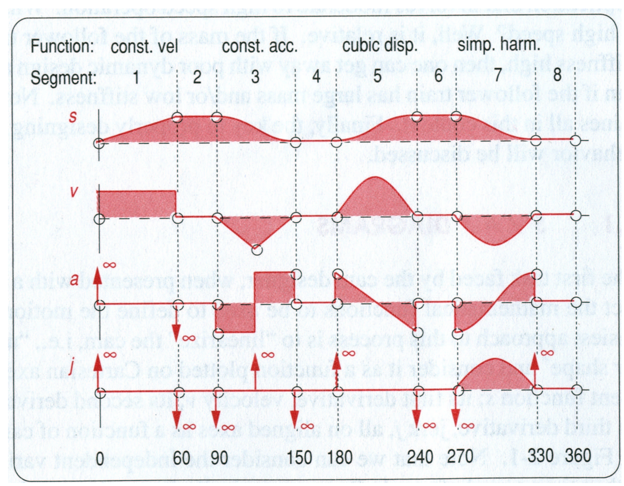

(b)

Figure 4.5 — Motion functions for a multi-dwell cam: (a) cam program specifications and (b) plots of cam-follower's position s, velocity v, acceleration a and jerk j, reproduced from [61].

4.2.2 Applications

Another possible application of cam-follower devices are in automated assembly machines, as illustrated in Figure 4.6. Two cams are shown, each of which drives a linkage that actuates tooling in one of several assembling stations along a conveyor line. The tooling will insert a part, crimp a fastener, or do some other operation on the product that is being automatically assembled as it is carried along on the conveyor. A machine of this type, may have several dozens of these cam-follower trains arrayed along one or more large camshafts that run the length of the machine (ten meters or more).

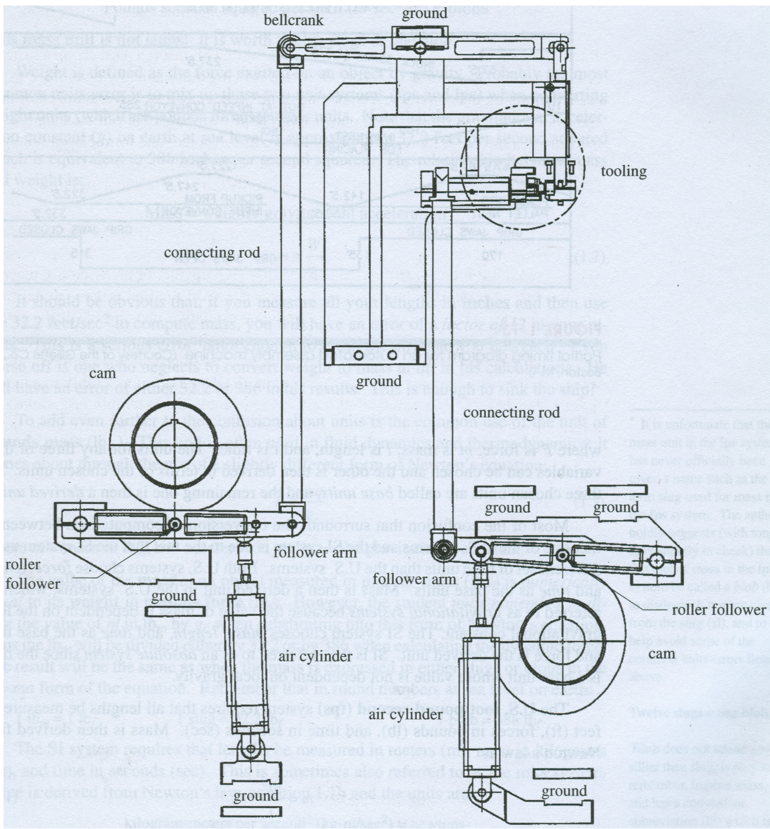

Figure 4.6 — Cam-follower mechanisms for one station of an automated assembly machine at the Gillette Co. Boston, MA, reproduced from [61].

Additional details on design and implementation of cam-follower systems are out of the scope of the current Chapter.

4.3 Internal combustion engines and the valve-float phenomenon

As stated in [44], internal combustion engines (ICE) date back to 1876 when Otto first developed the spark-ignition engine and 1892 when Diesel invented the compression-ignition engine. Since that time these engines have continued to develop as our knowledge of engine processes has increased, new technologies became available, demand for new types of engines arose, and environmental constraints on engine use changed. Internal combustion engines, and the industries that develop and manufacture them and support their use, play a dominant role in the fields of power, propulsion and energy. The purpose of internal combustion engines, is the production of mechanical power from the chemical energy contained in the fuel. In internal combustion engines, as distinct from external ones, this energy is released by burning or oxidizing the fuel inside the engine. The fuel-air mixture before combustion and the burned products after combustion are the actual working fluids. The work transfers which provide the desired power output occur directly between these working fluids and the mechanical components of the engine.

4.3.1 The four-stroke cycle

Internal combustion engines are reciprocating engines; i.e. where the piston moves back and forth in a cylinder and transmits power through a connecting rod and crank mechanism to the drive shaft (as in Figure 4.7). The steady rotation of the crank produces a cyclical piston motion. The piston comes to rest at the top-center (TC) crank position and bottom-center (BC) crank position when the cylinder volume is a minimum or maximum, respectively.

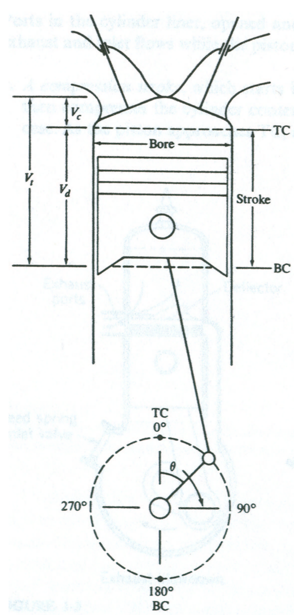

Figure 4.7 — A reciprocating engine, reproduced from [44].

The majority of reciprocating engines operate on what is known as the *four-stroke cycle*. Each cylinder requires four strokes of each piston – two revolutions of the crankshaft – to complete the sequence of events which produces one power stroke. This *four-stroke cycle* comprises (see Figure 4.8 for a schematic illustration):

1. An *intake stroke*, which starts with the piston at TC and ends with the piston at BC, which draws fresh mixture into the cylinder. To increase the mass inducted, the inlet valve opens shortly before the stroke starts and closes after it ends.

2. A *compression stroke*, when both valves are closed and the mixture inside the cylinder is compressed to a small fraction of its initial volume. Toward the end of the compression stroke, combustion is initiated and the cylinder pressure rises more rapidly.

3. A *power stroke*, or *expansion stroke*, which starts with the piston at TC and ends at BC as the high-temperature, high-pressure, gases push the piston down and force the crank to rotate. About five times as much work is done on the piston during the power stroke as the piston had to do during compression. As the piston approaches BC the exhaust valve opens to initiate the exhaust process and drop the cylinder pressure to close to the exhaust pressure.

4. An *exhaust stroke*, where the remaining burned gases exit the cylinder: first, because the cylinder pressure may be substantially higher than the exhaust pressure; then as they are swept out by the piston as it moves toward TC. As the piston approaches TC the inlet valve opens. Just after TC the exhaust valve closes and the cycle starts again.

Therefore, synchronized motion between piston and valves is mandatory for achievement of the required performance of the engine and avoidance of undesired emission of residuals to the environment. Such synchronization is assured by connecting the crank-shaft to the cam-shaft, this last transmitting the desired motion to the valve train (as in Figure 1.4).

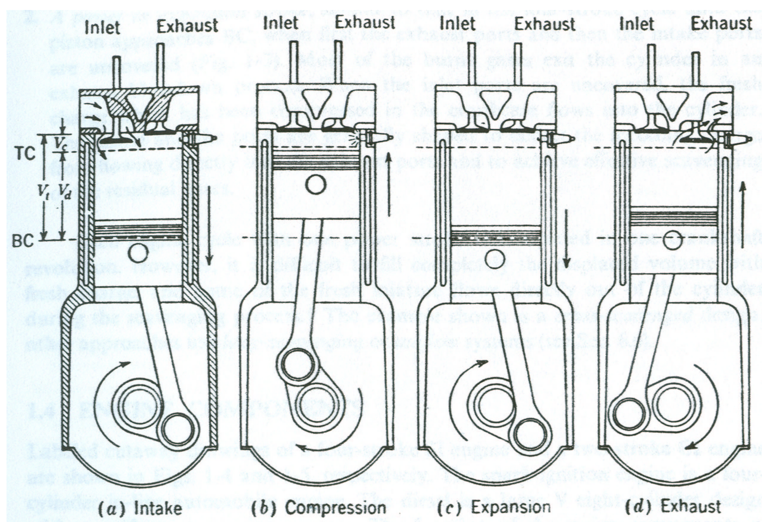

Figure 4.8 — Illustration of the *four-stroke cycle* in an internal combustion engine ICE, reproduced from [44].

4.3.2 Valve floating and bouncing

As stated previously, it is necessary to keep a controlled motion of the valves for a better performance of an ICE, situation translated in assurance of a permanent contact between the cam and follower bodies along the valve train. This is a crucial design tip related with maximum operational conditions allowed on the engine. Under such mode of operation, the rotation of the cam will exert a force on the valve (proportional to the torque) which exceeds the restoring force supplied by the spring in the force-closed joint configuration, allowing the bodies to detach and eventually to bounce (after impact) [51] [87] [29]. Moreover, it has been experimentally observed, that at a certain engine speed termed *limit speed*, the valve bounce amplitude increases dramatically, thereby resulting in what seems to be a chaotic valve motion [61].

Although the occurrence of the impacts sets narrow bounds onto the maximal engine velocity, there is a generic trend to advance the limit speed in both passenger and racing automobiles and/or motorbikes. Increasing the engine limit speed allows the engine to run faster and in turn to produce more power. In addition, operating at higher engine speed is also strongly desirable since it is possible to design smaller and lighter engines that produce the same power as larger, heavy engines.

For all of the above mentioned reasons, the reduction in valve bouncing and/or valve floating, as the velocity increases, is established as a primary goal of valve design based on the cam-follower mechanism [29], [54]. We remark that in current technology engines, a prefixed and sufficiently large spring force (and pre-load) is always applied to the cam follower joint to keep the contact throughout the entire rotation [74]. As a natural consequence, there is an increase in the contact force, which induces higher stresses possibly leading to early surface failure of the parts. Moreover, the high friction valve train reduces the efficacy of the engine system, that works harder to push the follower through its motions [93].

Understanding the complex dynamics of these systems can then be relevant in these applications where it is essential to avoid unwanted impacting behaviour. Indeed, a deeper insight of the post-detachment dynamics could unveil less conservative solutions for detachment avoidance. For example, bifurcation and chaos control techniques or active controllers could be used without requiring the use of a stiff closing spring or the design of much more complex desmodromic valves [26]. Also, an exhaustive study on the occurrence of gaps between connecting components will also allow a better understanding of the nature of the resulting noise, vibration, wear and mechanical stress often observed in applications.

4.4 Experimental rig

Figure 1.4 shows a cam-follower system used in automotive valve actuation. This is an overhead camshaft engine. The camshaft operates against an oscillating follower arm that in turn opens the valve. The cam-joint is force-closed by the valve spring. Maximum cam-speed in these kind of applications can range from about 2500 *rpm* in large automobile engines to over 10000 *rpm* in motorcycle racing engines. From the application viewpoint, the velocity is a crucial parameter to be properly controlled to induce a desired behaviour. Essentially, unwanted nonlinear behaviour, may be caused by impacts that have to be avoided.

Inspired by these kind of problems, a test-bench for a radial cam with a flat-faced follower was designed and built at the University of Naples - FEDERICO II. Details on design, modelling and instrumentation tips have been published in [6]. A summary of them is given as follows:

4.4.1 Design tips

Since our attention is focused on the nonlinear behaviour of the cam-follower mechanism, it is not necessary at this stage to explicitly consider the engine in the rig. Without loss of generality, a simple mechanical system composed by two rigid contacting bodies (the cam and the follower) is used as an experimental rig sufficient for the practical visualization of all the phenomena related with the bouncing of a follower over a cam surface. The presence of the spring tied to the follower/rocker arm, provides the necessary restoring force. An electric servo motor provides the motion of the cam according to a prefixed velocity profile. An illustration of the experimental rig, detailing the geometry of the mechanical core, is given by Figure 4.9.

Notice that it has been also possible to design a push-road translational cam-follower system, but the choice of a rotational rig seemed to be preferable for our experimental purposes, since an oscillating flat-faced follower provides a lower friction, lower wear rates and ease of replacement. Furthermore, our experimental and theoretical effort is based on the detection of multiple impacts, chattering, grazing contacts and so on.

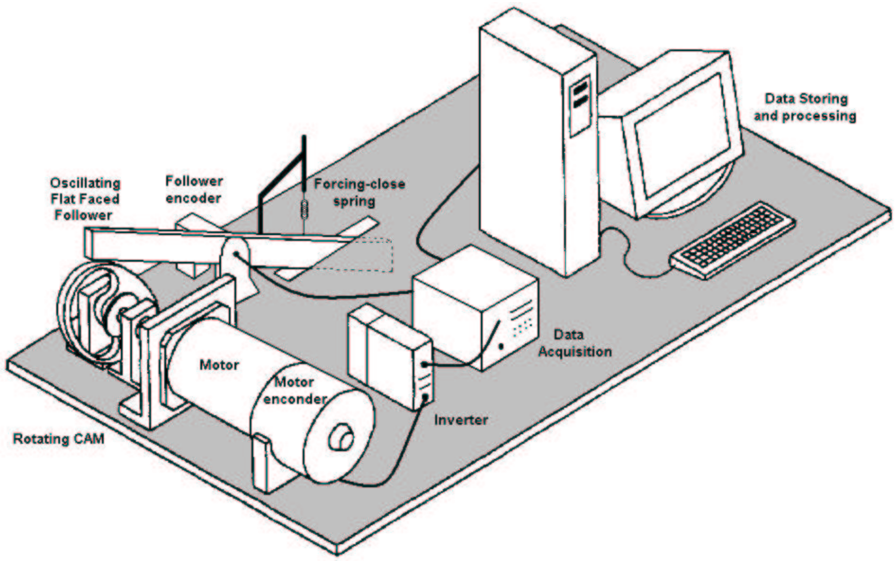

(a)

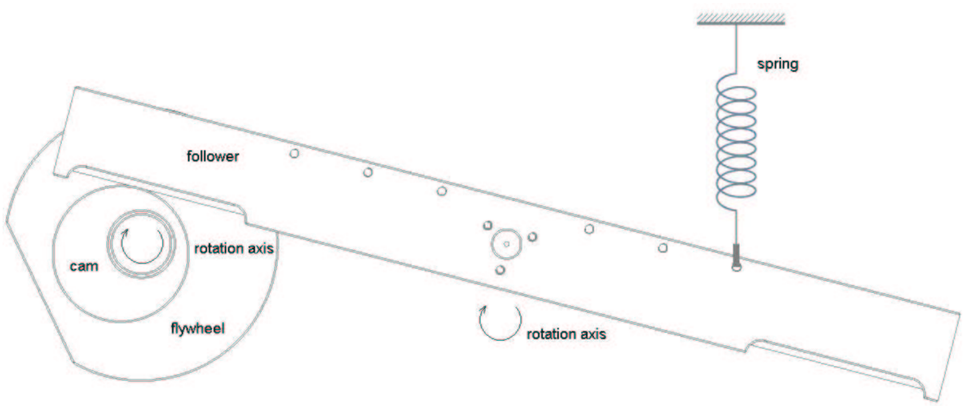

(b)

Figure 4.9 — Experimental rig: (a) schematic overview of system including mechanical and sensing/acquisition devices, and (b) detail of the mechanical core showing the particular geometry to be implemented.

This implies the necessity to perform reliable contact measurements. By choosing a push-road translational cam rig, this cannot be done easily, since the high frequency impacts do not suggest to employ proximity transducers, such as the piezoelectric ones, forcing to choose optical sensors, like high speed lasers, which are efficient, but expensive. Instead, by designing a rig based on a rotational geometry, measurements of the cam and follower positions are simply performed by incremental encoders placed on the cam-shaft and the follower-shaft.

4.4.2 The cam profile

An important aspect of cam-follower systems is the cam profile. This is typically designed in order to provide the forcing to the follower which is required for it to operate in some desired manner. Usually, the cam profile is obtained by solving a constrained optimization problem (see [61] for further details). Given the wide range of applications, there is a wide variety of possible cam geometries ranging from cycloidal cams to those designed using splines that can even provide discontinuous acceleration to the follower [62]. For this reason, the experimental rig was designed in order to allow easy and direct access to the cam and the flywheel for their possible replacement.

Currently two different types of cam can be alternatively mounted on the experiment which provide, respectively, a simple harmonic motion (eccentric circular cam) and a profile characterized by discontinuities in the acceleration. In this Thesis we will show experiments related to an eccentric circular cam, which are often used to produce motion in pumps or to operate steam engine valves [61]. Other examples of various applications based on the eccentric circular cam can be found in [19], [28], [35], [42], [94]. The use of circular cams in the automotive field is instead reported in [27] and [82]. On-going research activity is dealing with evaluating the effects on the follower motion of a discontinuity in the forcing [65] [66].

It is worth mentioning here that by appropriately designing the cam profile it would be possible to impart any type of desired motion to the follower. This makes the experiment described in this Thesis an extremely versatile and flexible tool to investigate the nonlinear dynamics of impacting mechanical systems.

4.4.3 Implementation

The physical implementation of the experimental rig described above is depicted in Figures 4.10 and 4.11, where the mechanical device is shown to be appropriately coupled to electronic systems for the acquisition, sampling, storage and processing of experimental data. The main features of the experimental set-up can be summarized as follows:

- The cam motion is controlled by a brushless motor driven through an embedded controller. Notice that the angular position and velocity of the cam and the driving motor are assumed to be identical because of a rigid coupling connecting the cam to the motor shaft.

- The measures of the cam and the follower angular positions are obtained through high-resolution optical encoders mounted respectively on the cam and follower shafts.

- The measure of the follower angular variation rate, is obtained with a gyroscope [86] fixed at its rotational axis. Notice that the follower performs partial circular motion (non complete revolutions), and then its rotational velocity should be measured as an angular rate. See Figure 4.11-(a).

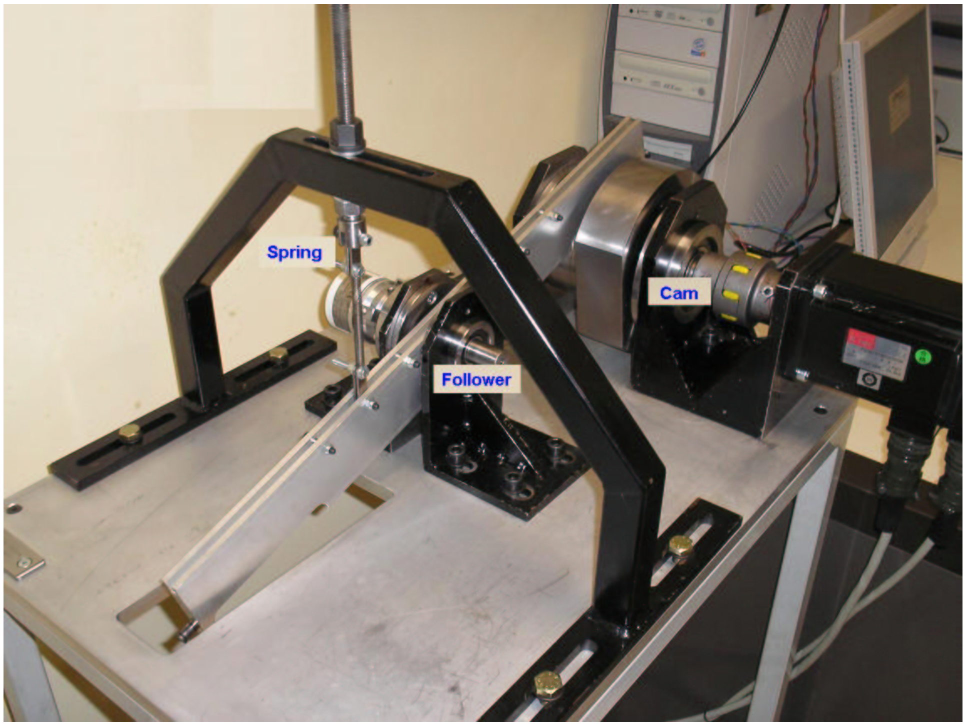

(a)

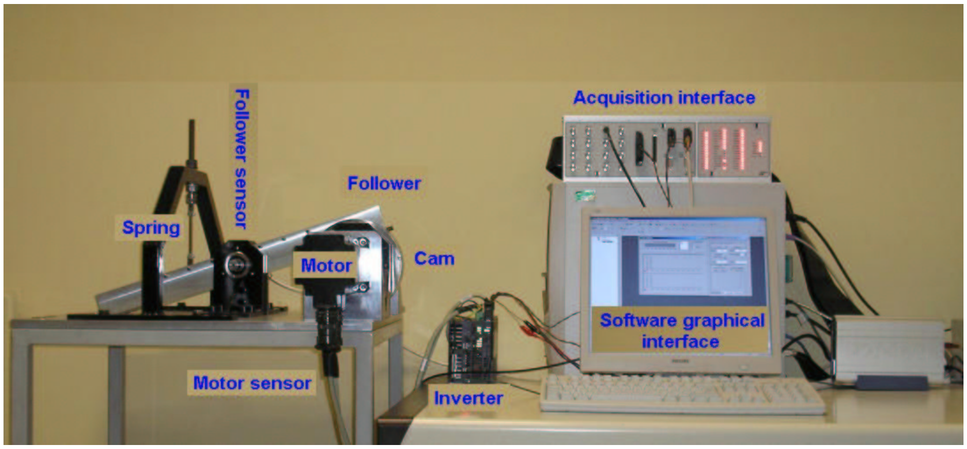

(b)

Figure 4.10 — Physical implementation of the experimental rig: (a) view from above; (b) front view.

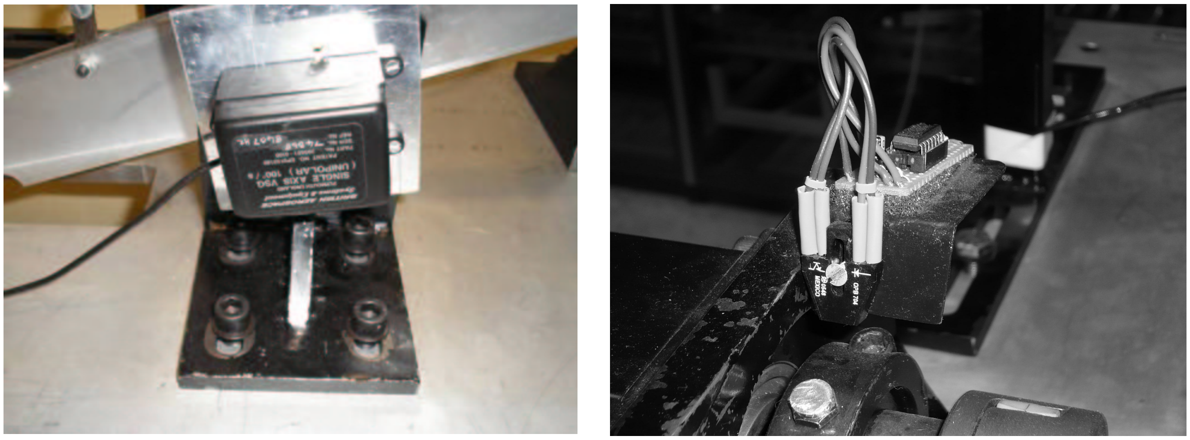

(a) (b)

Figure 4.11 — Additional hardware incorporated into the experimental rig: (a) gyroscope for measurement of the follower angular rate (for incomplete revolutions or swings); (b) hardware triggering for stroboscopic acquisition of samples.

- Reliable AD/DA conversions and signal processing are implemented through DSPACE [39], a widely used commercial data-acquisition integrated hardware/software system (16 bit, 250 MHz, PCI interface).
- External hardware triggering has been configured on the acquisition unit, in order to perform stroboscopic sampling. A circuit based on an opto-isolated device [64], has been built for this purpose. See Figure 4.11-(b) for an illustration.
- All signals acquired are processed and analyzed using MATLAB [45].

Additional details are included in Tables 4.1 and 4.2. A more extensive description of the experimental rig can be found in [10].

Table 4.1 — Details on materials and dimensions

Part	Description
cams, flywheels and follower contact surface	made of low-alloy hardened stainless steel *UNI38NiCrMo4*
follower body	made of aluminium *Al*
cam internal radius	30 mm
cam external radius	60 mm
cam eccentricity	15 mm
flywheel radius	80 mm
follower length	600 mm
follower width	16 mm
follower height	60 mm

Table 4.2 — Details on the instrumentation

Device	Description
servo (motor-driver) system	Sanyo-Denki Q-series [77]
data acquisition system	dSPACE ACE-kit ACE1104CLP [39]
follower position encoder	HENGSTLER RI-58 D [43]
cam position resolution	5000 pulses per revolution
follower position resolution	10000 pulses per revolution
follower velocity sensor	BAE systems, VSG 100°/s bipolar gyroscope [86]
reflective object sensor for trigger	Phototransistor OPTEK, OPB703 [64]

4.5 Modelling

In order to detect and study the main qualitative dynamical features of the follower motion and to validate the observed experimental behaviour, a proper mathematical model of the system should be derived [6]. The formulation of an appropriate model can be a challenging task for most applications. In the case of cam-follower systems, various models have been proposed characterized by different degrees of complexity, ranging from simple models with 1 DOF (*Degree Of Freedom*) [50] to complex models with 21 DOF [78] that use the additional DOF to include the effects of camshaft torsion and bending, backlash, squeeze of lubricant in bearings and so on. Nevertheless, there is general agreement, confirmed by experience in different applications, that a lumped parameter single degree of freedom model is adequate to represent most of the aspects of the dynamical behaviour of a cam-follower system (see for example [4], [13], [38] and [50]).

Rather than neglecting the presence of impacts, the cam-follower is regarded here as a single degree of freedom impacting oscillator with an unilateral constraint. More precisely, as explained in [18], we model the follower dynamics under the external forcing $u(t) \in \Re$ provided by the cam, as

$$\begin{aligned} &\ddot{q} = g\left(q, \dot{q}, u\right), \\ &f\left(q, t\right) \geq 0, \end{aligned} \tag{4.1}$$

where $q \in \Re^n$ is the vector of generalized coordinates of the follower motion, g is the system vector field and the real valued function f represents the unilateral constraint on the follower position q. Note that $u(t)$ is nonzero only when the two bodies are in contact (i.e. when $f(q,t) = 0$). Using the terminology of complementarity systems, we are able to say that the two variables f and u, are complementary in the sense that $0 \leq u \perp f \geq 0$ (see [18] for further details).

The hybrid structure of model (4.1) allows to deal mathematically with the presence of intermittent contacts between the system bodies. In particular, we can distinguish between two different phases of motion:

1. *Unconstrained mode*, when no contact occurs between the cam and the follower. From the modelling viewpoint, the follower dynamics simply reduces to an unforced harmonic oscillator; i.e. $f\left(q,t\right) > 0$ and $u(t) = 0$;

2. *Constrained mode*, when permanent contact between the two bodies is established. Here the follower dynamics are induced by the specific cam profile[1]; i.e. $f(q,t) = 0$ and $u(t) > 0$.

[1] The follower motion is constrained to a phase space region bounded by the angular position of the cam.

In the following, each particular mode of the follower motion will be modelled in accordance with both the schematic diagram depicted in Figure 4.12 and the general notation reported in Table 4.3.

Table 4.3 — Summary of the general notation used in section 4.5

Symbol	Description
θ_f	angular position of follower with counterclockwise sense of rotation
θ_c	angular position of cam with counterclockwise sense of rotation[2]
$\hat{\theta}_c$	angular displacement of the follower joint when in contact with the cam
$(\hat{t}, \hat{n})$	reference system attached to the follower
$(\tilde{x}, \tilde{y})$	reference system obtained by translating the axes (x, y) to (x_0, y_0)
$(\tilde{x}_c, \tilde{y}_c)$	reference system pivoted at the cam with origin (x_0, y_0)
$p_0 = (x_0, y_0)$	coordinates of the rotational center in the (x, y) system
$p_A = (x_A, y_A)$	hooking point for spring
$p_B = (x_B, y_B), p_P = (x_P, y_P)$	ending points of the mechanical element that avoids rotation of spring
$p_C = (x_c, y_c)$	point on the cam surface which is nearest to Σ
$p_E = (x_E, x_E)$	intersection between vertical line passing through p_A and $g(x) = \tan(\theta_f)x$
$p_F = (x_f, y_f)$	point of follower surface that will impact on the cam[3]
$p_G = (x_g, y_g)$	geometric center of the rotating cam
d	half height of follower
d_0	relaxed spring length
d_1	distance between p_B and p_P
d_2	distance between p_P and p_E
e	cam eccentricity
K	spring stiffness
J	follower moment of inertia
ρ	distance between the origin of the axis (x, y) and p_E
Σ	boundary of follower surface that becomes in contact with cam
h	distance between p_C and Σ[4]
$\overline{d}$	intersection between Σ and the axis y (it is equal to $-d/\cos(\theta_f)$)

4.5.1 Follower motion

To derive a valid mathematical model, we use a standard *Lagrangian* approach, with system description obtained by solving

$$\frac{d}{dt}\frac{\partial L}{\partial \dot{\theta}_f} - \frac{\partial L}{\partial \theta_f} = \tau \tag{4.2}$$

where L is the Lagrangian function, defined as the difference between the potential energy (U) and the kinetic energy (T) of the system

$$L = T - U, \tag{4.3}$$

[2]Measured as the relative rotation of the coordinate system $(\tilde{x}_c, \tilde{y}_c)$ with respect to $(\tilde{x}, \tilde{y})$.
[3]This point is $(l, -d)$ in the coordinate system $(\hat{t}, \hat{n})$ and (x_f, y_f) in the coordinate system (x, y).
[4]It is straightforward that under contact h is zero and Σ is tangent to the cam at point p_C.

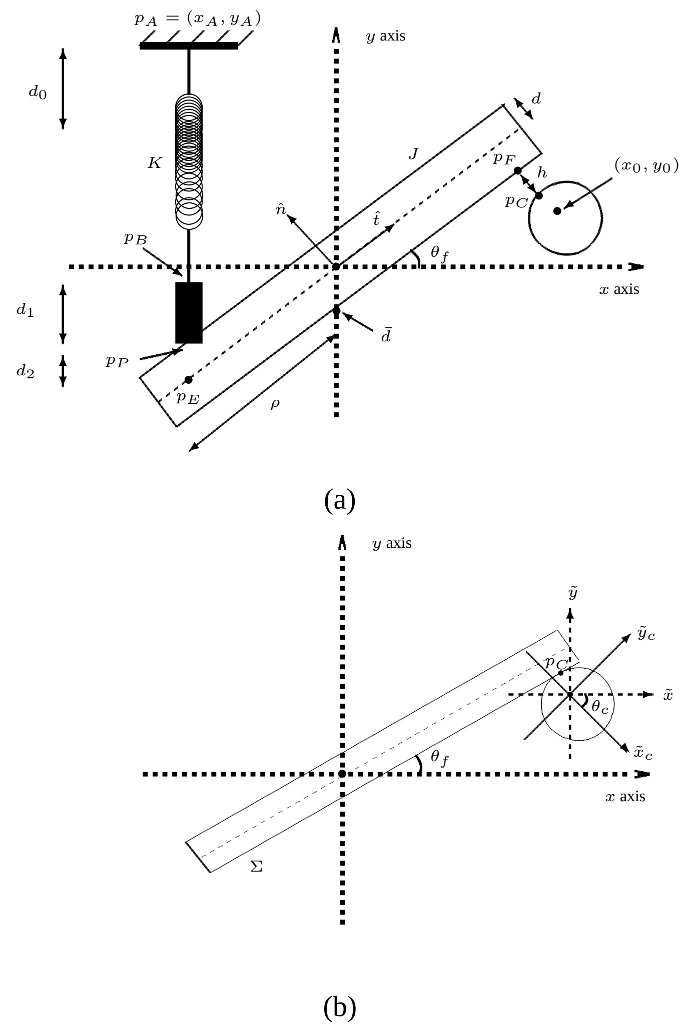

Figure 4.12 — Schematic diagram of the cam-follower system: (a) unconstrained mode; (b) constrained mode. All the labels are defined in Table 4.3.

and τ is the external torque given by the non conservative forces.

Let f_e be the elastic force exhibited by the spring. The change in the potential energy of the system can be stated as

$$
\begin{aligned}
\delta U &\triangleq -f_e^T(p_A - p_B) = \\
&= -K\left(y_A - y_E - d_0 - d_1 - d_2\right)\begin{bmatrix} 0 & 1 \end{bmatrix}\delta\begin{bmatrix} x_B \\ y_B \end{bmatrix} \\
&= -K\left(y_A - y_E - d_0 - d_1 - d_2\right)\begin{bmatrix} 0 & 1 \end{bmatrix}\delta\begin{bmatrix} x_B \\ y_E + d_1 + d_2 \end{bmatrix} \\
&= -K\left[(y_A - d_0) - (y_E + d_1 + d_2)\right]\delta\left(y_E + d_1 + d_2\right) \\
&= \delta\left[\frac{1}{2}K\left[(y_A - d_0) - (y_E + d_1 + d_2)\right]^2\right].
\end{aligned}
\tag{4.4}
$$

Here, only the potential energy of the spring has been considered, because the center of mass of the follower is assumed to be placed at a fixed point. Consequently the variation of the potential energy related to the gravity is assumed to be null.

Integration of (4.4) allows to generate an explicit expression for U

$$U = \frac{1}{2}K\left[(y_A - d_0) - (y_E + d_1 + d_2)\right]^2. \tag{4.5}$$

Notice that from Figure 4.12, d_2 can be expressed as function of the angular position of the follower θ_f and the parameter d, by

$$d_2\left(\theta_f\right) = \frac{d}{\cos(\theta_f)} \tag{4.6}$$

and since any spring rotation is avoided by design; *i.e.* $x_E = x_A$, it is straightforward to write

$$y_E(\theta_f) = x_A \tan(\theta_f). \tag{4.7}$$

Given that $T = \frac{1}{2}J\dot{\theta_f}^2$, after substitution of (4.6) and (4.7) into (4.5), an expression for L is found to be

$$L = \frac{1}{2}J\dot{\theta_f}^2 - \frac{1}{2}K\left[(y_A - d_0) - (x_A\tan(\theta_f) + d_1 + \frac{d}{\cos(\theta_f)})\right]^2. \tag{4.8}$$

Unconstrained Mode

Considering the result given by expression (4.8), the mathematical description for the unconstrained motion of the follower can be simply obtained by solving (4.2) in terms of its angular position θ_f, thus yielding

$$J\ddot{\theta}_f + K\left(x_A\tan(\theta_f) + \frac{d}{\cos(\theta_f)} - (y_A - d_0 - d_1)\right)\left(\frac{x_A}{\cos^2(\theta_f)} + d\frac{\sin(\theta_f)}{\cos^2(\theta_f)}\right) = 0. \tag{4.9}$$

Notice that the right hand side of the above equation is zero, since during unconstrained mode only the conservative elastic force has to be taken into account.

Constrained Mode

An expression for the contact mode, can be obtained by treating the cam as an external input acting directly on the follower. Let $\hat{\theta}_c(t)$ be the angular position of the follower when the two bodies are in contact, then the torque τ provided by the cam has to be such that $\theta_f = \hat{\theta}_c$. Including the external forcing of the cam τ into (4.9), we derive the dynamical equation during permanent contact as:

$$J\ddot{\theta}_f + K\left(x_A\tan(\theta_f) + \frac{d}{\cos(\theta_f)} - (y_A - d_0 - d_1)\right)\left(\frac{x_A}{\cos^2(\theta_f)} + d\frac{\sin(\theta_f)}{\cos^2(\theta_f)}\right) = \tau(t). \tag{4.10}$$

4.5.2 Impact law

To model the transient contact between the follower and the cam, we need to incorporate the action of a collision rule into the system equations. Letting t_k be the time instant when a generic impact occurs, such a rule gives the post-impact velocity, say $\dot{h}(t_k^+)$, as a function of the pre-impact velocity $\dot{h}(t_k^-)$. In general, we have

$$\dot{h}(t_k^+) = -r\dot{h}(t_k^-) \tag{4.11}$$

where r is the so-called coefficient of restitution [18], estimated later in the Chapter.

In the case of interest, if the velocity of the contact point p_C is continuous, we have

$$\nabla\Sigma \cdot \dot{p_F}(t_k^+) = \nabla\Sigma \cdot \dot{p_C}(t_k) - r\dot{h}(t_k^-), \tag{4.12}$$

where Σ is the lower side of the follower (assumed flat) oriented towards the cam (see Figure 4.12). Therefore, the impacting law will be obtained after recasting the quantities in (4.12) as functions of the angular position and velocity of the follower, relatives to the coordinates of the contact point p_C.

From the geometry depicted in Figure 4.12, h is the distance between the straight line of slope $\tan(\theta_f)$, passing through the point $(0, -\bar{d})$ in the (x, y) coordinate system and the point on the cam $p_C = (x_c, y_c)$. Then, simple geometric arguments yield to the following expression for h:

$$h(x_c, y_c, \theta_f) = \sin(\theta_f)x_c - \cos(\theta_f)y_c - d. \tag{4.13}$$

Differentiating (4.13) with respect to time, we have

$$\dot{h}(x_c, y_c, \theta_f) = \sin(\theta_f)\dot{x}_c - \cos(\theta_f)\dot{y}_c + (\cos(\theta_f)x_c + \sin(\theta_f)y_c)\,\dot{\theta_f}. \tag{4.14}$$

It is also possible to express Σ in the (x, y) coordinate system. Namely, from Figure 4.12, it follows that

$$\Sigma := \{(x, y) : y = \tan(\theta_f)x - \frac{d}{\cos(\theta_f)}\} \tag{4.15}$$

and then, by defining $\nabla\Sigma = \begin{bmatrix} -\sin(\theta_f) & \cos(\theta_f) \end{bmatrix}$ we obtain

$$\nabla\Sigma \cdot \dot{p_C} = -\sin(\theta_f)\dot{x}_c + \cos(\theta_f)\dot{y}_c. \tag{4.16}$$

Analogously, noticing that p_F has coordinates (x_f, y_f) related to $(l, -d)$ by the rotation matrix $\Xi(\theta_f)$, defined as

$$\Xi(\theta_f) = \begin{bmatrix} \cos(\theta_f) & -\sin(\theta_f) \\ \sin(\theta_f) & \cos(\theta_f) \end{bmatrix}, \tag{4.17}$$

it is possible to derive, after simple algebraic manipulations, an expression to $\nabla\Sigma \cdot \dot{p_F}$ given by

$$\nabla\Sigma \cdot \dot{p_F} = \begin{bmatrix} -\sin(\theta_f) & \cos(\theta_f) \end{bmatrix} \begin{bmatrix} -\sin(\theta_f)l + \cos(\theta_f)d \\ \cos(\theta_f)l + \sin(\theta_f)d \end{bmatrix} \dot{\theta_f} = l\dot{\theta_f}. \tag{4.18}$$

When an impact occurs, we also have $p_F \equiv p_C$, and therefore

$$l = \hat{t}^T \begin{bmatrix} x_c \\ y_c \end{bmatrix} = \cos(\theta_f)x_c + \sin(\theta_f)y_c. \tag{4.19}$$

Then, after substitution of (4.14),(4.16) and (4.18) into (4.12), the impact law can be finally expressed in terms of the follower angular position θ_f and velocity $\dot{\theta}_f$, as

$$\dot{\theta}_f(t_k^+) = -r\dot{\theta}_f(t_k^-) + (1+r)\,\frac{\cos(\theta_f)\dot{y}_c - \sin(\theta_f)\dot{x}_c}{\cos(\theta_f)x_c + \sin(\theta_f)y_c}. \tag{4.20}$$

Equation (4.20) depends explicitly on the coordinates of the contact point $p_C \equiv (x_c, y_c)$ and its derivatives. Such coordinates, are themselves functions of the cam geometry, position and velocity.

For the particular profile considered; i.e. eccentric and circular, the coordinates of the contact point in terms of the rotational angle of the cam θ_c, can be obtained by first subtracting the radius R from the distance between the point p_F (see Figure 4.12) and the geometric center of the cam $p_G = (x_g, y_g)$. The coordinates of p_G can be expressed in terms of the rotational center (x_0, y_0) and the eccentricity e of the profile, as:

$$\begin{cases} x_g(\theta_c) = e\cos(\theta_c) + x_0 \\ y_g(\theta_c) = e\sin(\theta_c) + y_0. \end{cases} \tag{4.21}$$

Therefore, straightforward algebraic manipulations give:

$$h\left(\theta_f, \theta_c\right) = \left[e\sin(\theta_c) + x_0\right]\sin(\theta_f) - \left[e\sin(\theta_c) + y_0\right]\cos(\theta_f) - d - R. \tag{4.22}$$

Notice that for a generic θ_c, it is possible to solve $h(\theta_f, \theta_c) = 0$; giving the angular displacement at the follower joint during contact mode. Hence, by equating (4.22) to zero, we can obtain an analytical expression for $\hat{\theta}_c$, as:

$$\hat{\theta}_c\left(\theta_c\right) = \arcsin\left(\frac{d+R}{\sqrt{(e\cos(\theta_c)+x_0)^2 + (e\sin(\theta_c)+y_0)^2}}\right) - \arctan\left(-\frac{e\sin(\theta_c)+y_0}{e\cos(\theta_c)+x_0}\right). \tag{4.23}$$

Now, let $\hat{n}$ be the unit vector lying along the direction of the lower side of the follower in contact with the cam. Clearly, $\hat{n}$ is given by:

$$\hat{n}(\hat{\theta}_c(\theta_c)) = \left[\begin{array}{cc} -\sin(\hat{\theta}_c(\theta_c)) & \cos(\hat{\theta}_c(\theta_c)) \end{array}\right]^T. \tag{4.24}$$

Then, by adding the vector having modulus equal to R (the radius of the cam) and direction orthogonal to $\hat{n}$, to the coordinates of the cam geometrical center p_G given in (4.21), the coordinates of the contact point p_C can be expressed as

$$\begin{cases} x_c(\theta_c) = e\cos(\theta_c) - R\sin(\hat{\theta}_c(\theta_c)) + x_0 \\ y_c(\theta_c) = e\sin(\theta_c) + R\cos(\hat{\theta}_c(\theta_c)) + y_0 \end{cases} \tag{4.25}$$

with corresponding derivatives, after time differentiation

$$\begin{cases} \dot{x}_c(\theta_c) = -e\sin(\theta_c)\dot{\theta}_c - R\cos(\hat{\theta}_c(\theta_c))\frac{\partial\hat{\theta}_c}{\partial\theta_c}(\theta_c)\dot{\theta}_c \\ \dot{y}_c(\theta_c) = \quad e\cos(\theta_c)\dot{\theta}_c - R\sin(\hat{\theta}_c(\theta_c))\frac{\partial\hat{\theta}_c}{\partial\theta_c}(\theta_c)\dot{\theta}_c \end{cases} \tag{4.26}$$

where $\hat{\theta}_c\left(\theta_c\right)$ refers to the angular position of the follower under contact mode.

The model derived above contains several nonlinearities and can be ill-conditioned (high stiffness coefficient). These are well-known obstacles for numerical integration schemes that may require extremely small time steps and robust integrators. It is not the purpose of the present Chapter to discuss integration methods but we are completely aware of the difficulties resulting from both non-linearities and high frequencies. To overcome the numerical problems here we used an integration algorithm with adaptive step-size available in the commercial platform MATLAB [45]. For further reference on the simulation method employed to evaluate the system equations (4.9), (4.10) and (4.20), check the extended event-driven algorithm described in Chapter 3.

4.6 Parameter fitting

Now that expressions for description of the follower motion have been derived, proper assignation of parameter values will confirm the correctness of the model by resembling the experimental data acquired from the physical implementation of the system. In doing so, two main set of parameters can be considered, namely: geometric and physical. Geometric includes all the main distances depicted in Figure 4.12, plus cam's eccentricity and radius, as listed in Table 4.4. On the other hand, physical parameters depend on the materials employed, including follower inertia J, spring coefficient K and the restitution coefficient r for inelastic impacts. This last is of remarkable importance for the dynamics, and will be treated later in section 4.6.1.

Table 4.4 — Model parameters

Parameter	Value	Units
R cam radius	0.045	$[m]$
e cam eccentricity	0.015	$[m]$
(x_0, y_0) center of rotation of the cam	$(0.249, 0)$	$[m]$
d half of the follower height	0.021	$[m]$
J moment of inertia of the follower	0.043	$[kg \cdot m^2]$
K spring coefficient	105	$[N/m]$
x_A x-coordinate of the spring hanging point	-0.031	$[m]$
$y_A - d_0 - d_1$ spring elongation distance	0.173	$[m]$

The nominal values for J and K are reported in Table 4.4. The ratio of these nominal values, $M = \frac{J}{K}$, has been optimized to fit the experimental unconstrained motion of the follower, as illustrated by Figure 4.13. As expected, the model shows a good agreement with the experimental data as highlighted from the time history of the error shown in Figure 4.13-(b).

The validity during constrained motion can be also verified by incorporating the information of the profile derived in expression (4.23). In this way, simulation of motion equations (with the extended event-driven approach described in Chapter 3) under low rotational speed ω, allows to confirm the accuracy on calculations by appreciating the similarity between experimental and numerical trajectories, as illustrated in Figure 4.14. Low values of ω will become clear in section 4.7.

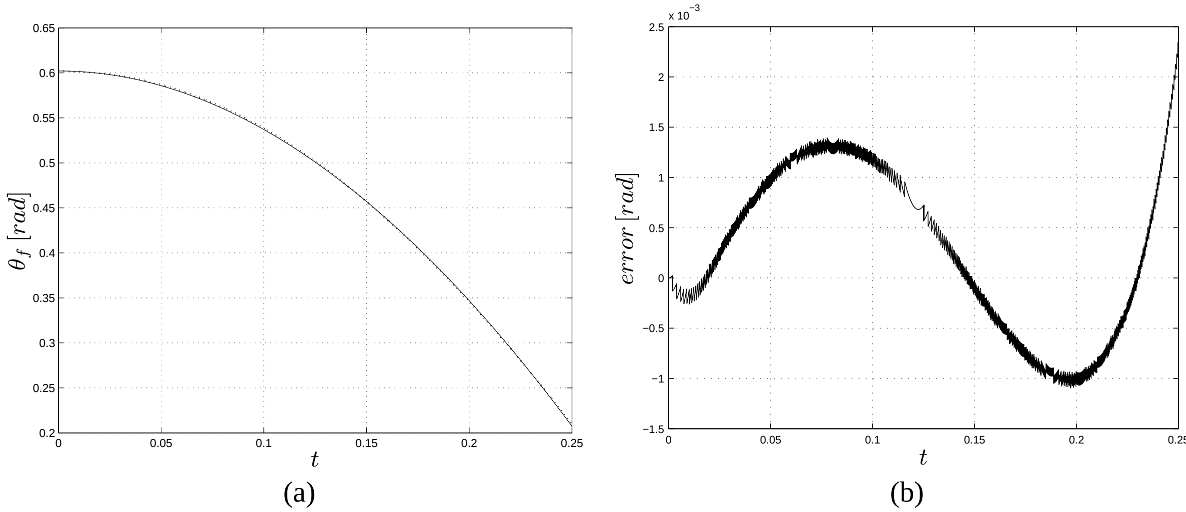

Figure 4.13 — Unconstrained mode, validation results. Time history of the free-fall motion of the follower: (a) $\theta_f(t)$ experimental (dashed) vs. numerical (solid); (b) estimation error corresponding to difference between data plotted in (a).

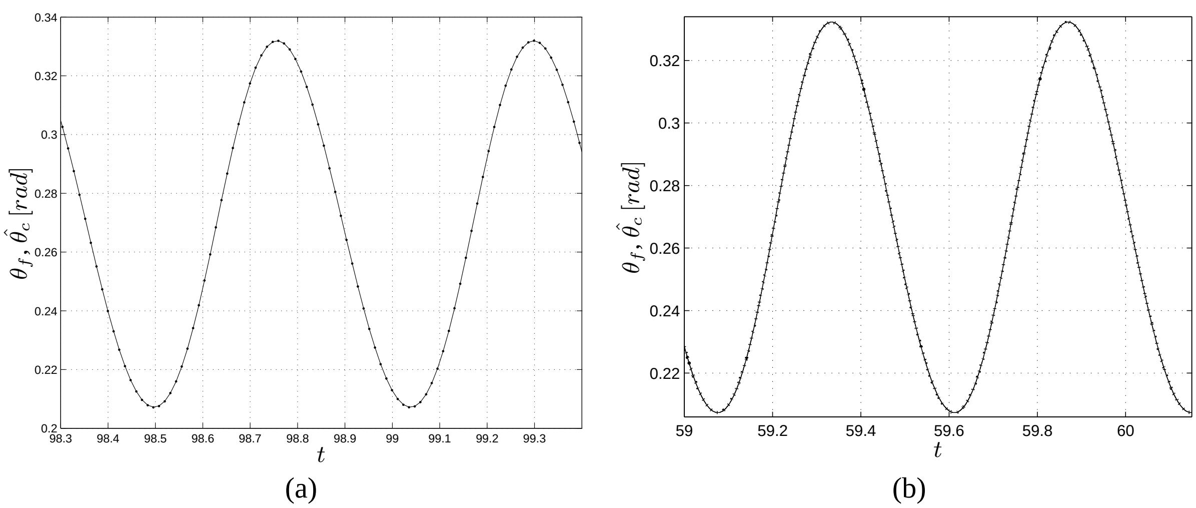

Figure 4.14 — Constrained mode, validation results. Time evolution of $\hat{\theta_c}$ (dotted line) and θ_f (solid line) for ω = 110 *rpm*, showing: (a) experimental and (b) simulated data. Notice the agreement achieved in values of amplitude and period of the forcing.

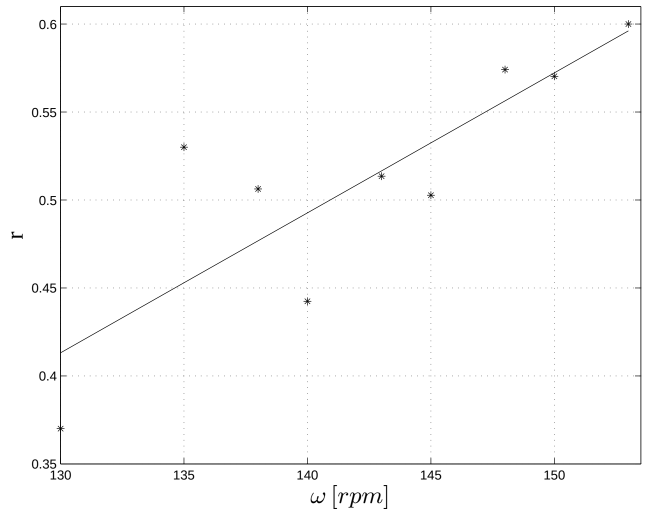

Figure 4.15 — Coefficient of restitution r as function of the cam velocity ω: identified values of r (asterisks) by matching simulated first bouncing amplitude with experimental data, and corresponding linear approximation (solid line).

4.6.1 Estimating the coefficient of restitution

The coefficient of restitution r is an index of how elastic a collision is. The problem of estimating r experimentally has been discussed in a large number of papers in the literature on impacting systems and it is usually based on bouncing ball experiments, see for example [3] and [83]. The most common methods are formulated in terms of high-speed data collection of the impact sounds as explained in [15], or on detailed analysis based on the use of high-speed cameras and force sensors as in [53]. The most basic approach is to consider r as a constant coefficient, whereas in practice it is well known that r is actually an unknown function of the impact speed [15].

Since the impact velocity is not easy to measure, in this work we assume that the coefficient of restitution r is a function of the cam rotational speed ω. This is motivated by the observation that higher cam velocities lead to larger detachment of the follower and hence higher approach speed at the impact. In particular, we identified different values of r by running a set of experiments at different constant values of ω ranging from 130 *rpm* to 155 *rpm* where the system experienced periodic multi-impacting motion (as will be evident in section 4.7). Hence, given a fixed cam velocity in the range of interest, the coefficient r is estimated by tuning its value in such a way to match the amplitude of the first bounce between the simulated and experimental data. Then, a least-square approach provides a linear interpolation of r as a function of ω. This last procedure is depicted in Figure 4.15.

Although using the cam velocity instead of the actual approach speed in estimating r is a strong approximation, the good agreement between simulations and experiments seems to confirm the validity of the adopted approach. This can be confirmed by the numerical results in Figure 4.16, where preservation of dissipative features after the first bounce are reflected under several values of ω.

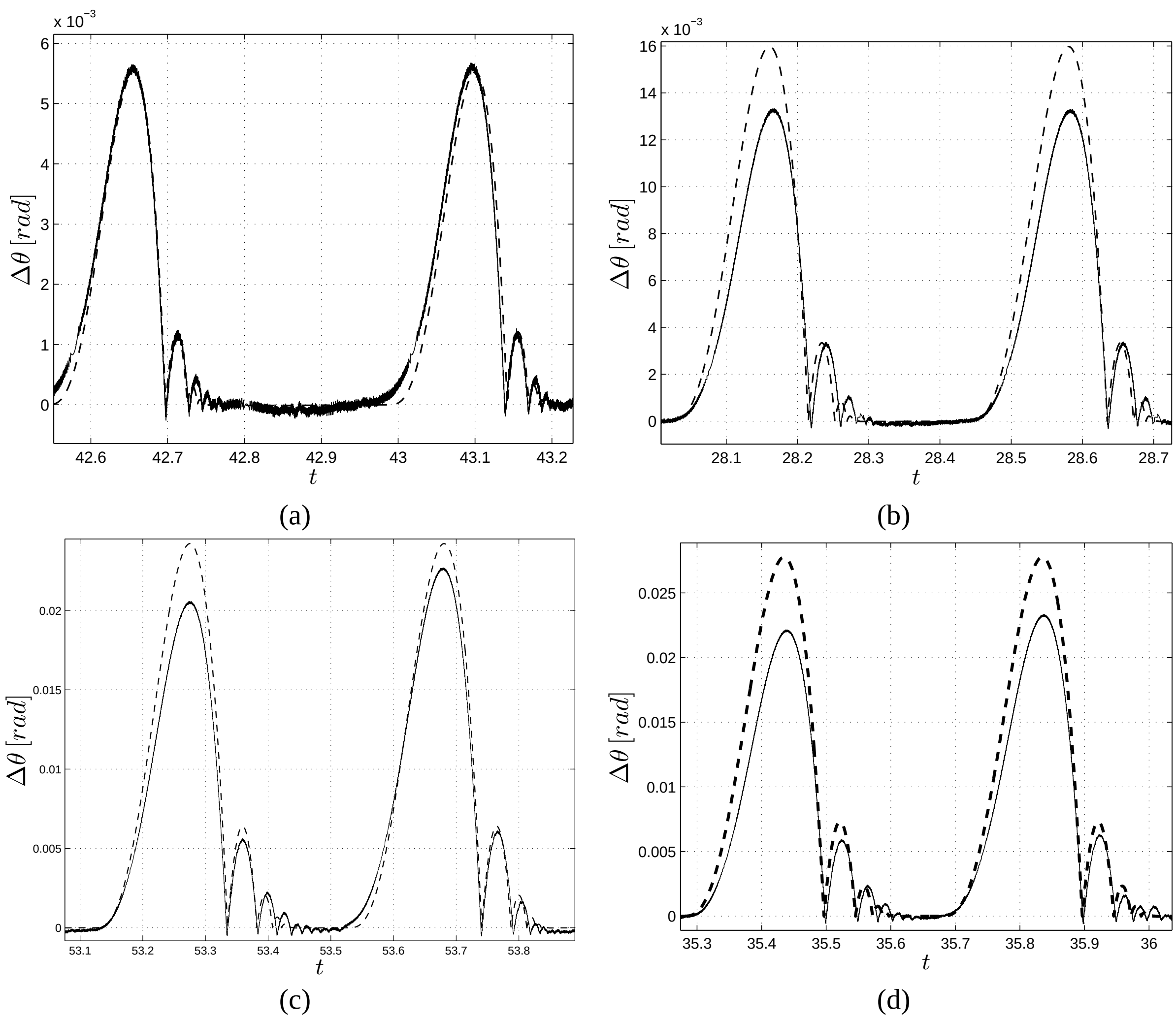

Figure 4.16 — Impact law, validation results. Comparison between sections of simulated (dashed) and experimental (solid) differential time series for (a) ω = 135 *rpm*, (b) ω = 143 *rpm*, (c) ω = 148 *rpm* and (d) ω = 150 *rpm*. This results evidence the preservation of dissipative features in the numerical approach from the first bounce. The vertical axis $\Delta\theta$, represents the difference $\theta_f - \theta_c$.

4.7 Experimental bifurcation diagram

Traditionally in a wide range of engineering applications, cam-follower systems are designed by assuming a constant speed. Nevertheless, especially in high speed cams, the presence of unavoidable camshaft fluctuations can affect the accuracy of the follower motion [31] [103]. Starting from the pioneering work of Rothbart [75], engineers have highlighted the potential advantages of using variable speed cams and embedding their variable-speed explicitly as a parameter into the design process. We wish to emphasize that the experimental investigation of the nonlinear dynamics of the follower after its detachment from the cam, can be used to improve the cam design. For example, bifurcation diagrams can be obtained to evaluate the influence on the cam-follower dynamics of various parameters including: the cam rotational speed, variable stiffness characteristics, different cam profiles, etc [104].

In so doing, and as a way to uncover and fully characterize the dynamical scenarios of the system introduced in section 4.4, Figure 4.17 shows the complete experimental bifurcation diagram containing the story of motion behaviour in the follower θ_f, as the angular velocity of the cam ω varies between 120 and 200 *rpm*. Here, the cam-follower system exhibits a complex dynamic behaviour characterized by different coexisting solutions, several bifurcations and chaos.

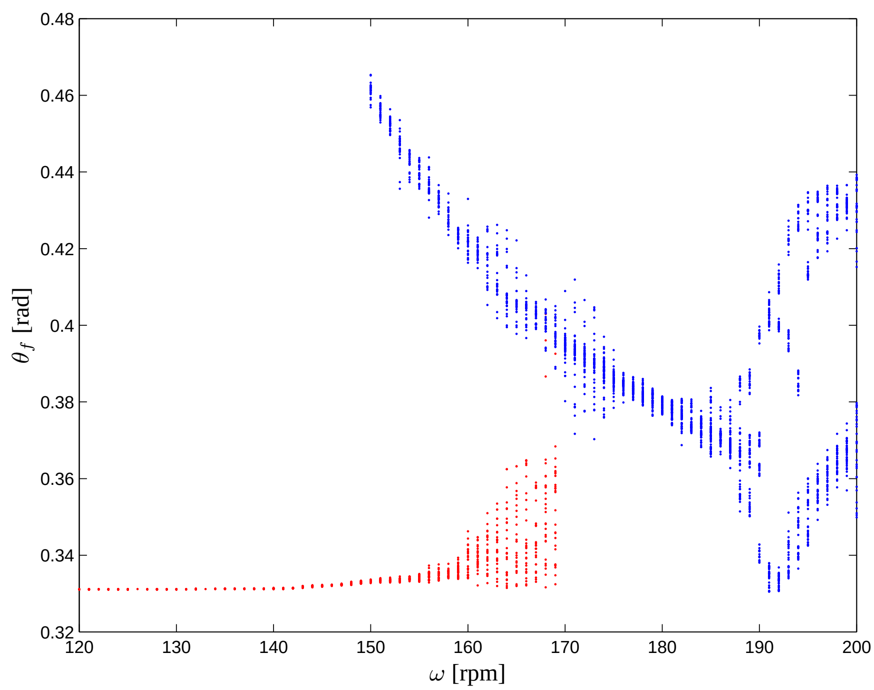

Figure 4.17 — Complete experimental bifurcation diagram. The diagram is characterized by different coexisting solutions. Red: *Scenario 1*. Blue: *Scenario 2*. The automated process of acquisition is described in [5].

In order to capture experimentally the two evident coexisting scenarios, different experimental runs were performed in an automated process described in [5]. Firstly, the cam velocity was swept forward from 120 to 200 *rpm*. For each value of the cam speed, 10 seconds after one minute transient in the measure of the

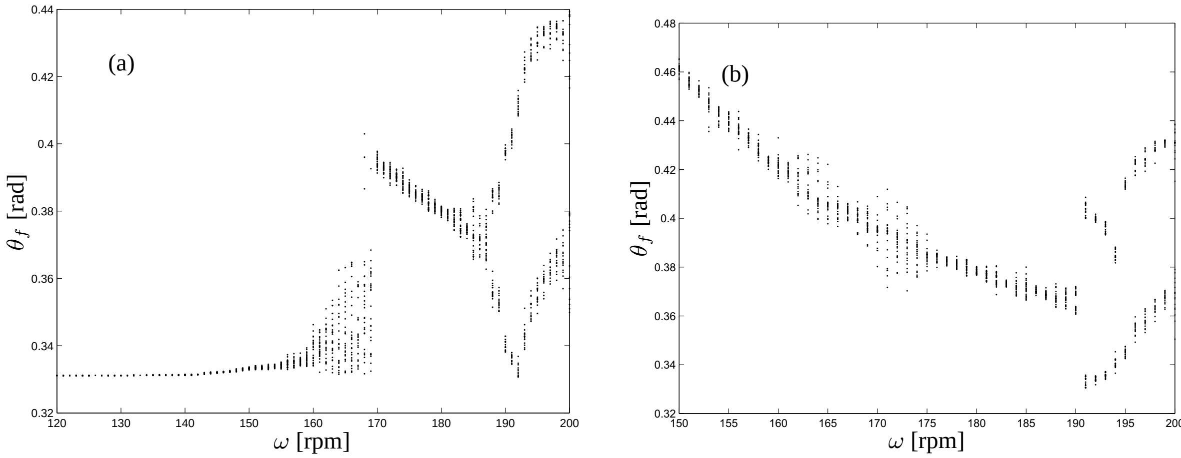

Figure 4.18 — Experimental bifurcation diagram: (a) forward parameter sweep; (b) backward parameter sweep.

angular position of the follower θ_f, were stored and the resulting stroboscopic points plotted. As a result, the *forward* bifurcation diagram has been obtained as depicted in Figure 4.18-(a). A second experiment was executed with the same philosophy as before, but this time for ω being decreased from 200 to 150 *rpm*. The resulting *backward* bifurcation diagram is plotted in Figure 4.18-(b). The complete bifurcation diagram of Figure 4.17, was then generated by overlapping the forward and backward experimental diagrams. It shows two main different coexisting routes to chaos, namely :

- a sudden transition to chaos seemingly due to the transition from a complete chattering sequence to an incomplete one; labelled as *Scenario 1* in the rest of the contents; and
- a classical period doubling cascade; labelled as *Scenario 2*.

In what follows, we study each of these scenarios in greater detail, complementing the experimental bifurcation diagram with experimental time series, phase-portraits and stroboscopic maps at the most significant values of the cam rotational speed ω.

The stroboscopic map Π, is obtained experimentally by measuring periodically at each $T = 2\pi/\omega$, both the angular position θ_f and velocity $\dot{\theta_f}$ of the follower. Hence, it is defined as

$$(\theta_{f_n}, \dot{\theta}_{f_n}) \longrightarrow (\theta_{f_{n+1}}, \dot{\theta}_{f_{n+1}}) \tag{4.27}$$

where $\theta_{f_n} = \theta_f(nT)$, $\dot{\theta}_{f_n} = \dot{\theta}_f(nT)$, and n is the number of forcing periods (or cam revolutions).

A generic nT-periodic orbit characterized by m impacts per period will be labelled as a $P(m, n)$ *orbit*. Therefore, nT-periodic orbits with sticking – characterized by the accumulation of an infinite number of impacts in finite time – will be denoted as $P(\infty, n)$.

4.7.1 Scenario 1: Chattering interruption

For the first scenario, four regions of different qualitative behaviour associated to different values[5] of ω, can be highlighted:

1. Permanent contact ($\omega < 125$ *rpm*), where the cam and the follower stay in contact for all time.
2. Periodic impacting behaviour ($125 < \omega < 155$ *rpm*), where the existence of a $P(\infty, 1)$ orbit is detected.
3. Sudden transition to chaos due to chattering interruption ($155 < \omega < 160$ *rpm*).
4. Aperiodic motion and chaos ($\omega > 160$ *rpm*).

We now give some experimental evidence for each of these scenarios.

Permanent contact - low velocity regime ($\omega < 125$ *rpm*)

The experimental investigation starts by using low values of the cam rotational speed. Experiments confirm the presence of permanent contact between the cam and the follower in this range of ω values. For example, in Figure 4.19, the dynamics of the follower at a constant cam angular velocity $\omega = 120$ *rpm*, are shown. At this velocity value, the restoring force of the follower is higher than the force exerted by the constraint represented by the cam. In this condition, the cam and the follower remain in contact for all time, hence we have $\theta_f = \hat{\theta}_c$ where $\hat{\theta}_c$ is the cam angular displacement at the follower joint, function of the cam angular position θ_c. It is important to note that permanent contact is experimentally detected up to approximately 125 *rpm*. We wish to emphasize the extremely small experimental measurement error shown in Figure 4.19 ($\varepsilon \approx 10^{-3}$).

Periodic impacting behaviour ($125 < \omega < 155$ *rpm*)

For values of $\omega \in [125, 155]$ *rpm*, the follower motion is observed to exhibit $1T$-periodic behaviour characterized by an infinite number of impacts per period ($P(\infty, 1)$-*orbit*).

One example of such periodic sticking orbit is depicted in Figure 4.20, where time histories of both the experimental cam and follower angular positions are shown, together with their difference at $\omega = 150$ *rpm*. Here, it is apparent that during every period an infinite number of impacts accumulate in finite time (complete chattering) before the sticking phase.

Chattering interruption ($155 < \omega < 160$ *rpm*)

For $155 < \omega < 160$ *rpm*, the system is observed to exhibit a sudden transition to chaos. A closer look at this parameter region shows that the transition is observed from a complete to an incomplete chattering sequence. Namely, as ω is varied past a critical value, a $P(\infty, 1)$ orbit turns into a $P(N, 1)$ solution with $N \gg 1$. Experimental evidence of such a transition is depicted in Figure 4.21, where a periodic orbit with sticking (a) is shown to turn into a periodic orbit without sticking (c), resulting in the interruption of the

[5]The maximum cam velocity during the experimental analysis is limited to $\omega = 200$ *rpm*. For higher velocity regimes the follower displacement is very close to the maximum admissible value and the energy dissipated in the impacting behaviour can even destroy the experimental rig.

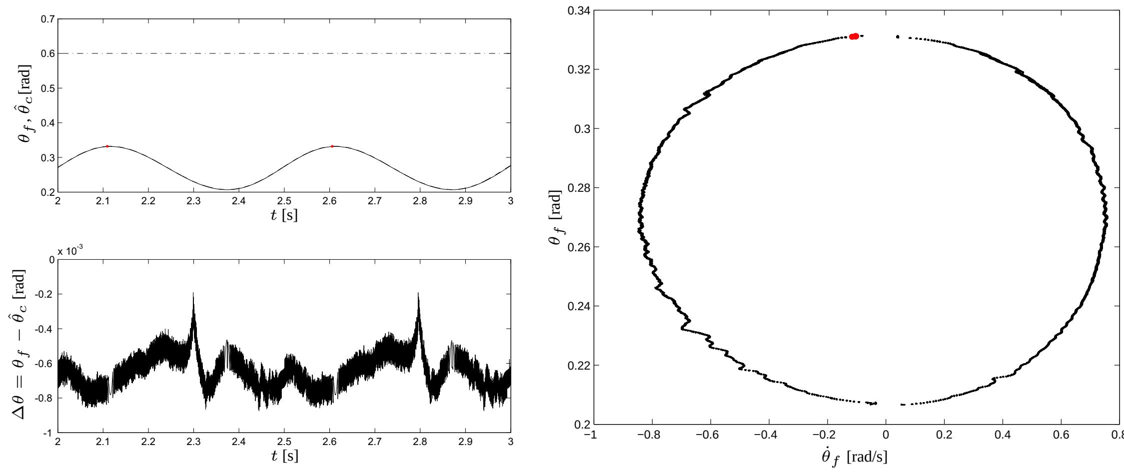

Figure 4.19 — Experimental results. Permanent contact at ω = 120 *rpm*. Left frame: time history of the cam (dashed line) and follower (solid line) angular positions (top panel), with their corresponding difference $\Delta\theta$ (bottom panel). Dash-dot line: maximum angular displacement of the follower. Right frame: phase portrait (θ_f v.s. $\dot{\theta}_f$). Red dots symbolize samples of the stroboscopic map Π given by (4.27).

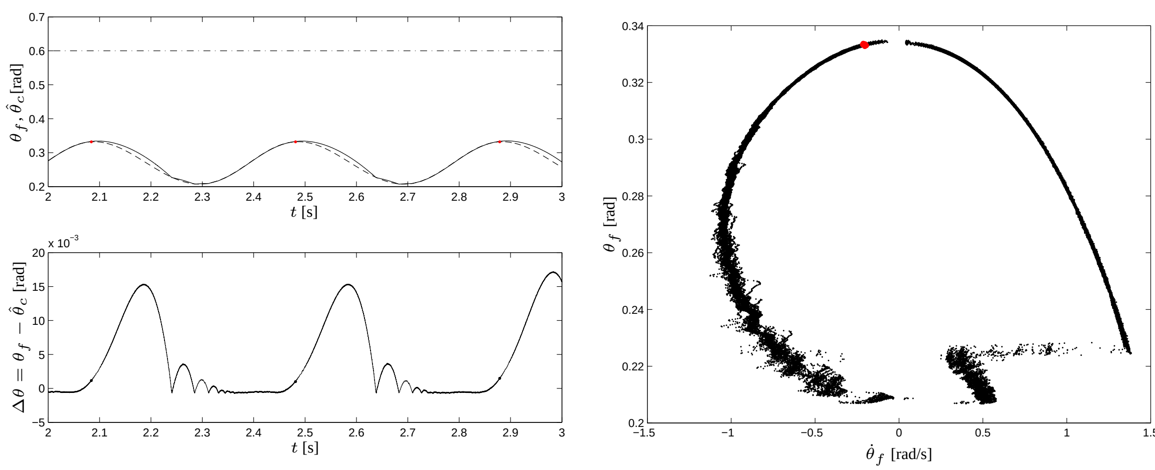

Figure 4.20 — Experimental results. $P(\infty, 1)$ orbit at ω = 150 *rpm*. Left frame: time history of the cam (dashed line) and follower (solid line) angular positions (top panel), with their corresponding difference $\Delta\theta$ (bottom panel). Dash-dot line: maximum angular displacement of the follower. Right frame: phase portrait (θ_f v.s. $\dot{\theta}_f$). Red dots symbolize samples of the stroboscopic map Π given by (4.27).

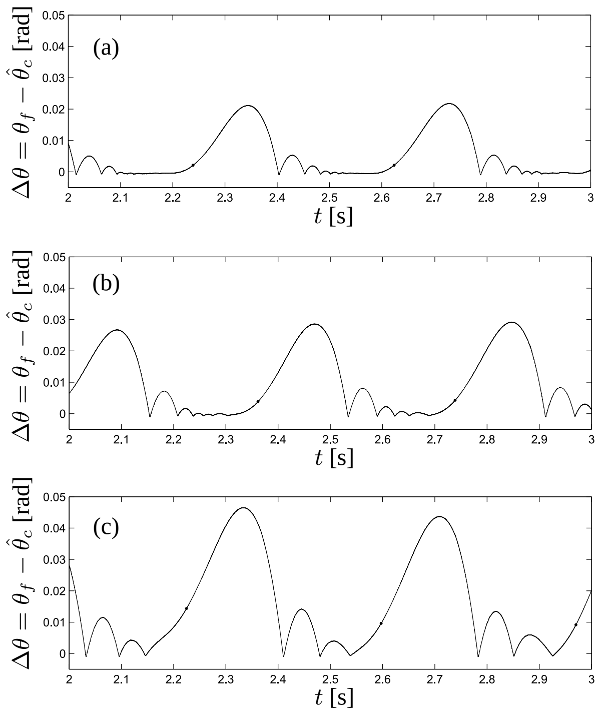

Figure 4.21 — Experimental results. Chattering interruption. Time history of difference $\Delta\theta$ between cam and follower angular positions at (a) ω=155, (b) ω=158 and (c) ω=160 *rpm*.

complete chattering sequence. This bifurcation scenario will be studied in further details with additional numerical tools in Chapters 5 and 6.

Past the critical value of the cam velocity, corresponding to $\omega = 160$ *rpm*, the follower starts exhibiting aperiodic behaviour and sensitive dependence on initial conditions. A representative case of this chaotic behaviour is shown in Figure 4.22, where the time history of the chaotic dynamics together with the corresponding phase portrait and stroboscopic points at $\omega = 165$ *rpm*, are depicted.

4.7.2 Scenario 2: period doubling cascade

As mentioned above, in the range $150 < \omega < 200$ *rpm*, the experimental system also undergoes a coexisting classical period-doubling cascade similar to those reported in the literature on impact oscillators [40] [16]. In particular, for $\omega \in [150, 188]$ *rpm*, the system exhibits large-amplitude periodic behaviour characterized by one impact per period, such as the one depicted in Figure 4.23 for $\omega = 165$ *rpm*.

When increasing the cam angular velocity beyond 188 *rpm*, the follower motion exhibits a period doubling bifurcation (see Figure 4.24). The resulting $P(2,2)$ orbit persists for all the admissible values of the cam speed. The sharp corner in the $P(2,2)$ branch observed in the experimental bifurcation diagram at $\omega \approx 191$ *rpm*, is only due to the transition of one of the impacts characterizing the $P(2,2)$ solution through the maximum of the cam profile.

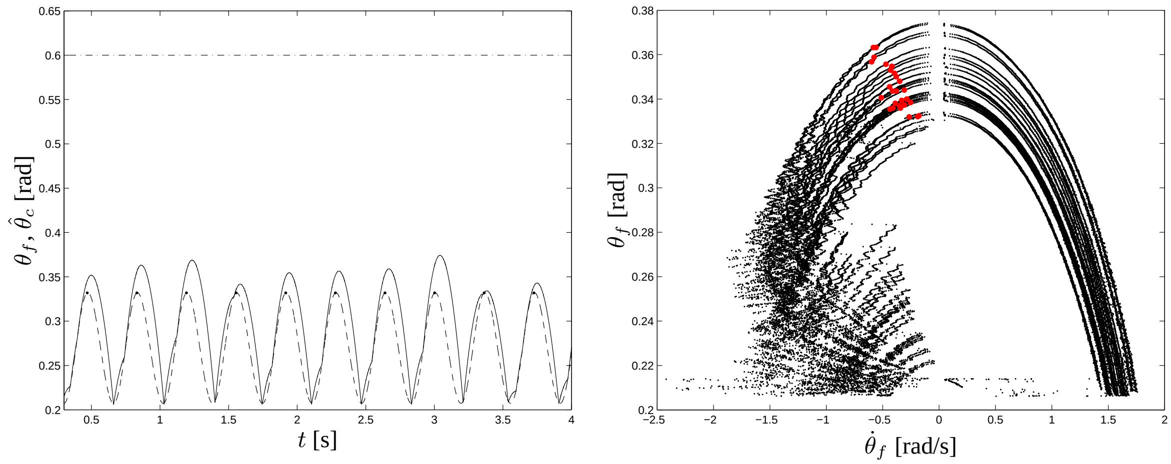

Figure 4.22 — Experimental results. Chaotic motion at ω = 165 *rpm*. Left frame: time history of the cam (dashed line) and follower (solid line) angular positions. Dash-dot line: maximum angular displacement of the follower. Right frame: phase plane portrait (θ_f v.s. $\dot{\theta}_f$). Red dots symbolize samples of the stroboscopic map Π given by (4.27).

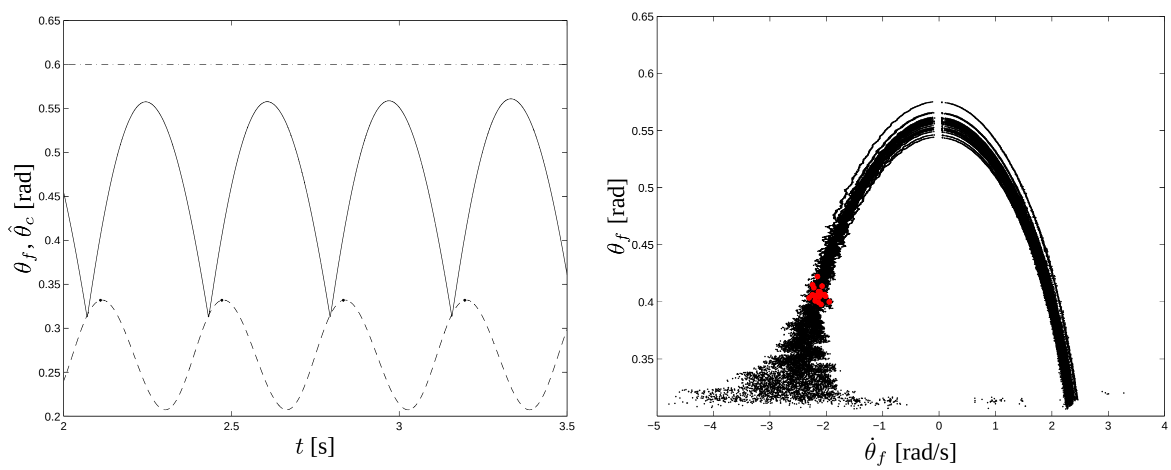

Figure 4.23 — Experimental results. P(1,1) orbit at ω = 165 *rpm*. Left frame: time history of the cam (dashed line) and follower (solid line) angular positions. Dash-dot line: maximum angular displacement of the follower. Right frame: phase portrait (θ_f v.s. $\dot{\theta}_f$). Red dots symbolize samples of the stroboscopic map Π given by (4.27).

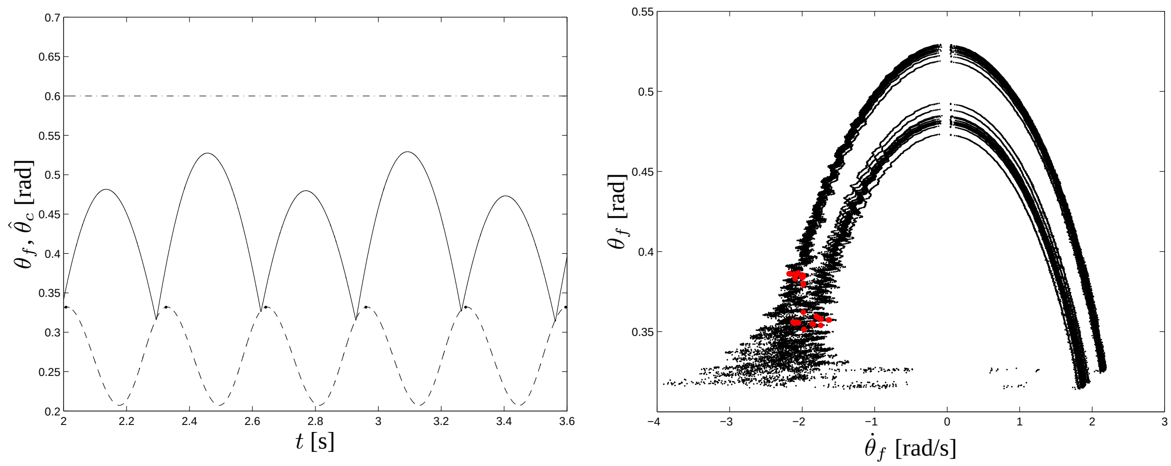

Figure 4.24 — Experimental results. P(2,2) orbit at ω = 188 *rpm*. Left frame: time history of the cam (dashed line) and follower (solid line) angular positions. Dash-dot line: maximum angular displacement of the follower. Right frame: phase portrait (θ_f vs. $\dot{\theta}_f$). Red dots symbolize samples of the stroboscopic map Π given by (4.27).

4.8 Discussion

The experimental results described so far, show several interesting features in the dynamical behaviour of the cam-follower impacting system described in section 4.4. In particular, the coexistence of two different scenarios is observed together with the novel sudden transition to chaos caused by interruption of complete chattering sequences. To better investigate these phenomena, exhaustive numerical analysis should be applied to the representative model of system motion given by equations (4.9), (4.10) and (4.20).

In the next Chapters, it will be demonstrated that after validation of the correctness of the model in capturing the main dynamical features experienced by the original system, the techniques described in Chapter 3, constitutes a powerful resource to unveil the mechanisms for bifurcations and changes of stability. More precisely, in Chapters 5 and 6 numerical local analysis will be performed in a vicinity of the chattering interruption to explain the novel bifurcation phenomenon involved. This degree of precision is unfeasible at an experimental level, and therefore will not be possible to perform such kind of analysis directly from real measurements.

Chapter 5

Numerical bifurcation analysis

5.1 Introduction

An important feature of impacting systems is the possibility for an infinite sequence of impacts to accumulate in finite time. This phenomenon, also termed as chattering or Zeno behaviour in the literature [22] [58] [57] [80], has been shown to be the key to uncover the intricate structure of the dynamics of an impacting system, as for example to predict the topology of its basins of attraction or regions where sticking occurs. Sticking in impact oscillators corresponds to the mass remaining in contact with the impacting obstacle over a finite time interval and has been recently related to the occurrence of so-called sliding solutions in piecewise-smooth flows [34]. In [57], it has been proposed that a new type of DIB occurs in impacting systems when, under parameter variations, a complete chattering sequence (leading to sticking) is interrupted. Basically, when one or more parameters are varied, a periodic orbit characterized by an infinite number of impacts accumulating in finite time suddenly looses its stability as the chattering sequence becomes incomplete, with the trajectory escaping the sticking region after a finite (large) number of impacts. The phenomenon described above has been observed by some authors in the existing literature and given the name of “rising bifurcation” or “chattering interruption”. A reference to this phenomenon can be found in [92], while numerical evidence of its occurrence in a two-degree-of-freedom impacting oscillator is reported in [95], [96] and [97]. Therefore, a pressing open problem is to fully investigate this novel bifurcation phenomenon which is unique to impacting systems.

It is worth mentioning here that despite its theoretical and numerical observations, this phenomenon has seldom been shown to occur experimentally before, making it even more important to study the complex behaviour exhibited by the physical implementation of the cam-follower device described in Chapter 4, where as conjectured, complex behaviour seems to be due to chattering and its interruption [65] [66].

The scope of this Chapter is to provide evidence that allows to unfold the observed bifurcation behaviour and characterize the dynamics of the system under investigation, by applying numerical analysis on the representative model of motion derived. In particular, emphasis will be given to showing that the interruption of a complete chattering sequence is indeed the mechanism that explains the sudden transition to chaos observed in the bifurcation diagram. Also, to analyze the coexistence of this novel discontinuity induced phenomenon with a traditional period-doubling cascade. To this aim, numerical simulation, continuation and computation of basins of attraction are performed, showing excellent agreement with results achieved experimentally. Related work and results are going to be published in [5] and [7].

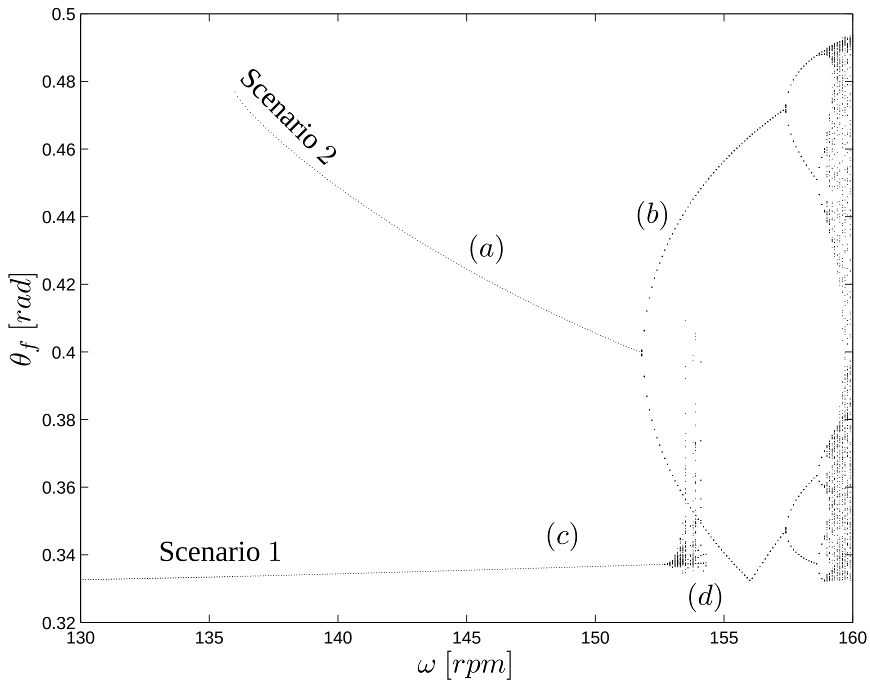

Figure 5.1 — Numerical bifurcation diagram. Vertical axis contain the steady state values of the follower angular position θ_f at different cam forcing frequencies ω, taken as bifurcation parameter. The diagram is complemented in Figure 5.2 with some numerical time series of the most meaningful follower dynamics, showing agreement with the experimental behaviour of the system described in Chapter 4.

5.2 Numerical bifurcation diagram

The bifurcation diagram predicted by numerical simulations of the analytical model given by equations (4.9), (4.10) and (4.20), is shown in Figure 5.1 (see also the time series in Figure 5.2). Simulations have been performed by implementing the extended event-driven approach described in Chapter 3. The diagram is obtained by brute-force simulation of the system for increasing and decreasing values of ω. For each parameter value, 300 cycles of the forcing were simulated and the last 100 stroboscopic points stored. The qualitative agreement between this numerical result and the experimental bifurcation diagram of Chapter 4, is remarkable. In particular, the model captures the coexistence of different solutions, the non-smooth chattering route to chaos and the smooth period-doubling cascade[1].

The only detectable difference between the experimental and numerical bifurcation diagrams, is related to the ranges of ω in which some of the scenarios described above are observed to take place. In Table 5.1, the quantitative comparison of the experimental and simulated behaviour of the cam-follower system is reported. Namely, the most significant dynamical scenarios are summarized together with the values of ω at which they occur in the experiments, ω_{exp}, and in the simulations, ω_{sim}. Despite the good qualitative agreement, results highlight that the most significant mismatch occurs at high velocity regimes when all the nonlinear effects, neglected into the model – such as for example friction, the presence of bearings or fluctuations in the torque acting on the cam – become more relevant. Other sources of uncertainty are the coefficient of restitution and the unavoidable presence of unmodelled dynamics. For example, the coefficient

[1] Actually, the existence of the period-doubling cascade was not detected experimentally at first. It was only because of the model prediction that *ad hoc* experiments were carried out to confirm its existence in the real physical system!

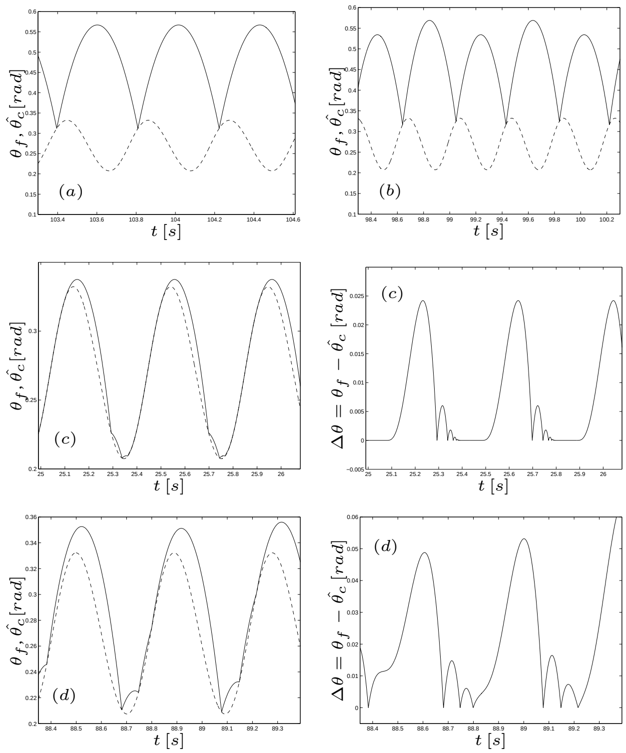

Figure 5.2 — Time series of the most meaningful follower dynamics observed in the numerical bifurcation diagram of Figure 5.1.

of restitution is theoretically an unknown nonlinear function of the approach speed and materials, all physical characteristics. Since the impact velocity cannot be measured easily with a sufficient precision, r can be estimated in the whole range of the operating conditions of the system with only a certain degree of accuracy. Furthermore, all the geometrical parameters necessary to describe the follower motion are obtained in the permanent contact region in the absence of impacts. In this operating condition, the spring works in its linear region and thus, by supposing a constant elastic coefficient, a good agreement between experiment and model can be achieved for the unconstrained follower motion [6]. Obviously, the hypothesis of a linear and constant spring introduces some approximation in the model which explains the mismatch between the predicted values of ω for higher velocity regimes or when the follower works around its maximum displacement.

5.2.1 Period-doubling cascade

The coexisting (large-amplitude) smooth period doubling cascade, can be observed numerically for $\omega \in [135, 160]$ *rpm* in accordance with the experimental observations reported in Chapter 4. The fundamental branch experiences a first period doubling close to $\omega = 152$ *rpm*. Another period doubling is then detected at $\omega \approx 157.5$ *rpm*. Figures 5.3, 5.4 and 5.5, illustrate this situation in detail by showing respectively the time series for the $P(1, 1)$, $P(2, 2)$ and $P(4, 4)$ orbits, also detected experimentally. Notice the excellent qualitative agreement between the experiments and the numerical predictions of Figures 5.3 and 5.4. Notice also that the orbit depicted in Figure 5.5 cannot be observed in practice, as its amplitude is greater than the maximum follower displacement allowed in the experiment.

To isolate with greater accuracy the period doubling bifurcation points, numerical continuation routines

Table 5.1 — List of the different values of ω at which the main dynamical events occurs respectively in experiments (ω_{exp}) and simulations (ω_{sim})

Main Dynamical Events	ω_{exp} [rpm]	ω_{sim} [rpm]
Permanent Contact	< 125	< 125
Detachment	125	125
$P(\infty, 1)$ orbits	$]125, 155]$	$]125, 152]$
Chattering route to Chaos	$]155, 160]$	[152.6, 154]
Chaos	$[160, 170]$	[154,154.5]
$P(1, 1)$ orbits	$]150, 188]$	[135, 151]
$P(2, 2)$ orbits	$]188, 200]$	[152, 170]

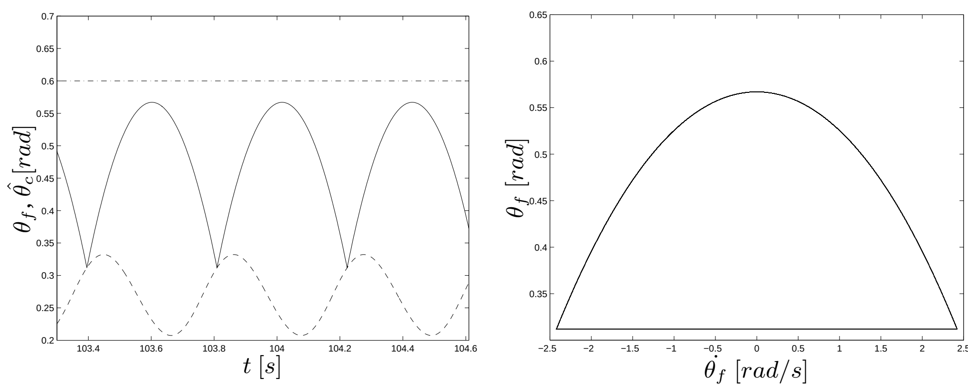

Figure 5.3 — Numerical results. $P(1, 1)$ orbit at $\omega = 145$ *rpm*. Left frame: cam (dashed) and follower (solid) trajectories. Dash-dot line: maximum angular displacement of the follower. Right frame: phase portrait.

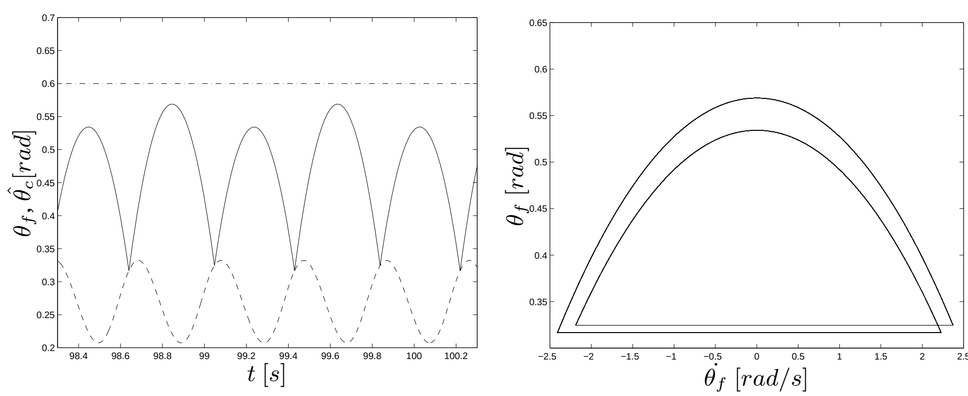

Figure 5.4 — Numerical results. $P(2, 2)$ orbit at $\omega = 152$ *rpm*. Left frame: cam (dashed) and follower (solid) trajectories. Dash-dot line: maximum angular displacement of the follower. Right frame: phase portrait.

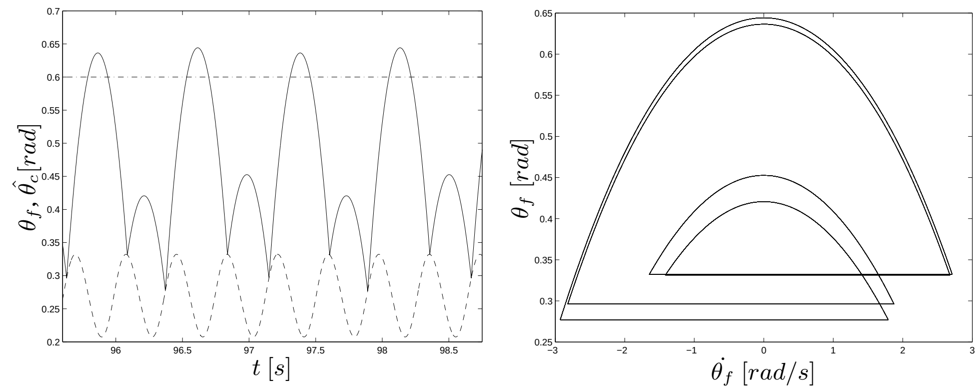

Figure 5.5 — Numerical results. $P(4,4)$ orbit at $\omega = 158$ *rpm*. Left frame: cam (dashed) and follower (solid) trajectories. Dash-dot line: maximum angular displacement of the follower. Right frame: phase portrait.

were adapted in order to cope with the discontinuous impacting nature of the cam-follower system. The results of such a continuation are reported in Figure 3.8 and were obtained using $\widehat{TC}$, a novel toolbox for AUTO developed by Thota and Dankowicz (see [89, 90] and Chapter 3 for further details). As shown in Table 5.2, the computed multipliers of the periodic orbit along the $P(1,1)$ branch show the occurrence of two smooth bifurcations. In particular at $\omega \approx 135.946$ *rpm*, one real multiplier is observed to cross the point $+1$ indicating the occurrence of a fold bifurcation through which the whole $P(1,1)$ branch originates. Also at $\omega = 151.65$ *rpm*, another real multiplier crosses the unit circle at -1. This confirms that a flip bifurcation is causing the period doubling observed in both the numerical and experimental bifurcation diagrams. This scenario can therefore be fully explained in terms of classical smooth bifurcations similar to those already studied in impact oscillators [40]. An interesting feature shown in Figure 3.8, is the seemingly global bifurcation involving the unstable solution branching from the fold and the chaotic evolution born as a result of the chattering interruption. This explains the abrupt disappearance of that chaotic attractor when $\omega = 154.5$ *rpm*.

We move now to the analysis of *Scenario 1*, which is instead organized by discontinuity-induced bifurcations unique to impacting dynamical systems [33].

Table 5.2 — Eigenvalue evolution across $P(1,1)$ branch computed by using a continuation algorithm

ω value [rpm]	eigenvalue 1	eigenvalue 2
135.946698873817	0.212856564951	0.996008664393
135.946850039257	0.214199564174	0.989769009976
135.947353924057	0.216351137284	0.979943000383
135.949033540057	0.220281698370	0.962513414400
135.951832900057	0.224549930832	0.944309362903
147.941373499943	-0.467436119698 - 0.300839993821i	-0.467436119698 + 0.300839993821i
148.962048199932	-0.521622451717 - 0.214489798539i	-0.521622451717 + 0.214489798539i
150.186857839919	-0.467765740979	-0.703735852712
151.656629407902	-0.353243069838	-0.970265166132
153.420355289483	-0.297944998464	-1.206154145399

5.2.2 Chattering route to chaos

The other scenario detected experimentally and captured by the numerical bifurcation diagram, emerges from the permanent contact solution shown in Figure 5.6. It consists of a branch of $P(\infty, 1)$ solutions undergoing a sudden transition to chaos when $\omega \approx 152.67$ *rpm*. The experimental investigation reported in Chapter 4, strongly suggested that the mechanism causing such a transition is the interruption of a complete chattering sequence. The numerically predicted $P(\infty, 1)$-orbit is shown in Figure 5.7, again in good qualitative agreement with the equivalent experimental time series.

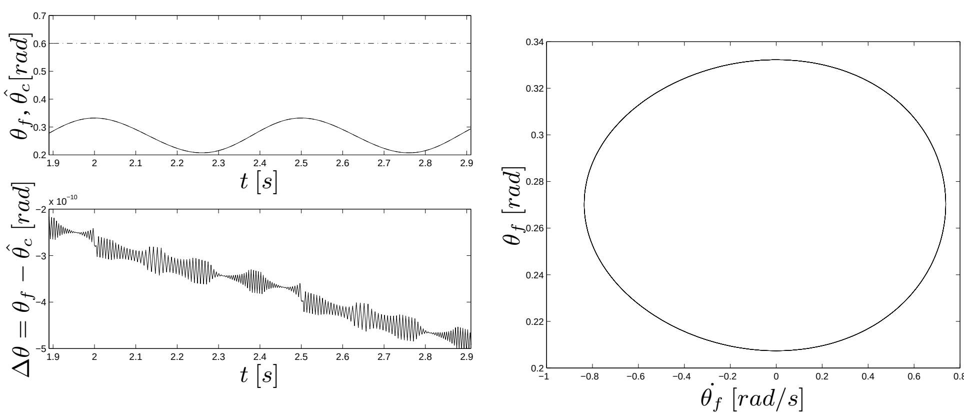

Figure 5.6 — Numerical results. Permanent contact at $\omega = 120$ *rpm*. Left frame: cam and follower trajectories (up) and their corresponding difference $\Delta\theta$ (bottom). Dash-dot line: maximum angular displacement of the follower. Right frame: phase portrait.

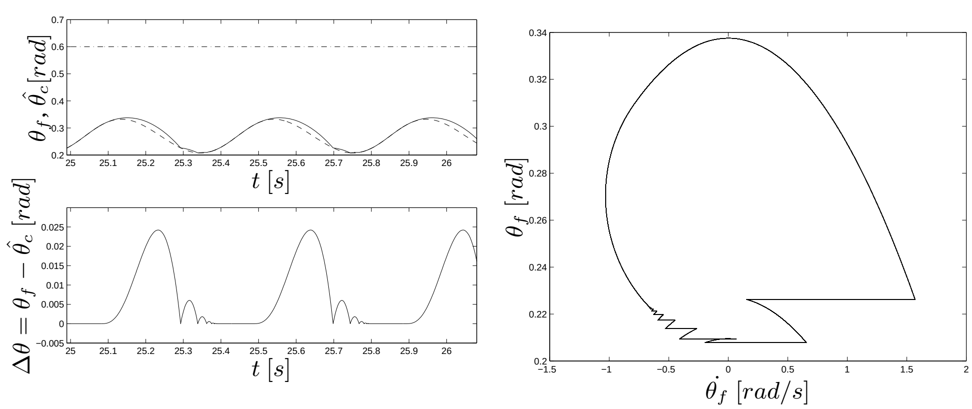

Figure 5.7 — Numerical results. $P(\infty, 1)$ orbit at $\omega = 148$ *rpm*. Left upper frame: cam (dashed) and follower (solid) trajectories and their corresponding difference $\Delta\theta$ at bottom. Dash-dot line: maximum angular displacement of the follower. Right frame: phase portrait.

Careful numerical simulations reported in Figure 5.8 confirm that the interruption of a chattering sequence is indeed the key phenomenon to explain the observed jump to chaos. Further confirmation is provided in Figure 5.9 where the system attractors are plotted before and after the transition to aperiodic regime. As ω is increased through the critical value, we observe the emergence of a fingered attractor – Figure 5.9 (c) – typical of discontinuous dynamical systems often associated to the occurrence of grazing bifurcations. The chaotic time series exhibited by the system when $\omega = 154.1$ *rpm* is shown in Figure 5.10.

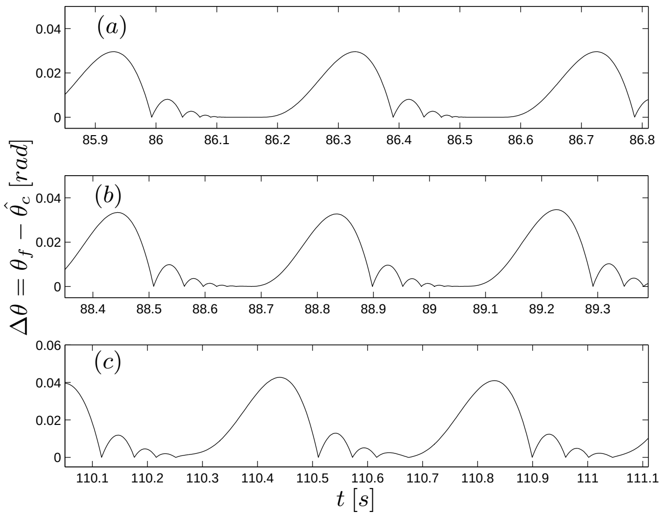

Figure 5.8 — Numerical results. Time evolution for the difference $\Delta\theta$ between cam and follower angles, showing: (a) complete chatter at $\omega = 151$ *rpm*, (b) slightly interrupted chatter at $\omega = 153.5$ *rpm* and (c) highly interrupted chatter at $\omega = 153.9$ *rpm*.

The derivation of the numerical bifurcation diagram close to the transition to chaos shown in Figure 5.11, reveals that a cascade of grazing bifurcations is taking place in a small neighborhood of the transition point. Such intricate cascade cannot be observed experimentally given that it accumulates over an extremely thin range of ω (about 0.003 *rpm*) further below the degree of resolution available experimentally. A more in-depth explanation of this cascade will be presented later in section 5.4 by applying local analysis. At the time being, we first chose to analyze only those phenomena that are relevant over a realistic range of ω. Therefore, we look now at the extremely important issue of understanding how large the regions of asymptotic stability (basins of attraction) are for different coexisting solutions and how these regions evolve under variation of the cam rotational speed ω.

5.3 Coexistence

A fundamental characteristic exhibited numerically and experimentally in the dynamics of the cam-follower system, is the coexistence of different attractors. In particular, by looking at the numerical bifurcation diagram of Figure 5.1, it can be highlighted that:

- for $\omega \in [135, 151]$ *rpm*, the multi-impacting orbits $P(\infty, 1)$ coexists with the periodic motion $P(1, 1)$ characterized by one impact per period;
- for $\omega \in [152, 152.6]$ *rpm*, the $P(\infty, 1)$ orbits coexists with $P(2, 2)$ solutions;
- for $\omega \in [152.6, 154]$ *rpm*, the chaotic motion originated from the interruption of complete chattering sequences coexists with the branch of $P(2, 2)$ orbits.

A more careful Monte Carlo-based bifurcation diagram, in the region $\omega \in [152, 160]$ *rpm*, is reported in Figure 5.12. Here, we see that there are actually three coexisting cascades occurring within this range: the interruption of the chattering sequence and the period-doubling cascades mentioned above together with the period-doubling of a period-three solution, which has not been detected experimentally.

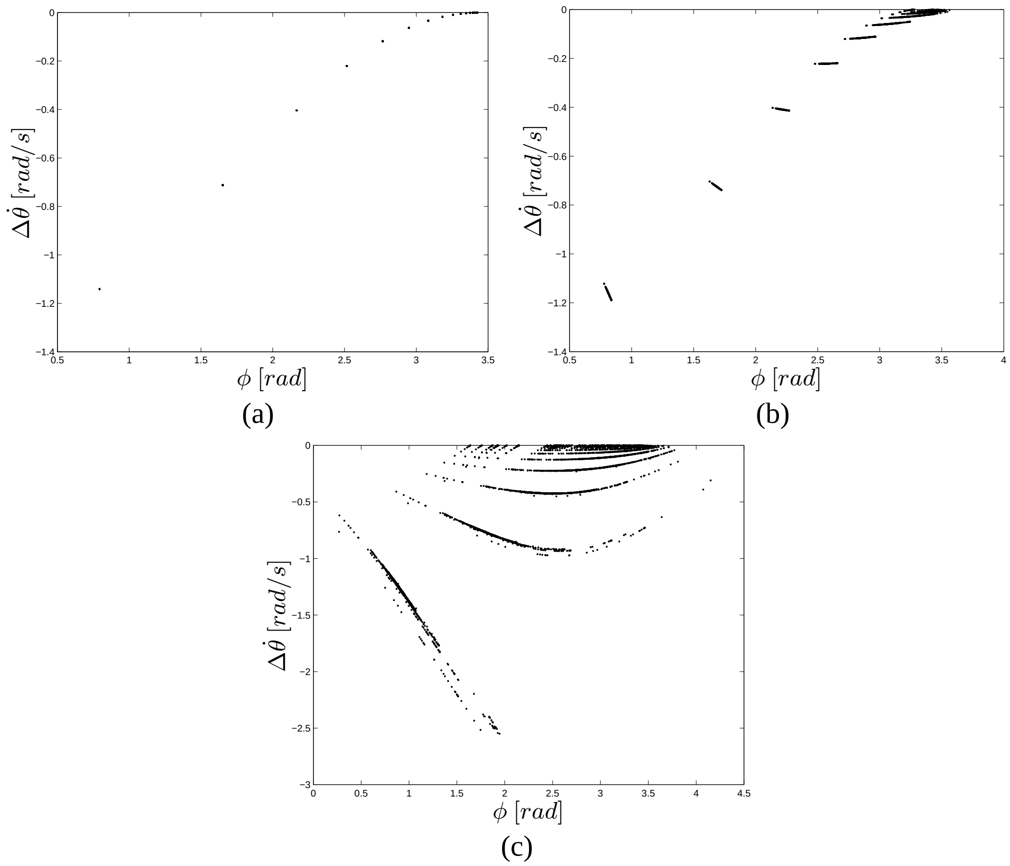

Figure 5.9 — Numerical results: chattering route to chaos. Impact maps showing relative velocity at impacts (vertical axis) vs. impact phase (horizontal axis) along $P(\infty, 1)$ chattering orbits: (a) complete chattering sequence at $\omega = 152.66$ *rpm*; (b) incomplete chattering sequence at $\omega = 152.882$ *rpm*; (c) chaotic impacting orbit at $\omega = 153.45$ *rpm*.

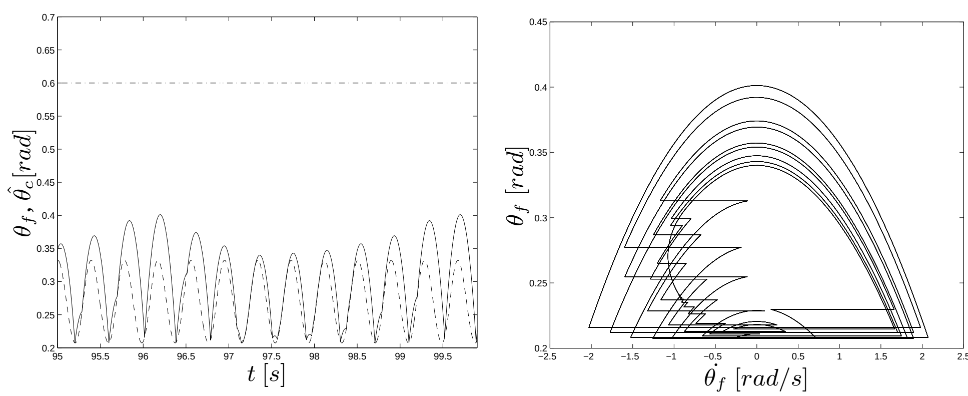

Figure 5.10 — Numerical Results. Chaotic motion at $\omega = 154.1$ *rpm*. Left frame: cam (dashed) and follower (solid) trajectories. Dash-dot line: maximum angular displacement of the follower. Right frame: phase portrait.

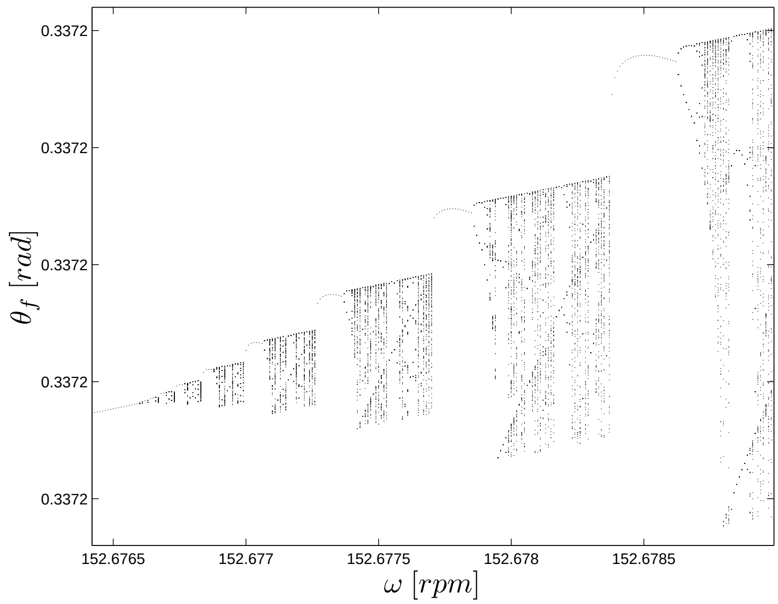

Figure 5.11 — Numerical results: chattering route to chaos. Detailed stroboscopic map close to aperiodicity onset for the multi-impacting orbit. Chain of chaotic windows with periodic frames in between.

5.3.1 Basins of attraction

The simultaneous existence of such different attractors makes the system behaviour dependent on the choice of initial conditions. Basins of attractions (BA) are an invaluable tool to characterize the coexistence and stability of different solutions [67]. A standard numerical method employed to approximate BA in dynamical systems, is the cell mapping method developed by Hsu [47].

Essentially, in the cell-to-cell algorithm the dynamics of the system are described by using a Poincaré map. The region of feasible initial conditions is subdivided into a large number N of small cells. All unfeasible initial conditions are regarded as a small number m of large cells, so-called sink cells. The mapping is applied to each center point (initial condition) and the cell containing the image is then located.

All of the $N + m$ cells point to initial conditions inside one of the other cells, except the sink cells which point to themselves by definition. Starting with cell 1, a sequence of cells is mapped by following the pointers defined by the system flow. This sequence either ends in a sink cell or in a repetitive cycle. This cycle can consist of one self-repeating cell (a fixed point, which could be a sink cell), or a number of cells. The repetitive cycle is identified and all cells in the sequence are labelled as belonging to the basin of attraction of that cycle. Then the procedure is repeated with all N cells. See Figure 5.13 for an illustration of the method. Interested readers are referred to [47] for further details.

Hence, by adapting the cell-to-cell mapping method to the cam-follower system of interest, several basins of attraction were computed for different values of the bifurcation parameter ω. Figure 5.14 shows the basin of attraction of both the period-one coexisting solutions $P(\infty, 1)$ and $P(1, 1)$, reported in Figure 5.15 when $\omega = 145$ *rpm*. We notice that both solutions are associated to well defined basins of attraction, with the $P(\infty, 1)$ orbit belonging to a consistent region of asymptotic stability for low values of initial position and velocity.

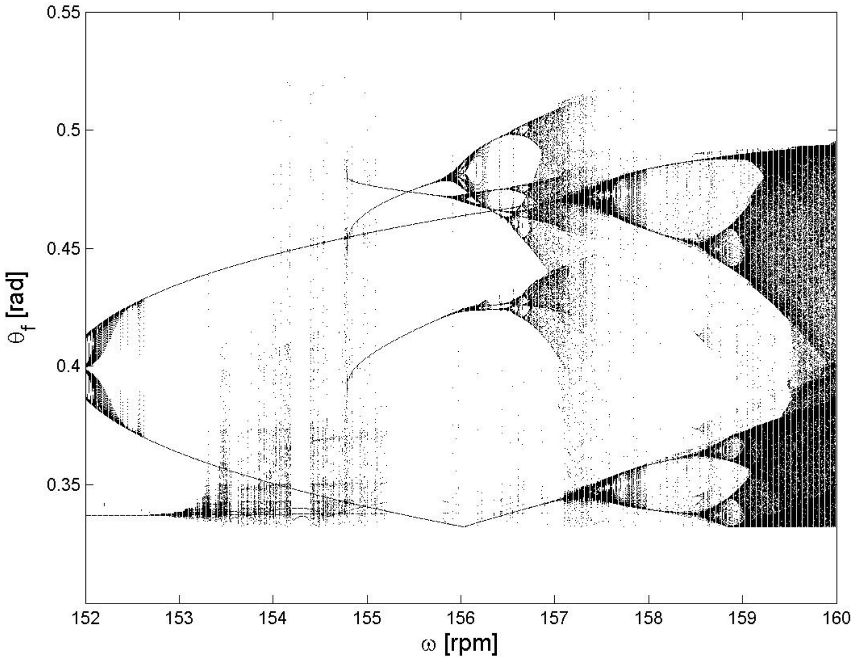

(a)

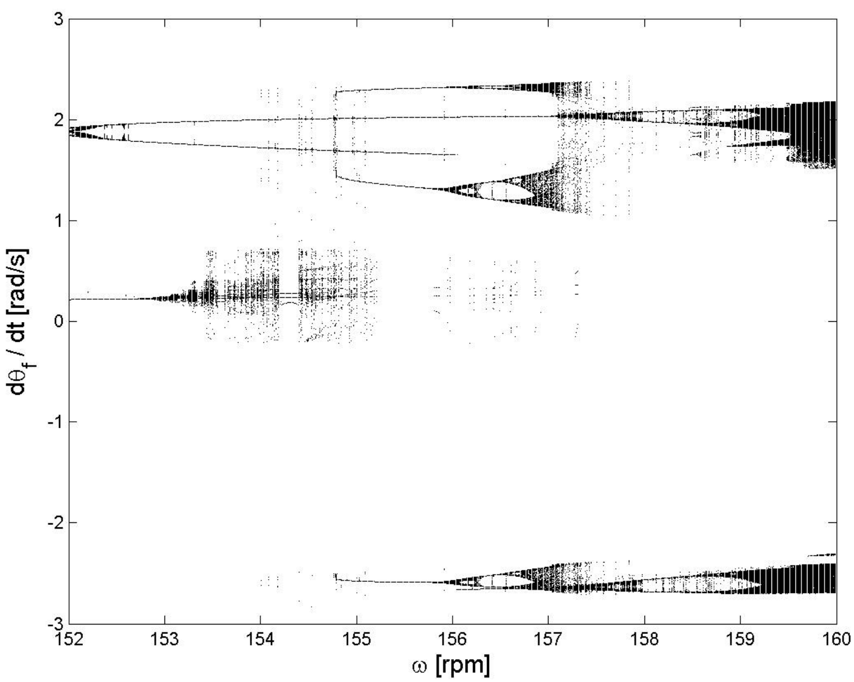

(b)

Figure 5.12 — Monte Carlo bifurcation diagram showing coexistence of solutions. The bifurcation diagram has been obtained by plotting stroboscopic samples of: θ_f in (a) and $\dot{\theta}_f$ in (b), taking the last 50 forcing cycles of 100, for 20 initial conditions distributed uniformly at several parameter values within the range $\omega \in [152, 160]$ *rpm*.

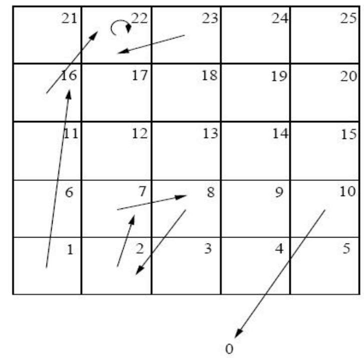

Figure 5.13 — Schematics of a cell mapping method.

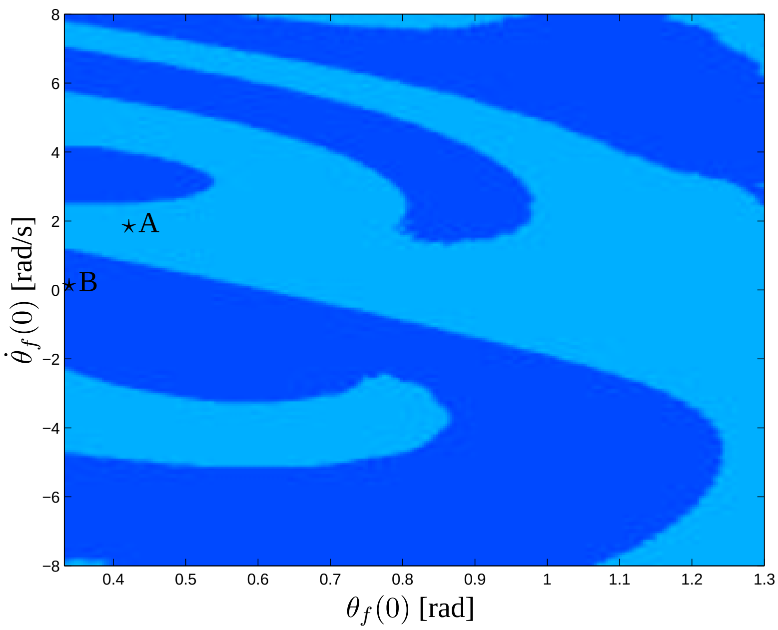

Figure 5.14 — BA of the two period-one coexisting solutions at ω = 145 *rpm*. Blue area correspond to $P(\infty, 1)$ basin, light blue ones to the $P(1, 1)$ basin. The point A label the initial condition $[0.42092, 1.84]^T$, while the point B corresponds to $[0.33704, 0.13333]^T$.

As ω is increased, such coexistence persists with the basin of attraction of the $P(\infty, 1)$ orbit becoming more and more intricate, assuming a clearer fractal structure as can be noticed from Figures 5.16 and 5.18.

In Figure 5.16, we notice the presence of the $P(2, 2)$ solution originating form the flip of the $P(1, 1)$ orbit, as shown in the related time series depicted in Figure 5.17. In Figures 5.18 and 5.19, the fractalization of the basins becomes increasingly clear, with the blue region corresponding now to the basin of the chaotic solution originating from the interruption of the complete chattering sequence.

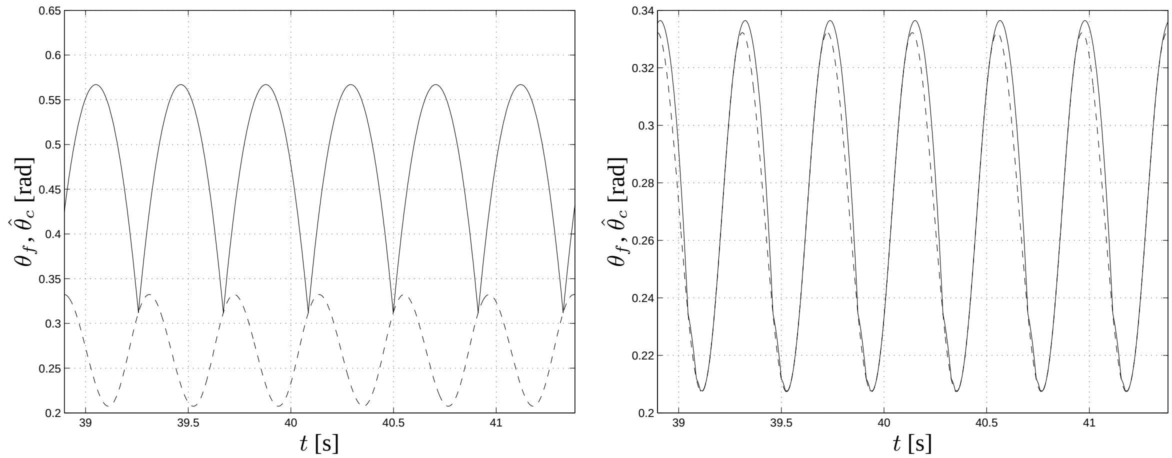

Figure 5.15 — Time series of the follower angular position θ_f corresponding to initial conditions A and B in Figure 5.14. Left frame: $P(1,1)$. Right frame: $P(\infty,1)$.

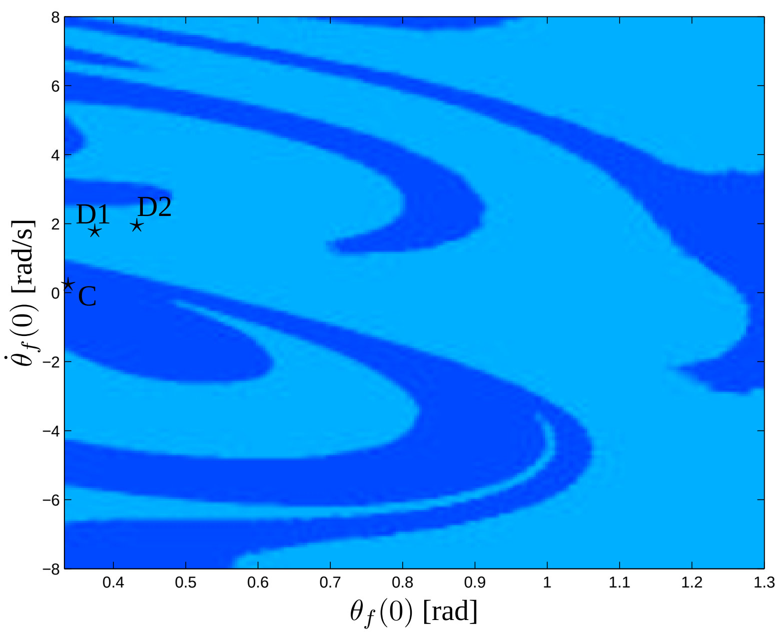

Figure 5.16 — BA of the two period-one coexisting solutions at ω = 152.3 *rpm*. Blue area correspond to $P(\infty,1)$ basin, light blue ones to the $P(2,2)$ basin. The point C label the initial condition $[0.33704, 0.24]^T$, while the points D1 correspond to $[0.37253, 1.7867]^T$ and D2 correspond to $[0.430593, 1.9466]^T$.

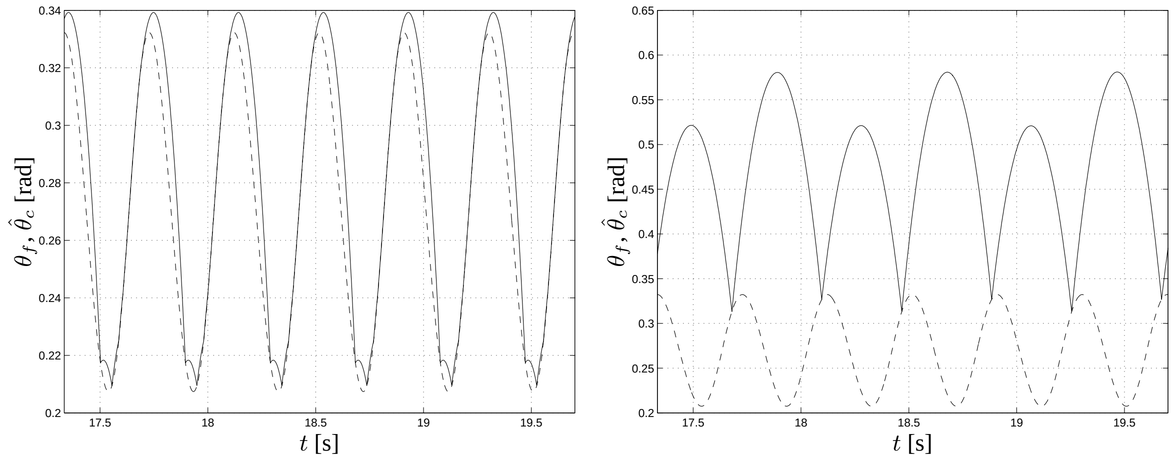

Figure 5.17 — Time series of the follower angular position θ_f corresponding to initial conditions C and D in Figure 5.16. Left frame: $P(\infty, 1)$. Right frame: $P(2, 2)$.

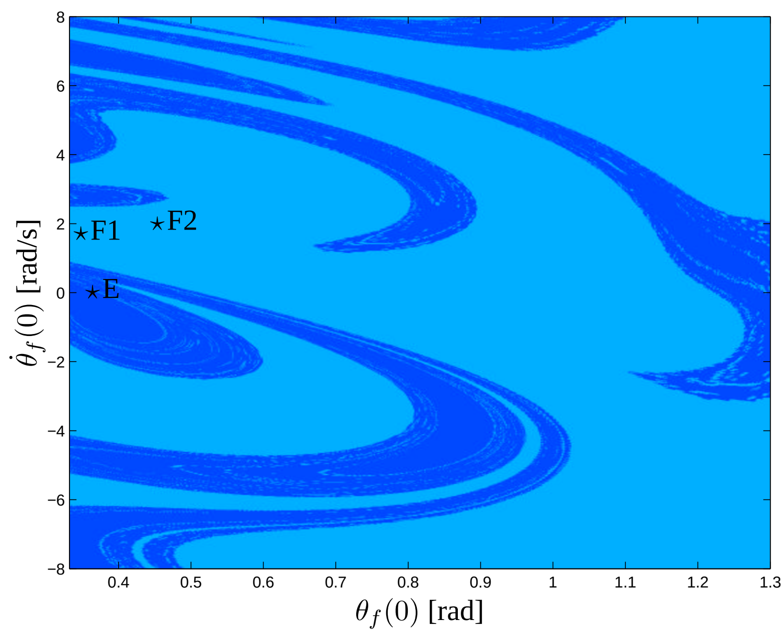

Figure 5.18 — BA of the two period-one coexisting solutions at $\omega = 154.2$ *rpm*. Blue area correspond to the basin of the chaotic regime originated by chattering interruption, light blue ones to the $P(2, 2)$ basin. The time series related to the initial conditions E ($[0.36365, 0.008]^T$) and F1 ($[0.34623, 1.704]^T$) are in Figure 5.19.

At higher values of ω, the basins of attraction now associated to the coexistence of periodic and chaotic attractors, show a high degree of mixing and fractalization. See for example Figure 5.20, obtained by computing the BA at $\omega = 156$ *rpm*. Here, we see the coexistence of the $P(2, 2)$ solution (blue region) with the $P(6, 6)$ solution uncovered in the bifurcation diagram shown in Figure 5.12. Note that the latter solution is associated with a thin basin of attraction (yellow region in Figure 5.20) explaining the fact that it was not detected experimentally. For the sake of completeness we show the BA when $\omega = 160.5$ *rpm* in Figure 5.22. We notice that the regions of initial conditions associated to periodic solutions have become extremely thin or even disappeared. The zoom of the basin at $\omega = 160.5$ *rpm* shown in Figure 5.23, reveals a ring-like structure of the BA which is highly reminiscent of the BA structure for impacting dynamical systems with chattering predicted analytically in the classical paper by Budd $\&$ Dux [22]. This offers further evidence that the interruption of a chattering sequence is undoubtedly at play in causing the sudden transition to chaos which was observed both experimentally and numerically.

5.4 Chattering interruption: local analysis

In Figure 5.1 we see that the solution branch denoted as *Scenario 1*, has a stable period-one solution for $\omega < 152.67$ *rpm* and high-periodic or chaotic motion for $\omega > 152.67$ *rpm*. Thus, it seems like the system has gone through a transition from period-one motion to period-n or chaotic motion, without performing the standard period-doubling route, and this occurred at $\omega \approx 152.67$ *rpm*. In Figure 5.9-(c), a chaotic (fingered) attractor for $\omega = 153.45$ *rpm* was shown, which further indicates a non-standard transition from stable period-one to chaotic motion. The relationship between such sudden transition to chaos and the interruption of chattering motion is suggested by results of Figures 1.3 and 5.24, where a critical value of $\omega \approx 152.67$ *rpm* is detected to cease the occurrence of sticking in the periodic trajectory.

The phenomenon, which is associated with the interruption of complete-chattering sequences, was studied by Budd & Dux [22] [23]. They analyzed what basins of attraction of periodic multi-impacting trajectories with complete chattering look like and how they are stretched due to the large number of low-velocity impacts. Furthermore, the change from periodic to high-periodic or chaotic motion was explained by considering the high sensitivity of the initial conditions for multi-impacting orbits close to this transition.

Given the discontinuous nature of the transition from stable to aperiodic motions, it can be classified as a DIB event. Discontinuity here has two meanings. One is associated to the discontinuous character of the flow, which is reflected in the instantaneous reset applied on the direction of velocity by the impact rule. The other, is related to the impact map, that is a valid discrete representation of an impact oscillator, where a grazing or zero-velocity collision, creates a discontinuity by missing an impact.

It was recently shown by Nordmark [57] that this transition or route to chaos is characterized by a sequence of periodic and chaotic windows that increases in size according to some scaling law. This is shown in Figure 5.11, depicting a zoom-in of a bifurcation diagram about $\omega \approx 152.67$ *rpm*. The periodic and chaotic windows are clearly visible and it seems like the size of the attractor grows according to some scaling law. We will concentrate our effort in approximating the local map associated with the transition from periodic motions with complete chattering to incomplete ones.

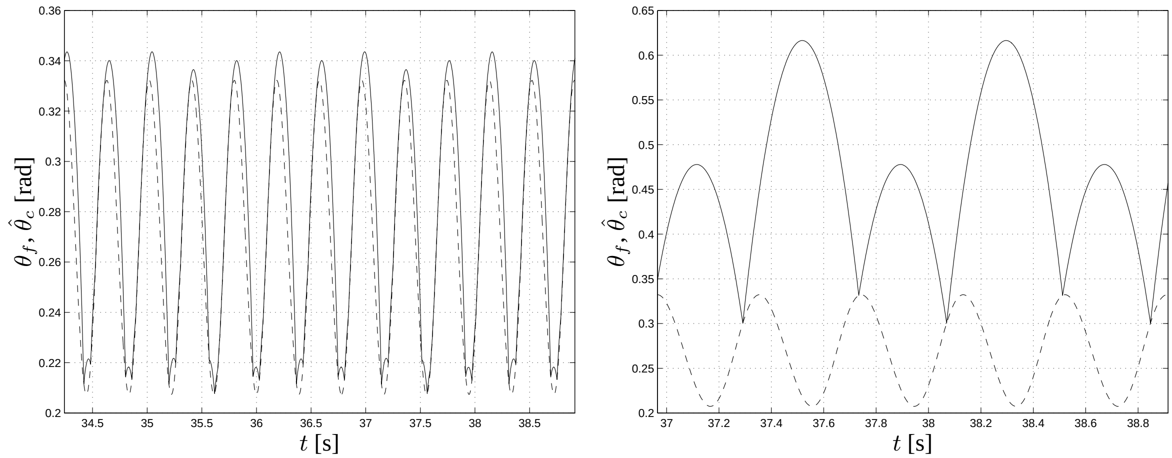

Figure 5.19 — Time series of the follower angular position θ_f corresponding to initial conditions E and F in Figure 5.18. Left frame: chaos. Right frame: $P(2,2)$.

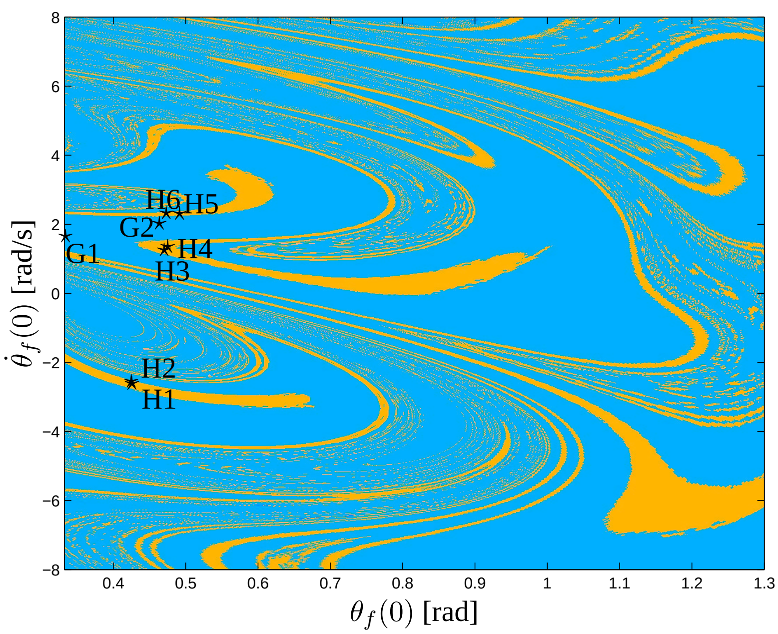

Figure 5.20 — BA at $\omega = 156$ *rpm*. Blue area corresponds to $P(2,2)$ basin, while the orange ones corresponds to higher periodic regimes. As an example, the time series related to the initial conditions G1 ($[0.33268, 1.656]^T$) and H1 ($[0.4226893, -2.552]^T$) are in Figure 5.21.

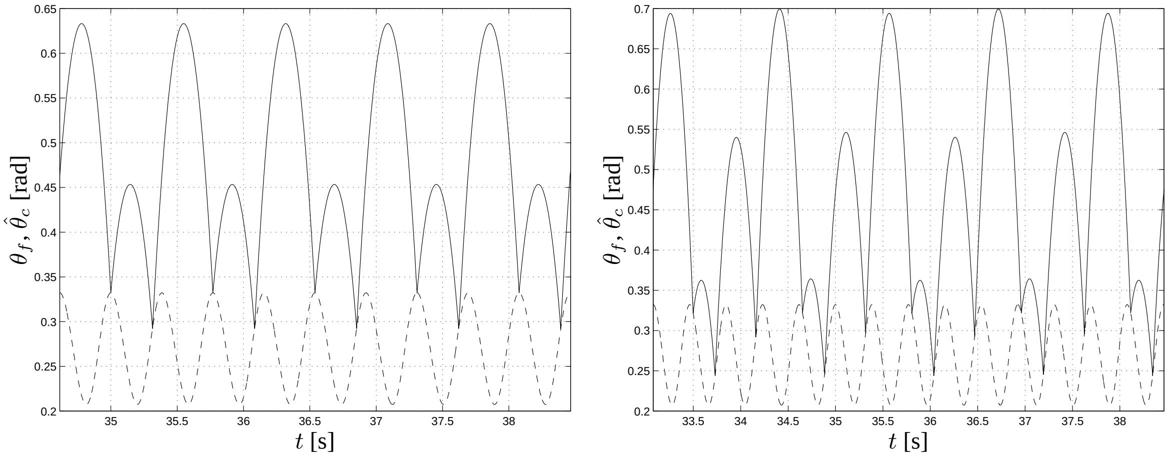

Figure 5.21 — Time series of the follower angular position θ_f corresponding to initial conditions G and H in Figure 5.20. Left frame: $P(2,2)$. Right frame: $P(6,6)$.

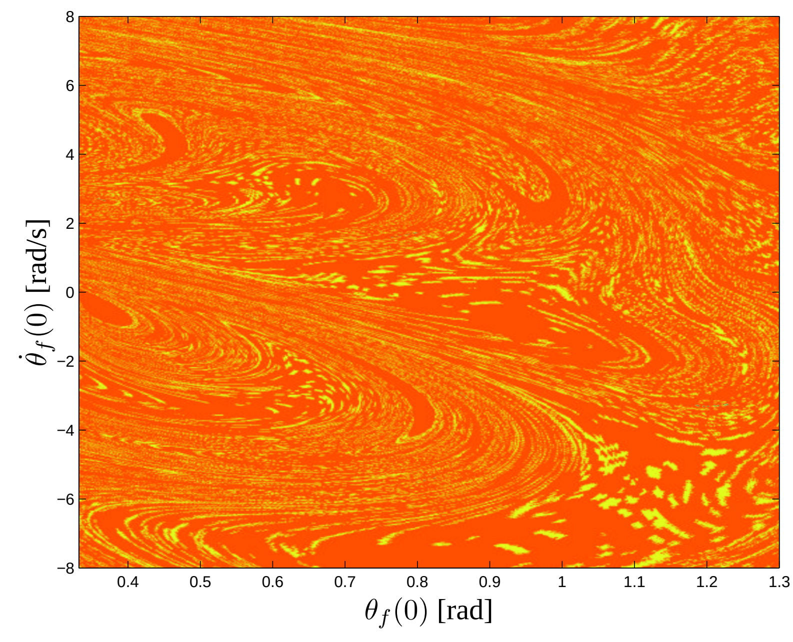

Figure 5.22 — BA at $\omega = 160.5$ *rpm*. The orange area corresponds to the chaotic regimes.

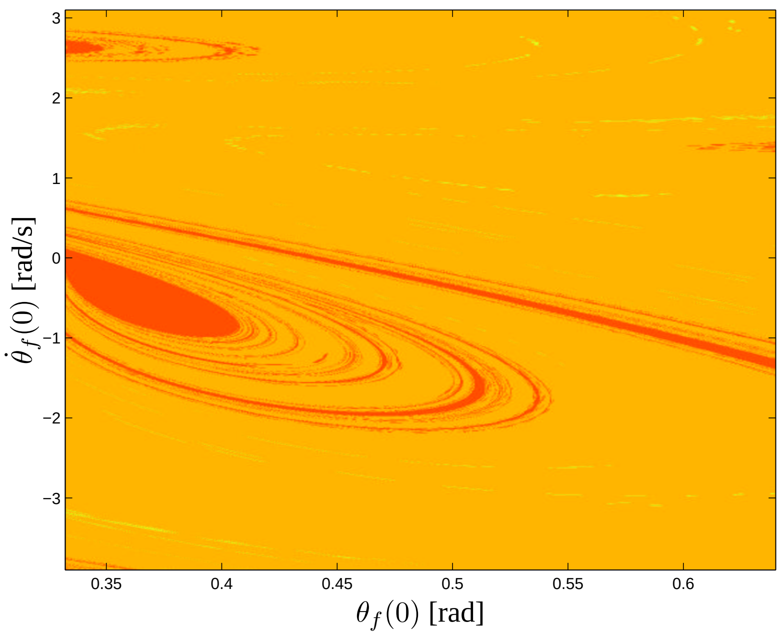

Figure 5.23 — Zoom of the BA at $\omega = 160.5$ *rpm*. The θ_f range is restricted to [0.3, 0.8]; $\dot{\theta}_f$ to [-4, 3.2].

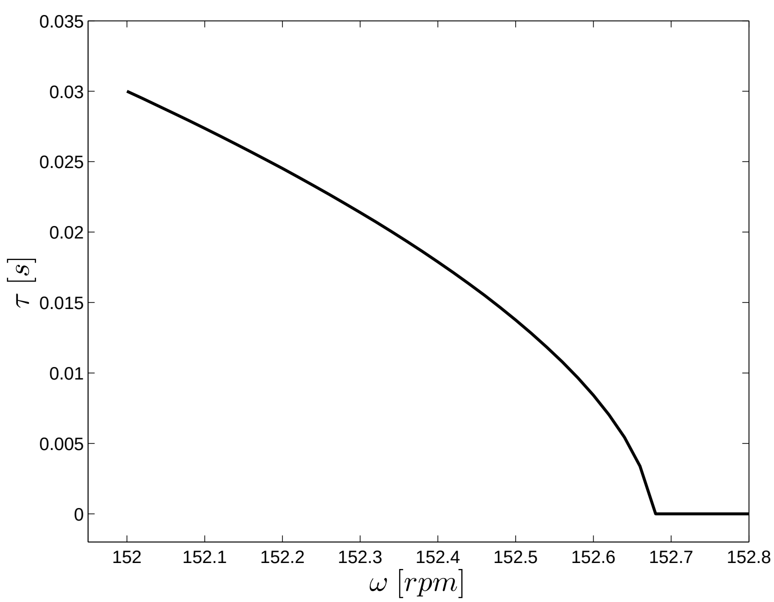

Figure 5.24 — Sticking time τ during each forcing period, as a function of the parameter ω, demonstrating a square-root shape in qualitative changes for system dynamics near the interruption of chattering.

5.4.1 Numerical derivation of the map

In order to get a better understanding of the particular phenomenon experienced by the system across *Scenario 1* (Figure 5.1), a local map in the vicinity of the critical parameter value ($\omega^* = 152.67$ *rpm*) can be approximated in three steps:

1) Define a Poincaré section Σ by

$$\Sigma = \left\{ x \in \mathbb{R}^3 \mid x_3 = \phi_0 \right\}, \tag{5.1}$$

for some ϕ_0. Let

$$x^* = \begin{pmatrix} x_1^* \\ x_2^* \\ x_3^* \end{pmatrix} = \begin{pmatrix} \theta_f^* \\ \dot{\theta}_f^* \\ \omega^* t^* \end{pmatrix}$$

correspond to a periodic orbit such that $x^* \in \Sigma$. Now we can define a map $\Pi(x)$ from Σ to Σ by simulating the system forward over a time $T = 2\pi/\omega^*$, which corresponds to one forcing period.

2) Let

$$\delta = \begin{pmatrix} \delta_\theta \\ \delta_{\dot{\theta}} \\ \delta_\omega \end{pmatrix}$$

and

$$\tilde{x} = \Pi(x^* + \delta),$$

i.e. $\tilde{x}$ is the forward map of a point in the vicinity of x^*.

3) Find a graphical relationship between $x^* + \delta$ and $\tilde{x}$ under the map Σ for all δ in an interval I.

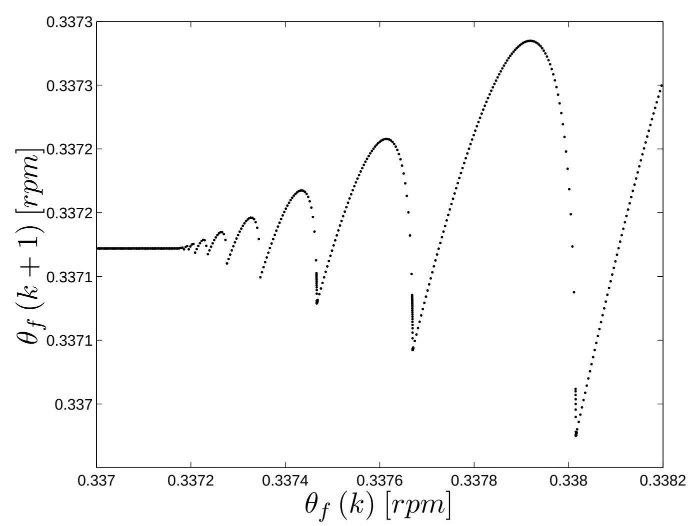

Figure 5.25 — Numerical deviation of local map close to DIB event at $\omega = 152.6$ *rpm*. Horizontal axis depicts current iteration while vertical does for the next iteration mapped. The perturbation δ_θ, corresponds with a percentage of $\theta_f^* = 0.3371\ rad$ equivalent to 1%.

Figure 5.25 depicts the numerically approximated map for $\omega^* = 152.6$ *rpm*, displaying the set of perturbed initial conditions $x^* + \delta$ on the horizontal axis and its mapped image on the vertical one (here $\delta_{\dot{\theta}} = 0$,

$\delta_\omega = 0$). Lobe-shaped features are immediately evident from this graph, which is in accordance with predictions by Nordmark [57].

There is a strong relationship between the repetitive structure of the lobes in Figure 5.25 and the periodic and chaotic windows shown in Figure 5.11. To understand the relationship between the map and the bifurcation diagram, one can study the evolution of fixed points of iterated maps under parameter variation. Basically, a change in a parameter value causes a horizontal translation of the map, see Figure 5.26. Initially only one unstable fixed point, a period-one solution with incomplete chattering, exists (see Figure 5.26-(a)). When a parameter is varied, the identity line becomes tangent to the middle lobe (Figure 5.26-(b)) then two new fixed points are created in a saddle-node bifurcation. When changing the parameter further, three fixed points exist locally, the original unstable one, and two new ones. The next thing that happens as the parameter is varied is that the original fixed point is annihilated in a grazing bifurcation (a DIB) (Figure 5.26-(c)). Further variation of the parameter makes the stable fixed point lose its stability in a period-doubling bifurcation (Figure 5.26-(d)) followed by a period-doubling cascade to chaos. At some point in this process two new fixed points are born in a saddle-node bifurcation, cf. Figure 5.26-(b). As the parameter is varied further the chaotic regime is annihilated where the slope of the map is infinite. This is due to the square-root term that models low-velocity impacts (grazing). Further varying the parameter value, this process is repeated for each lobe, that is increasing in size, and thus the dynamics shown in the bifurcation diagram of Figure 5.11 will follow this sequence.

Next we will try to use the numerically observed structure, to create an approximated analytical expression of the local map.

5.4.2 An approximated analytical mapping

In order to capture and understand the observed bifurcation scenario in Figure 5.11, we will introduce an analytical expression of the map Π that takes all visible features into account. To build the approximate map we will use the numerical results we have so far. The map Π will have the following features:

- To the left (or right) of a critical point on the x-axis, say x_c, the map is represented by a constant value associated with the unique fixed-point of Π, corresponding to the period-one orbit with complete chattering.
- The map $\Pi(x)$ is composed by an infinite sequence of lobes, given by $\Pi_k(x),\ k = 0, 1, \ldots, \infty$, as predicted by Nordmark [57]. The size of each lobe is approximated by a scaling law. For instance, if x_k and x_{k+1} represent the right- and leftmost points, respectively, of the k^{th} lobe and x_{k-1} represents the rightmost point of the $(k-1)^{st}$ lobe then we have

$$\log\left(\frac{x_{k+1} - x_k}{x_k - x_{k-1}}\right) = M. \tag{5.2}$$

  The coefficient M is assumed to be constant and is calculated by linear fitting of pairs of points for successive lobes. A similar estimation is done for $\Pi_k(x)$ to find a coefficient Q, which gives the ”height” of the lobes. For later reference we also define

$$\Delta_x = x_1 - x_0 \quad \text{and} \quad \Delta_\Pi = \Pi(x_1) - \Pi(x_0).$$

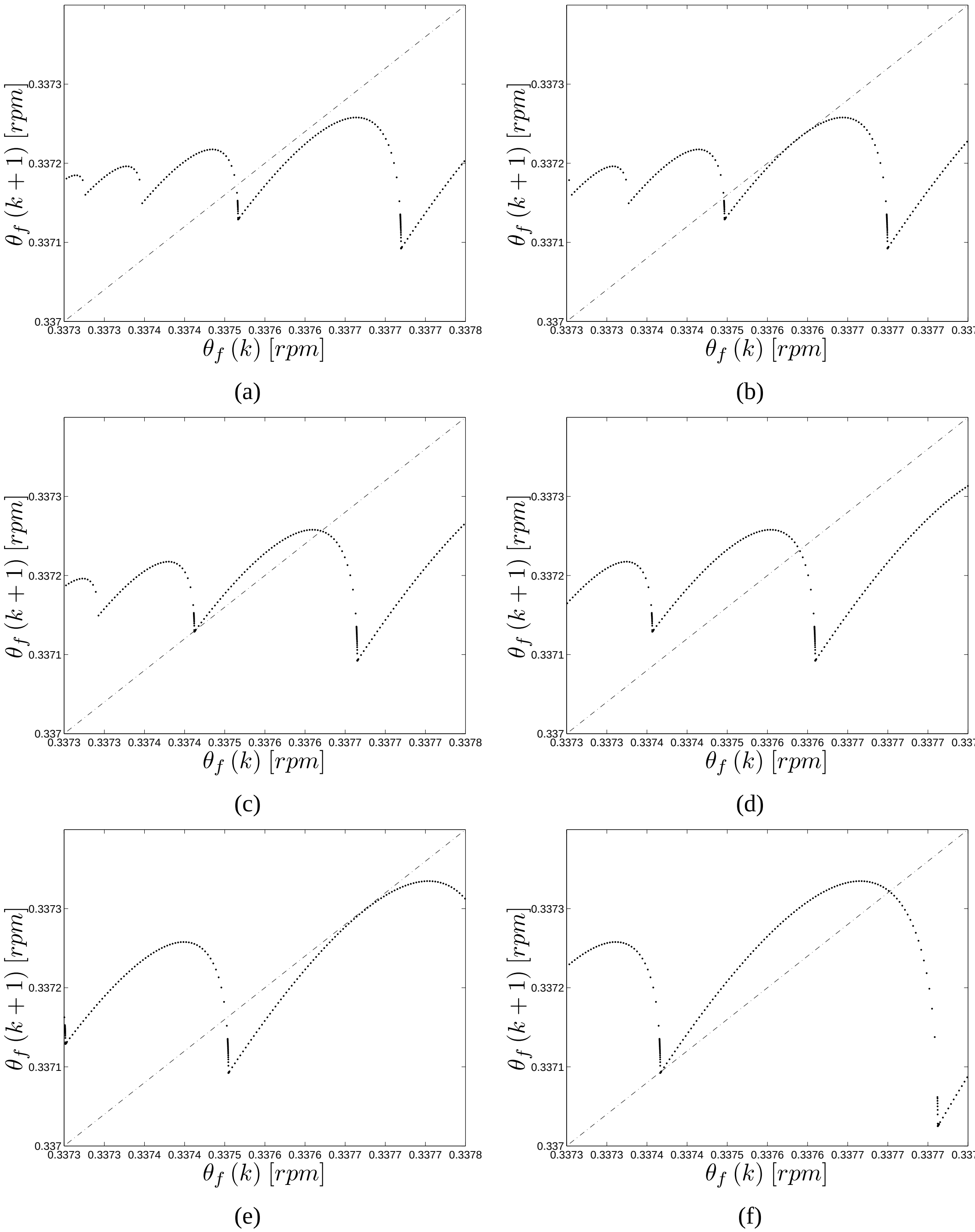

Figure 5.26 — Illustration of main bifurcations of the local map approximation, based on the cobweb diagram principle with dashed trace meaning for the unit-slope tangent line: (a) solution branch in the previous lobe, (b) saddle-node event where a new fixed point is created, (c) annihilation of solution branch in the previous lobe by a border collision event, (d) beginning of a period-doubling sequence followed by a sudden transition to chaos, (e) new saddle-node bifurcation after intersection with a successive lobe and (f) annihilation of chaotic regime at square-root border of the lobe, as in (c).

- Each lobe is approximated by a nth-order polynomial curve of the form

$$p(x) = \sum_{i=0}^{n} c_i x^i + d\sqrt{x_0 - x}, \tag{5.3}$$

  where the square-root term is included to take into account the infinite slope at the right-hand side of each lobe, due to low-velocity (grazing) impacts. The degree of the polynomial, n, depends on the precision required for the numerical approximation. For $n = 3$ we have been able to get an approximation that is accurate enough for the current study. The unknown coefficients c_i and d can be calculated by solving a linear system, so that the left- and rightmost points are correctly placed and the points where the first derivative is $-1, 0$ and 1 have a perfect match.

Following the above procedure, the local mapping $\Pi(x)$ can now be expressed as

$$\Pi(x) = \begin{cases} \Pi_0(x), & x \in [x_1, x_0) = I_0, \\ \Pi_1(x), & x \in [x_2, x_1) = I_1, \\ \quad\vdots & \quad\vdots \\ \Pi_N(x), & x \in [x_{N+1}, x_N) = I_N, \\ \Pi_{N+1}(x), & x \in [x_{N+2}, x_{N+1}) = I_{N+1}, \\ \quad\vdots & \quad\vdots \end{cases} \tag{5.4}$$

where

$$I_j = \{x \in \mathbb{R} \mid x \in [x_j - \beta_j \Delta_x, x_j)\},$$

and

$$\Pi_j(x) = \gamma_j p\left(x_0 + \frac{x - x_j}{\beta_j}\right) + \alpha_j,$$

with $p(x)$ defined as in equation (5.3) and

$$\gamma_j = e^{jQ},\ Q < 0,$$

$$\beta_j = e^{jM},\ M < 0,$$

$$\alpha_j = \Delta_\pi \sum_{k=0}^{j-1} \gamma_k + p(x_0)[1 - \gamma_j],$$

$$x_j = x_0 - \Delta_x \sum_{k=0}^{j-1} \beta_k.$$

In Figure 5.27 a schematic of the map $\Pi(x)$ is shown.

For continuity we must have

$$\lim_{x \to x_{j+1}} \Pi_{j+1}(x) = \Pi_j(x_{j+1}).$$

Also, as a consequence of the square-root term,

$$\lim_{x \to x_j} \frac{d\Pi_j(x)}{dx} = -\infty.$$

Notice further that:

$$\lim_{j\to\infty}\gamma_j = 0 \equiv \gamma_\infty,$$

$$\lim_{j\to\infty}\beta_j = 0 \equiv \beta_\infty,$$

$$\lim_{j\to\infty}\alpha_j = \Delta_\pi \sum_{k=0}^{\infty}\gamma_k + p\left(x_0\right)\left[1-\gamma_\infty\right] = \Delta_\pi\left(\frac{1}{1-e^Q}\right) + p\left(x_0\right) \equiv \alpha_\infty, \tag{5.5}$$

$$\lim_{j\to\infty} x_j = x_0 - \Delta_x \sum_{k=0}^{\infty}\beta_k = x_0 - \Delta_x\left(\frac{1}{1-e^M}\right) \equiv x_\infty,$$

and therefore

$$\Pi\left(x_\infty\right) = \lim_{j\to\infty}\Pi_j\left(x_j\right) = \alpha_\infty.$$

This means that $\Pi(x_\infty) = x_\infty$, which is an expected result given the equilibrium (fixed point) nature of the accumulation point x_∞ in terms of the map Π.

Table 5.3, contains calculated values for Q, M, Δ_π, Δ_x, x_0, the coefficients of $p(x)$ in expression (5.3) and any other constant involved in derivation of the map equation.

It is important to remark the strong influence that the value of the fixed point $x_c \equiv x_\infty$ has for the quantitative agreement on the dynamical features of the system obtained by iterating the equivalent local map (5.4). Therefore by applying the continuation methods described in Chapter 3, an accurate estimation of such fixed point has been found to be $x_c \equiv \theta_f = 0.33717$ *rad*. This value is easily reproduced after evaluation of equation (5.5) with the quantities of Table 5.3.

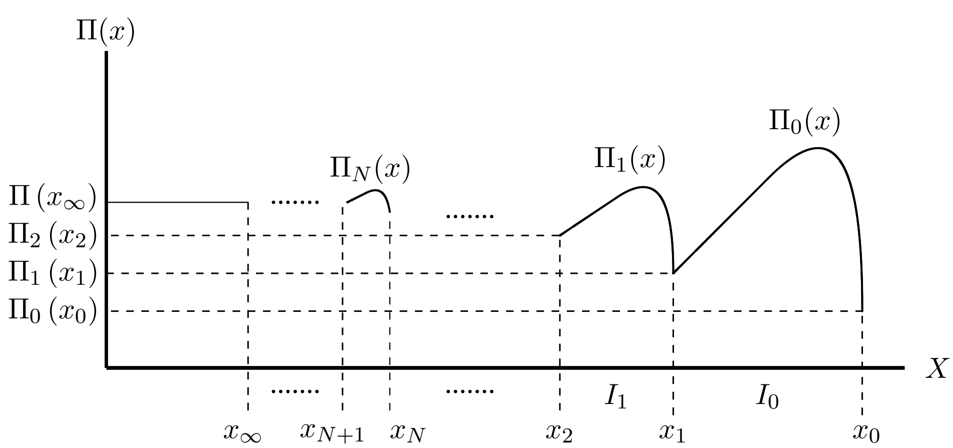

Figure 5.27 — Graphical interpretation of mathematical expressions defining local map at bifurcation of the multi-impacting orbit.

Then, after finding a reliable approximation of the map, its iteration under several parameter values can be used to obtain information about the dynamics of the system. As a result, Figure 5.28 shows fixed points of the iterated map, capturing successfully the qualitative features of Figure 5.11; i.e. showing a cascade of windows of increasing amplitude developing a period-doubling sequence ending with a sudden transition. This is also in accordance with the graphical analysis of Figure 5.26.

Table 5.3 — Values for constants employed in analytic expression of local map at the non-smooth event.

Parameter	Description	Value
Q	scale coefficient on $\pi-$direction	-0.62
M	scale coefficient on $x-$direction	-0.535
Δ_π	$\Pi(x_1) - \Pi(x_0)$	$2.243 * 10^{-4}$
Δ_x	$x_1 - x_0$	$1.022 * 10^{-3}$
c_3 in (5.3)	coefficient of x^3 in polynomial	-44486.71
c_2 in (5.3)	coefficient of x^2 in polynomial	44927.06
c_1 in (5.3)	coefficient of x in polynomial	-15119.51
c_0 in (5.3)	polynomial independent term	1695.91
d in (5.3)	coefficient for square-root term	0.12089
x_0	$X-$ starting point from the left	0.33964
$p\,(x_0)$	$\Pi(x)-$ starting point from below	0.33667
α_∞	critical value at limit	0.33715
x_∞	accumulation point on $x-$axis	0.33717

5.5 Discussion

The results presented in this Chapter, confirmed the validity of the model developed in Chapter 4, by capturing the main dynamical features of the system observed numerically and experimentally. In particular, the coexistence between a traditional period-doubling route to chaos and an abrupt discontinuity-induced event were replicated. Of special interest is then to uncover the novel bifurcation phenomena experienced by the system at *Scenario 1*, associated with the interruption of complete chattering sequences, as demonstrated by the numerical evidence supplied. The local analysis performed numerically, gave a remarkable approximation of the transition exhibited by a multi-impacting period-one orbit, into aperiodic regime, showing a repetitive structure in the local map characterized by square-root singularities. The question to solve now is how to perform a more accurate investigation and classification of the discontinuity-induced bifurcations involved. This can be achieved by applying an analytical treatment, based on series expansion of the motion trajectories near the critical event. This will allow the derivation of a rigorous mathematical expression of the local map. In doing so, some degree of complexity will be added by the realistic character of our model including strong nonlinearities in the flow and a non-transcendental formulation. This will be the main subject of next Chapter.

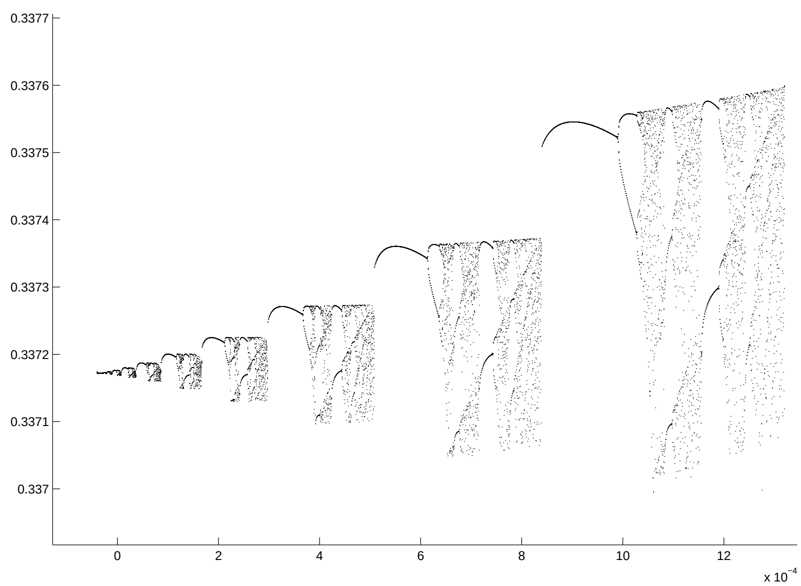

Figure 5.28 — Bifurcation diagram within the sudden transition to chaos after chattering interruption generated by iteration of analytical expression of the local map. The diagram shows qualitative agreement with dynamical features generated by strobing system flow at Figure 5.11.

Chapter 6

Bifurcations involving Chattering in impacting systems

6.1 Introduction

Impacting oscillators experiencing complete chattering motion have been studied first by Budd & Dux [22], who explained the intricate geometry of their basins of attraction with repetitive patterns representing the so-called grazing manifold. A recent derivation, can be also found in [33] (Chapter 6). A remarkable feature detected under such regime is the robustness experienced by the multi-impacting orbits being attracted towards the sticking set.

Chattering and sticking are natural features of motion for periodically forced impact oscillators, just because of the possibility of the forcing to attract the particle into the collision surface. Therefore, it is important to understand how chattering – the infinite number of collisions before stick – and its interruption, can affect the dynamics of such robust motion. In [22], it has also been shown that for trajectories evolving near the boundary of the grazing manifold, the robust trajectory will experience a sudden jump into a chaotic attractor. This was confirmed in [21] by relating the observed aperiodic behaviour with the intermittency generated by a mixture of high-velocity and low-velocity collisions. Furthermore, by isolating the low-velocity collisions it was demonstrated that a one-dimensional discontinuous map is sufficient to describe the properties between a low-velocity impact and the next. When such a low-velocity impact reaches the zero velocity condition, a grazing bifurcation takes place and consequent irregular behaviour is experienced by the system. Grazing bifurcations have been verified to occur often in dynamics of impacts oscillators, from the early predictions of Nordmark [59] till nowadays [101] [73].

Despite its relevance, few contributions have been presented in the literature explaining the possible transitions associated to chattering. Numerical evidence associated with the interruption of chattering in a two-degree-of-freedom impact oscillator can be found in [95], [96] and [97], under the name of “rising bifurcations” but without proofs. On the other hand, one of the few analytical treatments available was done recently by Lenci and Demeio [30], where an asymptotic estimate of the chattering time in multi-impacting motion of an inverted pendulum shows a square-root proportionality with the amplitude of the forcing.

A relevant result is also given by Nordmark and Piiroinen in [58] when approximating a mapping for the accumulation of events at the sticking phase during periodic-chattering motion, developed for simulation purposes. The counterpart of it has been treated in [57], with an analytical formulation for derivation of the local map after chattering interruption in the case of a simplified harmonic oscillator.

The scope of this Chapter, is then to employ and generalize derivations of [57], for the application case of interest; i.e. the cam-follower system. As shown in previous Chapters, the dynamics of the cam-follower model includes a sudden transition to chaos after the interruption of periodic complete-chattering motion. Therefore, the analytical local map will confirm the mechanism under which the system reaches such aperiodic condition, confirming the pattern of translated and scaled lobes obtained by means of the pseudo-analytical approach presented in Chapter 5.

Related results have been discussed in [9] and [8].

6.2 The Chattering phenomenon

Consider the dynamics of a normalized single degree of freedom harmonic oscillator, composed of an undamped-driven mass bouncing against a wall. This can be described as the PWS dynamical system [22] [23]:

$$\begin{aligned} \ddot{x} + x = g(t), &\quad x < \sigma \\ \dot{x} \to -r\dot{x}, &\quad x = \sigma, \end{aligned} \tag{6.1}$$

with $g(t) = cos(\omega t)$ representing an external periodic driving-force, as depicted in Figure 1.1.

As can be noticed, Newton's restitution law with coefficient $0 < r < 1$, is applied over the state each time the mass reaches the boundary $x = \sigma$. This reset map has been proposed to model with sufficient accuracy the transition between collisions of rigid bodies, when working at arbitrary macroscopic scales [18].

By considering that parameters in (6.1) are fixed, there are two main possible long-term modes of oscillation depending on the value assigned to σ:

- an unconstrained mode when $|x\,(t)| < \sigma$, for the which the system is just a pure harmonic oscillator;
- and a constrained mode with collisions when $|x\,(t) - g\,(t)| > \sigma$.

It is the class of oscillations characterized by constrained modes that is particularly interesting in the analysis of systems with impacts. Therefore, in the following we should assume to be working on such a special case. Moreover, the parameter dependence will be focused mainly on the forcing frequency ω (excluding the resonance value $\omega = 1$ rad/s) setting the remaining quantities to constant values. Interested readers are advised to consult [23] for a detailed study of the parameter dependence of (6.1).

6.2.1 Chattering

There is a possibility for the mass hitting the wall of remaining temporarily in contact with the boundary at $x = \sigma$, depending on acceleration conditions. In other words, a positive acceleration of the particle[1] will exert a force pushing the mass towards the surface itself, and then in the absence of impacts the two bodies

[1] Here, the reference for the horizontal axis has been taken as the zero of $g\,(t)$, being consequently positive onto the right. For a different formulation of the problem, the sticking condition can be associated with negative acceleration values.

should stick. In general, this *sticking* condition is reached after dissipation of bouncing amplitudes through an infinite succession of inelastic impacts occurring in finite time, giving rise to what is technically termed as the Zeno phenomenon (already defined in Chapter 2) or *chattering*. See Figure 1.2 for an illustration.

More rigorously, let's consider that the driving force and parameters in (6.1) have been chosen to allow multi-impacting behaviour during a forcing period. Then, if the acceleration of the particle is positive, we have

$$\begin{aligned} &\ddot{x}(t) + x(t) = g(t) \\ &\Rightarrow \ddot{x}(t) = g(t) - x(t) > 0 \Rightarrow g(t) > x(t); \end{aligned} \tag{6.2}$$

i.e. $g(t) > x(t) = \sigma$ under constrained motion. This latter condition generates a boundary condition for the existence of sticking, that can be easily expressed by introducing a new variable $\phi \equiv mod\,(t, T)$ with $T = 2\pi/\omega$, taking advantage of the periodic character of the forcing. Therefore, according to (6.2) it is possible to define the sticking set $\mathcal{Z}$, including the phase values from which the particle will be attracted towards the surface along one forcing period as:

$$\begin{aligned} &g\,(t) \equiv g\,(\phi) = \cos\left(\omega\phi\right) > \sigma \\ &\Rightarrow \mathcal{Z} = \{(x, \dot{x}, \phi) : x = \sigma; \dot{x} = 0; \cos\left(\omega\phi\right) \geq \sigma\} \equiv \left(\sigma, 0, [0, \phi_\alpha] \cup [\phi_\beta, T]\right). \end{aligned} \tag{6.3}$$

In particular, setting $\sigma = 0$ we have:

$$\mathcal{Z} = \{(x, \dot{x}, \phi) : x = 0; \dot{x} = 0; \cos\left(\omega\phi\right) \geq 0\} = \left(0, 0, \left[0, \frac{T}{4}\right] \cup \left[\frac{3T}{4}, T\right]\right). \tag{6.4}$$

The term ϕ_α acquires a great relevance, given that it represents the boundary where the sticking condition vanishes. In the following, ϕ_α will be refereed as the "releasing" phase.

Then, by starting from an impact at $\phi = \phi_0$ that occurs with non-null velocity v_0, the particle will be pushed instantaneously away from the boundary, following the trajectory:

$$\begin{aligned} &x\,(\phi - \phi_0) = \left(\tfrac{1}{1-\omega^2}\right)\cos\left(\omega\left[\phi - \phi_0\right]\right) + \left(x_0 - \tfrac{1}{1-\omega^2}\cos\left(\omega\phi_0\right)\right)\cos\left(\phi - \phi_0\right) + \\ &+ \left[-rv_0 + \tfrac{\omega}{1-\omega^2}\sin\left(\omega\phi_0\right)\right]\sin\left(\phi - \phi_0\right), \end{aligned} \tag{6.5}$$

which is the solution of the unconstrained motion of (6.1), with $x_0 = x\,(0) = \sigma$ and $\frac{dx}{d\phi}\Big|_{\phi=\phi_0} \equiv -rv_0$.

Under the assumption of positive acceleration, the particle will hit back the surface at a given phase $\phi = \phi_1 > \phi_0 \in \mathcal{Z}$, satisfying:

$$\begin{aligned} &x\,(\phi_1 - \phi_0) = \sigma = \left(\tfrac{1}{1-\omega^2}\right)\cos\left(\omega\left[\phi_1 - \phi_0\right]\right) + \left(\sigma - \tfrac{1}{1-\omega^2}\cos\left(\omega\phi_0\right)\right)\cos\left(\phi_1 - \phi_0\right) + \\ &+ \left[-rv_0 + \tfrac{\omega}{1-\omega^2}\sin\left(\omega\phi_0\right)\right]\sin\left(\phi_1 - \phi_0\right). \end{aligned} \tag{6.6}$$

The motion then restarts from ϕ_1 till the next impact at some $\phi = \phi_2$, after updating the mass velocity according to the restitution law. Iterations will then continue infinitely between successive impacts, whenever (6.2) holds. During each collision, the particle dissipates energy by reduction in the starting velocity and consequently the amplitude of the bouncing and flight times will decrease, accumulating into a single point of the set $\mathcal{Z}$ where the two bodies finally stick together, as in Figure 1.2. The sticking regime will be maintained until the acceleration becomes negative at $\phi = \phi_\alpha$, when the particle is released again. This describes qualitatively an orbit with complete chattering.

6.2.2 Impact map

As the dynamics of system (6.1) is closely related with the collision condition, we can construct an equivalent discrete representation of the motion by evolving (6.6) through impacts.

Consequently, following [22] let's consider the low-order series expansion of the trajectory around ϕ_0, where a low-velocity impact under positive acceleration is expected to occur. Then, after defining $\Lambda = \phi - \phi_0$, equation (6.6) can be written as:

$$\begin{aligned} &x(\phi - \phi_0) \equiv x(\Lambda) = x|_{\phi=\phi_0} + \left.\tfrac{dx}{d\phi}\right|_{\phi=\phi_0}(\phi-\phi_0) + \tfrac{1}{2}\left.\tfrac{d^2x}{d\phi^2}\right|_{\phi=\phi_0}(\phi-\phi_0)^2 + \mathcal{O}\left((\phi-\phi_0)^3\right) \\ &\equiv x|_{\phi=\phi_0} + \left.\tfrac{dx}{d\phi}\right|_{\phi=\phi_0}\Lambda + \tfrac{1}{2}\left.\tfrac{d^2x}{d\phi^2}\right|_{\phi=\phi_0}\Lambda^2 + \mathcal{O}\left(\Lambda^3\right). \end{aligned} \tag{6.7}$$

If Λ is small enough, a parabolic approximation for the trajectory is admissible, and then, the next collision phase $\phi = \phi_1$ can be estimated by using the condition:

$$\begin{aligned} &x(\phi_1 - \phi_0) = \sigma \approx x|_{\phi=\phi_0} + \left.\tfrac{dx}{d\phi}\right|_{\phi=\phi_0}(\phi_1-\phi_0) + \tfrac{1}{2}\left.\tfrac{d^2x}{d\phi^2}\right|_{\phi=\phi_0}(\phi_1-\phi_0)^2 \\ &\equiv \sigma - rv_0\Lambda + \tfrac{a_0}{2}\Lambda^2 \Rightarrow \tfrac{a_0}{2}\Lambda^2 - rv_0\Lambda = 0, \end{aligned} \tag{6.8}$$

with v_0 and a_0 representing respectively, the velocity and acceleration of the particle at the collision phase ϕ_0.

Solving (6.8) for Λ, we get $\Lambda = 0$ or $\Lambda = 2r\frac{v_0}{a_0}$; i.e. $\phi_1 = \phi_0$ or $\phi_1 = \phi_0 + 2r\frac{v_0}{a_0}$.

Analogously, from the velocity expression, we get:

$$\begin{aligned} &\dot{x}(\phi_1 - \phi_0) = v_1 \equiv \left.\tfrac{dx}{d\phi}\right|_{\phi=\phi_0} + \left.\tfrac{d^2x}{d\phi^2}\right|_{\phi=\phi_0}(\phi_1-\phi_0) + \mathcal{O}\left((\phi_1-\phi_0)^2\right) \\ &\equiv -rv_0 + a_0\Lambda + \mathcal{O}\left(\Lambda^2\right) \approx -rv_0 + a_0\Lambda = -rv_0 + a_0\left(\tfrac{2rv_0}{a_0}\right) = rv_0. \end{aligned} \tag{6.9}$$

Expressions (6.8) and (6.9) constitute a single-return map P_I between consecutive impacts, that can be formalized as:

$$\begin{bmatrix} \phi \\ v \end{bmatrix}_{k+1} = P_I\left(\begin{bmatrix} \phi \\ v \end{bmatrix}_k\right) \triangleq \begin{bmatrix} \phi \\ v \end{bmatrix}_{k+1} = \begin{bmatrix} 1 & \frac{2r}{a_k} \\ 0 & r \end{bmatrix}\begin{bmatrix} \phi \\ v \end{bmatrix}_k. \tag{6.10}$$

The map (6.10) is valid in a strictly local sense and under the assumption of positive acceleration. Hence by starting at a phase value belonging to $\mathcal{Z}$, an infinite set of low-velocity collisions (iterations of (6.10)) is expected to converge onto the fixed point $(\phi_\infty, 0)$, i.e. the particle eventually will reach the sticking condition after performing a complete chattering sequence. This can be easily computed from (6.10) by noticing that

$$\phi_{k+1} = \phi_k + \frac{2r}{a_k}v_k \equiv \phi_k + \frac{2}{a_k}v_{k+1}.$$

Then, after n iterations of (6.10) from a given initial condition (ϕ_0, v_0) the mapped coordinates become:

$$\begin{pmatrix} \phi_n \\ v_n \end{pmatrix} = \begin{pmatrix} \phi_{n-1} + \frac{2}{a_{n-1}}v_n \\ r^n v_0 \end{pmatrix}.$$

Hence, in the limit

$$\lim_{n\to\infty}\begin{pmatrix}\phi_n\\ v_n\end{pmatrix}=\lim_{n\to\infty}\begin{pmatrix}\phi_{n-1}+\frac{2}{a_{n-1}}v_n\\ r^n v_0\end{pmatrix},$$

this can be reduced to

$$\lim_{n\to\infty}\begin{pmatrix}\phi_{n-1}\\ 0\end{pmatrix}\triangleq\begin{pmatrix}\phi_\infty\\ 0\end{pmatrix},$$

given that $0<r<1$ and therefore $v_n\to 0$ for a large n.

This last remark reflects the stability of the chattering regime, associated to a wide range of initial conditions leading to the sticking condition. In other words, a fixed point of (6.10) obtained under complete chattering regime, should necessarily belong to $\mathcal{Z}$, given that in the absence of impacts the velocity of the particle is null, and then the particle sticks. For a complete determination of the set of values leading to complete chattering in the system (6.1), see [22].

The structural stability of the trajectory can be dramatically modified for $\phi_\infty\to\phi_\alpha$, given that in the limiting case the last impact occurs with zero velocity at the releasing point, leading to a non-transversal collision or graze. It is well known that grazing constitutes the main mechanism for losing stability in impact oscillators [59] and, consequently, the map governing the dynamics close to the boundary of a complete chattering motion contains the mechanism for the transition to aperiodic behaviour. For additional considerations on grazing, transversality conditions and motion of impacting trajectories see section 2.4.

Budd et al [23], performed an estimation of the Jacobian of the impact map P_I, directly from (6.6):

$$J_{P_I}=\begin{bmatrix}\frac{\partial\phi_1}{\partial\phi_0} & \frac{\partial\phi_1}{\partial v_0}\\ \frac{\partial v_1}{\partial\phi_0} & \frac{\partial v_1}{\partial v_0}\end{bmatrix}\Rightarrow|J_{P_I}|=r^2\frac{v_0}{v_1}, \tag{6.11}$$

with:

$$\begin{gathered}\frac{\partial\phi_1}{\partial\phi_0}=\frac{1}{v_1}\left.\frac{\partial x}{\partial\phi_0}\right|_{x=\sigma}, \qquad \frac{\partial\phi_1}{\partial v_0}=-\frac{1}{v_1}\left.\frac{\partial x}{\partial v_0}\right|_{x=\sigma},\\ \frac{\partial v_1}{\partial\phi_0}=\left.\frac{\partial v}{\partial\phi_0}\right|_{\phi=\phi_1}+\left.\frac{d^2x}{d\phi^2}\right|_{x=\sigma}\frac{\partial\phi_1}{\partial\phi_0}, \quad \frac{\partial v_1}{\partial v_0}=\left.\frac{\partial v}{\partial v_0}\right|_{\phi=\phi_1}+\left.\frac{d^2x}{d\phi^2}\right|_{x=\sigma}\frac{\partial\phi_1}{\partial v_0},\end{gathered} \tag{6.12}$$

showing the singularity of the map when predicting an impact with zero velocity. Obviously, this result should have a counterpart in the local result given by expression (6.10) developed under the assumption of positive acceleration. In such a case the singularity is verified for $a_k=0$, being the only possible way for an impact with zero velocity to occur during a complete chattering motion. This confirms that the qualitative behaviour of the multi-impacting trajectory is associated to the stretching in the state-space derived from the dissipative effect of impacts, inducing certain boundaries on the state-space where the map should be reformulated.

6.2.3 Local unidimensionality of map

The impact map (6.10), constitutes a continuous discrete representation of the discontinuous dynamical system (6.1). Nevertheless, as shown in (6.11), under impacts of null velocity the smoothness of the map can be lost. This includes a discontinuity of the map associated with the possibility of missing an impact. Then, following an analogous treatment as in [21], Figure 6.1 depicts this situation in a sequential way.

It shows a trajectory (A) that experiences a low-velocity collision, a one footed in (B) that experiences a zero-velocity impact and one eventually missing the collision in (C).

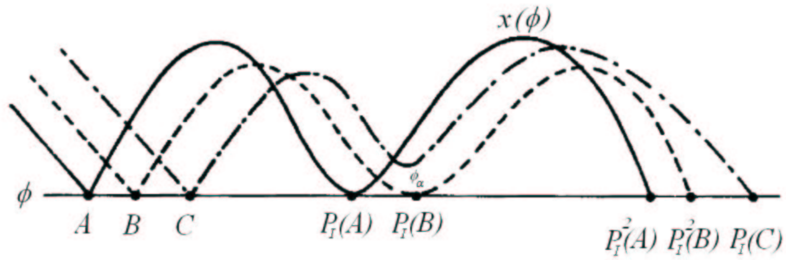

Figure 6.1 — Impacting trajectory depicting the situation where an impact is missed, reproduced from [23].

It is then convenient to define at this point, the set of coordinates (ϕ, v) say $\mathcal{S}^1$, leading to a zero-velocity collision at the releasing phase, after mapping once through P_I:

$$\mathcal{S}^1 = \{(\phi, v) : P_I(\phi, v) = (\phi_\alpha, 0)\}, \tag{6.13}$$

that in the following will be referenced as the discontinuity set of the map (6.10). Consequently $B \in \mathcal{S}^1$ in Figure 6.1. The set $\mathcal{S}^1$ can be alternatively defined as the pre-image of the point $(\phi_\alpha, 0)$ through P_I; i.e. $\mathcal{S}^1 \equiv P_I^{-1}(\phi_\alpha, 0)$.

Equivalently, the dual of $\mathcal{S}^1$ or the images of $(\phi_\alpha, 0)$ through P_I, can be also defined as:

$$\mathcal{W}^1 = \{(\phi, v) : (\phi, v) = P_I(\phi_\alpha, 0)\}, \tag{6.14}$$

with further iterated versions of both:

$$\begin{aligned} \mathcal{S}^n &= P_I^{-n}(\phi_\alpha, 0); \\ \mathcal{W}^n &= P_I^{n}(\phi_\alpha, 0), \end{aligned} \tag{6.15}$$

from which $\mathcal{W}^1 \equiv P_I^2\left(\mathcal{S}^1\right)$.

The sets $\mathcal{S}^n$ and $\mathcal{W}^n$ delimit the loci on the state-space for points of a multi-impacting trajectory including a zero velocity impact. In other words, the sets $\mathcal{S}^n$ and $\mathcal{W}^n$ constitute the grazing manifold $\mathcal{G}$, i.e:

$$\mathcal{G} = \bigcup_{i=0}^{n} \mathcal{S}^i \quad \cup \quad \bigcup_{j=0}^{n} \mathcal{W}^j. \tag{6.16}$$

In particular, $\mathcal{G}$ represents a fundamental structure affecting the dynamics at a global level. This can be demonstrated by analyzing the intricate structure of the associated basins of attraction for systems experiencing chattering, as shown in Chapter 5. Moreover, in [33] an alternative formulation of $\mathcal{G}$ has been done by taking stroboscopic samples of a trajectory with grazing, traced backwards in time. Such an approach,

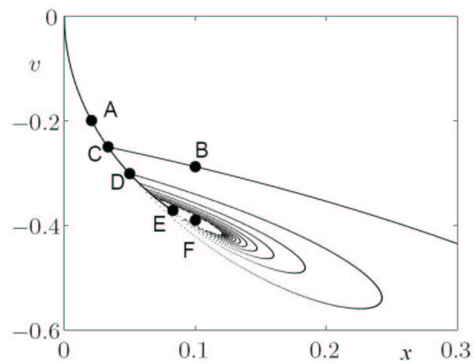

Figure 6.2 — Fundamental structure of the grazing manifold G, reproduced from [33].

employs different choices of an initial point corresponding to a zero velocity impact for phase values outside $\mathcal{Z}$. Intersections with an appropriately chosen Poincaré section are then plotted as shown in Figure 6.2. There, an inner-looped structure is evident, differentiating trajectories by the number of collisions, and most remarkably, converging all into a fundamental branch where a new collision is created (or equivalently destroyed) by a graze.

Figure 6.3 includes detailed time series for labelled points of Figure 6.2, when the Poincaré surface is located at $\phi = t = 0$. Here, label A represents an orbit with no impacts and one graze; B an orbit with an impact and a graze; C an intersection point where a new collision in the orbit is created by a graze; D a trajectory close to C with an additional impact; E the special case where the starting point belongs to $\mathcal{Z}$ with consequently sticking and F where infinite collisions take place during a complete chattering sequence.

Analogously, Figure 6.4 shows the incidence of that single structure at a more global level, by flowing backwards 5 forcing periods. From here, it is evident the complex structure derived for coexisting solutions that creates a strong sensitivity on initial conditions, affecting the overall dynamical scenario.

As chattering is a local phenomenon, we will restrict ourselves to work in a vicinity of the boundary of $\mathcal{Z}$ represented by F in Figure 6.3. It has been demonstrated by Budd and Dux [22] that in the limit:

$$\mathcal{C} = \lim_{n\to\infty} \mathcal{S}^n, \tag{6.17}$$

the set $\mathcal{S}^n$ constitutes an invariant region under the action of the map P_I, or equivalently $P_I(\mathcal{C}) = \mathcal{C}$, and consequently any trajectory starting from a point belonging to $\mathcal{C}$ will necessarily experience complete chattering with a final coordinate $(\phi_\alpha, 0)$. Furthermore, the sets $\mathcal{S}^n$ accumulate as parabolas in a vicinity of $\mathcal{C}$, reducing the map P_I into an equivalently scalar function $f(\lambda)$, with the argument λ parameterizing the set of curves given by:

$$\mathcal{T}_\lambda = \left\{ (\phi, v) : v = \omega\lambda \left(\phi_\alpha - \phi\right)^2 \right\}. \tag{6.18}$$

For the specific case of system (6.1), the function f takes the form:

$$f(\lambda) = \frac{\left[-r\lambda + \sin\left(\omega\phi_\alpha\right) s - \frac{1}{2}\sin\left(\omega\phi_\alpha\right) s^2\right]}{\left(1-s\right)^2}, \tag{6.19}$$

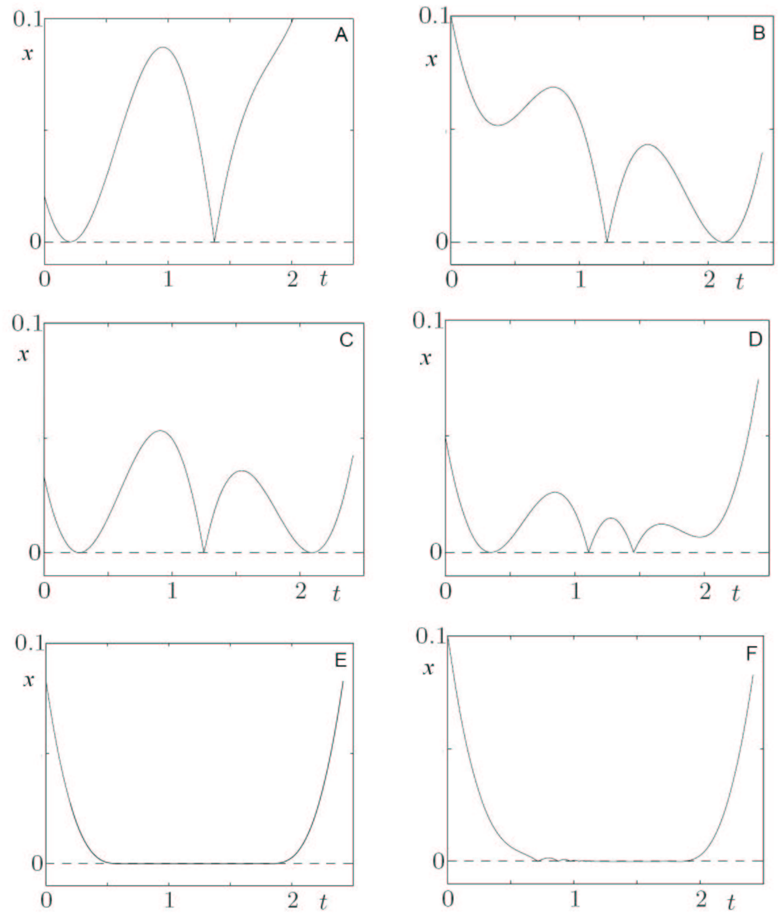

Figure 6.3 — Time series resembling selected points of Figure 6.2, reproduced from [33].

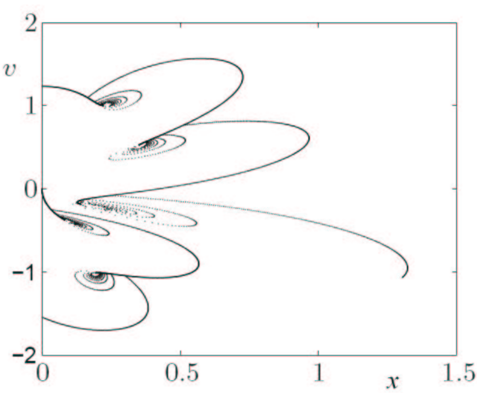

Figure 6.4 — Global portrait of the grazing manifold G, reproduced from [33].

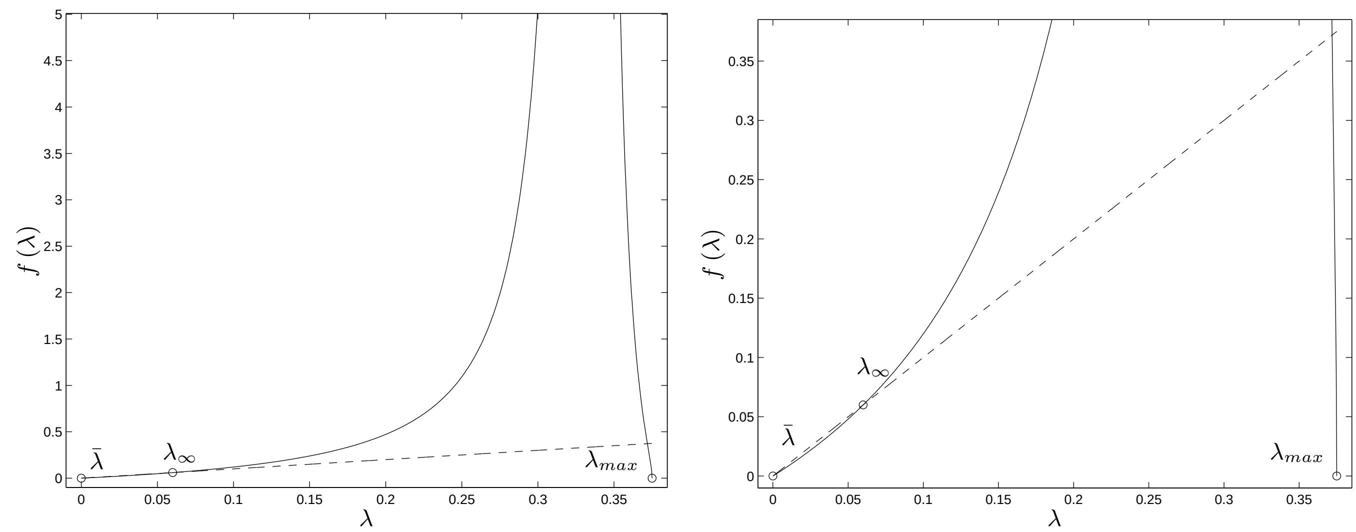

(a) (b)

Figure 6.5 — Scalar function $f(\lambda)$ approximating the map P_I in a vicinity of the invariant set $\mathcal{C}$ in solid line, with the unit-slope bisectrix dashed. (a) The map as a discontinuous function in the overall range of λ and (b) detail for fixed points in the left branch.

with $s \equiv s(\lambda) = \frac{3}{2} - \frac{1}{2}\sqrt{\frac{9-24r\lambda}{\sin(\omega\phi_\alpha)}}$.

Hence, the invariant set $\mathcal{C}$ can be expressed in terms of a special value of the parameter $\lambda = \lambda_\infty$ accomplishing $f(\lambda_\infty) = \lambda_\infty$, i.e. such that:

$$\mathcal{C} \equiv \left\{(\phi, v) : v = \omega\lambda_\infty (\phi_\alpha - \phi)^2\right\}. \tag{6.20}$$

Then, from (6.19), the function $f(\lambda)$ or the scalar equivalent for the map in a vicinity of $\mathcal{C}$, can be characterized as having the following features [22]:

- The function is discontinuous at $\lambda = \frac{\sin(\omega\phi_\alpha)}{3r}$;
- The map has a fixed point at $\bar{\lambda} = 0$;
- The map has a non-zero fixed point at $\bar{\lambda} < \lambda_\infty < \frac{\sin(\omega\phi_\alpha)}{3r}$;
- The slope of the map $f_\lambda \equiv \frac{df}{d\lambda}$, is monotonically increasing from $f_\lambda|_{\lambda=\bar{\lambda}} = r < 1$, passing through $f_\lambda|_{\lambda=\lambda_\infty} = 1$, until $f_\lambda|_{\lambda=\frac{\sin(\omega\phi_\alpha)}{3r}} \to \infty$;
- The map is stable for the condition associated with complete chattering regime $\lambda < \lambda_\infty$, and
- the map is real-valued for $\lambda < \lambda_{\max} = \frac{3\sin(\omega\phi_\alpha)}{8r}$.

A graphical illustration of $f(\lambda)$ taking $\frac{\sin(\omega\phi_\alpha)}{r} = 1$, is given in Figure 6.5.

The last condition referring the upper boundary on the domain of $f(\lambda)$, is directly related with the set $\mathcal{S}^1$, as demonstrated in [22]:

Lemma: *If ϕ is close to ϕ_α, then $\mathcal{S}^1$ has a component which coincides with the parabola $\mathcal{T}_{\lambda_{\max}}$.*

In other words, the map $f(\lambda)$ comprises the accumulation of the sets $\mathcal{S}^n$ for $n \to \infty$, $\forall\, \lambda \in (\lambda_\infty, \lambda_{max}]$. This important remark is fundamental to perform the analysis of interrupted chattering sequences by studying the map $f(\lambda)$ in a vicinity of the critical value λ_∞, as we will show later in the Chapter.

Finally, the sets $\mathcal{C}$ in (6.20) and $\mathcal{Z}$ in (6.4), enclose a region $\mathcal{D}$ invariant under the action of the map P_I, i.e:

$$\mathcal{D} \subseteq \{\mathcal{C} \cup \mathcal{Z}\}, \tag{6.21}$$

and then under the assumption that there is not a fixed point of P_I belonging to $\mathcal{D}$, any trajectory falling into it should experience complete chattering with sticking. The set $\mathcal{D}$ will be referenced in the following as the chattering region (or trapping region).

6.3 The Chattering map

The results presented in the previous section have proven the conditions under which a system of the form (6.1) can undergo a complete chattering regime, by establishing the trapping region $\mathcal{D}$. Another important result is the limit condition in a vicinity of the releasing point ϕ_α that allows an equivalent representation for the map P_I in terms of the scalar function f of the parameter λ. This serves as the preamble for studying the transition to aperiodic regime experienced by the system including multiple low-velocity impacts.

Previous studies in impact oscillators have shown the interaction between system modes in solution trajectories combining high and low-velocity collisions, during intermittent motion between pure-periodic and chaotic regimes. By isolating low-velocity collisions, it is possible to show the destabilizing effects of zero velocity impacts in terms of one-dimensional maps (see [21] and [59] for further details). Therefore, the scope of this section is to extend these concepts to the case of a trajectory with an infinite number of such low-velocity collisions. Specifically, based on the developments of Nordmark et al [57], an expression for the map describing a trajectory with complete chattering will be formulated for a generic impact oscillator, giving a further explanation for the transition into aperiodic regime by perturbing. Those developments will be employed to uncover the particular bifurcation scenario experienced by a real cam-follower impacting model.

6.3.1 The case of a triple integrator

Consider the system described by the set of differential equations

$$F(x, v, a) = F(X) = \begin{bmatrix} \dot{x} \\ \dot{v} \\ \dot{a} \end{bmatrix} = \begin{bmatrix} v \\ a \\ 1 \end{bmatrix}, \tag{6.22}$$

i.e, the vector field relating dynamics of a triple integrator with a solution vector $X = \begin{bmatrix} x(t) & v(t) & a(t) \end{bmatrix}^T$, subjected to the constraint:

$$\Phi(X, t - t_0) = \begin{cases} X; & x > 0 \\ R(X); & x = 0, \end{cases} \tag{6.23}$$

where $\Phi(X, t - t_0)$ represents the system flow, or coordinates in state space at a given time t by flowing from an initial time t_0. Analogously, $R(X)$ corresponds with an instantaneous reset applied each time the position is null through the trajectory, mapping coordinates before (-) and after (+) the event, by:

$$X^+ = R\left(X^-\right) = X^- + \begin{bmatrix} 0 \\ -(1+r) \\ 0 \end{bmatrix} v^-, \tag{6.24}$$

with coefficient of restitution $0 < r < 1$ for inelastic collisions. This situation reflects the interaction with a boundary surface, that in the following we should interpret as an impact; i.e. the boundary is rigid.

Impacts are the main phenomena introduced by nonsmoothness in (6.23). Then in order to analyze the system dynamics, it is necessary to develop accurate expressions for the maps describing trajectories with a single (λ map) and an infinite sequence (β map) of collisions.

The λ map

The free-flight motion or unconstrained mode between impacts for (6.22) can be easily solved to be:

$$\begin{aligned} a(t-t_0) = &\ (t-t_0) + a_0 \\ v(t-t_0) = &\ \tfrac{1}{2}(t-t_0)^2 + a_0(t-t_0) + v_0 \\ x(t-t_0) = &\ \tfrac{1}{6}(t-t_0)^3 + \tfrac{a_0}{2}(t-t_0)^2 + v_0(t-t_0) + x_0, \end{aligned} \tag{6.25}$$

with $a_0 = t_0$ and

$$\begin{bmatrix} x_0 \\ v_0 \\ a_0 \end{bmatrix} = X_0 = \Phi(X, 0).$$

Then, defining a trajectory that starts at $t = t_0 < 0$ with $x(t_0) = 0$, $v(t_0) = v_0 \neq 0$, under the action of negative acceleration (meaning that the particle will be attracted towards the surface), the time t_1 for the next collision must satisfy:

$$x(t_1 - t_0) = 0 = \frac{1}{6}(t_1-t_0)^3 + \frac{a_0}{2}(t_1-t_0)^2 + v_0(t_1-t_0), \tag{6.26}$$

given that $x_0 = x(0) = 0$ by definition. Now, by taking $\Lambda = t_1 - t_0$, the time between impacts can be calculated as:

$$\Lambda = \frac{-3a_0}{2} + 3\sqrt{\left(\frac{a_0}{2}\right)^2 - \frac{2v_0}{3}}, \tag{6.27}$$

where the choice of the positive root is justified for the next impact occurring forward in time.

Additionally, by using the particular formulation for acceleration and phase given at (6.25), a parabolic relationship between phase and (low) velocity at impacts can be assumed, i.e. such that for some λ we have:

$$\lambda = \frac{v}{t^2}, \tag{6.28}$$

then expression (6.27) can be reformulated in terms of λ and t, as:

$$\Lambda = \frac{-3t_0}{2} + \frac{3t_0}{2}\sqrt{1 - \frac{8}{3}\lambda_0}, \tag{6.29}$$

where:

$$\lambda_0 = \frac{v_0}{t_0^2} \equiv \frac{v_0}{a_0^2}. \tag{6.30}$$

Finally, the time for the next impact will be:

$$t_1 = \Lambda + t_0 = \frac{-t_0}{2} + \frac{3t_0}{2}\sqrt{1 - \frac{8}{3}\lambda_0} = \left(\frac{3s-1}{2}\right) t_0, \tag{6.31}$$

with:

$$s = s\left(\lambda_0\right) = \sqrt{1 - \frac{8}{3}\lambda_0}. \tag{6.32}$$

Equation (6.31) defines a mapping for the next impact phase in terms of the previous value of λ, i.e:

$$t_1 = \left(\frac{3s-1}{2}\right) t_0 \triangleq h\left(\lambda_0\right) t_0. \tag{6.33}$$

Consider now the next value of λ. We have:

$$\lambda_1 = \frac{v_1}{t_1^2} = \frac{-rv_{01}}{\left(h\left(\lambda_0\right) t_0\right)^2} = f\left(\lambda_0, r\right), \tag{6.34}$$

with v_{01} representing the final value of the velocity in the interval Λ, that after combining (6.25), (6.30), (6.32) and (6.33), can be expressed as:

$$\begin{aligned}
&v_{01} = v\left(t_1 - t_0\right) \\
&= \tfrac{1}{2}\left(t_1 - t_0\right)^2 + t_0\left(t_1 - t_0\right) + \lambda_0 t_0^2 \\
&= \tfrac{1}{2}\left(h\left(\lambda_0\right) t_0 - t_0\right)^2 + t_0\left(h\left(\lambda_0\right) t_0 - t_0\right) + \lambda_0 t_0^2 \\
&= t_0^2\left[\tfrac{1}{2}(h\left(\lambda_0\right) - 1)^2 + \left(h\left(\lambda_0\right) - 1\right) + \lambda_0\right] \\
&= t_0^2\left[\tfrac{1}{2}h\left(\lambda_0\right)^2 - \tfrac{1}{2} + \lambda_0\right] \\
&= t_0^2\left[\tfrac{1}{2}\left(\tfrac{3s-1}{2}\right)^2 - \tfrac{1}{2} + \left(\tfrac{3\left(1-s^2\right)}{8}\right)\right].
\end{aligned} \tag{6.35}$$

Then, after substituting (6.35) into (6.34), a mapping from λ_0 to λ_1 can be derived as:

$$\begin{aligned}
&\lambda_1 = f\left(\lambda_0, r\right) \equiv f\left(s, r\right) \\
&= \frac{-r\left(t_0^2\left[\frac{1}{2}\left(\frac{3s-1}{2}\right)^2 - \frac{1}{2} + \left(\frac{3\left(1-s^2\right)}{8}\right)\right]\right)}{\left(\left(\frac{3s-1}{2}\right)t_0\right)^2} \\
&= \frac{-r\left(\left(\frac{(3s-1)^2}{8}\right) - \frac{1}{2} + \left(\frac{3\left(1-s^2\right)}{8}\right)\right)}{\left(\frac{3s-1}{2}\right)^2} \\
&= \frac{-r\left(\left(\frac{(3s-1)^2 + 3\left(1-s^2\right)}{2}\right) - 2\right)}{(3s-1)^2} \\
&= \frac{-r\left(3s^2 - 3s\right)}{(3s-1)^2} = r\frac{3s(1-s)}{(3s-1)^2} = r\frac{\left(\sqrt{9-24\lambda_0} - 3 + 8\lambda_0\right)}{\left(\sqrt{9-24\lambda_0} - 1\right)^2}.
\end{aligned} \tag{6.36}$$

Finally, equations (6.33) and (6.36) allow to construct the evolution of a low-velocity multi-impacting trajectory, by multiple iteration of the single-return map:

$$\begin{bmatrix} t_{k+1} \\ \lambda_{k+1} \end{bmatrix} = \begin{bmatrix} h(\lambda_k)\, t_k \\ f(\lambda_k, r) \end{bmatrix}. \tag{6.37}$$

Note that from (6.36), the dynamics of λ_n is completely decoupled from that of t_k. Hence, we will refer to (6.37) as the λ-map.

The β map

The λ map given by (6.37) defines the transition of velocity and phase coordinates from one impact to the next under the assumption of impacts occurring with low velocity.

Supposing that now we are interested in developing an expression to describe the interruption of a sequence of infinite iterations of such a map, let's consider the limiting case when the last impact of a trajectory with complete chattering occurs at the phase where the acceleration becomes positive (i.e. $t_\infty = t_\alpha = 0$). Then, by defining the Poincaré section:

$$P = \left\{ X \in \Re^3 : a = a_P = t_P > t_\alpha \right\}, \tag{6.38}$$

a series expansion of the trajectory around t_α allows to express the velocity and position at P with infinite precision, whenever the low-velocity assumption at $a = a_P$ holds, i.e. a parabolic relationship between phase and velocity being valid at $t = t_P$. Hence, this can be expressed mathematically (for instance in the case of the velocity) as:

$$\begin{aligned}
&v_P = v(t_P) \\
&= v(t_\alpha) + \left(\left.\tfrac{dv}{dt}\right|_{t=t_\alpha} \right)(t_P - t_\alpha) + \left(\left.\tfrac{d^2v}{dt^2}\right|_{t=t_\alpha} \right) \tfrac{(t_P - t_\alpha)^2}{2} + \mathcal{O}\left((t_P - t_\alpha)^3 \right) \\
&= v_\alpha + a_\alpha (t_P - t_\alpha) + \tfrac{1}{2}(t_P - t_\alpha)^2 \\
&= v_\alpha + a_\alpha t_P - a_\alpha t_\alpha + \tfrac{t_P^2}{2} - t_P t_\alpha + \tfrac{t_\alpha^2}{2} \\
&= v_\alpha - \tfrac{t_\alpha^2}{2} + \tfrac{t_P^2}{2} \\
&= \tfrac{t_P^2}{2} + t_\alpha^2 \left[\lambda_\alpha - \tfrac{1}{2} \right],
\end{aligned} \tag{6.39}$$

where the subindex "α" indicates a coordinate evaluated at the last impact time, when $t = t_\alpha$. Furthermore, by employing the λ map, (6.39) can be reformulated in terms of the last impact before t_α (that we will label as "1"):

$$\begin{aligned}
&v_P = \tfrac{t_P^2}{2} + t_\alpha^2 \left[\lambda_\alpha - \tfrac{1}{2} \right] \\
&= \tfrac{t_P^2}{2} + (h(\lambda_1)\, t_1)^2 \left[f(\lambda_1, r) - \tfrac{1}{2} \right],
\end{aligned} \tag{6.40}$$

or equivalently in the limit, as:

$$\begin{aligned}
&v_P = \tfrac{t_P^2}{2} + (h(\lambda_1)\, t_1)^2 \left[f(\lambda_1, r) - \tfrac{1}{2} \right] \\
&= \tfrac{t_P^2}{2} + (h(\lambda_1)\, h(\lambda_2)\, t_2)^2 \left[f(f(\lambda_2, r), r) - \tfrac{1}{2} \right] \\
&= \ldots \\
&= \tfrac{t_P^2}{2} + \lim_{n\to\infty} \left(\left(\left[\prod_{i=1}^{n} h(\lambda_i) \right] t_n \right)^2 \left[f^n(\lambda_n, r) - \tfrac{1}{2} \right] \right),
\end{aligned} \tag{6.41}$$

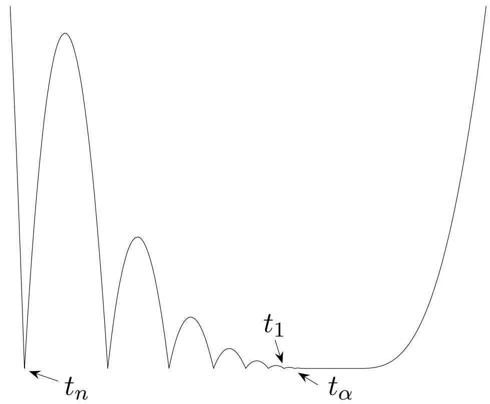

Figure 6.6 — Illustration for a trajectory with complete chattering and sticking labelling the impacts in accordance with developments of expression (6.41).

See Figure 6.6 for an explanation of the notation employed in (6.41).

Labelling "$*$" the coordinates of the first impact considered to satisfy the low-velocity condition (equivalent in (6.41) to t_n), the velocity coordinate at the Poincaré surface (6.38) when the trajectory experiences a complete chattering sequence finishing exactly at α, can then be expressed from (6.41) as:

$$v_P = \frac{t_P^2}{2} + \beta\left(\lambda^*\right) t^{*2}, \tag{6.42}$$

where

$$\beta(\lambda^*) \triangleq \lim_{n\to\infty} \left(\left(\prod_{i=1}^{n} h\left(\lambda_i\right) \right)^2 \left[f^n\left(\lambda_n, r\right) - \frac{1}{2} \right] \right), \tag{6.43}$$

contains information about the infinite sequence of impacts through the variable λ.

More interestingly, $\beta(\lambda)$ contains information about finite sequences of low-velocity impacts, when the perturbation of the critical value $\bar{\lambda}$ – depicted as a fixed point in Figure 6.5 – causes interruption of chatter, that is:

$$\beta\left(\tilde{\lambda} + \bar{\lambda}\right) = \begin{cases} \left(\prod_{i=1}^{N} h\left(\tilde{\lambda}_i\right) \right)^2 \left[f^N\left(\tilde{\lambda} + \bar{\lambda}, r\right) - \frac{1}{2} \right] & ; \tilde{\lambda} > 0 \\ 0 & ; \tilde{\lambda} < 0, \end{cases} \tag{6.44}$$

for N representing a finite value of n in (6.43); $\tilde{\lambda} = \lambda^* - \bar{\lambda}$, the deviation of the critical value $\bar{\lambda}$ satisfying:

$$f\left(\bar{\lambda}, r\right) - \bar{\lambda} = 0; \tag{6.45}$$

and $\tilde{\lambda}_i \equiv f^i\left(\tilde{\lambda} + \bar{\lambda}, r\right)$.

Here it is important to note that being $\beta(\lambda)$ a composition of (6.33) and (6.34) iterated infinitely, the domain of its argument, that is of λ, should be automatically scaled at each iteration.

The scaling-law

A perturbation in the first low-velocity impact, will cause a shift in the location of the last collision. The amount of such deviation will depend on the number of iterations of the map λ in β, or equivalently, on how many impacts occur before release.

Taking the fundamental iteration, that is from λ^* to the next value of λ, the function $\beta(\lambda)$ will lead to:

$$\begin{aligned}&\beta\left(\lambda^*\right)=h\left(\lambda^*\right)^2\left[f\left(\lambda^*,r\right)-\tfrac{1}{2}\right]\\&=\left(\tfrac{3s-1}{2}\right)^2\left(r\tfrac{3s(1-s)}{(3s-1)^2}-\tfrac{1}{2}\right)\\&=s^2\left[\tfrac{-3}{4}\left(r+\tfrac{3}{2}\right)\right]+s\left[\tfrac{3}{4}\left(1+r\right)\right]-\tfrac{1}{8}\\&=\left(3+2r\right)\lambda^*+\tfrac{1}{4}\left(r+1\right)\sqrt{9-24\lambda^*}-\tfrac{1}{4}\left(3r+5\right),\end{aligned}\tag{6.46}$$

after combining (6.32), (6.33), (6.36) and (6.42).

Equation (6.46) represents an extremely important result, given that it defines analytically the fundamental structure of the map between two points inside the chattering region $\mathcal{D}$ in (6.21), and therefore will allow to confirm the transition into aperiodic regime suggested by the graphic cobweb-analysis performed in Chapter 5 for the numerical approximation of the map .

Because of (6.44), where the meaning of $\bar{\lambda}$ was introduced, the domain of λ^* in (6.46) is constrained to be:

$$\mathcal{I}_f=\left\{\lambda^*\in\Re:\bar{\lambda}\leq\lambda^*\leq\frac{3}{8}\right\}.\tag{6.47}$$

Hence, the fundamental structure (6.46) will be repeated continuously on a given interval of perturbations of $\bar{\lambda}$, with subintervals representing the transition between impacts before release, each corresponding with scaled versions of (6.47). Mathematically:

$$\begin{aligned}&\mathcal{I}=\left\{\lambda\in\Re:\lambda\geq\bar{\lambda}\right\}\\&=\bigcup_{i=1}^{\infty}\mathcal{I}_i\equiv\bigcup_{i=1}^{\infty}\tfrac{\mathcal{I}_f}{q^i},\end{aligned}\tag{6.48}$$

with a scale factor q, given by:

$$q=\frac{1}{f_\lambda\left(\bar{\lambda},r\right)}\equiv\left.\left(\frac{\partial f}{\partial\lambda}\right)^{-1}\right|_{\lambda=\bar{\lambda}},\tag{6.49}$$

taking advantage of the linear approximation of f and its reciprocal, in a vicinity of $\bar{\lambda}$.

Each time an impact is lost, the amplitude of the map is increased by a given factor, let's say p. In order to define it, we need to establish conditions for the convergence of (6.44) in the limit when $N\to\infty$, that is, for the existence of (6.42). This can be reduced to simply studying the convergence of:

$$\lim_{n\to\infty}\prod_{i=1}^{n}h\left(\lambda_i\right).\tag{6.50}$$

Then, for such a limit to exist, any sequence of its partial sums must converge. This can be assured by rewriting (6.50) as:

$$\lim_{n\to\infty}\prod_{i=1}^{n}h\left(\lambda_i\right)\equiv\left(\lim_{n\to\infty}\prod_{i=1}^{n}\frac{h\left(\lambda_i\right)}{h\left(\bar{\lambda}\right)^n}\right)h\left(\bar{\lambda}\right)^N,\tag{6.51}$$

where:

$$h\left(\bar{\lambda}\right) \geq h\left(\lambda_i\right) \forall i = 1, 2, ..., n. \tag{6.52}$$

Then if $N \to \infty$ in (6.51), the equality applies. If not, the remaining "convergent" expression will be increased by a factor $p = h\left(\bar{\lambda}\right)$ each time an impact is missed, and consequently from (6.44) the amplitude of $\beta(\lambda)$ will be scaled by p^2.

In summary, a perturbation in the critical value $\bar{\lambda}$ under which a complete chattering sequence accumulates at the point of release (where acceleration becomes positive), will cause the interruption of chattering with an evolution described by the map β behaving in patterns following a fundamental structure that is being translated and scaled. In particular, the evolution of an attractor experiencing such a transition is expected to be enveloped by $|\beta| \leq \tilde{\lambda}^{\kappa}$, where:

$$\kappa = \frac{\log\left(p^2\right)}{\log\left(q\right)}, \tag{6.53}$$

or equivalently $q^{\kappa} = p^2$.

Coordinates at the Poincaré surface

Following the same procedure as in (6.40), an expression for x_P can be found to be:

$$x_P = \frac{t_P^3}{6} + t_\alpha^2 \left[t_P\left(\lambda_\alpha - \frac{1}{2}\right) + t_\alpha\left(\frac{1}{3} - \lambda_\alpha\right)\right], \tag{6.54}$$

that under the assumption of $t_\alpha \approx 0$, can be approximated by:

$$x_P = \tfrac{t_P^3}{6} + t_\alpha^2\left[t_P\left(\lambda_\alpha - \tfrac{1}{2}\right)\right] = \tfrac{t_P^3}{6} + \beta\left(\lambda^*\right) t^{*2} t_P, \tag{6.55}$$

employing extension of results in (6.41) and (6.42).

In this way, we are able to express the coordinates at the Poincaré surface P in terms of the map $\beta(\lambda)$ by:

$$\begin{aligned} v_P = &\ \tfrac{1}{2}t_P^2 + \beta\left(\lambda^*\right) t^{*2} \\ x_P = &\ \tfrac{1}{6}t_P^3 + \beta\left(\lambda^*\right) t^{*2} t_P \\ a_P = &\ t_P. \end{aligned} \tag{6.56}$$

In other words, equation (6.56) describes the final state $X_P = [x_P, v_P, a_P]^T$ of a trajectory with low-velocity impacts starting at $X^* = [0, v^*, a^*]^T$. As an illustration, consider Figure 6.7 where a periodic trajectory with complete chattering is depicted. Here, the mapping is performed between the X^* coordinates denoted by a triangle in the Figure and the Poincaré surface X_P with corresponding squares. Figure 6.7 will be recalled later in section 6.7.1, where numerical calculations on a realistic application model are detailed.

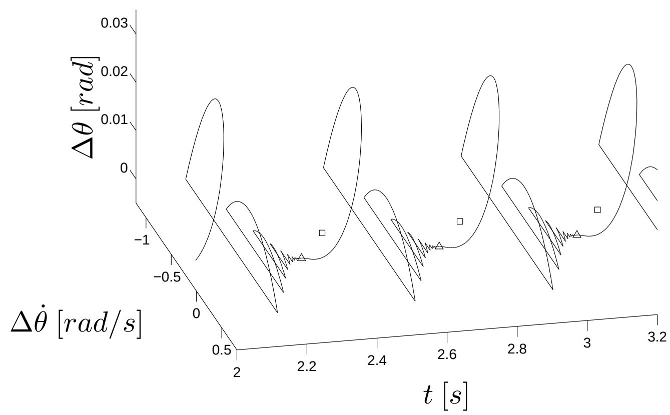

Figure 6.7 — Illustration of a trajectory with periodic chattering motion denoting the chattering region $\mathcal{D}$ on which the local analysis is applied. Equation (6.56), will map information from a point labelled by a triangle in the Figure into a point in the Poincaré surface represented by a square. These results will be treated again in section 6.7.1.

6.4 The case of a general periodically forced impact oscillator

Consider the vertical undamped-harmonic motion of a particle hanging from a spring with unitary elastic coefficient, attached to a fixed surface. Such unforced non-autonomous system, can be described by the set of differential equations:

$$F(y,v,t) = F(Y,t) = \begin{bmatrix} \dot{y} \\ \dot{v} \end{bmatrix} = \begin{bmatrix} v(t) \\ -y(t) \end{bmatrix}. \tag{6.57}$$

Suppose now that a constrain, consisting of a vertically oscillating rigid-boundary of the form:

$$g(t) = \sin(\omega t) + \sigma, \tag{6.58}$$

is imposed over (6.57). Then, by defining the vector of relative coordinates:

$$\bar{Y} = \begin{bmatrix} \bar{y} \\ \dot{\bar{y}} \end{bmatrix} = \begin{bmatrix} y - g \\ \dot{y} - \dot{g} \end{bmatrix}, \tag{6.59}$$

the analysis of the forced dynamics can be equivalently accomplished in terms of the relative motion between the mass and the boundary; i.e:

$$F\left(\bar{Y},t\right) = F\left(\bar{y},\dot{\bar{y}},t\right) = \begin{bmatrix} \dot{\bar{y}} \\ \ddot{\bar{y}} \end{bmatrix} = \begin{bmatrix} \ddot{\bar{y}} \\ -\bar{y} - (\ddot{g} + g) \end{bmatrix}, \tag{6.60}$$

subject to the constraint:

$$\Phi\left(\bar{Y}, t - t_0\right) = \begin{cases} \bar{Y}; & \bar{y} > 0 \\ R\left(\bar{Y},t\right); & \bar{y} = 0, \end{cases} \tag{6.61}$$

where: $F\left(\bar{Y},t\right)$ is the vector field with solution $\bar{Y}(t)$, $\Phi(\bar{Y}, t - t_0)$ represents the system flow at a given time t from t_0 and $R\left(\bar{Y},t\right)$ defines an instantaneous reset:

$$\bar{Y}^+ = R\left(\bar{Y}^-\right) = \bar{Y}^- + \begin{bmatrix} 0 \\ -(1+r) \end{bmatrix} \dot{\bar{y}}^-, \tag{6.62}$$

with coefficient of restitution $0 < r < 1$ for inelastic collisions.

Given the similarity between equations governing dynamics of the relative motion in (6.61)-(6.62) and those of the triple integrator (6.23)-(6.24), the aim of this section is to establish the conditions over which results developed in section 6.3.1 can be extended for studying the interruption of sequences with complete chatter, in a more general class of impact oscillator.

6.4.1 Equations of motion

During the unconstrained mode $(\bar{y} > 0)$, the trajectory in (6.61) is described by the equation:

$$\ddot{\bar{y}} + \bar{y} = -(g + g) = \left(\omega^2 - 1\right)\sin(\omega t) - \sigma, \tag{6.63}$$

that can be solved for $\bar{y}$ employing elementary theory of ODE.

For the non-homogeneous case, the particular solution of (6.63) is given by:

$$\begin{aligned}
&\bar{y}_p = A\cos(\omega t) + B\sin(\omega t) + C \Rightarrow \\
&\dot{\bar{y}}_p = \omega B\cos(\omega t) - \omega A\sin(\omega t); \\
&\ddot{\bar{y}}_p = -\omega^2 A\cos(\omega t) - \omega^2 B\sin(\omega t).
\end{aligned} \tag{6.64}$$

Substituting (6.64) in (6.63), we have;

$$\begin{aligned}
&\ddot{\bar{y}}_p + \bar{y}_p = \left(\omega^2 - 1\right)\sin(\omega t) - \sigma \\
&\left[-\omega^2 A\cos(\omega t) - \omega^2 B\sin(\omega t)\right] + \left[A\cos(\omega t) + B\sin(\omega t) + C\right] = \left(\omega^2 - 1\right)\sin(\omega t) - \sigma \\
&A\left(1 - \omega^2\right)\cos(\omega t) + B\left(1 - \omega^2\right)\sin(\omega t) + C = \left(\omega^2 - 1\right)\sin(\omega t) - \sigma,
\end{aligned} \tag{6.65}$$

and then, by equating coefficients:

$$\bar{y}_p = -\sin(\omega t) - \sigma. \tag{6.66}$$

For the homogeneous case, solution of (6.63) is given by:

$$\bar{y}_h = D\cos(t) + E\sin(t), \tag{6.67}$$

with D and E satisfying conditions on the general solution, defined by:

$$\bar{y}(t) = \bar{y}_h + \bar{y}_p = D\cos(t) + E\sin(t) - \sin(\omega t) - \sigma, \tag{6.68}$$

and hence:

$$\begin{aligned}
&\bar{y}(0) = D - \sigma \Rightarrow D = \bar{y}(0) + \sigma; \\
&\dot{\bar{y}}(t) = E\cos(t) - D\sin(t) - \omega\cos(\omega t) \Rightarrow E = \dot{\bar{y}}(0) + \omega.
\end{aligned} \tag{6.69}$$

Finally, the dynamics of the relative free-flight motion between impacts can be written as:

$$\bar{y}(t - t_0) = \left[\bar{y}(t_0) + \sigma\right]\cos(t - t_0) + \left[\dot{\bar{y}}(t_0) + \omega\right]\sin(t - t_0) - \sin(\omega\left[t - t_0\right]) - \sigma, \tag{6.70}$$

with corresponding relative velocity, acceleration and jerk (acceleration time-derivative), given by:

$$\begin{aligned}
&\dot{\bar{y}}(t - t_0) = \left[\dot{\bar{y}}(t_0) + \omega\right]\cos(t - t_0) - \left[\bar{y}(t_0) + \sigma\right]\sin(t - t_0) - \omega\cos(\omega\left[t - t_0\right]); \\
&\ddot{\bar{y}}(t - t_0) = \omega^2\sin(\omega\left[t - t_0\right]) - \left[\bar{y}(t_0) + \sigma\right]\cos(t - t_0) - \left[\dot{\bar{y}}(t_0) + \omega\right]\sin(t - t_0); \\
&\dddot{\bar{y}}(t - t_0) = \omega^3\cos(\omega\left[t - t_0\right]) + \left[\bar{y}(t_0) + \sigma\right]\sin(t - t_0) - \left[\dot{\bar{y}}(t_0) + \omega\right]\cos(t - t_0).
\end{aligned} \tag{6.71}$$

6.4.2 Extension of the λ map

An interesting question to answer at this point is what is the expression for the next impact time, because evidently, applying the same procedure as in (6.26) to (6.70) will lead to an unsolvable transcendental equation.

In order to overcome such a difficulty, we must restrict ourselves to work in a highly local sense by considering that $(t - t_0) \to 0$. Physically, this means that the bouncing time should be sufficiently small, as it is often the case when working inside the low-velocity impact region.

Then, considering the low-order Taylor approximation for the trigonometric terms in (6.70):

$$\begin{aligned}&\cos(t-t_0) \approx 1 - \tfrac{(t-t_0)^2}{2};\\ &\sin(t-t_0) \approx (t-t_0) - \tfrac{(t-t_0)^3}{6},\end{aligned} \tag{6.72}$$

we get:

$$\begin{aligned}&\bar{y}(t-t_0) \approx \\ &[\bar{y}(t_0)+\sigma]\left(1-\tfrac{(t-t_0)^2}{2}\right)+[\dot{\bar{y}}(t_0)+\omega]\left((t-t_0)-\tfrac{(t-t_0)^3}{6}\right)-\left(\omega(t-t_0)-\tfrac{\omega^3(t-t_0)^3}{6}\right)-\sigma.\end{aligned} \tag{6.73}$$

Now, by defining $\Lambda = (t - t_0)$, a rearrangement of (6.73) yields:

$$\begin{aligned}&\bar{y}(\Lambda) \approx \Lambda^3\left[\tfrac{1}{6}\left(\omega^3-\omega-\dot{\bar{y}}(t_0)\right)\right]+\Lambda^2\left[-\tfrac{1}{2}\left(\bar{y}(t_0)+\sigma\right)\right]+\Lambda\left[\dot{\bar{y}}(t_0)\right]+\bar{y}(t_0)\\ &\equiv \tfrac{1}{6}\dddot{\bar{y}}_0\Lambda^3+\tfrac{1}{2}\ddot{\bar{y}}_0\Lambda^2+\dot{\bar{y}}_0\Lambda+\bar{y}_0.\end{aligned} \tag{6.74}$$

Considering an impact as the starting point (i.e. $\bar{y}(t-t_0)|_{t=t_0} = \bar{y}_0 = \bar{y}(t_0) = 0$), allows to solve (6.74) in terms of Λ for the next collision, obtaining:

$$\Lambda = \frac{-\frac{1}{2}\ddot{\bar{y}}_0+\sqrt{\left(\frac{1}{2}\ddot{\bar{y}}_0\right)^2-\frac{4}{6}c\dot{\bar{y}}_0}}{\frac{1}{3}c}, \tag{6.75}$$

where the positive value in the square root term again is such that, for the next impact to occur forward in time, and

$$c = \dddot{\bar{y}}_0 = \left.\dddot{\bar{y}}(t-t_0)\right|_{t=t_0}. \tag{6.76}$$

The equations above are a generalization of such previously presented in section 6.3.1, and therefore equation (6.75) should reflect the compression factor between impact times introduced by the function h in (6.33). In order to achieve it, let's consider first $c\dot{\bar{y}}_0 = \lambda\ddot{\bar{y}}_0^2$ in (6.75). Hence, we obtain:

$$\begin{aligned}&\Lambda = \tfrac{3}{c}\left(-\tfrac{1}{2}\ddot{\bar{y}}_0+\sqrt{\left(\tfrac{1}{2}\ddot{\bar{y}}_0\right)^2-\tfrac{4}{6}\lambda\ddot{\bar{y}}_0^2}\right)\\ &= \tfrac{3}{c}\left(-\tfrac{1}{2}\ddot{\bar{y}}_0+\ddot{\bar{y}}_0\sqrt{\tfrac{1}{4}\left(1-\tfrac{8}{3}\lambda\right)}\right) = \tfrac{3\ddot{\bar{y}}_0}{2c}(s-1),\end{aligned} \tag{6.77}$$

after use of (6.32).

If the system described by equations (6.61)-(6.62) is under period-one complete chattering motion, an infinite number of impacts is expected to accumulate, in general, at a certain phase where the relative acceleration in still negative.

Now, for derivation of the map λ in the case of a periodically-forced impact oscillator, we assume once again the critical case when the accumulation point corresponds with the phase at which the relative acceleration changes from negative to positive, let's say at $t = t_\alpha > 0$. Therefore, claiming that $(t_1 - t_0) \to 0$ implies:

$$(t_1 - t_0) \triangleq [(t_\alpha - t_0) - (t_\alpha - t_1)] \to 0 \quad \forall \quad 0 \leq t_0 \leq t_1 \leq t_\alpha, \tag{6.78}$$

and then, by working locally to the point where the acceleration crosses the zero, it is possible to consider for its associated function, a linear equivalent of the form:

$$\ddot{y}\,(t - t_0) \triangleq \ddot{y}\,([t_\alpha - t] - [t_\alpha - t_0]) = c\,(t - t_0) + \ddot{y_0} \quad \forall \quad t \in [t_0, t_1], \tag{6.79}$$

with c as defined in (6.76).

If $t_\alpha = t_1$, then:

$$\begin{array}{l} \ddot{y}\,(t_\alpha - t_0) = 0 = c\,(t_\alpha - t_0) + \ddot{y_0} \Rightarrow \ddot{y_0} = c\,(t_0 - t_\alpha) \\ \Rightarrow \;\; \ddot{y}\,(t - t_0) = c\,(t - t_0) + c\,(t_0 - t_\alpha) = c\,(t - t_\alpha) \quad \forall \quad t \in [t_0, t_\alpha]. \end{array} \tag{6.80}$$

Noticing that $h(\lambda_0)$ in (6.33) represents a contracting function for negative values of t towards zero, or – as defined earlier – a proportionality factor, the same behaviour should be achieved in (6.77) when considering contraction in the distance $(t_\alpha - t)$ from t_α, or which is the same, for negative values towards zero of a new variable $\tau \equiv (t - t_\alpha)$.

According to this:

$$\begin{array}{l} \Lambda = (t_1 - t_0) \triangleq (t_\alpha - t_0) - (t_\alpha - t_1) = -\tau_0 + \tau_1 \\ \Rightarrow \tau_1 = \tau_0 + \Lambda = \tau_0 + \frac{3\ddot{y_0}}{2c}\,(s - 1)\,; \\ \ddot{y_0} = c\,(t_0 - t_\alpha) \triangleq c\tau_0 \\ \Rightarrow \tau_1 = \tau_0 + \tau_0 \frac{3}{2}\,(s - 1) = \tau_0 \left(\frac{3s-1}{2}\right) = \tau_0 h\,(\lambda_0) \\ \Rightarrow (t_\alpha - t_1) = h\,(\lambda_0)\,(t_\alpha - t_0)\,, \end{array} \tag{6.81}$$

where a replication of (6.33) in terms of τ is evident. It implies that the assumption on the quantity $c\dot{y_0}$ made for (6.77) is valid, and then for $\lambda \equiv \lambda_0$ it yields:

$$\lambda_0 = \frac{c\dot{y_0}}{\ddot{y_0}^2} \equiv \frac{c\dot{y_0}}{(c\tau_0)^2} = \frac{\dot{y_0}}{c\tau_0^2} = \frac{\dot{y_0}}{c\,(t_0 - t_\alpha)^2}, \tag{6.82}$$

with c accomplishing the condition of zero acceleration at $t = t_\alpha$.

An extension of (6.81) and (6.82) through (6.80), can be formulated for an arbitrary interval between impacts in a vicinity of t_α, based on the assumption that the linear approximation for the acceleration still applies. This is enforced by noticing that $\ddot{y}$ is not considered in the reset law (6.62).

Therefore:

$$\begin{array}{l} \Lambda = (t_{k+1} - t_k) \triangleq (t_\alpha - t_k) - (t_\alpha - t_{k+1}) = -\tau_k + \tau_{k+1} \\ \Rightarrow \tau_{k+1} = \tau_k h\,(\lambda_k) \\ \Rightarrow (t_\alpha - t_{k+1}) = h\,(\lambda_k)\,(t_\alpha - t_k)\,, \end{array} \tag{6.83}$$

with:

$$\lambda_k = \frac{\dot{y_k}}{c\left(t_k - t_\alpha\right)^2} \equiv \frac{\dot{y_k}}{c\tau_k^2}, \tag{6.84}$$

and c accomplishing again the condition of zero acceleration at $t = t_\alpha$; i.e. calculated at the last impact of the sequence.

Now, in an analogous way to what developed for (6.34) and (6.35), consider the variation of λ between impacts:

$$\lambda_1 = \frac{\dot{y_1}}{c\left(t_1 - t_\alpha\right)^2} = \frac{\dot{y_1}}{c\tau_1^2} = \frac{-r\dot{y_{01}}}{c\tau_1^2}, \tag{6.85}$$

where $\dot{y_{01}}$ represents the value of the relative velocity at the end of the trajectory between two consecutive collisions, labelled as "0" and "1", with associated expression:

$$\begin{aligned}
&\dot{y_{01}} = \dddot{y}\left(t_1 - t_0\right) \equiv \dddot{y}\left(\left[t_\alpha - t_0\right] - \left[t_\alpha - t_1\right]\right) = \dddot{y}\left(-\tau_0 + \tau_1\right) = \dddot{y}\left(\tau_1 - \tau_0\right) \\
&= \left[\dddot{y}_0 + \omega\right]\cos\left(\tau_1 - \tau_0\right) - \left[\bar{y}_0 + \sigma\right]\sin\left(\tau_1 - \tau_0\right) - \omega\cos\left(\omega\left[\tau_1 - \tau_0\right]\right) \\
&\approx \left[\dddot{y}_0 + \omega\right]\left(1 - \tfrac{\left(\tau_1 - \tau_0\right)^2}{2}\right) - \left[\bar{y}_0 + \sigma\right]\left(\left(\tau_1 - \tau_0\right) - \tfrac{\left(\tau_1 - \tau_0\right)^3}{6}\right) - \omega\left(1 - \tfrac{\omega^2\left(\tau_1 - \tau_0\right)^2}{2}\right) \\
&\approx \left[\dddot{y}_0 + \omega\right]\left(1 - \tfrac{\left[h(\lambda_0)\tau_0 - \tau_0\right]^2}{2}\right) - \left[\bar{y}_0 + \sigma\right]\left(\left[h\left(\lambda_0\right)\tau_0 - \tau_0\right] - \tfrac{\left[h(\lambda_0)\tau_0 - \tau_0\right]^3}{6}\right) - \omega\left(1 - \tfrac{\omega^2\left[h(\lambda_0)\tau_0 - \tau_0\right]^2}{2}\right) \\
&\approx \dddot{y}_0 + \omega - \tfrac{\left[\dddot{y}_0 + \omega\right]\left[h(\lambda_0)\tau_0 - \tau_0\right]^2}{2} - \left[\bar{y}_0 + \sigma\right]\left(\left[h\left(\lambda_0\right)\tau_0 - \tau_0\right] - \tfrac{\left[h(\lambda_0)\tau_0 - \tau_0\right]^3}{6}\right) - \omega + \tfrac{\omega^3\left[h(\lambda_0)\tau_0 - \tau_0\right]^2}{2} \\
&\approx c\tau_0^2\lambda_0 - \tfrac{\left[\dddot{y}_0 + \omega\right]}{2}\left[h\left(\lambda_0\right) - 1\right]^2\tau_0^2 + \tfrac{\omega^3}{2}\left[h\left(\lambda_0\right) - 1\right]^2\tau_0^2 - \left[\bar{y}_0 + \sigma\right]\left(\left[h\left(\lambda_0\right) - 1\right]\tau_0 - \tfrac{\left[h(\lambda_0) - 1\right]^3}{6}\tau_0^3\right) \\
&\approx \left[c\lambda_0 + \tfrac{\left[\omega^3 - \dddot{y}_0 - \omega\right]}{2}\left[h\left(\lambda_0\right) - 1\right]^2\right]\tau_0^2 - \left[\bar{y}_0 + \sigma\right]\left(\left[h\left(\lambda_0\right) - 1\right]\tau_0 - \tfrac{\left[h(\lambda_0) - 1\right]^3}{6}\tau_0^3\right),
\end{aligned} \tag{6.86}$$

generated after substitution of (6.72), (6.81) and (6.82) in (6.71), and valid when $\left(\tau_1 - \tau_0\right) \rightarrow 0$.

Also, from (6.71) we know that:

$$\begin{aligned}
&\ddddot{y}\left(t - t_0\right)\big|_{t=t_0} \equiv \ddddot{y}_0 = \omega^3 - \dddot{y}_0 - \omega = c; \\
&\dddot{y}\left(t - t_0\right)\big|_{t=t_0} \equiv \dddot{y}_0 = -\left[\bar{y}_0 + \sigma\right] \equiv c\tau_0,
\end{aligned} \tag{6.87}$$

$\tau_0 \rightarrow 0 \Rightarrow t_0 \rightarrow t_\alpha$, and consequently the cubic term in (6.86) can be neglected.

Hence, an equivalent reformulation of (6.86) is:

$$\begin{aligned}
&\dot{y_{01}} \approx \left[c\lambda_0 + \tfrac{c}{2}\left[h\left(\lambda_0\right) - 1\right]^2\right]\tau_0^2 + c\tau_0\left[h\left(\lambda_0\right) - 1\right]\tau_0 \\
&\approx \left[\tfrac{1}{2}\left[h\left(\lambda_0\right) - 1\right]^2 + \left[h\left(\lambda_0\right) - 1\right] + \lambda_0\right]c\tau_0^2 = \left[\tfrac{1}{2}h\left(\lambda_0\right)^2 - \tfrac{1}{2} + \lambda_0\right]c\tau_0^2,
\end{aligned} \tag{6.88}$$

that after substitution into (6.85) yields:

$$
\begin{aligned}
&\lambda_1 = f\left(\lambda_0, r\right) = f\left(s, r\right) = -r\frac{\dot{y_{01}}}{c\tau_1^2} = -r\frac{\dot{y_{01}}}{c[h(\lambda_0)\tau_0]^2} = -r\frac{\dot{y_{01}}}{c\left[h(\lambda_0)^2\tau_0^2\right]}\\
&\approx -r\frac{\left[\frac{1}{2}h(\lambda_0)^2-\frac{1}{2}+\lambda_0\right]c\tau_0^2}{c\left[h(\lambda_0)^2\tau_0^2\right]} = -r\frac{\left[\frac{1}{2}h(\lambda_0)^2-\frac{1}{2}+\lambda_0\right]}{h(\lambda_0)^2}\\
&= \frac{-r\left[\frac{1}{2}\left(\frac{3s-1}{2}\right)^2-\frac{1}{2}+\left(\frac{3\left(1-s^2\right)}{8}\right)\right]}{\left(\frac{3s-1}{2}\right)^2}\\
&= \frac{-r\left[\left(\frac{(3s-1)^2}{8}\right)-\frac{1}{2}+\left(\frac{3\left(1-s^2\right)}{8}\right)\right]}{\left(\frac{3s-1}{2}\right)^2}\\
&= \frac{-r\left[\left(\frac{(3s-1)^2+3\left(1-s^2\right)}{2}\right)-2\right]}{(3s-1)^2}\\
&= \frac{-r\left(3s^2-3s\right)}{(3s-1)^2} = r\frac{3s(1-s)}{(3s-1)^2} = r\frac{\left(\sqrt{9-24\lambda_0}-3+8\lambda_0\right)}{\left(\sqrt{9-24\lambda_0}-1\right)^2},
\end{aligned}
\tag{6.89}
$$

resembling, as expected, the analogous expression given in (6.36).

Finally, a combination of (6.83) and (6.89) constitutes the generalized version of the two-dimensional single-return impact map, for the case of a periodically forced harmonic oscillator:

$$
\begin{bmatrix} \tau_{k+1} \\ \lambda_{k+1} \end{bmatrix} = \begin{bmatrix} h\left(\lambda_k\right)\tau_k \\ f\left(\lambda_k, r\right) \end{bmatrix}. \tag{6.90}
$$

6.4.3 Extension for the β map

Similarly to the case of the triple integrator model, in order to develop an expression for the map describing a complete chattering sequence in a general periodically forced harmonic oscillator, we need to firstly define the chattering region $\mathcal{D}$, or equivalently the subset of the state space accomplishing the parabolic relationship of λ in (6.84). Mathematically:

$$
\mathcal{D} = \left\{\left(\bar{Y}, \tau\right) : \dot{y}\left(\tau\right) \to 0, \ddot{y}(\tau) \leq 0\right\} \cup \left\{\left(\bar{Y}, \tau\right) : \tau_\alpha \leq \tau \leq \tau_P\right\} = \mathcal{D}_\lambda \cup \mathcal{D}_P, \tag{6.91}
$$

with $\bar{Y}$ as in (6.59) and τ_P defining the location of a Poincaré surface given by:

$$
P = \left\{\bar{Y}(\tau) \in \Re^2 : \tau = \tau_P > \tau_\alpha\right\}, \tag{6.92}
$$

where the linearity condition for the acceleration should be satisfied; i.e. such that:

$$
\ddot{y}\left(t - t_0\right)\big|_{t=t_P} \equiv \ddot{y}\left(\tau - \tau_0\right)\big|_{\tau=\tau_P} = \ddot{y}\left(\tau_P - \tau_0\right) \triangleq c\tau_P \quad \forall \quad \tau_P < 0 \ . \tag{6.93}
$$

Hence, $\mathcal{D}_\lambda$ allows to define the initial point (that we will define as "$*$") from the which multiple iteration of (6.90) will lead to the last impact of the sequence before release (defined as "α"). In other terms, (6.90) will map a boundary of $\mathcal{D}$, let's say $\mathcal{D}_\lambda^* \equiv \lambda^*$, into another $\mathcal{D}_\lambda^\alpha \equiv \lambda_\alpha$, through multiple iterations. Then, the coordinates for velocity and position at the end of the chattering region, can be projected through $\mathcal{D}_P$ as a series expansion around τ_α.

Therefore, by considering that an impact occurs at $\tau_\alpha = \tau_0$ using (6.80) and (6.84), the velocity at the Poincaré surface (6.92) can be expressed as:

$$\begin{aligned}
&\dot{\bar{y}}_P \equiv \dot{\bar{y}}\left(\tau-\tau_0\right)\big|_{\tau=\tau_P} = \dot{\bar{y}}\left(\tau_P-\tau_0\right)\\
&= \dot{\bar{y}}\left(\tau_\alpha-\tau_0\right) + \left[\left.\frac{d\dot{\bar{y}}}{d\tau}\right|_{\tau=\tau_\alpha}\right]\left[\tau_P-\tau_\alpha\right] + \left[\left.\frac{d^2\dot{\bar{y}}}{d\tau^2}\right|_{\tau=\tau_\alpha}\right]\frac{\left[\tau_P-\tau_\alpha\right]^2}{2} + \mathcal{O}\left(\left[\tau_P-\tau_\alpha\right]^3\right)\\
&\approx \dot{\bar{y}}_\alpha + \ddot{\bar{y}}_\alpha\left[\tau_P-\tau_\alpha\right] + \dddot{\bar{y}}_\alpha\tfrac{1}{2}\left[\tau_P-\tau_\alpha\right]^2\\
&= \lambda_\alpha c\tau_\alpha^2 + c\tau_\alpha\left[\tau_P-\tau_\alpha\right] + c\tfrac{1}{2}\left[\tau_P-\tau_\alpha\right]^2\\
&= \lambda_\alpha c\tau_\alpha^2 + c\tau_\alpha\tau_P - c\tau_\alpha^2 + c\tfrac{1}{2}\left[\tau_P^2 - 2\tau_P\tau_\alpha + \tau_\alpha^2\right]\\
&= \lambda_\alpha c\tau_\alpha^2 + c\tau_\alpha\tau_P - c\tau_\alpha^2 + \tfrac{1}{2}c\tau_P^2 - c\tau_P\tau_\alpha + \tfrac{1}{2}c\tau_\alpha^2\\
&= \lambda_\alpha c\tau_\alpha^2 - \tfrac{1}{2}c\tau_\alpha^2 + \tfrac{1}{2}c\tau_P^2\\
&= \tfrac{1}{2}c\tau_P^2 + c\tau_\alpha^2\left[\lambda_\alpha - \tfrac{1}{2}\right].
\end{aligned} \tag{6.94}$$

Equivalently for the position, we have:

$$\begin{aligned}
&\bar{y}_P \equiv \bar{y}\left(\tau-\tau_0\right)\big|_{\tau=\tau_P} = \bar{y}\left(\tau_P-\tau_0\right)\\
&= \bar{y}\left(\tau_\alpha-\tau_0\right) + \left[\left.\frac{d\bar{y}}{d\tau}\right|_{\tau=\tau_\alpha}\right]\left[\tau_P-\tau_\alpha\right] + \left[\left.\frac{d^2\bar{y}}{d\tau^2}\right|_{\tau=\tau_\alpha}\right]\frac{\left[\tau_P-\tau_\alpha\right]^2}{2} + \left[\left.\frac{d^3\bar{y}}{d\tau^3}\right|_{\tau=\tau_\alpha}\right]\frac{\left[\tau_P-\tau_\alpha\right]^3}{6} + \mathcal{O}\left(\left[\tau_P-\tau_\alpha\right]^4\right)\\
&\approx \bar{y}_\alpha + \dot{\bar{y}}_\alpha\left[\tau_P-\tau_\alpha\right] + \ddot{\bar{y}}_\alpha\tfrac{1}{2}\left[\tau_P-\tau_\alpha\right]^2 + \dddot{\bar{y}}_\alpha\tfrac{1}{6}\left[\tau_P-\tau_\alpha\right]^3\\
&= \lambda_\alpha c\tau_\alpha^2\left[\tau_P-\tau_\alpha\right] + c\tau_\alpha\tfrac{1}{2}\left[\tau_P-\tau_\alpha\right]^2 + c\tfrac{1}{6}\left[\tau_P-\tau_\alpha\right]^3\\
&= \lambda_\alpha c\tau_\alpha^2\tau_P - \lambda_\alpha c\tau_\alpha^3 + c\tau_\alpha\tfrac{1}{2}\left[\tau_P^2 - 2\tau_P\tau_\alpha + \tau_\alpha^2\right] + c\tfrac{1}{6}\left[\tau_P^3 - 3\tau_P^2\tau_\alpha + 3\tau_P\tau_\alpha^2 - \tau_\alpha^3\right]\\
&= \lambda_\alpha c\tau_\alpha^2\tau_P - \lambda_\alpha c\tau_\alpha^3 + \tfrac{1}{2}c\tau_\alpha\tau_P^2 - c\tau_\alpha^2\tau_P + \tfrac{1}{2}c\tau_\alpha^3 + \tfrac{1}{6}c\tau_P^3 - \tfrac{1}{2}c\tau_P^2\tau_\alpha + \tfrac{1}{2}c\tau_P\tau_\alpha^2 - \tfrac{1}{6}c\tau_\alpha^3\\
&= \lambda_\alpha c\tau_\alpha^2\tau_P - \lambda_\alpha c\tau_\alpha^3 - \tfrac{1}{2}c\tau_\alpha^2\tau_P + \tfrac{1}{3}c\tau_\alpha^3 + \tfrac{1}{6}c\tau_P^3\\
&= \tfrac{1}{6}c\tau_P^3 + c\tau_\alpha^2\left[\lambda_\alpha\tau_P - \lambda_\alpha\tau_\alpha - \tfrac{1}{2}\tau_P + \tfrac{1}{3}\tau_\alpha\right]\\
&= \tfrac{1}{6}c\tau_P^3 + c\tau_\alpha^2\left[\tau_P\left[\lambda_\alpha - \tfrac{1}{2}\right] + \tau_\alpha\left[\tfrac{1}{3} - \lambda_\alpha\right]\right] \approx \tfrac{1}{6}c\tau_P^3 + c\tau_P\tau_\alpha^2\left[\lambda_\alpha - \tfrac{1}{2}\right].
\end{aligned} \tag{6.95}$$

Equations (6.94) and (6.95) give information about the coordinates of P from an impact experienced at τ_α. Taking into account that such an impact represents the history of events accumulated through infinite iterations of the relationship given by (6.90) under a complete chattering regime starting at $\mathcal{D}_\lambda^* \equiv \lambda^*$, the generalization for the map β describing the final state $\bar{Y}_P = \left[\bar{y}_P, \dot{\bar{y}}_P\right]^T$ of a trajectory with low-velocity impacts starting at $\bar{Y}^* = \left[0, \dot{\bar{y}}^*\right]^T$, can be given as:

$$\begin{aligned}
\dot{\bar{y}}_P &= \tfrac{1}{2}c\tau_P^2 + \beta\left(\lambda^*\right)c\tau^{*2}\\
\bar{y}_P &= \tfrac{1}{6}c\tau_P^3 + \beta\left(\lambda^*\right)c\tau^{*2}\tau_P\\
\ddot{\bar{y}}_P &= c\tau_P,
\end{aligned} \tag{6.96}$$

where:

$$\beta\left(\lambda^*\right) = \lim_{n\to\infty}\left(\prod_{i=1}^{n} h\left(\lambda_i\right)\right)^2\left[f^n\left(\lambda^*, r\right) - \frac{1}{2}\right], \tag{6.97}$$

being applicable to **any dynamical system** of the form (6.61)-(6.62) experiencing period-one complete chattering regime, under the assumptions considered.

6.5 The map in terms of variational equations

Developments performed through the Chapter, allowed for derivation of expression (6.96) giving a mapping inside the chattering region $\mathcal{D}$ for a generic periodically-forced impact oscillator. Now, it is time to employ such information to evaluate the stability of a periodic orbit experiencing complete-chattering motion. Then, as introduced in Chapter 2, this should be done in terms of the structural stability associated with variations of parameters in the system.

Therefore, it is fundamental at this stage to incorporate an explicit parameter dependence on (6.96), that given the application problem considered, should rely on the forcing frequency ω. This correspondence will be approximated numerically later in section 6.7.3 for a real cam-follower impacting model, on the basis of local perturbations. The latter is the aim of current section, where we will introduce the linear approximation for the problem of perturb locally a periodic orbit with chattering. This procedure is commonly termed as analysis of the first variational equations.

According to the conditions over which the map (6.96) has been defined, the multi-impacting orbit with chattering should be critical; i.e. the accumulation point is also the releasing one. Then, in order to study the transition under such a critical condition, the analysis of perturbations around the equilibrium must be performed. In so doing, let's start by consider the non-linear nature of λ in terms of its arguments:

$$\lambda \triangleq \frac{v}{c\left(t-t_\alpha\right)^2} = l\left(v,t\right). \tag{6.98}$$

Expansion in series of λ about $\lambda^* = l\left(v^*,t^*\right)\ \forall\ \lambda \in \mathcal{D}$, gives:

$$\lambda = l\left(v,t\right) \equiv l\left(v^*,t^*\right) + \left.\frac{\partial l}{\partial v}\right|_{\left(v^*,t^*\right)}\left(v-v^*\right) + \left.\frac{\partial l}{\partial t}\right|_{\left(v^*,t^*\right)}\left(t-t^*\right) + \mathcal{O}\left(\left(t-t^*\right)^2\right), \tag{6.99}$$

that can be approximated to the first order by assuming small perturbations, deriving:

$$\begin{aligned}
&\tilde{\lambda} = \lambda - \lambda^* \equiv l\left(v,t\right) - l\left(v^*,t^*\right)\\
&\approx \left.\left[\begin{array}{cc} \frac{\partial l}{\partial v} & \frac{\partial l}{\partial t}\end{array}\right]\right|_{\left(v^*,t^*\right)}\left[\begin{array}{c} v-v^*\\ t-t^*\end{array}\right]\\
&= \left.\left[\begin{array}{cc} \frac{1}{c(t-t_\alpha)^2} & \frac{-2v}{c(t-t_\alpha)^3}\end{array}\right]\right|_{\left(v^*,t^*\right)}\left[\begin{array}{c} v-v^*\\ t-t^*\end{array}\right]\\
&= \left[\begin{array}{cc} C_1 & C_2\end{array}\right]\left[\begin{array}{c} v-v^*\\ t-t^*\end{array}\right]\\
&\equiv C\left[\begin{array}{c} \tilde{v}\\ \tilde{t}\end{array}\right].
\end{aligned} \tag{6.100}$$

In this way, (6.97) can be expressed in terms of variations of $\lambda^* = \bar{\lambda}$, as:

$$\beta\left(\lambda\right) = \beta\left(\tilde{\lambda}+\bar{\lambda}\right) \equiv \beta\left(\bar{\lambda} + C\left[\begin{array}{c}\tilde{v}\\ \tilde{t}\end{array}\right]\right) = \begin{cases} \lim\limits_{n\to\infty}\left(\prod\limits_{i=1}^{n} h\left(\bar{\lambda}\right)\right)^2\left[f^n\left(\bar{\lambda},r\right)-\frac{1}{2}\right] & ;\tilde{\lambda}=0\\ \left(\prod\limits_{i=1}^{N} h\left(\tilde{\lambda}_i\right)\right)^2\left[f^N\left(\bar{\lambda}+C\left[\begin{array}{c}\tilde{v}\\ \tilde{t}\end{array}\right],r\right)-\frac{1}{2}\right] & ;\tilde{\lambda}>0\\ 0 & ;\tilde{\lambda}<0,\end{cases} \tag{6.101}$$

with $\tilde{\lambda}_i \equiv f^i\left(\bar{\lambda}+C\left[\begin{array}{c}\tilde{v}\\ \tilde{t}\end{array}\right],r\right)$ and $f\left(\bar{\lambda},r\right)-\bar{\lambda}=0$, in an equivalent way to what developed for (6.44).

On the other hand, from (6.94) and (6.95), the action of $\beta\left(\lambda\right)$ at the last impact before release, can be expressed in terms of $\varepsilon \equiv \varepsilon\left(\tau,\lambda\right)$ as:

$$\left[\begin{array}{c}\dot{\bar{y}}_P\\ \bar{y}_P\end{array}\right] = \left[\begin{array}{c}\frac{1}{2}c\tau_P^2 + c\tau^2\left[\lambda-\frac{1}{2}\right]\\ \frac{1}{6}c\tau_P^3 + c\tau_P\tau^2\left[\lambda-\frac{1}{2}\right]\end{array}\right] = \left[\begin{array}{c}\frac{1}{2}c\tau_P^2 + c\varepsilon\\ \frac{1}{6}c\tau_P^3 + c\tau_P\varepsilon\end{array}\right] = \left[\begin{array}{c}\Gamma\left(\varepsilon\right)\\ \Omega\left(\varepsilon\right)\end{array}\right]. \tag{6.102}$$

Therefore, expansion of (6.102) around $\varepsilon_\alpha \equiv \varepsilon(\tau_\alpha, \lambda_\alpha)$ gives:

$$\begin{aligned} &\begin{bmatrix} \dot{\bar{y}}_P \\ \bar{y}_P \end{bmatrix} = \begin{bmatrix} \Gamma(\varepsilon) \\ \Omega(\varepsilon) \end{bmatrix} \equiv \begin{bmatrix} \Gamma(\varepsilon_\alpha) \\ \Omega(\varepsilon_\alpha) \end{bmatrix} + \begin{bmatrix} \frac{d\Gamma}{d\varepsilon} & \frac{d\Omega}{d\varepsilon} \end{bmatrix}^T \Big|_{\varepsilon=\varepsilon_\alpha} (\varepsilon - \varepsilon_\alpha) + \mathcal{O}\left((\varepsilon-\varepsilon_\alpha)^2\right) \\ \Rightarrow &\begin{bmatrix} \dot{\bar{y}}_P \\ \bar{y}_P \end{bmatrix} - \begin{bmatrix} \Gamma(\varepsilon_\alpha) \\ \Omega(\varepsilon_\alpha) \end{bmatrix} \triangleq \begin{bmatrix} \tilde{v}_P \\ \tilde{x}_P \end{bmatrix} \approx \begin{bmatrix} c \\ c\tau_P \end{bmatrix} (\varepsilon - \varepsilon_\alpha) = \begin{bmatrix} c \\ c\tau_P \end{bmatrix} \tilde{\varepsilon} = B\tilde{\varepsilon}, \end{aligned} \tag{6.103}$$

where $\tilde{\varepsilon}$ corresponds to the propagation through β to the perturbation taken at the chattering region. Therefore, perturbations at the Poincaré surface (6.92) can be expressed in terms of perturbations at $\lambda^* = \bar{\lambda}$, as:

$$\begin{bmatrix} \tilde{v}_P \\ \tilde{x}_P \end{bmatrix} = B\tilde{\varepsilon} \triangleq B\beta\left(\lambda^* + \tilde{\lambda}\right) = B\beta\left(\bar{\lambda} + C\begin{bmatrix} \tilde{v} \\ \tilde{t} \end{bmatrix}\right). \tag{6.104}$$

6.6 Constructing the Poincaré map of a Chattering orbit

In the more general case of PWS dynamical systems, the concept of discontinuity mappings was introduced in section 2.6. There, the dynamics of the events associated to the interaction with discontinuities were coupled with the global behaviour of the trajectory by composition between the corresponding local and global maps. In this section we study a periodic orbit with chattering. This is illustrated in Figure 6.8 by a trajectory crossing two boundaries, representing each the map associated with the local β, and global Θ, dynamics.

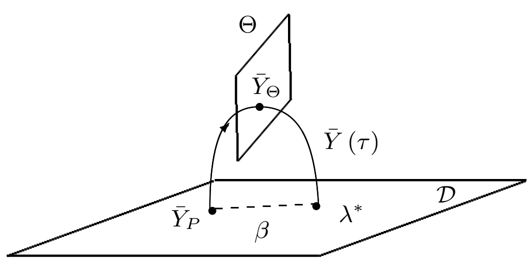

Figure 6.8 — Graphical illustration of the composition between local and global behaviour of a trajectory with chattering. For all the calculations of section 6.6, $\bar{Y}_\Theta = \bar{Y}^* \equiv \lambda^* \equiv \mathcal{D}^*_\lambda$. In the graph, they were taken as different points for illustration of the concept.

According to the Figure, for all the following calculations $\bar{Y}_\Theta = \bar{Y}^* \equiv \lambda^* \equiv \mathcal{D}^*_\lambda$.

The qualitative behaviour of an orbit with period-one complete chattering accumulating at the releasing point, is essentially the same when thinking about the interaction between the system flow and the restitution map after collisions. The key in order to establish a boundary, is the definition of the chattering region $\mathcal{D}$ in (6.91), containing the subset of the state space in which the chattering map (6.96) can be applied.

Once this set has been defined, the remaining part of the trajectory $\bar{Y}(\tau)$ is confined to the complementary set by a mapping Θ from P in (6.92) to $\mathcal{D}^*_\lambda \equiv \lambda^*$; i.e.

$$\Theta : P \in \Re^2 \rightarrow \Pi_* \in \Re^2 \equiv (v_P, x_P) \rightarrow (v^*, t^*), \tag{6.105}$$

with Π_* defining the region:

$$\Pi_* = \left\{ \bar{Y}(\tau) \in \Re^2 : \tau = \tau^* \in \mathcal{D}_\lambda \right\}. \tag{6.106}$$

In general, we can assume that such a map is smooth without grazings or complete chattering outside $\mathcal{D}$. Then a linear approximation of the map Θ around $\mathcal{D}^*_\lambda$ can be obtained in terms of variational equations. Therefore, it is possible to perform analysis of variations (perturbations) of the equilibrium in the periodic – of period $\tau = T$ – multi-impacting trajectory with chattering.

As defined in section 2.2.5, the linear equivalent of the map Θ around the equilibrium $\bar{Y}^*$, corresponds to:

$$\Theta^*_{\bar{Y}} = A \equiv \left(I - \frac{F\left(\bar{Y}^*\right) H^*_{\bar{Y}}}{H^*_{\bar{Y}} F\left(\bar{Y}^*\right)} \right) \Phi_{\bar{Y}} \left(\bar{Y}^*, T - [\tau_P - \tau^*] \right), \tag{6.107}$$

where $H^*_{\bar{Y}}$ represents the gradient of the constraint $H = \bar{y}$, evaluated at λ^*; $F\left(\bar{Y}\right)$ the system vector field as in (6.60) and $\Phi_{\bar{Y}}\left(\bar{Y}^*, T - [\tau_P - \tau^*]\right)$ the Jacobian of the multi-impacting trajectory within the set $\bar{\mathcal{D}} = \Re^3 - \mathcal{D}$, evaluated at the boundary of $\mathcal{D}_\lambda \equiv \lambda^*$; or equivalently, the Monodromy matrix.

Using (6.107), it is then possible to write:

$$\begin{bmatrix} \tilde{v} \\ \tilde{t} \end{bmatrix} \approx A \begin{bmatrix} \tilde{v}_P \\ \tilde{x}_P \end{bmatrix}, \tag{6.108}$$

and hence, by appending the results generated for β in equation (6.104), variations (perturbations) across the overall trajectory can be approximated by the composition of the linear equivalent of the mappings, as:

$$\begin{bmatrix} \tilde{v} \\ \tilde{t} \end{bmatrix}_{k+1} = AB\beta \left(\lambda^* + C \begin{bmatrix} \tilde{v} \\ \tilde{t} \end{bmatrix}_k \right) \triangleq \Theta \circ \beta \left(\lambda^* + \tilde{\lambda} \right). \tag{6.109}$$

Notice that despite the dimension is preserved under the action of Θ in (6.105), there is not a correspondence between coordinates. This is a direct consequence of the reduction of dimensionality performed inside the chattering region, that essentially annihilates information in the direction of position. The matrix B will play a key role in matching coordinates between the composed maps, as will be shown later in the application example of section 6.7.4.

Also, notice that according to equation (6.101), the contribution of β in the overall dynamics (6.109) can be neglected when no variations are applied to the equilibrium. This is an expected result, given that under small (or null) perturbations the linearity assumption holds and therefore the composition of the maps can be translated in superposition of the individual effects.

6.7 Chattering bifurcation in a practical case: the cam-follower model

Results presented so far, have demonstrated that it is possible to perform a local description of the transition into aperiodicity experienced by a general impact oscillator of the form (6.57), after interruption of a complete chattering regime. Then, these can be employed to explain the bifurcation scenario derived from the interaction between the cam and follower bodies in the configuration depicted in Figure 4.9-(b), resembling the mechanical core governing synchronization in the motion of valves of an internal combustion engine [6].

This kind of cam-follower systems has been discussed in Chapter 4, together with their physical implementation, modelling and experimental results. For the sake of clarity, some of the expressions given in Chapter 4 will be repeated here.

The motion of the follower can be described with the time evolution of its angular displacement and velocity, being modelled in terms of a hybrid scheme with two main modes of operation:

$$J\ddot{\theta}_f + K\left(x_A\tan(\theta_f) + \frac{d}{\cos(\theta_f)} - (y_A - d_0 - d_1)\right)\left(\frac{x_A}{\cos^2(\theta_f)} + d\frac{\sin(\theta_f)}{\cos^2(\theta_f)}\right) = \begin{cases} 0, \\ M(t). \end{cases} \quad (6.110)$$

Namely: 1) a *free flight* when the follower detaches from the cam behaving as an unforced harmonic oscillator and 2) a *constrained mode* corresponding with the two bodies being in contact; i.e. when the periodic forcing exerted by the cam, $M(t)$, is non zero.

The transition between such modes at the discontinuity boundary is given by the restitution law:

$$\dot{\theta}_f(t_k^+) = -r\dot{\theta}_f(t_k^-) + (1+r)\,\omega\frac{d}{d\phi}\hat{\theta}_c, \quad (6.111)$$

with $0 < r < 1$ being the restitution coefficient for inelastic collisions, ω the rotational velocity of the cam (taken as parameter), $\phi \equiv \omega t$ the forcing phase and $\hat{\theta}_c$ the angular projection of the contact point. See Chapter 4 for further details.

The system (6.110)-(6.111) is formulated in a way which fits the description of (6.61)-(6.62) and therefore the results described in section 6.4 can be applied to it, as will be shown in what follows.

6.7.1 The Chattering region

In order to study the transition from an orbit with complete chattering in a vicinity of the releasing phase $\phi_\alpha \equiv mod\,(t_\alpha, T)$ with $T = 2\pi/\bar{\omega}$, the first thing we need to define is the critical parameter value $\bar{\omega}$ for which the last impact of a period-one complete chattering motion occurs close enough to the releasing point; i.e. such that $|\phi_\alpha - \phi_\infty| \to 0$, justifying a local analysis of it.

In doing so, continuation of the multi-impacting trajectory with a test function based on monitoring the time of sticking was performed as described in section 3.5.1. As a result, an estimated value of $\bar{\omega} \approx 152.67658$ rpm, with a precision of 10 decimal digits was calculated. See Figure 3.9 for details.

Then, under such a critical parameter value, the numerical error detected or the difference between last impact and releasing phases corresponds to $\Delta\phi = \phi_\alpha - \phi_\infty \approx 0.4201 * 10^{-5}$ $[s]$. This difference, constitutes a reference for quantification of the analysis in a local sense and therefore should be employed as criterion for choosing the valid set of points defining the boundaries of $\mathcal{D}$ in (6.91).

Hence, by selecting a value of $\bar{\omega}^* = 152.67$ rpm, an orbit with complete chattering accumulating in a vicinity[2] of the releasing phase is expected to occur. The set of values defining the chattering region for such $\bar{\omega}^*$ are given in Table 6.1 and depicted in Figures 6.9 and 6.10.

[2] The validity of the local sense for such a value is confirmed by the results obtained numerically, as will be shown later in the Chapter.

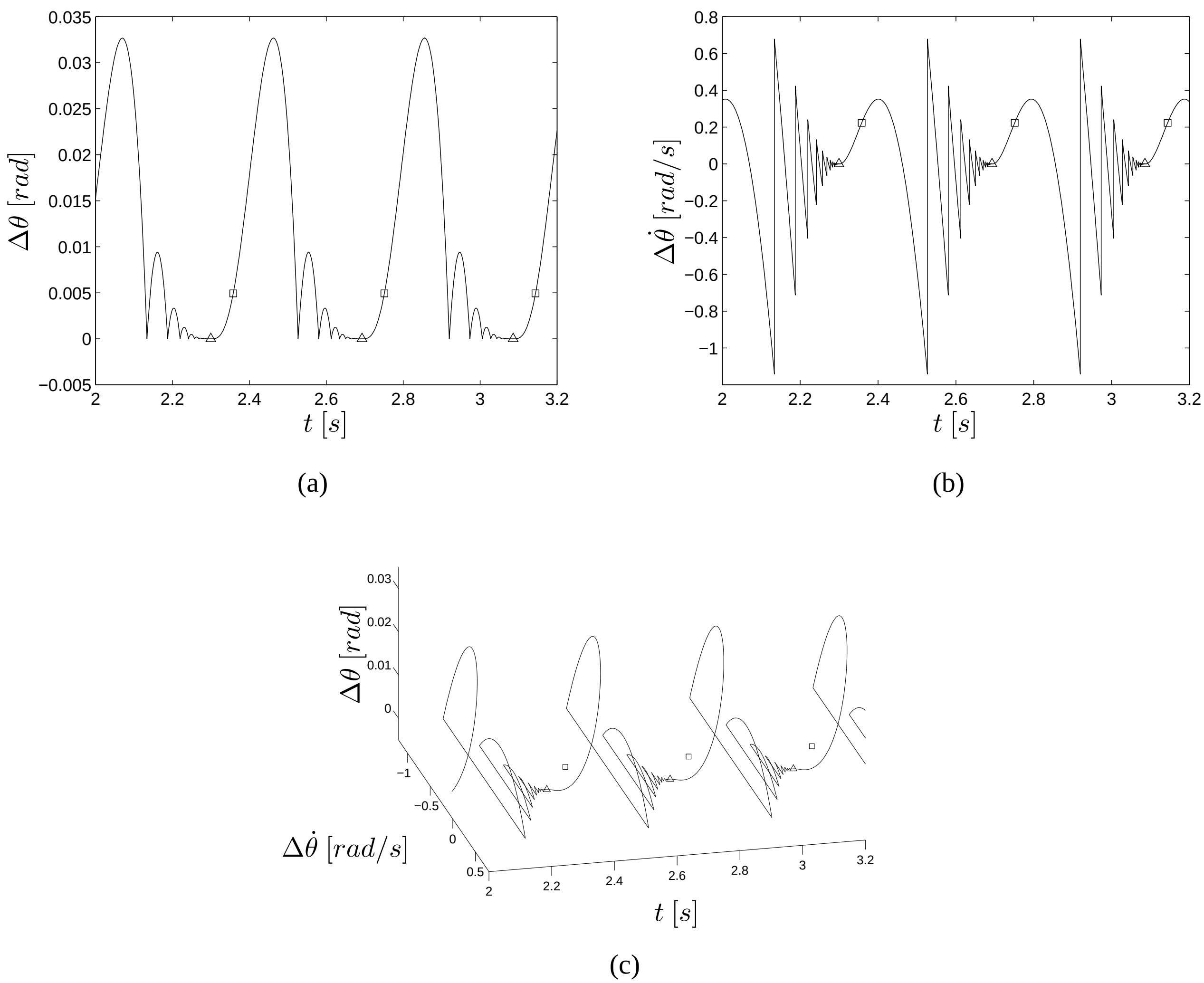

Figure 6.9 — Periodic trajectory with complete chattering for $\bar{\omega}^* = 152.67\ rpm$. Time evolution for relative position in (a) and relative velocity in (b) of the particle – the follower – with a combination of the two in (c). In all graphs, a triangle represents the boundary of $\mathcal{D}$ equivalent to $\mathcal{D}^*_\lambda$ as analogously a square depicts the location for $\phi_P \in \mathcal{D}_P$.

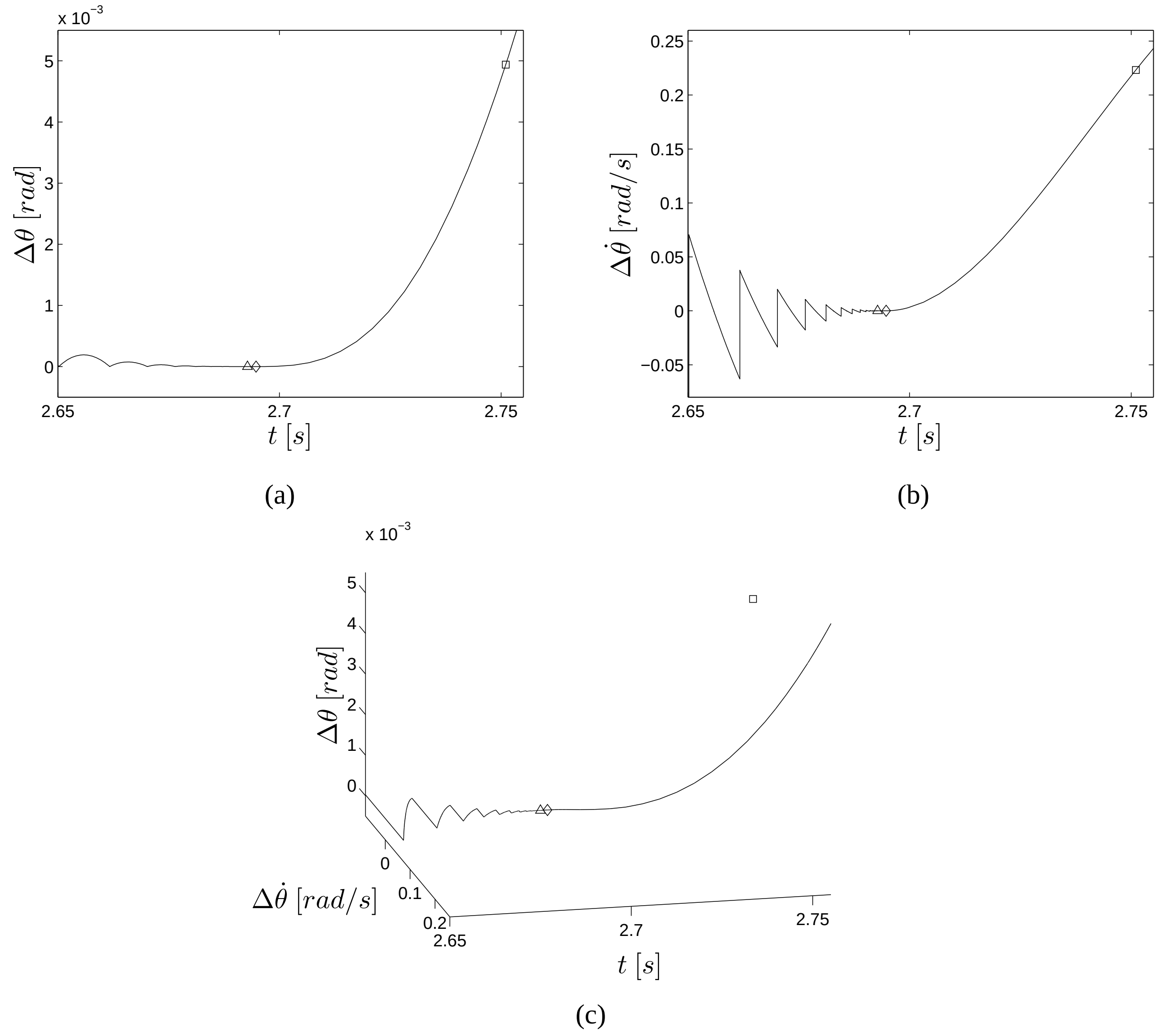

Figure 6.10 — Detail for a trajectory with complete chattering for $\bar{\omega}^* = 152.67\ rpm$, depicting the region where local analysis can be applied. Time evolution for relative position in (a) and relative velocity in (b) of the particle – the follower – with a combination of the two in (c). In all graphs, a triangle represents the boundary of $\mathcal{D}$ equivalent to $\mathcal{D}^*_\lambda$ as analogously a square depicts the location for $\phi_P \in \mathcal{D}_P$. In addition, a diamond is intended to denote $\mathcal{D}^\alpha_\lambda$.

Table 6.1 — Boundaries of the set $\mathcal{D}$ in (6.91) with $\tau \equiv \phi$, and related quantities defining the chattering region for $\bar{\omega}^* = 152.67\ rpm$.

Set of points	coordinates in $Y = (\theta_f, \dot{\theta}_f, \phi)$	coordinates in $\bar{Y} = (\Delta\theta, \Delta\dot{\theta}, \phi)$
$\mathcal{D}^*_\lambda$	$(0.30531, 0.86956, 0.33474)$	$(2.72953 * 10^{-10}, -5.00814 * 10^{-8}, 0.33474)$
$\mathcal{D}^\alpha_\lambda$	$(0.30698, 0.84854, 0.33668)$	$(2.76467 * 10^{-10}, -0.02595 * 10^{-8}, 0.33668)$
ϕ_P	$T\ [s]$	$T\ [s]$
$y_P \equiv \theta_f\ (\phi_P)$	$0.33717\ [rad]$	$0.00494\ [rad]$
$\dot{y}_P \equiv \dot{\theta}_f\ (\phi_P)$	$0.22313\ [rad/s]$	$0.22315\ [rad/s]$
$T \equiv 2\pi/\bar{\omega}^*$	$0.39300\ [s]$	$0.39300\ [s]$
$\Delta\phi = \phi_\alpha - \phi_\infty$	$0.00194\ [s]$	$0.00194\ [s]$

The parabolic relationship between state variables inside $\mathcal{D}$ – fundamental condition for applying the mapping (6.96)-(6.97) – is proven to be extensible even for choices of $\mathcal{D}^*_\lambda$ slightly far from ϕ_α, as demonstrated by the replication of the impacting trajectory in Figure 6.11 after use of (6.90), where the location of the "$*$" point was selected 5 impacts before such referenced in Table 6.1. Here, the accuracy in prediction of the accumulation point for the multi-impacting trajectory is remarkable. Associated values can be found in Table 6.2. Notice that there the time has not been taken in modulus. Nevertheless from the definition of the mapping, same behaviour is expected to occur when $t = \phi \equiv mod\,(t, T)$.

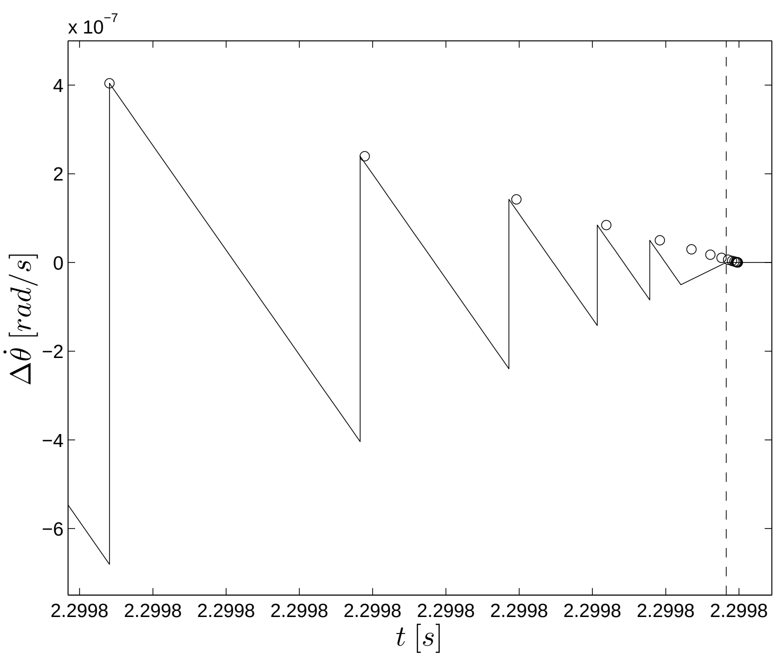

Figure 6.11 — Validation for the local impact map. Circles showing the prediction for impact events by iteration of (6.96), demonstrating agreement with results generated by simulation of the system flow. The dashed line at the right indicates the accumulation time t_∞ calculated numerically.

An important quantity: c in (6.84), has been estimated numerically from system equations (6.110)-(4.23),

Table 6.2 — Parameter values employed to reproduce the local impacting behaviour within the set $\mathcal{D}$ for $\bar{\omega}^* = 152.67\ rpm$ for a single forcing period.

Quantity	description	value
$\Delta\theta^*$	relative initial velocity	$4.03908 * 10^{-7}\ [rad/s]$
t_α	releasing time	$2.3017041\ [s]$
t^*	initial time	$2.2997622\ [s]$
c	jerk at zero acceleration	238.81
λ^*	λ initial $\equiv \frac{\Delta\theta^*}{c(t^*-t_\alpha)^2}$	$4.48514 * 10^{-4}$
t_∞	accumulation time calculated numerically	$2.2997661\ [s]$
$\hat{t}_\infty$	accumulation time predicted by mapping	$2.2997664\ [s]$

as:

$$\begin{aligned}
&c \equiv \Delta\dddot{\theta}|_{\phi=\phi_\alpha} \Rightarrow \\
&\Delta\ddot{\theta} = M(t) - \tfrac{K}{J}\left[x_A \tan\left(\theta_f\right) + \tfrac{d}{\cos\left(\theta_f\right)} - (y_A - d_0 - d_1)\right]\left[\tfrac{x_A + d\sin\left(\theta_f\right)}{\cos^2\left(\theta_f\right)}\right] \equiv M(t) - m(\theta_f) \\
&\Rightarrow M \equiv \tfrac{d^2}{d\phi^2}\hat{\theta}_c \tfrac{d^2}{dt^2}\phi = \omega^2 \tfrac{d^2}{d\phi^2}\hat{\theta}_c \Rightarrow \Delta\ddot{\theta} = \omega^2 \tfrac{d^2}{d\phi^2}\hat{\theta}_c - m(\theta_f) \\
&\Delta\dddot{\theta} = \tfrac{d}{dt}\Delta\ddot{\theta} = \omega^3 \tfrac{d^3}{d\phi^3}\hat{\theta}_c - \tfrac{d}{d\theta_f} m \tfrac{d}{dt}\theta_f = \omega^3 \tfrac{d^3}{d\phi^3}\hat{\theta}_c - \dot{\theta}_f \tfrac{d}{d\theta_f} m \\
&\Rightarrow c = \omega^3 \tfrac{d^3}{d\phi^3}\hat{\theta}_c - \dot{\theta}_f \tfrac{d}{d\theta_f} m\Big|_{\phi=\phi_\alpha}.
\end{aligned} \tag{6.112}$$

An illustration of the jerk $\Delta\dddot{\theta}$ and the location of c on it, are depicted in Figure 6.12.

6.7.2 Local behaviour: perturbation of states

Once the chattering region has been defined, it is possible to perform the local analysis of the system dynamics in terms of variational equations, by employing the results derived in section 6.5.

Hence, by considering a multi-impacting trajectory with complete chattering described locally in terms of the set of points listed in Table 6.1, the validation of the predictions of the map can be performed by comparison with the results generated by simulating perturbed versions of the trajectory, as schematically depicted in Figure 6.13. Here, the perturbation at the beginning of the chattering region $\mathcal{D}^*_\lambda$, has been applied on a single direction, the velocity, in order to analyze independently its effect in the overall dynamics, as an

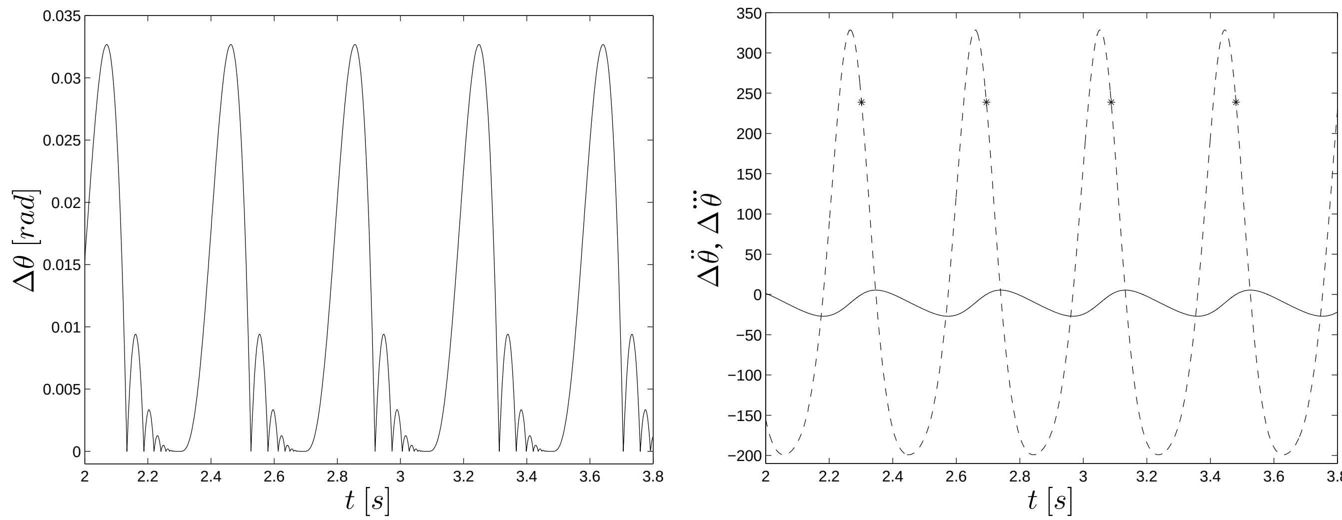

(a) (b)

Figure 6.12 — Numerical calculation of jerk value at releasing. (a) Time evolution for relative position of the particle – the follower – under periodic chattering. (b) Relative acceleration (solid); i.e. $d^2\Delta\theta/dt^2$ and relative jerk (dashed); i.e. $d^3\Delta\theta/dt^3$, showing the value of c in (6.112) at zero acceleration by an asterisk. Note that this zero acceleration phase ϕ_α coincides with the accumulation point of the multi-impacting trajectory and is periodic.

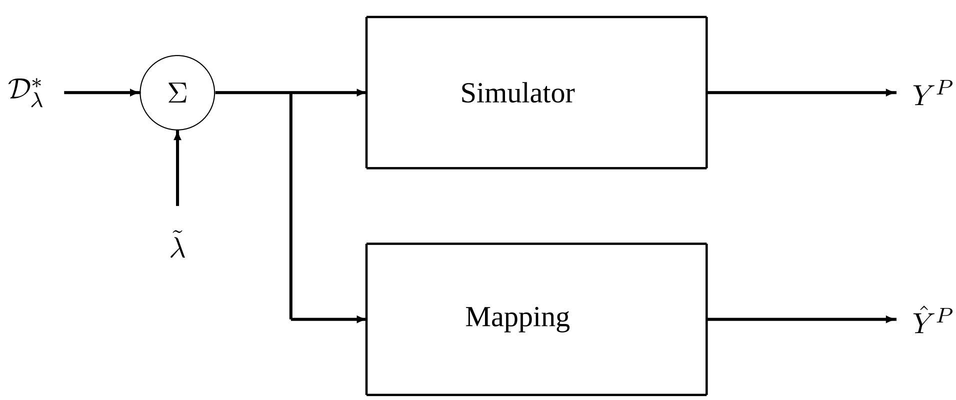

Figure 6.13 — Illustration of the methodology employed to validate local predictions of the chattering map, within the set $\mathcal{D}$.

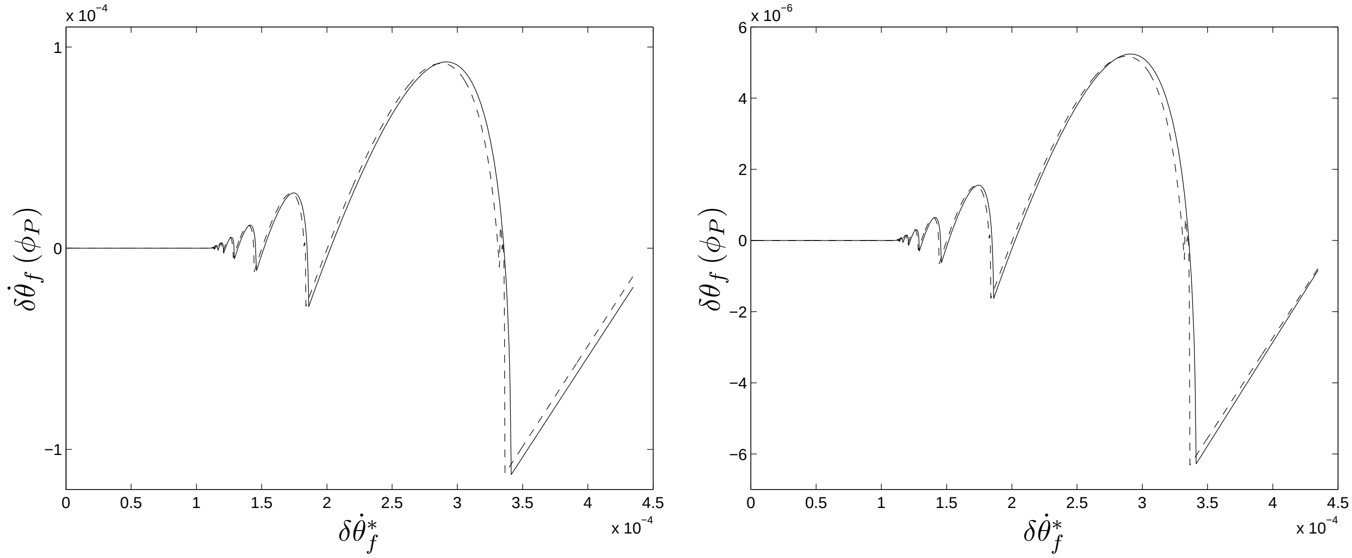

(a) (b)

Figure 6.14 — Reconstruction of variations in absolute coordinates for: (a) velocity and (b) position; at the Poincaré surface (6.92) by employing information of the local map between boundaries of the set $\mathcal{D}$. The perturbation $\tilde{\lambda}$ has been applied in the direction of velocity. For both, the solid line represents calculations performed by simulation of system flow, with dashed mapping predictions.

illustration of the subsequent composed behaviour. Therefore from (6.104):

$$
\begin{aligned}
&\tilde{\lambda} \triangleq C \begin{bmatrix} \tilde{v} \\ \tilde{t} \end{bmatrix} = \begin{bmatrix} \frac{1}{c(t-t_\alpha)^2} & \frac{-2v}{c(t-t_\alpha)^3} \end{bmatrix}\Big|_{(v^*,t^*)} \begin{bmatrix} v - v^* \\ t - t^* \end{bmatrix} \\
&\Rightarrow \tilde{\lambda} = \begin{bmatrix} \frac{1}{c(\phi-\phi_\alpha)^2} & \frac{-2\Delta\dot{\theta}}{c(\phi-\phi_\alpha)^3} \end{bmatrix}\Big|_{(\Delta\dot{\theta}^*,\phi^*)} \begin{bmatrix} \dot{\theta}_f - \dot{\theta}_f^* \\ \phi - \phi^* \end{bmatrix} \\
&= \begin{bmatrix} \frac{1}{c(\phi^*-\phi_\alpha)^2} & \frac{-2\Delta\dot{\theta}^*}{c(\phi^*-\phi_\alpha)^3} \end{bmatrix} \begin{bmatrix} \delta\dot{\theta}_f^* \\ 0 \end{bmatrix} = \frac{\delta\dot{\theta}_f^*}{c(\phi^*-\phi_\alpha)^2} \\
&\Rightarrow \lambda = \lambda^* + \tilde{\lambda} \equiv \mathcal{D}_\lambda^* + \frac{\delta\dot{\theta}_f^*}{c(\phi^*-\phi_\alpha)^2} \\
&\Rightarrow \begin{bmatrix} \tilde{v}_P \\ \tilde{x}_P \end{bmatrix} \equiv \begin{bmatrix} \delta\dot{\theta}_f\,(\phi_P) \\ \delta\theta_f\,(\phi_P) \end{bmatrix} \triangleq B\beta\left(\mathcal{D}_\lambda^* + \frac{\delta\dot{\theta}_f^*}{c(\phi^*-\phi_\alpha)^2}\right) = \begin{bmatrix} c \\ c\,(\phi_P - \phi_\alpha) \end{bmatrix} \beta\left(\mathcal{D}_\lambda^* + \frac{\delta\dot{\theta}_f^*}{c(\phi^*-\phi_\alpha)^2}\right) \\
&\Rightarrow \hat{Y}_P = \begin{bmatrix} \theta_f\,(\phi_P) \\ \dot{\theta}_f\,(\phi_P) \\ \phi_P \end{bmatrix} + \begin{bmatrix} \delta\theta_f\,(\phi_P) \\ \delta\dot{\theta}_f\,(\phi_P) \\ 0 \end{bmatrix},
\end{aligned}
\tag{6.113}
$$

with $\hat{Y}_P$ denoting an estimate of the absolute coordinates Y_P at the Poincaré section P in (6.92), generated after simulation of the system equations.

Results obtained numerically for $\delta\dot{\theta}_f^*$, equivalent to a percentage of 0.05% for $\dot{\theta}_f^*$ in Table 6.1, are depicted in Figure 6.14. Here it is evident the good matching obtained when resembling the variation of coordinates at the Poincaré section P, confirming the validity of the mapping and of the assumptions for local analysis. Note also that a large degree of precision (i.e. for infinitesimally small perturbations), is constrained by the finite resolution available in the numerical representation and manipulation of data.

Taking into account the linearization performed by the local analysis, an analogous matching between numerical and analytical predictions is expected when perturbing only the direction of ϕ, and consequently for a superposition of both. Nevertheless, for such a case the higher sensitivity of the time derivatives doesn't allow to illustrate associated results in a clear manner as in the case of velocity, and then have been avoided.

6.7.3 Local behaviour: parameter incidence

Following and analogue procedure to what just developed for the case of perturbation in coordinates of the chattering region, it is possible to address the relevant problem of studying the parameter dependence of system dynamics in terms of variation of the forcing frequency ω.

Then, in order to be performed, it is necessary to include an additional term in the series expansion of λ in (6.100), representing the action of $\tilde{\omega}^*$. Physically, this corresponds with a change in the location of ϕ_α and consequently of c, and hence:

$$\begin{aligned}
\tilde{\lambda} &= \lambda - \lambda^* \equiv l\left(\Delta\dot{\theta}, \phi, \omega\right) - l\left(\Delta\dot{\theta}^*, \phi^*, \bar{\omega}^*\right) \\
&\approx \left[\begin{array}{ccc} \partial l/\partial\Delta\dot{\theta} & \partial l/\partial\phi & \partial l/\partial\omega \end{array}\right]\Big|_{\left(\Delta\dot{\theta}^*, \phi^*, \bar{\omega}^*\right)} \left[\begin{array}{c} \dot{\theta}_f - \dot{\theta}_f^* \\ \phi - \phi^* \\ \omega - \bar{\omega}^* \end{array}\right] \\
&= \left[\begin{array}{ccc} C_1 & C_2 & C_3 \end{array}\right] \left[\begin{array}{c} \dot{\theta}_f - \dot{\theta}_f^* \\ \phi - \phi^* \\ \omega - \bar{\omega}^* \end{array}\right] \\
&\equiv C \left[\begin{array}{c} \delta\dot{\theta}_f \\ \tilde{\phi} \\ \tilde{\omega}^* \end{array}\right].
\end{aligned} \tag{6.114}$$

Analogously, the distance $(\phi_P - \phi_\alpha)$ necessary for reproduction of the coordinates at the Poincaré section, is affected by $\tilde{\omega}^*$. Therefore, from (6.103) we have:

$$\begin{aligned}
&\left[\begin{array}{c} \Delta\dot{\theta}(\phi_P) \\ \Delta\theta(\phi_P) \end{array}\right] = \left[\begin{array}{c} \frac{1}{2}c(\omega)\left[\phi_P - \phi_\alpha(\omega)\right]^2 + c(\omega)\varepsilon \\ \frac{1}{6}c(\omega)\left[\phi_P - \phi_\alpha(\omega)\right]^3 + c(\omega)\left[\phi_P - \phi_\alpha(\omega)\right]\varepsilon \end{array}\right] \\
&= \left[\begin{array}{c} \Gamma(\varepsilon, \omega) \\ \Omega(\varepsilon, \omega) \end{array}\right] \equiv \left[\begin{array}{c} \Gamma(\varepsilon^*, \bar{\omega}^*) \\ \Omega(\varepsilon^*, \bar{\omega}^*) \end{array}\right] + \left[\begin{array}{cc} \frac{\partial}{\partial\omega}\Gamma & \frac{\partial}{\partial\varepsilon}\Gamma \\ \frac{\partial}{\partial\omega}\Omega & \frac{\partial}{\partial\varepsilon}\Omega \end{array}\right]\Bigg|_{(\varepsilon^*, \bar{\omega}^*)} \left[\begin{array}{c} \omega - \bar{\omega}^* \\ \varepsilon - \varepsilon^* \end{array}\right] + \mathcal{O}\left(\left[\begin{array}{c} \omega - \bar{\omega}^* \\ \varepsilon - \varepsilon^* \end{array}\right]^2\right) \\
&\Rightarrow \left[\begin{array}{c} \Delta\dot{\theta}(\phi_P) \\ \Delta\theta(\phi_P) \end{array}\right] - \left[\begin{array}{c} \Gamma(\varepsilon^*, \bar{\omega}^*) \\ \Omega(\varepsilon^*, \bar{\omega}^*) \end{array}\right] \equiv \left[\begin{array}{c} \delta\dot{\theta}_f(\phi_P) \\ \delta\theta_f(\phi_P) \end{array}\right] \approx \left[\begin{array}{cc} \frac{\partial}{\partial\omega}\Gamma & \frac{\partial}{\partial\varepsilon}\Gamma \\ \frac{\partial}{\partial\omega}\Omega & \frac{\partial}{\partial\varepsilon}\Omega \end{array}\right]\Bigg|_{(\varepsilon^*, \bar{\omega}^*)} \left[\begin{array}{c} \omega - \bar{\omega}^* \\ \varepsilon - \varepsilon^* \end{array}\right] \\
&= \left[\begin{array}{cc} \frac{\partial}{\partial\omega}\Gamma & \frac{\partial}{\partial\varepsilon}\Gamma \\ \frac{\partial}{\partial\omega}\Omega & \frac{\partial}{\partial\varepsilon}\Omega \end{array}\right]\Bigg|_{(\varepsilon^*, \bar{\omega}^*)} \left[\begin{array}{c} \tilde{\omega}^* \\ \tilde{\varepsilon}^* \end{array}\right] = B \left[\begin{array}{c} \tilde{\omega}^* \\ \tilde{\varepsilon}^* \end{array}\right],
\end{aligned} \tag{6.115}$$

with ε denoting the contribution of the map $\beta(\lambda)$ at the releasing phase.

Given the transcendental nature of the system equations, it is not straightforward to solve for explicit expressions indicating the dependence of c and ϕ_α on ω. Therefore, heuristic estimation for the quantities $\frac{\partial l}{\partial\omega}\Big|_{\left(D^*_{\lambda}, \bar{\omega}^*\right)}$, $\frac{\partial\Gamma}{\partial\omega}\Big|_{(\varepsilon^*, \bar{\omega}^*)}$ and $\frac{\partial\Omega}{\partial\omega}\Big|_{(\varepsilon^*, \bar{\omega}^*)}$, has been accomplished by taking advantage of the linear character

Table 6.3 — Numerical values employed to reconstruct the variation on coordinates at the Poincaré surface, by perturbing the parameter $\bar{\omega}^*$.

Quantity	description	value
$\bar{\omega}^*$	reference parameter value	$152.67\ rpm$
$\tilde{\omega}^*$	maximum deviation percentage	0.1%
$\frac{\partial}{\partial\omega} l\Big\rvert_{(D^*_\lambda,\bar{\omega}^*)}$	coefficient for dependence of λ on ω	3.9
$\frac{\partial}{\partial\omega}\Gamma\Big\rvert_{(\varepsilon^*,\bar{\omega}^*)}$	coefficient for dependence of Γ on ω	0.009647
$\frac{\partial}{\partial\omega}\Omega\Big\rvert_{(\varepsilon^*,\bar{\omega}^*)}$	coefficient for dependence of Ω on ω	0.0002305

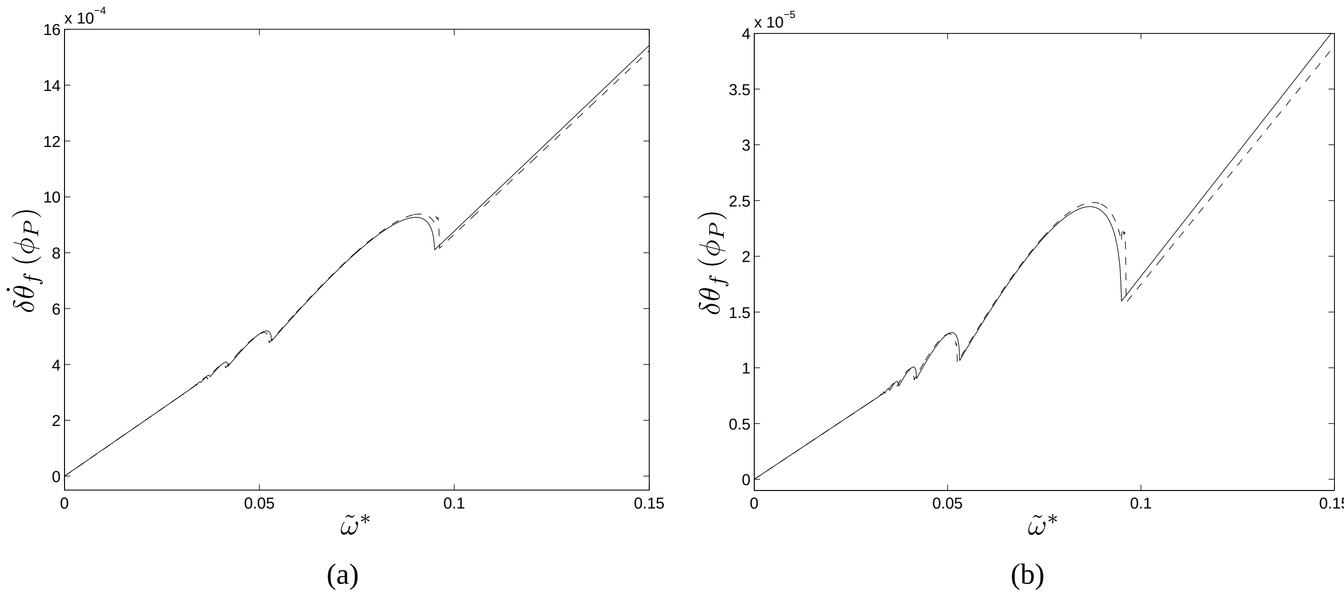

Figure 6.15 — Reconstruction of variations in absolute coordinates for: (a) velocity and (b) position; at the Poincaré surface (6.92) by employing information of the local map between boundaries of the set $\mathcal{D}$. The perturbation has been applied in the direction of the parameter $\bar{\omega}^*$. For both, the solid line represents calculations performed by simulation of system flow, with dashed mapping predictions.

of local expansions; i.e. by isolating the contribution of perturbations in the direction of the parameter $\tilde{\omega}^*$ and superimposing the remaining ponderation terms, previously calculated for the case of non-parameter dependence. Related results are listed in Table 6.3 and validated in Figure 6.15 with a remarkable resemblance. Note that essentially the effect characterizing the variation of the parameter, is a rotation (tilt) on the mean value of the map, whilst preserving – as expected – its lobed shape.

6.7.4 Global behaviour: closing the loop

Adoption of results developed in section 6.6 allows the accurate estimation of the Monodromy matrix and related quantities at $\mathcal{D}^*_\lambda$, in order to develop the linear equivalent for the map Θ in (6.107). Table 6.4

summarizes the main quantities employed in calculations of equation (6.116):

$$\begin{bmatrix} \delta\theta_f^* \\ \delta\dot{\theta}_f^* \\ \tilde{\phi}^* \end{bmatrix}_{k+1} = B \left[K_\beta \beta \left(\lambda^* + K_C C A \begin{bmatrix} \delta\theta_f^* \\ \delta\dot{\theta}_f^* \\ \tilde{\phi}^* \end{bmatrix}_k \right) \right], \tag{6.116}$$

with:

$$B = \begin{bmatrix} c\,(\phi_P - \phi_\alpha) & 0 \\ 0 & c \\ 0 & 0 \end{bmatrix}; \qquad C = \begin{bmatrix} 0 & \frac{1}{c(\phi^* - \phi_\alpha)^2} & \frac{-2\Delta\dot{\theta}^*}{c(\phi^* - \phi_\alpha)^3} \end{bmatrix}. \tag{6.117}$$

Notice that an attempt has been done in order to attenuate sources of mislead in computations by limiting, for example, the local region to the minimum allowable set $\mathcal{D} = \mathcal{D}_\lambda \cup \{\emptyset\}$, with $|\phi_\alpha - \phi_\infty| \to 0$ and by applying the minimum range of perturbations detected numerically. Nevertheless, the sensitivity of the variations in a fine range implies the necessity of a scale compensation in order to overcome the impossibility of having an infinite resolution in data. In such a way it is possible to approximate the map for an entire period, as depicted in Figure 6.16, where effects of nonlinearities and round-off errors become evident.

Table 6.4 — Numerical values employed to reconstruct the variation on coordinates at the releasing phase ϕ_α, by perturbing in the direction of velocity during a complete forcing period.

Quantity	description	value
$\bar{\omega}^*$	reference parameter value	$152.67658\ rpm$
$\mathcal{D}_\lambda^* \equiv \lambda^*$	initial coordinate for iteration of the chattering map β	$(0.30697, 0.84867, 0.33665)$
$\delta\theta_f^*$	maximum deviation percentage	0.0001%
$\phi_\alpha - \phi_\infty$	error on estimation of the zero sticking time	$0.4201 * 10^{-5}\ [s]$
$\Phi_{\bar{Y}}$	Monodromy Matrix for an entire period	$\begin{bmatrix} 0.00026 & 0.00005 & 0.05310 \\ 0.01247 & 0.00235 & -0.69201 \\ 0 & 0 & 1 \end{bmatrix}$
$\Theta_{\bar{Y}}^* = A$	Linearization of Θ map in a vicinity of $\mathcal{D}_\lambda^*$	$\begin{bmatrix} 0 & 0 & 0 \\ 0.01597 & 0.00301 & 0.00130 \\ -0.04830 & -0.00912 & -8.55305 \end{bmatrix}$
$1/K_\beta$	inverse of the compensation in y-scale for the mapping β	$3.145 * 10^{-10}$
K_C	compensation in x-scale for the mapping β	$5.24 * 10^{-12}$

6.8 Discussion

After developing an analytical study of the transition into aperiodicity of a stable multi-impacting trajectory with chattering, the following results were obtained.

- An equivalent normal form, for the local map in a vicinity of the phase where periodic sequences with complete-chattering are interrupted has been developed and generalized for smooth-periodically forced impact oscillators.

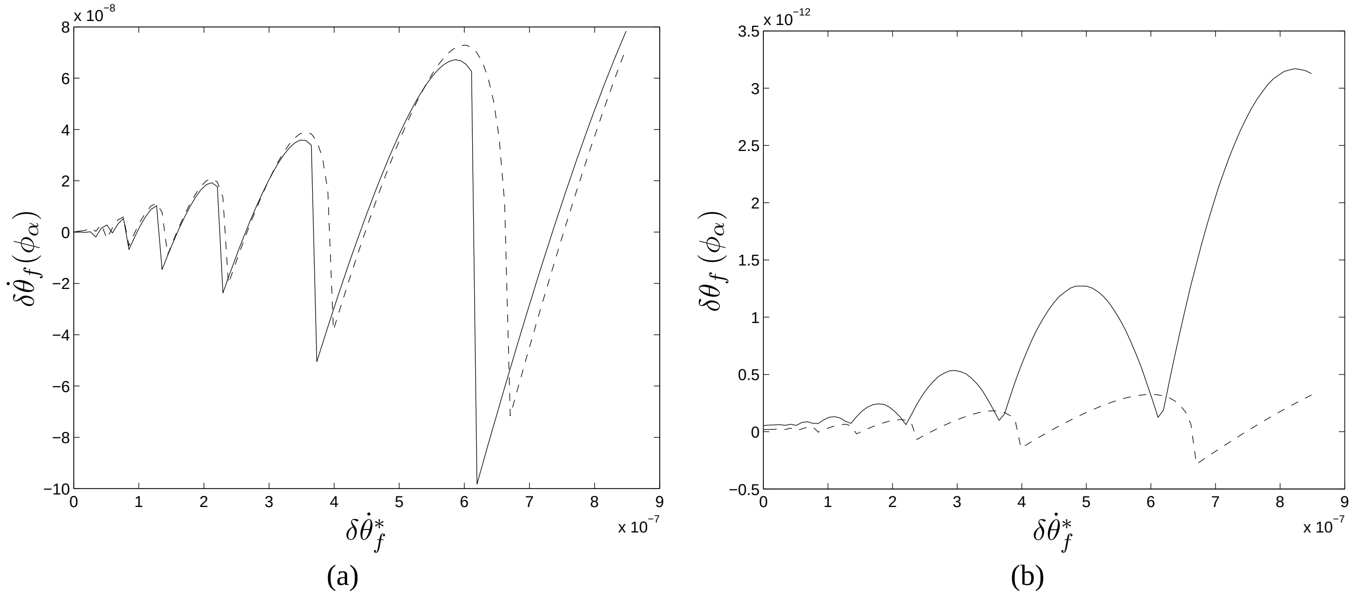

Figure 6.16 — Reconstruction of variations in absolute coordinates for: (a) velocity and (b) position; at the releasing phase ϕ_α by employing (global) information of the local map through a complete period. The perturbation $\tilde{\lambda}$ has been applied in the direction of velocity. For both, the solid line represents calculations performed by simulation of system flow, with dashed mapping predictions.

- Numerical analysis has shown good agreement between the analytical predictions and the simulation results when perturbations are considered close to the boundary of the chattering region $\mathcal{D}$ for a realistic cam-follower system.

- Numerical results have also demonstrated, that the extension of local analysis across the overall periodic trajectory is constrained by the impossibility to perform perturbations at an infinitesimal range.

- In practical terms, this implies the necessity to compensate by appropriate scaling the analytical formulas, taking advantage of the repetitive structure of the mapping.

Chapter 7

Conclusions

In this Thesis we presented the analysis and explanation of the complex dynamics experienced by a practical impact oscillator: the cam-follower system. The study of the system was performed by combining experimental, numerical and analytical procedures that allowed to unveil the coexistence between a classical period-doubling route to chaos and a novel discontinuity-induced bifurcation phenomenon generated at interruption of a periodic complete-chattering motion.

In particular, after introducing in **Chapter 2** some background of the general theory of piecewise-smooth dynamical systems, in **Chapter 3** the description was developed of the main techniques used to perform the numerical study of models with discontinuities. Attention was focused onto the specific case of complex dynamics introduced by the detachment of the follower from the cam.

Chapter 4 dealt with this topic in detail within the context of the practical problem associated to valve-float in combustion engines. Main contributions of this Chapter included the design, modelling, implementation and instrumentation of a versatile experimental rig for the analysis and verification of the analytical predictions related with complex dynamics and bifurcation behaviour of piecewise-smooth dynamical impacting systems. Results of this Chapter were published in [6, 10, 5]. The work presented in this Chapter was partly carried out together with: Stefania Santini, Umberto Montanaro, Gustavo Osorio, Giuseppe Giordano and Giovanni Rea, from the University of Naples - FEDERICO II.

Chapter 5 presented a more in depth numerical study of the cam-follower impacting model resembling the dynamical features captured experimentally. The main contributions of this Chapter are: the employment of novel simulation and continuation techniques for explanation of the most representative zones depicted in the stroboscopic bifurcation diagram. Additionally, a novel semi-analytic approach for approximation of the map in a vicinity of the interruption of complete chattering sequences was performed numerically. The results of this Chapter will be submitted for publication in [5, 7]. The work presented in this Chapter was partly carried out together with: Petri Piiroinen (from the National University of Ireland - Galway), Phanikrishna Thota and Joanna Mason (from the University of Bristol - U.K.) and Gerard Olivar Tost (from the National University of Colombia - Manizales).

Chapter 6 complemented with some analysis the numerical predictions generated in Chapter 5 for the multi-impacting orbit with chattering. In particular, the main contributions of this Chapter included the linking performed between the preliminary results of Budd & Dux in [22] and those of Nordmark & Kitisu in [57]. Also, the adaptation of the results in the latter for a realistic cam-follower impacting model through the development of the equivalent analytical expression for the local map, describing the abrupt transition into aperiodicity experienced by the system after interruption of periodic complete-chattering motion. Related results have been discussed in [9] and [8]. Collaborators of the work presented in this Chapter were: Chris Budd and Stephen Pring (from the University of Bath - U.K.) and again Petri Piiroinen (from the National University of Ireland - Galway).

In summary, we have performed the derivation of experimental, numerical and analytical evidence for a novel discontinuity-induced-bifurcation phenomenon **not fully** explained before in the literature, by means of a structured and integrated study of the dynamical behaviour of a representative model inspired from applications.

7.1 Further research topics

The work described in this Thesis can be continued in many different directions. Some ideas for possible future work are described below.

- Development of the discontinuity mapping (DM) for a multi-impacting orbit with chattering by composition of the chattering map just derived, with the representative equivalent of the remaining part of the trajectory. In this way, generalization of results currently available for single-grazing trajectories [33] will be achieved. In doing so, refinement of calculations in the vicinity of the chattering interruption should be performed, as well as to derive a generalized linear equivalent for a multi-impacting, non-chattering orbit.

- Experimental verification of the incidence on the dynamics of a cam-follower impacting system for discontinuous profiles. To this aim, preliminary results achieved by Osorio et al [65] [66], can be employed in parallel with the facilities of the experimental rig, for testing the discontinuous-acceleration profile currently available.

- Analysis of further novel bifurcation scenarios generated by modifying the features of the discontinuity boundary. As an example, consider a multi-impacting trajectory experiencing complete chattering motion being accumulated into a boundary intersection of corner type. Hence, it will be likely for the system to experience some sort of corner-chattering phenomenon.

- Implementation of control strategies to manipulate in a desired manner the dynamics of the cam-follower system.

- Further investigation in continuation algorithms of piecewise-smooth dynamical systems, pointing towards detection of DIBs (i.e. monitor functions) and the possible employment of predicted solution branches as *a priori* information for online control purposes.

References

[1] V. Acary. An overview of nonsmooth dynamical systems. higher order Moreau's sweeping process, numerical methods and links with optimization. *Optimization and its applications. Oberwolfach reports. Mathematisches Forschungsinstitut Oberwolfach*, 2005.

[2] V. Acary and F. Pérignon. Modelling, Simulation and Control of Nonsmooth Dynamical Systems: software website. Technical report, INRIA, Grenoble - France, http://siconos.gforge.inria.fr/, 2006.

[3] C. E. Aguiar and F. Laudares. Listening to the coefficient of restitution and the gravitational acceleration of a bouncing ball. *American Journal of Physics*, 71:499—-501, 2003.

[4] K. Akiba and H. Sakai. A comprehensive simulation of high speed driven valve trains. *SAE Transactions - Society for Automotive Engineers*, 1981.

[5] R. Alzate, M. di Bernardo, G. Giordano, G. Rea, and S. Santini. Experimental and numerical investigation of coexistence, novel bifurcations and chaos in a cam-follower system. *Submitted to SIAM*, May 2008.

[6] R. Alzate, M. di Bernardo, U. Montanaro, and S. Santini. Experimental and numerical verification of bifurcations and chaos in cam-follower impacting systems. *Nonlinear Dynamics - Springer. The Netherlands*, 50, N^o 3:409–429, November 2007.

[7] R. Alzate, M. di Bernardo, and P. T. Piiroinen. Transition from complete to incomplete chatering in impacting systems: the case of a representative cam-follower device. *In preparation*.

[8] R. Alzate, M. di Bernardo, and P. T. Piiroinen. Interrupted chattering and related non-smooth events causing destabilization of dynamics in systems with impacts. In *Proceedings of the Dynamics Days Europe 2008 conference,* August 2008. Delft, The Netherlands.

[9] R. Alzate, M. di Bernardo, and P. T. Piiroinen. Chattering: a novel route to chaos in cam-follower impacting systems. In *Proceedings of the 8th World Congress on Computational Mechanics WCCM8 and 5th European Congress on Computational Methods in Applied Sciences and Engineering ECCOMMAS 2008*, July 2008. Venice, Italy.

[10] R. Alzate, M. di Bernardo, and S. Santini. Deliverable wp6. d6.4: Experimental validation of nonsmooth bifurcations. part iii. Technical report, SICONOS Project - University of Naples, 2006.

[11] M. Anitescu and F. A. Potra. A time-stepping method for stiff multibody dynamics with contact and friction. *International journal for numerical methods in engineering*, 55:753–784, 2002.

[12] B. Azejczyk, T. Kapitaniak, J. Wojewoda, and R. Barron. Experimental-observation of intermittent chaos in a mechanical system with impacts. *Journal of Sound and Vibration*, 178:272–275, 1994.

[13] P. Barkan. Calculation of high speed valve motion with a flexible overhead linkage. *SAE Transactions - Society for Automotive Engineers*, 61:687–700, 1953.

[14] P V Bayly and L N Virgin. An experimental study of an impacting pendulum. *Journal of Sound and Vibration*, 164(2):364–374, 1993.

[15] A. Bernstein. Listening to the coefficient of restitution. *American Journal of Physics*, 45:41—-44, 1977.

[16] S. R. Bishop. Impact oscillators. *Phil. Tran. R. Soc. Lon.*, pages 347–351, 1994.

[17] B. Blazejczyk-Okolewska, K. Czolczynski, and J. Kapitaniak, T. Wojewoda. *Chaotic Mechanics in Systems with Impacts and Friction*. World Scientific, Singapore, 1999.

[18] B. Brogliato. *Nonsmooth Mechanics – Models, Dynamics and Control*. Springer–Verlag, New York, 1999.

[19] G. Brooker. Development of a w-band scanning conscan antenna based on thetwist-reflector concept. *Proceedings of the ICMMT - 2nd International Conference on Microwave and Millimeter Wave Technology*, pages 436–439, 2000.

[20] C. Budd and F. Dux. *The dynamics of impact oscillators*. PhD thesis, University of Bristol, 1992.

[21] C. Budd and F. Dux. Intermittency in impact oscillators close to resonance. *Nonlinearity*, 7:1191–1224, 1994.

[22] C. Budd and F. Dux. Chattering and related behaviour in impact oscillators. *Philosophical transactions: physical sciences and engineering*, 347, N^o 1683:365–389, May 1994.

[23] C. Budd, F. Dux, and A. Cliffe. The effect of frequency and clearance variations on single-degree-of-freedom impact oscillators. *Journal of sound and vibration*, 184, N^o 3:475–502, 1995.

[24] C.J. Budd and P. Piiroinen. Corner bifurcations in non-smoothly forced impact oscillators. *Physica D*, 220:127–145, 2006.

[25] K. Camlibel and J.M. Schumacher. *Complementarity methods in the analysis of piecewise linear dynamical systems*. PhD thesis, Katholieke Universiteit Brabant, 2001.

[26] A. Carlini, A. Rivola, G. Dalpiaz, and A. Maggiore. Valve motion measurements on motorbike cylinder heads using high speed laser vibrometer. *Proceedings of the Conference on Vibration Measurements by Laser Techniques*, 2002.

[27] J. A. Caton. Operating charactheristing of a spark-ignition engine using the second law of thermodynamics: Effect of speed and load. *SAE Transactions - Society for Automotive Engineers, paper 2000-01-0952*, 2000.

[28] An Chae and J. Hollerbach. Dynamic stability issues in force control of manipulators. *Proceedings of the IEEE International Conference on Robotics and Automation*, 4:890–896, 1987.

[29] T. D. Choi, O. J. Eslinger, C. T. Kelley, J. W. David, and M. Etheridge. Optimization of automotive valve train components with implicit filtering. *Optimization and Engineering*, 1(1):9 – 27, 2000.

[30] L. Demeio and Lenci S. Asymptotic analysis of chattering oscillations for an impacting inverted pendulum. *Quarterly Journal of Mechanics and Applied Mathematics*, 59(3):419—-434, 2006.

[31] B. Demeulenaere and J. De Schutter. Dynamically compensated cams for rigid cam-follower systems with fluctuating cam speed and dominating inertial forces. *IEEE/ASME International Conference on Advanced Intelligent Mechatronics*, pages 763 – 767, 2001.

[32] A. Dhooge, W. Govaerts, Y. Kuznetsov, W. Mestrom, A. Riet, and B. Sautois. MATCONT and CL_MATCONT: continuation toolboxes in Matlab. Technical report, Universiteit Gent, Belgium; Utrecht University, The Netherlands, 2006.

[33] M. di Bernardo, C. J. Budd, A. R. Champneys, and P Kowalczyk. *Bifurcation and Chaos in Piecewise Smooth Dynamical Systems – Theory and Applications*. Springer–Verlag, UK, 2007.

[34] M. di Bernardo, P. Kowalczyk, and A. Nordmark. Bifurcations of dynamical systems with sliding: derivation of normal-form mappings. *Physica D*, 170:175–205, 2002.

[35] D. J. Dickrell, D. B. Dooner, and W. G. Sawyer. The evolution of geometry for a wearing circular cam: Analytical and computer simulation with comparison to experiment. *Journal of Tribology*, 125:187 – 192, 2003.

[36] E. Doedel. Auto: a program for the automatic bifurcation analysis of autonomous systems. In *Proceedings of the 10th Manitoba Conference on Numerical Mathematics and Computing*, Sept, 1980. Winnipeg, Canada.

[37] E. J. Doedel. Lecture notes on numerical analysis of nonlinear equations. Concordia University, Montreal - Canada, 2007.

[38] T. L. Dresner and P. Barkan. New methods for the dynamical analysis of flexible single-input and multi-input cam-follower systems. *Journal of Mechanical Design*, 17:151, 1995.

[39] dSPACE. DS1104 R&D Controller Board: Features. Technical report, dSPACE Inc., http://www.dspaceinc.com/ww/en/inc/home.cfm, 2005.

[40] S. Foale. Analytical deternination of bifurcations in an impact oscillator. *Proc. R. Soc. Lon.*, pages 354–364, 1994.

[41] J. Guckenheimer and P. Holmes. *Nonlinear oscillations, dynamical systems, and bifurcations of vector fields*. Springer-Verlag, 1983.

[42] H. R. Hamidzadeh and M. Dehghani. Dynamic stability of flexible cam follower systems. *Proceedings of the Institution of Mechanical Engineers, Part K: Journal of Multi-body Dynamics*, 213(1):45 – 52, 1999.

[43] Hengstler. Incremental Shaft Encoders: Type RI 58. Technical report, HENGSTLER, http://www.hengstler.de/, 2001.

[44] J. Heywood. *Internal combustion engine fundamentals*. McGraw-Hill, New York, 1998.

[45] D. J. Higham and N. J. Higham. *Matlab guide*. Philadelphia: Society for Industrial and Applied Mathematics, 2000.

[46] N. Hinrichs, M. Oestreich, and K. Popp. Experiments, modelling and analysis of friction and impact oscillators. *Zeitschrift fur angewandte mathematik und mechanik*, 79:S95–S96, 1999.

[47] C.S. Hsu. Global analysis by cell mapping. *International Journal of Bifurcation and Chaos*, 2:727–771, 1992.

[48] K.H. Johansson, J. Lygeros, S. Sastry, and M. Egerstedt. Simulation of zeno hybrid automata". *IEEE Conference on Decision and Control. Phoenix, AZ*, 1999.

[49] H. B. Keller. *Numerical solution of bifurcation and nonlinear eigenvalue problems, in: P.H. Rabinowitz (Ed.), Applications of bifurcation theory*. Academic Press, New York, 1977.

[50] M. P. Koster. *Vibrations of Cam Mechanisms*. Phillips Technical Library Series, Macmillan Press Ltd.: London, 1974.

[51] M. Kushwaha and H. Rahnejat. Valve-train dynamics: a simplified tribo-elasto-multi-body analysis. *Proceedings of the Institution of Mechanical Engineers, Part K: Journal of Multi-body Dynamics*, 214:1464–4193, 2001.

[52] Y. A. Kuznetsov. *Elements of applied bifurcation theory*. Springer-Verlag, New York, 1998.

[53] L. Labous, A. Rosato, and R. N. Dave. Measurement of collisional properties of spheres using high-speed video analysis. *Physical Review E*, 56:5717—-5725, 1997.

[54] J. J. Liou, G. Huang, and W. Hsu. Experimental study of a variable pressure damper on an automotive valve train. *Journal of mechanical design*, 120(2):279–281, 1998.

[55] N. Metropolis and S. Ulam. The Monte Carlo method". *Journal of the american statistical association*, 44. N° 247:335–341, 1949.

[56] A. Nordmark. *Grazing conditions and chaos in impacting systems*. PhD thesis, Royal Institute of Technology, Stockholm, Sweden, 1992.

[57] A. Nordmark and R. Kisitu. On chattering bifurcations in 1 dof impact oscillator models. *Royal Institute of Technology, Sweden*, 2003.

[58] A. Nordmark and P. T. Piiroinen. Simulation and stability analysis of impact systems with complete chattering. *Submitted*.

[59] A. B. Nordmark. Non-periodic motion caused by grazing incidence in impact oscillators. *Journal of sound and vibration*, 2:279–297, 1991.

[60] A. B. Nordmark. Discontinuity mappings for vector fields with higher order continuity. *Dynamical systems: An international journal*, 17:359–376, 2002.

[61] R. Norton. *Cam design and manufacturing handbook*. Industrial-Press, Inc, New York, 2002.

[62] R.L. Norton, J. Eovaldi, D.and Westbrook, and R. L. Stene. Effect of the Valve-Cam Ramps on Valve Train Dynamics. *SAE Transactions - Society for Automotive Engineers, paper 1999-01-0801*, 1999.

[63] M. Oestreich, N. Hinrichs, K. Popp, and C. J. Budd. Analytical and Experimental Investigation of an Impact Oscillator. *Proceedings of the ASME - American Society Of Mechanical Engineers, 16th Biennal Conference on Mechanical Vibrations and Noise*, DETC97VIB-3907:1–11, 1997.

[64] OPTEK. Reflective Object Sensors: types OPB703, OPB704 and OPB705. Datasheet. Technical report, Optek Technology, Inc. Texas., 1996.

[65] G. Osorio, M. Di Bernardo, and S. Santini. Chattering and complex behavior of a Cam-follower system. In *Proceedings of the European Nonlinear Dynamics Conference (ENOC)*, 2005. Eindhoven, The Netherlands.

[66] G. Osorio, M. di Bernardo, and S. Santini. Corner-impact bifurcations: a novel class of discontinuity-induced bifurcations in cam-follower systems. *SIAM JOURNAL ON APPLIED DYNAMICAL SYSTEMS*, 7(1):18–28, 2008.

[67] E. Ott. *Chaos in Dynamical Systems*. Cambridge University Press, Second Edition, 2002.

[68] F. Peterka. Part 1: Theoretical analysis of n-multiple $(1/n)$-impact solutions. *CSAV Acta Technica*, 26(2):462–473, 1974.

[69] F. Peterka. Results of analogue computer modelling of the motion. Part 2. *CSAV Acta Technica*, 19:569–580, 1974.

[70] F. Peterka. Transition to chaotic motion in mechanical systems with impacts. *Journal of sound and vibration*, 154:95–115, 1992.

[71] P. T. Piiroinen and H. Dankowicz. *Recurrent dynamics of nonsmooth systems with applications to human gait*. PhD thesis, Royal Institute of Technology, Sweden, 2002.

[72] P. T. Piiroinen and Y. A. Kuznetsov. An event driven method to simulate filippov systems with accurate computing of sliding motions. *ACM Transactions on Mathematical Software*, 34(3), 2008.

[73] P. T. Piiroinen, L. N. Virgin, and A. R. Champneys. Chaos and Period-Adding; Experimental and Numerical Verification of the Grazing Bifurcation. *Journal of Nonlinear Science*, 14:383–404, 2004.

[74] E. Raghavacharyulu and J.S. Rao. Jump Phenomena in Cam-Follower Systems a Continuous-Mass-Model Approach. *American Society of Mechanical Engineers, Proceedings of the Winter Annual Meeting*, pages 1–8, 1976.

[75] H. A. Rothbart. *Cams-Design, Dynamics, and Accuracy*. Wiley, 1956.

[76] A. Salinger et al. Library Of Continuation Algorithms: theory and implementation manual. Technical report, Sandia National Laboratories, Albuquerque, USA, 2002.

[77] Sanyodenki. SANMOTION Q: AC Servo Systems. Technical report, Sanyo-Denki Ltd, http://www.sanyo-denki.com/, 2002.

[78] S. Seidlitz. Valve train dynamics - a computer study. *SAE Transactions - Society for Automotive Engineers*, 1989.

[79] R. Seydel. *Practical bifurcation and stability analysis: from equilibrium to chaos*. Springer Verlag, 2nd edition, 1994.

[80] S. W. Shaw and P. J. Holmes. Periodically forced linear oscillator with impacts: Chaos and long-period motions. *Phys. Rev. Lett.*, 51:623–626, 1983.

[81] S. W. Shaw and P. J. Holmes. A periodically forced piecewise linear oscillator. *Journal of sound and vibration*, 90:129–155, 1983.

[82] R. H. Sherman and P. N. Blumberg. The influence of induction and exhaust processes on emissions and fuel consumption in the spark ignited engine. *SAE Transactions - Society for Automotive Engineers, paper 770990*, 1997.

[83] I Stensgaard and E. Laegsgaard. Listening to the coefficient of restitution – revisited. *American Journal of Physics*, 69:301—-5, 2001.

[84] A. Stensson and A. Nordmark. Experimental investigation of some consequences of low velocity impacts in the chaotic dynamics of a mechanical system. *Philosophical transactions : Physical sciences and engineering. Royal Society of London, A*, 347:439–448, 1994.

[85] S. H. Strogatz. *Nonlinear dynamics and chaos*. Perseus Books Publishing, 1994.

[86] BAE systems. VSG - vibrating structure gyroscope: typical performance guide. Technical report, http://www.besystems.com/, 2007.

[87] M. Teodorescu, V. Votsios, H. Rahnejat, and D. Taraza. Jounce and impact in cam-tappet conjunction induced by the elastodynamics of valve train system. *Meccanica*, 41(2):157 – 171, 2006.

[88] J. Thompson and H. Stewart. *Nonlinear Dynamics and Chaos*. John Wiley, New York, 1986.

[89] P. Thota. *PhD Dissertation: Analytical and Computational Tools for the Study of Grazing Bifurcations of Periodic Orbits and Invariant Tori*, `http://scholar.lib.vt.edu/theses/available/etd-02142007-140350/`. PhD thesis, Department Engineering Science and Mechanics, Virginia Tech, USA., 2007.

[90] P. Thota and H. Dankowicz. TC-HAT ($\widehat{TC}$): A novel toolbox for the continuation of periodic trajectories in hybrid dynamical systems. *SIAM Journal on Applied Dynamical Systems*, 7(4):1283–1322, 2008.

[91] M. D. Todd and L. N. Virgin. An experimental impact oscillator. *Chaos, Solitons and Fractals*, 8:699–714, 1997.

[92] C. Toulemonde and C. Gontier. Sticking motions of impact oscillators. *Euro. J. Mech. A/Solids*, 17(2):339–366, 1998.

[93] T. S. Tumer and Y. Samim Unlusoy. Nondimensional analysis of jump phenomenon in force-closed cam mechanisms. *Mechanism and Machine Theory*, 6:421–432, 1991.

[94] A. M. Urin. Experience with the use of pk-profile joints in agricultural machines. *Research, Design, Calculations, and Experience of Operation of Chemical Equipment Technology, Chemical and Petroleum Engineering*, 34(8):534 – 536, 1998.

[95] D. J. Wagg. Rising phenomena and the multi-sliding bifurcation in a two-degree of freedom impact oscillator. *Chaos, Solitons and Fractals*, 22:541–548, 2004.

[96] D. J. Wagg. Periodic sticking motion in a two-degree-of-freedom impact oscillator. *International Journal of Non-Linear Mechanics*, 40:1076–1087, 2005.

[97] D. J. Wagg. Multiple non-smooth events in multi-degree-of-freedom vibro-impact systems. *Nonlinear Dynamics*, 43:137–148, 2006.

[98] G. Whiston. Singularities in vibro-impact dynamics. *Journal of sound and vibration*, 152:427–460, 1992.

[99] G. S. Whiston. The vibro-impact response of a harmonically excited and preloaded one-dimensional linear oscillator. *J. Sound Vib.*, 115:303–324, 1987.

[100] M. Wiercigroch and B. de Kraker. *Applied Nonlinear Dynamics and Chaos of Mechanical Systems with Discontinuities*. World Scientific Publishing, 2000.

[101] M. Wiercigroch and E. Pavlovskaia. Nonlinear dynamics of vibro-impact systems: Theory and experiments. *Modern Practice In Stress And Vibration Analysis*, 440-4:513–520, 2003.

[102] S. Wiggins. *Introduction to applied nonlinear dynamical systems and chaos*. Springer-Verlag, 1996.

[103] H. S. Yan, M.C. Tsai, and M. H. Hsu. An Experimental Study of the Effect of the Cam Speed on Cam-Follower Systems. *Mechanism and Machine Theory*, 31:397—-412, 1996.

[104] W. Zang and M. Ye. Local and Global Bifurcations of Valve Mechanism. *Nonlinear Dynamics*, 6:301–316, 1994.